Mode of occurrence and geochemistry of magnetite from magnetite ± apatite mineralization in the Singhbhum Shear Zone, eastern India: implications for mineralization and trace element-based discriminators

Submitted to fulfill the requirements for the degree of
Doctor of Philosophy (Science)

by

Subhadip Adak

Department of Geological Sciences,
Jadavpur University, Kolkata-700032, India
June, 2022

Dedicated to

My parents

My Supervisor

And to Alexandra Elbakyan

Acknowledgement

First of all I want to thank my supervisor professor Dipak Chandra Pal. I am not able to write precisely about how much I am indebted to my supervisor as whatever I'll write, it will still remain underrepresented. I just want to say that apart from introducing me to the art of using geochemistry as a tool to unravel complex geological history this person is acknowledged not only because he is my supervisor, but also for trying hard not to break my confidence when I am asking apparently stupid questions .

I am grateful to University Grants Commission, Government of India for providing me the fellowship for the tenure period. The expenditure for field work and EPMA and LA-ICPMS analyses were met partly from "Departmental support towards upgradation in research" in the thrust area "Advanced material research" to my supervisor through JU RUSA 2.0 of the University Grants Commission, Government of India and also from the financial support by Centre of Advanced Studies (CAS) of the Department of Geological Sciences, Jadavpur University. I am thankful to A. K. Sarangi for providing samples from the vertical shaft and also for granting us the permission to work in the mine.

I want to acknowledge professor Dewashish Upadhay, professor Biswajit Mishra (of IIT Kharagpur) for providing their lab to analyze (in SEM, EPMA and LA-ICPMS) the samples used in the present study. Professor Kamal lochan Pruseth is thanked for his help when one of those machines malfunctioned.

Rupashree Das, Sameer Ranjan , Sarita Patel, Kumar Abhinay, Boddepalli Govindarao, Ashim Patel, Suman Mondal are thanked for their help during the analysis at IIT Kharagpur and Rupashree Saha's name needs to be bold/italicized as she didn't just stop by doing the help needed during analysis.

Souryadip Ghosh, Rajdeep Mondal, Kushal Mandal, Devalina Jha and Arijit Das who worked under my supervisor for their Masters dissertation, were extremely helpful during the field and subsequent tasks that needed to be done. Eileena Das is acknowledged here for her help during the field work but she should actually be thanked for having expertise on 'Miyazaki' or 'Geisha' or even 'Sumo wrestling' and spreading some of her knowledge sporadically. On the other hand Kinjal Ganguly is acknowledged for having deep knowledge about music, cinema, society etc. (inclusive of 'Japan') and sharing them whenever/wherever

possible (not ‘sporadically’). Shibasish Mukhopadhyay, another doctoral student of my supervisor is thanked for his help during the printing of my thesis.

Although Abu Saeed Baidya and Giridas Maity should be acknowledged for zillions of reasons but I prefer not to do that and so Abu is acknowledged just because he suggested me this specific paper in the initial stage of my PhD – “Hydrothermal magnetite – A review” by Patrick Nadoll and Giridas is thanked for sharing his knowledge about Western classical music. Perhaps a ‘Ctrl-F’ inserting ‘Nadoll’ would shed some light on the importance of Abu’s suggestion.

Debadrita Jana, Debmalya Sain, Biplab Mahata, Rhitam Mitra, Debarshi Das, Krittish Roy, Sudip Kumar Mandal, Anupam Shikari all are acknowledged for being there when I needed their help or something of that sort even after knowing that the corollary is not true.

Pankaj Mahata and Arpan Hota are thanked for listening to my frequent rants about research progress/problems although their research/work area ‘Power electronics’ is miles apart from mine. They’ve played the role of a great listener so that I can sharpen my skills on ‘How to present your Science to people from different subject background’. Moulika Sajwal is thanked for the same reason because she listens to me although it’s a great deal for her not to talk for apparently long time span.

There are some people who are ‘strange’ in a way as they’ve asked me to put their name in the acknowledgement section of my PhD thesis (so I’m doing it). Swarnali Barua and Mohai Menul Hasan are that kind of a person for me. Bidisha Basu and Sayanta Das is acknowledged for giving me the feeling that wherever I go/whatever I do, I can never make food tastes so brilliant (put any adjective) like them. Pragnaditya Malakar is thanked and I don’t even know why. On the contrary Sohom Roy is acknowledged for having long serious scientific discussion which seems to be beneficial for both of us and to scientific purpose in general. There are also some people who helped me unexpectedly (perhaps some of them will never know that they deserve a place in this list of acknowledgement unless I go and tell them). Dhananjoy Patra is one of such people. In this regard I also want to mention that I don’t want to thank my family as it may sound too clichéd.

I am thankful to Asmita Banerjee for gifting me a book which I consider is somewhat life-changing. The name of the book is “Man’s Search for Meaning”. I am grateful to Shamik Sarkar for recovering field photographs from a defected memory card using skills I was

unaware of otherwise I have to run to field again during pandemic which was probably the only option left for me.

Although Karl Marx said “Last words are for fools who haven’t said enough” in a different context but the thing is that this statement is actually his last statement and it amazes me to some extent. However I think that last words are always important for those who have said enough like Karl Marx and also for people who haven’t said enough. So it is advised to the reader that the last sentence of this acknowledgement section should be taken very seriously. I think that this is high time to consider that each thesis ‘acknowledgement section’ should also contain a mandatory incorporation of ‘Un-acknowledgement’ section. A limit on words also must be suggested in order to keep the section not too heavy.

Abstract

The Singbhum Shear Zone (SSZ) located in eastern India is one of the most important polymetallic mineralized provinces in India and known for multiple locales of U, Cu, magnetite-apatite mineralization and elevated REE concentration in the U ores. The present study investigates magnetite mineralization in different locations of this shear zone to decipher the origin of magnetite ± apatite mineralization integrating the mode of occurrence, texture and geochemistry of magnetite. Magnetite occurring in a wide variety of host rocks and bearing the imprints of multiple hydrothermal alterations and superimposed deformation and metamorphism gives the present study an opportunity to decipher the physicochemical constraints attached to the mineralizing processes.

In Bagjata, magnetite is associated with different alteration types. Magnetite in brecciated apatite-magnetite rocks of Ca-Fe ± K alteration and magnetite in biotite schist of K-Fe± LREE alteration assemblage show consistently higher concentrations of Vanadium and Ga and higher V/Sn ratios than the magnetite in chlorite schist of hydrolytic alteration, which indicates that the former alterations occurred at relatively higher T and lower fO_2 conditions. The interpretation on relative temperature of formation is in accordance with the thermometric results from Mg-in-magnetite thermometry, Ti-in-biotite thermometry and chlorite thermometry. Magnetite associated with all the aforementioned hydrothermal alterations are discriminated compositionally from magmatic magnetite using Ti vs. Ni/Cr diagram.

In Pathargora, magnetite occurs in magnetite-ilmenite pods and magnetite + apatite veins with biotite selvages; the former is interpreted to have formed by magmatic process whereas the latter formed by hydrothermal process. Unlike in Bagjata, the Ti vs. Ni/Cr and (Ti + V) wt% vs. (Al + Mn) wt% discriminators do not correlate with the origin of magmatic magnetite in Pathargora, the latter discriminator has been suggested to discriminate magnetite from different types of deposits including iron oxide-copper-gold (IOCG), Kiruna apatite–magnetite/iron Oxide apatite (IOA), banded iron formation (BIF), porphyry, skarn and Fe-Ti, V deposits. The inconsistency has been interpreted to be the result of subsolidus oxy-exsolution of ilmenite from and associated change in host magmatic magnetite chemistry. The effect of subsolidus oxy-exsolution is further manifested in the result of Mg-in-magnetite thermometry where the resulting T is higher for hydrothermal magnetite in magnetite + apatite vein than the magmatic magnetite because Mg was partitioned into ilmenite during oxy-exsolution resulting in underestimation of temperature. The hydrothermal variety of

magnetite in Pathargora formed from fluid which is REE-rich, F^--dominated and reducing in nature as evidenced from the specific values of Eu/Eu* and Ce/Ce*, decoupling of Y from Ho and geochemistry of accompanying fluor-apatite.

The magnetite in Mohuldih U deposit and Turamdih area is hosted in banded magnetite quartzite akin to magnetite formed by sedimentary processes such as Banded Iron Formation. However, the magnetites from the bands are rich in most of the trace elements which are typical of high temperature magnetite and opposed to low T sedimentary depositional conditions. Based on trace element geochemistry including REEs the magnetite has been interpreted to form by hydrothermal/metamorphic fluid-induced process with significant inputs possibly from a mafic protolith. High concentrations of Ga and V and low concentration of Cr in Turamdih magnetite alongside the presence of ilmenite ± apatite instead of rutile accompanying magnetite in case of neighbouring Mohuldih hints at variation of formation conditions for magnetite between these two areas, albeit being hosted in similar banded quartzite unit.

The results from the deposit-type discriminators using (Ti + V) wt% vs. (Al + Mn) wt% and (Ti + V) wt% vs. Ni/(Cr + Mn) wt% - two of the most widely used plot yield conflicting results for magnetite of the present study and often the results from these two plots, suggested to be used in conjunction, vary widely. In case of Bagjata where the magnetites are of indisputable hydrothermal origin and the alteration patterns emerging from the bulk rock chemistry are indicative of their similarity to IOCG-like alteration pattern, only a few samples remain restricted to the domain assigned for IOCG-type deposits. On the contrary using some key transitional elements such as Vanadium and Ni and post-transitional elements such as Ga, the present study demonstrate that magnetite from the IOCG deposits can be discriminated from magnetite from the IOA deposits i.e Kiruna-type (*sensulato*). The suggested discriminator of V/Ni vs. Ni/Ga also separate magnetite associated with HT K-Fe alterations from the magnetite associated with the HT Ca-Fe alteration using magnetite from globally-known IOCG deposits (Igrape Bahia, Alemao, Alvo, Salobo and Sossego from Carajás province, Brazil; Ernest Henry and Olympic dam from Australia; Candelaria from Chile, and Kwyjibo from Canada) and IOA deposits (Kiruna and Rektorn from Sweden; El Romeral from Chile; Pilot Knob; Pea Ridge and Lyon mountain from USA and Savage river deposit). The same plot successfully discriminates magnetite and biotite in U-mineralized (containing uraninite) rock from non-mineralized rock. This study suggests use of key first row transition and post transition elements such as V, Mn, Co, Ni and Ga is key to the success of trace elements based discrimination.

Table of Contents

List of Figures

List of Tables

Chapter 1 Introduction

1.1 Introduction

Understanding ore-forming processes utilizing mode of occurrences and trace element geochemistry of robust mineral phases (e.g. magnetite, apatite, tourmaline) has been a key step forward refining our existing knowledge on ore-genesis after the recent advancements in in-situ micro-analytical techniques such as Laser Ablation Inductively Coupled Plasma Mass Spectrometer (LA-ICPMS) and Secondary Ion Mass Spectrometer (SIMS).

Magnetite is an ubiquitous accessory mineral in many igneous, sedimentary, and metamorphic rocks and also a common mineral in ore deposits formed via magmatic/magmatic-hydrothermal, hydrothermal and sedimentary process. Many of these ore deposits hosts several economically important critical metals such as U, Cu and REEs and the demands of these metals are on the rise~~in rise~~. Studying magnetite as a petrogenetic indicator thus provides multifaceted benefits both by understanding the underlying physicochemical process of formation and to fingerprint the traces of critical metal mineralization. In this introductory chapter, the regional geology of the Singhbhum Craton and a brief overview of the polymetallic mineralization in Singhbhum Shear Zone (SSZ) along with the description of local geology in and around the study area are provided. Previous metallogenic models will be reviewed in addition to the latest/existing models related to the polymetallic mineralization in the SSZ and the ever-standing debates surrounding it. In the following section the use of magnetite in understanding the petrogenesis or to reveal the deposit type affiliation will be discussed with the context of how understanding the magnetite mineralization in Singbhum Shear Zone can help us to

understand the process of formation and also resolve the age old dilemma/debate about the polymetallic mineralization in SSZ. Aside that in the preceding section, some of the key areas

would be mentioned which remained underexplored/not at all explored in order to utilize the other potential implications of magnetite as an accessory mineral. In the given context, this chapter ends with categorizing the concise objective and methodologies which have been used in the present work and outlining the chapters of this thesis.

1.2. Geology and polymetallic mineralization in the Singhbhum Shear Zone: A brief overview

1.2.1 Regional Geology

Peninsular India comprises of 5 major cratons namely Aravalli, Bundelkhand, Singhbhum, Dharwar and Bastar craton and these cratons are surrounded by Proterozoic Mobile Belts, collectively known as The Greater Indian Proterozoic Fold Belt (GIPFOB) (Fig. 1.1) (adapted from Jain et al., 2020). The Singhbhum craton and supracrustal provinces in eastern India records evidences of Hadean to Neoproterozoic rocks (Miller et al., 2018; Chaudhuri et al., 2018) and preserves several generations of gneisses, granites and greenstone sequences providing important insights about supercontinent assembly and breakdown, pre-plate tectonic differentiation of the crust and mantle and early oxygenation of the atmosphere (Mukhopadhyay et al., 2014; Dey et al., 2017; Kumar et al., 2017; Das et al., 2017; Chowdhury et al., 2021). The ~200 km long arcuate shaped brittle-ductile (Ghosh and Sengupta, 1987; Sengupta and Ghosh, 1997) Singhbhum Shear Zone occurs close to the boundary between the Archaean cratonic nucleus to the south and the Proterozoic North Singhbhum Mobile Belt to the north (Fig. 1.2).

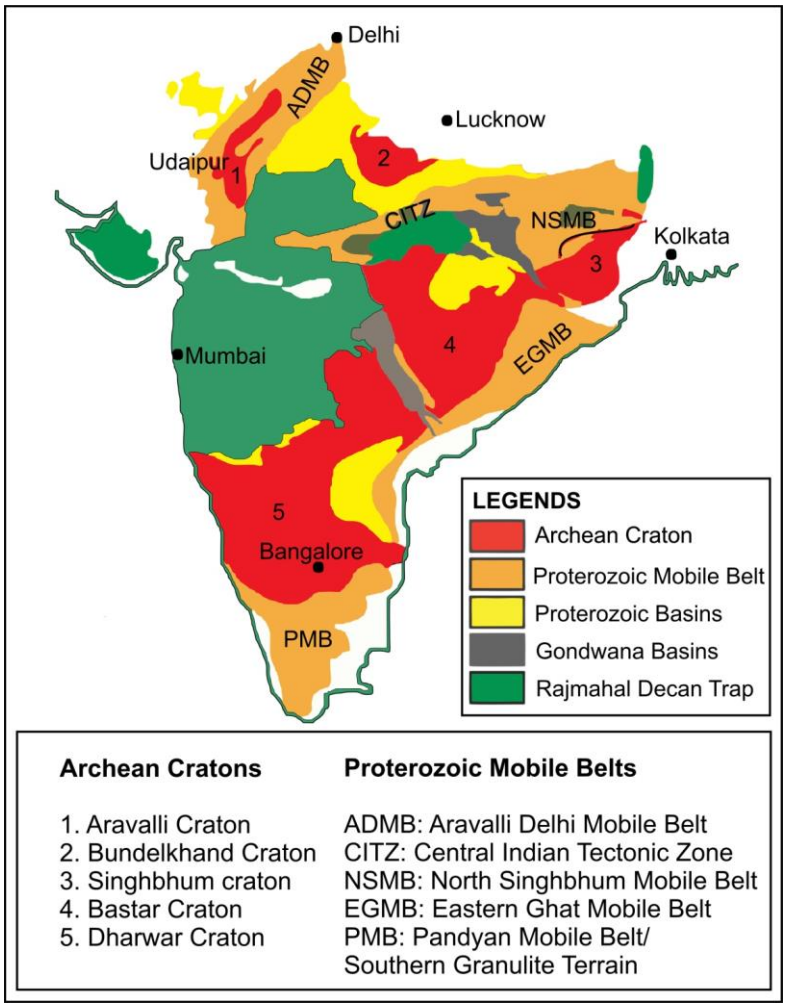

Figure 1.1 Distribution of Archean Cratons and Proterozoic Mobile Belts in the Indian subcontinent

Note the position of the Archean Singhbhum craton and the eastern extension of the Central Indian tectonic Zone, known as North Singhbhum Mobile Belt (NSMB). The Singbhum Shear zone occurs along the boundary between Archean Singhbhum craton and Proterozoic North Singhbhum Mobile Belt NSMB). The Singbhum Shear zone occurs along the boundary between Archean Singhbhum craton and Proterozoic North Singhbhum Mobile Belt. The map is redrawn from Jain et al. (2020).

The Singhbhum craton, a granite-greenstone terrain, comprises Paleoarchean tonalite-trondhjemite-granodiorite-granite (Older Metamorphic Tonalite Gneisses and Singhbhum granitoid complex; 3.45–3.29 Ga) (Moorbath et al., 1986; Goswami et al., 1995; Mishra et al., 1999; Acharyya et al., 2010; Tait et al., 2011; Nelson et al., 2014; Upadhyay et al., 2014; Dey et al., 2017; Olierook et al., 2019; Pandey et al., 2019), Paleoarchean to Mesoarchean high-grade supracrustals (Older Metamorphic Group) and greenstone sequences (low-grade volcano-sedimentary rocks of the Iron Ore Group) (Saha, 1994; Mukhopadhyay et al., 2008). Proterozoic Dhanjori, Jagannathpur and Simlipal volcano-sedimentary basins surround the Archean cratons. The craton is bordered on the north by the supracrustal province of the North Singhbhum Mobile Belt comprising the Chaibasa, Dhalbhum, Dalma and Chandil Formations (from south to north). The rocks in the North Singhbhum Mobile Belt are interpreted to have deposited in rift basins diachronously over a protracted period (Mazumder and Sarkar, 2004; De et al., 2015; Mazumder et al., 2015; Bhattacharya et al., 2015; Olierook et al., 2019)

1.2.2 Local Geology: Geology of the Singhbhum Shear Zone (SSZ)

The Singhbhum Shear Zone, an arcuate structure, occurs between the Mesoarchean Singhbhum craton and Mesoproterozoic North Singhbhum Mobile Belt (NSMB). The SSZ is a brittle-ductile shear zone that passes close to the stratigraphic contact between the Chaibasa Formation and the Dhanjori Group in the east and between Chaibasa Formation and Iron Ore Group on the West (Fig. 1.2). Thickness of the shear zone is variable - comparatively narrower (<1 kKm. of width from Narwapahar deposit towards the Eastern extension of this shear zone) compared to the western segment where the thickness of the shear zone reached

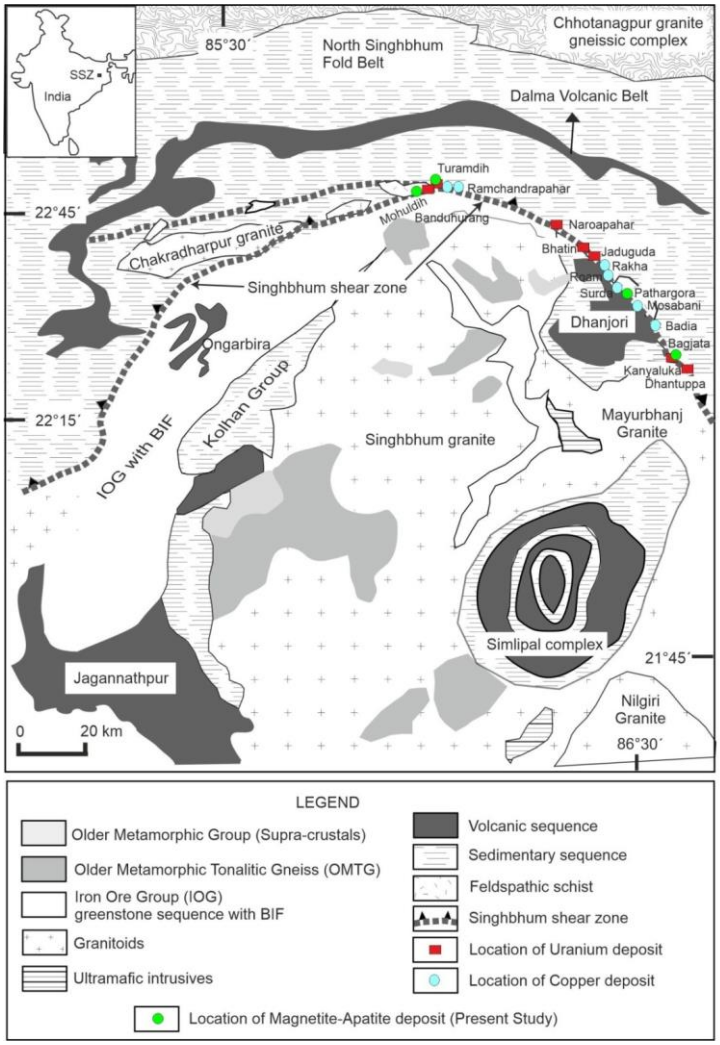

Figure 1.2 Regional geologic map of the eastern Indian shield showing the stretch and locations of the Singhbhum Shear Zone

Note the location of magnetite-apatite deposit/mineralized areas (only the areas covered in the present study) are shown in the map along with the important U-Cu deposits over the regional stretch of the Singhbhum Shear Zone. (redrawn from Saha, 1994)

>3 km of width and extending towards the Western extension of this shear zone (Sarkar and Gupta, 2012). In the Western segment, the SSZ get bifurcated with Chakradharpur Granite in the middle (Figure 1.2). The different rock types in the shear zone are albite schist/feldspathic schist (described as "soda granite" by Dunn and Dey, 1942) biotite schist, quartz–biotite schist, chlorite schist, quartz–chlorite schist, sericite schist, quartz–sericite schist, garnetiferous muscovite schist, tourmalinite (tourmaline bearing rocks, tourmaline exceeding >15% in modal abundances), quartzite, meta-conglomerate, kyanite-quartzite and kyanite-sericite schist (Pal et al., 2009, 2011; Sarkar and Gupta, 2012; Pal et al., 2021).

Mylonitization is very common in rocks of Singhbhum Shear Zone, varying in orientation and style. Mylonitized rocks of the SSZ shows down-dip stretching lineation and the mylonitic foliation is further folded by progressive ductile deformation (Ghosh and Sengupta, 1987; Sengupta and Ghosh, 1997; Sengupta et al., 2005), suggesting that ductile shearing was initiated at the early stage of the evolving shear zone. All folds within this shear

The prograde metamorphism in the SSZ that culminated in epidote-amphibolite facies accompanied and outlasted the ductile shearing and the peak metamorphic temperature-pressure calculated from the garnet-biotite thermometer and the garnet-muscovite-plagioclase-biotite geobarometer respectively were 480 ± 40 °C and 6.4 ± 0.4 kbar (Sengupta et al., 2005 and the references therein). The retrograde metamorphism, which led to hydration of prograde assemblage resulting in chloritization of biotite, garnet, chloritoid and muscovitization of kyanite is interpreted to have taken place at similar temperature range calculated via garnet-chlorite thermometry. This metamorphism event took place at the waning stage of deformation and postdating the ductile shearing (Sengupta et al., 2005).

1.2.3 Polymetallic Mineralization in SSZ: Occurrence and Ore Genetic Models

1.2.3.1 Polymetallic mineralization in SSZ: U-REE-Magnetite ± Apatite

The Singhbhum Shear Zone is well known and well explored polymetallic mineral province historically known for its U and Cu deposits (Rao and Rao, 1983d, 1983c; Sarkar, 1984; Sarkar and Gupta, 2012; Pal and Rhede, 2013). The distribution of various ore deposits exposed within the regional stretch has been shown in a simplified geological map of this shear zone (Fig. 1.3). Uranium deposits/mineralizations occur almost in the entire stretch of the SSZ whereas the Cu deposits are predominantly found in the eastern sector of the shear zone (Sarkar, 1982, 1984; Sarkar and Gupta, 2012). Jaduguda U deposit (since 1968) is the first area where the U mining started. The presently working underground mines are Bhatin (from 1986), Narwapahar (since 1995), Turamdih (since 2003), Bagjata (since 2008) and Mohuldih (from 2012),and Banduhurang (since 2009) mine have been developed as an open cast mine (Sinha, 2018). In the present thesis work samples have been also collected from the last 2 underground mines i.e. from Bagjata and Mohuldih area (Fig. 1.3). Mo, Ni ± Co bearing minerals – molybdenite, millerite, pyrite gersdorffite, melonite are abundantly present at Jaduguda- Bhatin associated with U ores and considered to be up to the scale of small deposit (Sarkar, 1982). This shear zone also holds potential for REE mineralization despite the main focus being on U-Cu mineralization (the area was initially known as ‘Cu thrust belt’- Bhola et al., 1966) and the abundant presence of REE-bearing phases associated with the U-Cu ores have been reported (Pal et al., 2011, 2021). LREE-bearing phases such as monazite, allanite, churchite and Y-HREE-bearing phases such as xenotime, florencite are frequently reported (Pal et al., 2011, 2022) in close association with U mineralization in

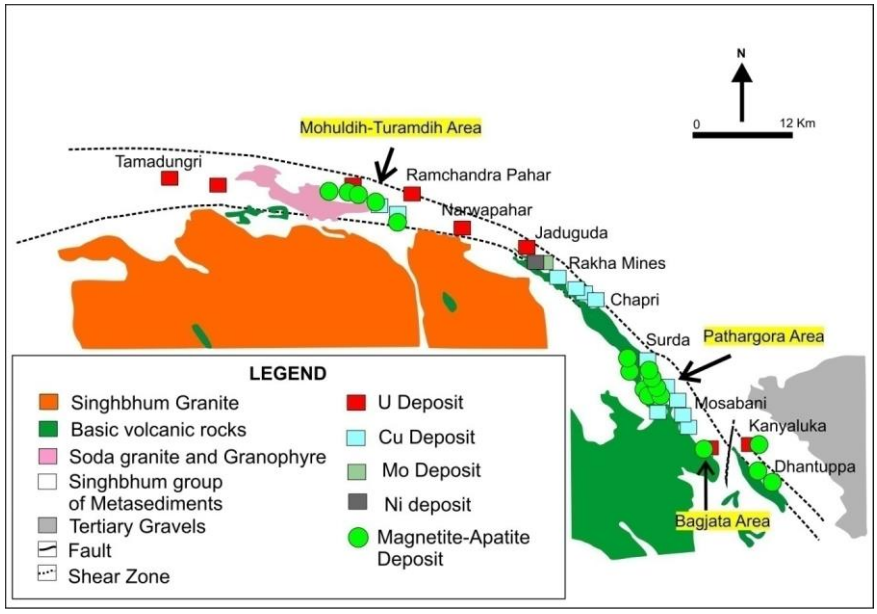

Figure 1.3 Simplified Regional Geological map of the Singhbhum Shear Zone showing notable occurrences of U-Cu-Mo-Ni and magnetite-apatite deposits

Magnetite ± apatite mineralization in the highlighted areas has been investigated in the present work. Note the close occurrence of U deposits in case of Mohuldih-Turamdih Bagjata area. (This map has been redrawn from Deb and Sarkar, 2017 and reference therein)

various known U deposits. Pal and Rhede (2013) reported uraninites from Jaduguda U deposit to be rich in REEs. REE occurrences found not only in association with U but also in forms of apatite-magnetite veins all over the shear zone (Rao and Rao, 1983b; Sarkar, 1984; Sarkar and Gupta, 2012) . Although the potential of REE mineralization in SSZ remain underexplored compared to U-Cu mineralization recently in Bagjata and Kanyaluka REE beneficiation from U-bearing schistose rock has been started and estimation of around 600 t~~T~~ons of xenotime reserve near Kanyaluka boost further interest in exploration of REEs (Singh, 2020b, 2020a).

Apart from U-Cu which has been traditionally explored from SSZ magnetite-apatite deposits are also known to be economically viable for phosphate exploration. The abundance of magnetite often reach to economic grade leading to recovery of magnetite as by-product of U-mining (e.g. at Jaduguda U-deposit). The present study focused on selected key areas of which Bagjata and Pathargora belongs to the roughly divided eastern sector and Mohuldih and Turamdih belongs to the western sector (Fig. 1.2 and 1.3); U ± REE mineralization is associated in case of Bagjata and Mohuldih. Presence of apatite-magnetite vein in association with U mineralization has been noted in some of the previous studies (Rao and Rao, 1983b; Sarkar and Gupta, 2012; Pal and Bhowmick, 2015). Apart from the spatial relation with U mineralization, magnetite ± apatite is found as a gangue mineral throughout the shear zone (Rao and Rao, 1980). In fact in some of the U deposits (e.g. Narwapahar), concentration of magnetite and apatite are as high as 10-15% (Rao and Rao, 1983b). In case of Turamdih U deposit Pal and Bhowmick (2015) reported that the richest U ores are hosted in quartz-chlorite schist containing abundant apatite-magnetite. Magnetite-apatite veins/patches/tongues also occur in the intensely deformed and fine grained quartz-chlorite schist which host the U mineralization in Banduhurang U deposit (the first open cast U mine in India) (Ghosh et al., 2013). Apart from the spatial closeness of magnetite-apatite mineralization with the U deposits in the SSZ, significant enrichment of REEs in the metasomatized schistose rock and in magnetite-apatite bearing veins (Pal et al., 2011; Singh, 2020a, 2020b) has also been reported. The other host of the polymetallic mineralization in SSZ i.e. the albite schist also contain elevated concentration of HREE (Ramachandran et al., 1989). Pal et al. (2011) reported extreme enrichment of REEs (up to ~4.8 wt percent ΣREEs) in allanite-magnetite-apatite bearing biotite schist from Bagjata U deposit.

Constraining the age of the polymetallic mineralization in a highly deformed, metamorphosed and intensely altered domain like the SSZ is difficult as conventional

petrographic and micro-structural indicators are largely obscured by successive deformation-metamorphism-fluid flux events (Sarkar and Gupta, 2012; Pal and Rhede, 2013). Rao et al. (1979) suggested an age of 1580 Ma for U mineralization following U-Pb and Pb-Pb ages of uraninite samples from Narwapahar, Bhatin, Surda and Rakha Mine and Johnson et al. (1993) reported 1766 ± 82 Ma for sulfide mineralization. Two ages for apatite mineralization at ca. 1950 ± 100 Ma and ca 1600 ± 50 Ma and for magnetite mineralization at ca. 1950 ± 100 Ma suggested by (Vinogradov et al., 1964). The most recent studies by (Pal et al., 2021) incorporating the mode of occurrence, textures and in-situ EPMA/LA-ICPMS dating of allanite (Pal et al., 2011), uraninite (Pal and Rhede, 2013) and allanite, epidote, monazite, florencite, titanite (Pal et al., 2021) from different important deposits in the shear zone suggested that most of the U-Cu-REE-magnetite-apatite mineralization initiated prior to the ductile deformation and metamorphism. Earliest event of LREE and U mineralization initiated at 1.8–1.9 Ga (≥1.82 Ga), both of which later got superimposed by successive hydrothermal events at ca. 1.66 Ga and ca. 1.0 Ga (op. cit.). The earliest event of LREE/U metasomatism was followed by another event of LREE metasomatism at 1.80 Ga (Pal et al., 2021). The 950 ± 50 Ma marks the last pervasive event of alteration in the Singhbhum Shear Zone.

1.2.3.2 Models about the polymetallic mineralization in SSZ

Most of the current working models regarding the polymetallic mineralization in this shear zone support the hydrothermal origin but the working ore-genetic models are diverse. Earlier models for the mineralization range from magmatic-hydrothermal (Dunn and Dey, 1942) to metamorphogenic related to migmitization (Banerji and Talapatra, 1966; Banerji, 1981) to affinity to the volcanogenic massive sulphide deposits (VMS for sulphide ores), unconformity/vein-type U-mineralization (Sarkar, 1984) and shear-zone controlled hypothermal alteration of mafic rock (magnetite-apatite mineralization) (Sarkar, 1984; Sarkar

and Gupta, 2012). Bhola et al.(1966) proposed circulating solutions from the "soda granite" along the zones of shearing and fracturing caused mineralization. Additionally, Banerji et al. (1972) who opted for origin related to migmatization reject the possibility of U sourced from the metasediments within the shear zone. Rao and Rao who published a series of papers on U mineralization (Rao and Rao, 1983a, 1983d, 1983b, 1983c) restrict to any of the specific models mentioned before and remained contentious, discussed the plausibility of various different mechanisms (Rao and Rao, 1983b).

On the other hand the most recent studies, based on multiple lines of converging evidences suggest that the mineralization in the Singhbhum Shear Zone most closely resemble IOCG type mineralization (Pal et al., 2009, 2010, 2011; Pal and Rhede, 2013; Pal and Chaudhuri, 2016). Amalgamating all the prior findings Pal et al.(2021) suggested the polymetallic mineralization of SSZ to be a close variant of world class IOCG-type deposits from the following series of important observations –

A. The characteristic ore mineralogy including uraninite, Co-rich pyrite, molybdenite, LREE/HREE-bearing phases (allanite, monazite, xenotime, florencite, churchite) and most importantly low-Ti magnetite which is commonly observed in many IOCG-type deposits worldwide (Groves et al., 2010; Barton, 2014);

B. Pervasive IOCG-type alkali and superimposed acidic alteration all along the shear zone. The author recommends that the mineralizing fluid were sourced from the marine evaporates/basinal brine and present evidences of high salinity fluid in the mineralized zone (Pal et al., 2008, 2010).

1.3. Petrogenetic implications of studying magnetite

Magnetite is one of the most abundant oxide minerals in the continental crust and its robust mechanical and chemical stability (Grigsby, 1990; McClenaghan, 2005) has been recognized and utilized as an important indicator for petrogenetic and geochemical studies since the early 20th century (Nadoll et al., 2014 and references therein). Magnetite has an inverse spinel structure and the general stoichiometric formula of magnetite is - AB_2O_4 (Bragg, 1915; Fleet, 1981), where bivalent cations (Mg, Fe^{2+}, Ni, Mn, Co, or Zn) are represented as A and trivalent cations (Al, Fe^{3+}, Cr, V, Mn, Ga) are represented as B (Lindsley, 1976a; Wechsler et al., 1984). Octahedral sites are occupied by ferric (Fe^{3+}) and ferrous (Fe^{2+}) ions and tetrahedral sites are strictly restricted to the ferric irons as the structural formula stands - $Fe^{3+}[Fe^{2+}Fe^{3+}]O_4$ (Wechsler et al., 1984; Waychunas and Ribbe, 1991).

The log fO_2-T diagram with the barriers of Fe-O-S system and a schematic fO_2-fS_2 phase diagram for Fe-O-S system (Fig. 1.4) (redrawn from Nadoll et al., 2014 and references therein) show that the minimum fO_2 for magnetite stability at any given T is the iron-magnetite (IM) or magnetite-wüstite (MW) buffer (Buddington and Lindsley, 1964; Frost, 1990). The fayalite–magnetite–quartz (FMQ) buffer denotes the boundary above which Fe is predominantly incorporated in magnetite and below which Fe gets incorporated into silicates mainly. The upper limit of the magnetite stability range is marked as HM buffer and above the HM buffer, hematite is the principal Fe-oxide mineral phases (Buddington and Lindsley, 1964; Frost, 1990; Lindsley, 2018). The presence of octahedral and tetrahedral sites in magnetite crystal structure allows incorporation of foreign cations via isovalent and coupled substitution at both octahedrally and tetrahedrally coordinated sites in magnetite crystal lattice in response to changing (P)-T-fO_2conditions over the broad range of geological environment (magmatic, hydrothermal, magmatic-hydrothermal, metamorphic, sedimentary

environments) along with the controls of intrinsic crystallographic parameters such as charge and radius of the substituting elements (Goldschmidt, 1954; Fleet, 1981; Wechsler et al., 1984). Detailed review about the element substitution over the wide range of formation environment has been published in many Studies (Bowles et al., 2011; Nadoll et al., 2014; Lindsley, 2018). The B site as mentioned in the general structural formula, is often occupied by titanium (charge +4)via the coupled substitution with a divalent cation (Wechsler et al., 1984). Alongside Ti, there is a large no. of other important spinel elements/non-spinel elements which can replace Fe^{2+} or Fe^{3+} into magnetite crystal structure inclusive of –lithophile (V^{3+}, Cr^{3+}, Al^{3+}, Si^{4+},Mg^{2+}, Ca^{2+}, Nb^{5+}, W^{4+},Ta^{5+}),

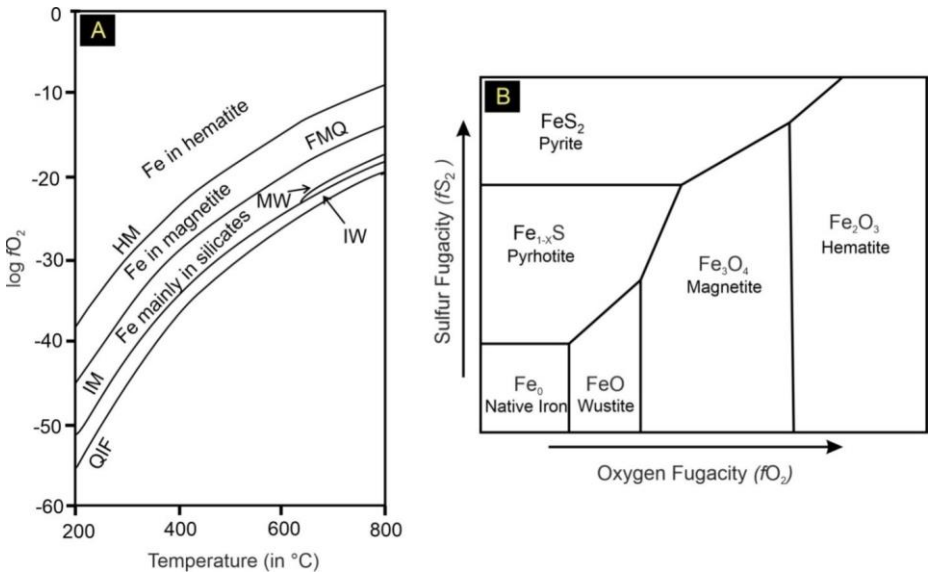

Figure 1.4 Log fO_2–T diagram showing relevant buffers for the Fe–Si–O system (A) and Schematic phase diagram for the system Fe–O–S in fO_2–fS_2 space (B)

Abbreviations used - HM: hematite–magnetite, FMQ: fayalite–magnetite–quartz, MW: magnetite–wüstite, IW: iron–wüstite, IM: iron-magnetite, and QIF: quartz–iron–fayalite (Both the diagrams are redrawn following Nadoll and Mauk, 2011; Nadoll et al., 2014 and references therein)

siderophile (Cu^{2+},Mo^{4+},Mn^{2+}, Ni^{2+}, Co^{2+}) and chalcophile (Ge^{4+},Sn^{4+},As^{3+},Ga^{3+},Zn^{2+}) elements (Barnes and Roeder, 2001; Righter et al., 2006).The substitution of these various elements via isovalent/coupled substation mechanism has been stated before to be essentially representative of/controlled by the formation environment i.e. physicochemical conditions making magnetite an ideal proxy to understand a broad spectrum of geological processes.

1.3.1 Trace element systematics in magnetite: implication for identifying formation process and post-formational changes

Considering the presence of magnetite over the broad P-T-fO_2 conditions in magmatic, hydrothermal, magmatic-hydrothermal, metamorphic, sedimentary environments vis-à-vis the potential implications of incorporation of a large no. of cations (Nb^{5+},Ta^{5+},Mo^{4+},W^{4+},Ti^{4+},Si^{4+},Ge^{4+},Sn^{4+},V^{3+},Cr^{3+},Al^{3+},As^{3+},Ga^{3+},Mn^{2+},Zn^{2+},Ni^{2+},Co^{2+},Cu^{2+}, Mg^{2},Ca^{2+}) in octahedral/tetrahedral coordinated crystal lattice via isovalent or coupled substitution mechanism sensitive to formation-environment has been utilized in many classic studies. Magnetites show variable composition in response to variables such as –

A. composition of magma (Buddington and Lindsley, 1964; Dare et al., 2012, 2014; Liu et al., 2015) or composition of the hydrothermal fluid (Carew, 2004; Dare et al., 2014; Nadoll et al., 2014; Acosta-Góngora et al., 2014; Chen et al., 2015a; Huang et al., 2016; Heidarian et al., 2016).

B. Parameters controlling the physicochemical conditions of ore formation(T, rate of cooling, fO_2 and fS_2 etc.) and thus controlling the partition coefficients of element incorporation (Buddington and Lindsley, 1964; Toplis and Carroll, 1995; Toplis and Corgne, 2002; Righter et al., 2006; Turner et al., 2008; Reguir et al., 2008; Nadoll et al., 2014; Sievwright et al., 2017)

C. Influence of co-crystallizing phases (Carew, 2004; Dare et al., 2012; Huang et al., 2014; Nadoll et al., 2014; Acosta-Góngora et al., 2014).

Elements with variable valence state which are compatible into magnetite during fractionation (V and Cr in particular) have been used to trace the evolution of the melt and effect of magma-mixing considering that V has the maximum value of partition coefficient (D_v) in magnetite at QFM which explain the change in V concentration between the uppermost (Fe-Ti-P Zone) and lowermost part (Fe-Ti-V Zone) of the layered intrusions in case of Bushveld Complex and Sept Iles layered intrusion (Toplis and Corgne, 2002; Barnes et al., 2004; Tollari et al., 2008). In case of sulfide melt (Dare et al., 2012) has showed the gradual depletion in concentration of lithophile elements (Ti, V, Cr) in residual melt (residual Cu rich sulfide liquid) compared to the early-forming magnetite from Fe-rich sulfide cumulates as in contrast to silicate magma the entire budget of lithophile elements goes into magnetite and varies in concentration with fractionation trends.

Although in most of the cases the experimental partitioning data between magnetite and hydrothermal fluid is not available for hydrothermal-relevant conditions unlike magmatic conditions, some key difference between hydrothermal and magmatic magnetite has been observed in terms of both magnetite-compatible vs. less-compatible elements (Dare et al., 2014; Nadoll et al., 2014). It's now well-known that incorporation of Ti, Ga and Al in magnetite are T-dependent (Toplis and Carroll, 1995; Nadoll et al., 2014; Salazar et al., 2020) and this lead many researcher to understand the thermal evolution of a system moving from magmatic to magmatic-hydrothermal regime by using trace element concentration of these specific elements correlating with thermometric calculations. In case of Los Colorado, El Romeral and Mariela (Chile), Palma et al. (2021) showed that the systematic change in Ti and Ga are consistent with the gradual shifting in depositional environment of magnetite from purely magmatic (~ 1000 to 800 °C), to late magmatic or magmatic-hydrothermal (~ 800 to

600 °C), to purely hydrothermal (< 600 °C) conditions and the results agree well with oxygen isotope thermometry and Mg-based magnetite thermometry (Bilenker et al., 2016; Tornos et al., 2016; Canil and Lacourse, 2020). Vanadium, Ni, Co, Sn, Zn, Mn are reported to be consistently higher in case of high T hydrothermal environment than the magnetite precipitated from low T hydrothermal fluid (Dare et al., 2014). Fluid/Rock ratio and host rock buffering exert significant control over the composition of hydrothermal magnetite as seen in case of hydrothermal skarn magnetite where enrichment of Mg and Mn in magnetite observed due to the extensive interaction between fluid and rock (Meinert, 1987; Nadoll et al., 2015). It is important to note that magnetite formed by hydrothermal/magmatic-hydrothermal processes can hold up to tens of thousands ppm of elements either incorporated structurally in sector/growth zones or in form of micro/nano-inclusion (Deditius et al., 2018; Huang and Beaudoin, 2021; Huang et al., 2022) and characterization of these nano-sized inclusions suggested to be useful in differentiating between magnetite formed via igneous and hydrothermal processes (Huang and Beaudoin, 2021).

Composition of metamorphic magnetite depends primarily on metamorphic grade and thereby the partitioning of elements are mainly controlled by T and fO_2 (Evans and Frost, 1976; Frost, 1990; Skublov and Drugova, 2003; Nadoll et al., 2012). Based on empirical assumption that concentration of V and both V and Ti are lower in case of hydrothermal magnetite than metamorphic magnetite and igneous magnetite respectively, the high-grade metamorphic magnetite samples of Minhaudi mafic complex (SW China) shown to be distinguished from igneous and hydrothermal magnetite by typical Fe/Ti ratio and content of Vanadium (Liu et al., 2020). Conversely low-grade metamorphic magnetite contains very low trace element content and are compositionally homogeneous (Frost, 1990; Nadoll et al., 2012).

Numerous studies have used magnetite and its potential applications in identifying the underlying physicochemical processes based on the premises of overall stable composition during subsequent chemical alterations or weathering (Huang and Beaudoin, 2019). However texture and chemical composition of magnetite might change by many post-formational processes such as hydrothermal re-equilibration of igneous magnetite, subsolidus oxy-exsolution, hematitization, coupled dissolution-reprecipitation (Hu et al., 2014, 2015; Wen et al., 2017) etc. and may lead to improper identification of formation process. Understanding how the subsequent post-formational processes change the magnetite chemistry and in turn impact the use of magnetite as petrogenetic tool hasn't received the required attention. Only few recent studies (Wen et al., 2017; Huang and Beaudoin, 2019, 2021) address the issue of post-crystallization changes in magnetite texture and geochemistry compared to the large volumes of studies using magnetite composition to understand the formation process.

1.3.2 Trace element systematics in magnetite: implication for identifying deposit-type

Formation of magnetite via myriads of ore-forming processes as have been demonstrated earlier makes it a common mineral to be studied in many deposits including but not restricted to Iron Oxide-Copper-Gold (IOCG), Kiruna-type apatite–magnetite, Banded Iron Formation (BIF), porphyry Cu, Fe-Cu skarn, Mg-skarn, Fe-Ti-P, Fe-Ti-V, REE, Ni-Cu-PGE, Cu-Zn-Pb volcanogenic massive sulfide (VMS) and Archean Au-Cu porphyry and Opemiska Cu veins. A set of elements commonly referred as 'spinel elements' (Mg, Al, Si, P, Ca, Sc, Ti, V, Cr, Mn, Co, Ni, Cu, Zn, Ga, Ge, Y, Zr, Nb, Mo, Sn, Hf, Ta, W, and Pb – suggested by Dare et al., 2014) are present in variable concentrations in magnetite in most of the deposit types that can be measured by in-situ micro-analytical techniques like EPMA/LA-ICPMS. Since the publication of the classic paper by Dupuis and Beaudoin (2011) where IOCG and IOA magnetites are proposed to be discriminated from Fe-Ti-V, porphyry, skarn and BIF deposits by using (Ti + V) vs. Ca + Al + Mn) or (Ni/(Cr + Mn) plots and also

different fields respective to different deposit types were suggested based on the magnetite samples from different deposits analyzed in EPMA, these diagrams are in rigorous use. Recent literatures have seen a tremendous surge in using in-situ trace element geochemistry of magnetite to decipher the ore-forming processes in a broad spectrum of deposits including Iron Oxide Copper Gold (Acosta-Góngora et al., 2014; Huang et al., 2019), Iron Oxide Apatite (Knipping et al., 2015a, 2015b; Heidarian et al., 2016; Broughm et al., 2017), skarn (Zhao and Zhou, 2015; Liu et al., 2019), porphyry Cu (Wu et al., 2019), rare earth elements (REE) deposits (Huang et al., 2015), Banded Iron Formations (BIF) (Gourcerol et al., 2016). Dare et al. (2014) proposed bulk continental crust normalized multi-element variation diagram that yields characteristic pattern for magnetite of different origin/deposit types with the primary focus being on magnetite chemistry to differentiate between magnetite formed via magmatic vs. hydrothermal processes, which have been used to discriminate magnetite samples from IOA-IOCG deposits later (Knipping et al., 2015b; Huang et al., 2019). Partial least square discriminate analysis (PLS-DA)- based binary score plot separate magnetite samples from IOA and IOCG deposits from Porphyry, Ni-Cu, VMS deposits and VMS-related BIFs (Makvandi et al., 2016a, 2016b).Magnetite geochemistry is one of the most important geochemical proxies used to solve the long-standing debate over IOCG-IOA connection in case of Chilean IOA deposits. Knipping et al. (2015) suggested the 'Flotation model' based on his study on magnetite samples from Los Colorado, which involves crystallization of magnetite microlites from a silicate melt, nucleation of aqueous fluid bubbles on magnetite surfaces, and formation and ascent of buoyant fluid bubble-magnetite aggregates, and all the stages are mostly consistent with the typical changing pattern of the Ti, V, Al, Mn ± Ga manifested in the deposit-type/process type discriminator (Knipping et al., 2015a, 2015b). The transition from high T (temperature) IOA-type environment to comparatively shallower IOCG-type environment observed to be persistent with the cooling

trend and in majority of the cases reflected in the (Ti + V) vs. (Al + Mn) from other deposits from the Andean clan of deposits (Salazar et al., 2020; Palma et al., 2020; Rodriguez-Mustafa et al., 2020). Sn/Ga and Al/Co ratios have been suggested to distinguish magnetite from VMS, skarn, IOCG, and Broken Hill-type clastic-dominated Pb–Zn deposits (Singoyi et al., 2006).

However considering the background premises of various ore genesis models regarding the polymetallic mineralization in the SSZ, ranging from magmatic-hydrothermal vs. migmitization related to metamorphism vs. shear zone controlled hypothermal alteration (magnetite-apatite mineralization) vs. purely hydrothermal to a close variant of IOCG or volcanogenic massive sulphide deposits (VMS for sulphide ores) like ore-forming mechanism, no previous study tried to utilize the magnetite geochemistry in order to resolve the ore genesis conundrum despite the abundant presence of magnetite throughout the shear zone with or without being associated with U-Cu-REE mineralization. The deposit-type discriminators suggested in literature and used in the present study are not inclusive of all different metallogenic model suggested for the polymetallic mineralization and do not warrant the results to be conclusive in all the cases. But the use of these deposit-types discriminator based on well-characterized dataset from over the globe provide the present study a useful first hand empirical tool to compare and evaluate the existing ore genesis models .

1.3.3Trace element systematics in magnetite: implication for tracing critical metal (U-REE) mineralization

Many of the deposit types including but not restricted to IOCG and IOA deposits which have been shown to be identifiable based on characteristic trace element geochemistry of magnetite, hosts several economically important critical metals such as U and REEs. It has been predicted that the demand of these critical metals will exponentially rise in near future

corresponding to the global shift of energy consumption from fossil fuel to nuclear fission/fusion or various other forms of renewable energy resources (Grantham 2012, Milinovic 2021, Bell 2020, Bradshaw et al. 2013). Apart from the main commodity resources (Cu/Fe/U) significant REE potential has been reported and also being recovered as a by-product of mining the main commodity mineral/resources in case of Olympic Dam IOCG deposit (Johnson and Barton, 2006), Blackbird IOCG deposit (Slack, 2006), Pea ridge IOA deposit (Aleinikoff et al., 2016; Neymark et al., 2016), Sossego IOCG deposit and Kiruna deposit (Johnson and Barton, 2006). Despite this spatio-temporal closeness of magnetite-apatite mineralization with the key critical metal like U/REEs with these deposits, it is observed that only a few studies (Rusk et al., 2010; Huang et al., 2015) have attempted to utilize trace element geochemistry of magnetite to differentiate mineralized and non-mineralized zones in the context of critical metal mineralization which might have implications in exploration of these important critical raw materials. This is somewhat surprising as most of the well-known polymetallic mineral provinces (Olympic dam, Australia; Great Bear Magmatic Zone, Canada; Ernest Henry, Australia; Salobo, Brazil) all over the globe are characterized by the presence of these critical metals and in most of the cases Fe-oxides are accompanying accessory phase with the mineralization.

The Singhbhum Shear Zone (SSZ) where the present work is based on is one of the most important polymetallic mineral belts in India which hosts several uranium, copper and many magnetite-apatite ore bodies (Rao and Rao, 1983b; Pal et al., 2011b; Sarkar and Gupta, 2012; Ghosh et al., 2013). Magnetite is ubiquitous in the U and Cu ores in the SSZ often reaching to economic grade leading to its recovery as by-products. Until the end of the last century SSZ was the only known phosphatic-iron ore producing region of Eastern India (Sarkar, 1984). Alongside, SSZ has also produced Au, Ag, Te, Mo, Ni and Co as byproducts of uranium and copper mining and the ores are reported to have elevated concentrations of

rare-earth elements (in particular LREEs) (Pal et al., 2011a, 2021). Despite the spatial closeness of the U, Cu, REE mineralization with magnetite-apatite mineralization in this shear zone and the common presence of magnetite ± apatite with the U and Cu ores there are only limited studies (Sarkar, 1984) exploring the magnetite-apatite mineralization in SSZ and the relationship of magnetite-apatite mineralization with U mineralization (Rao and Rao, 1983b), while the main thrust has been on studying the U and Cu mineralization (Rao and Rao, 1980, 1983a, 1983c; Pal and Rhede, 2013). In the present thesis work the location of magnetite ± apatite mineralization are often closely associated with U-REE mineralization. All the samples used in this study from underground U mine are from precisely known location with reference to ore-bearing zones and barren zones, which extends the reach of the present study to further explore the possibility to make use of magnetite as a tracer for U mineralization.

1.4. Objective vis. a vis. Methodologies

The present study was undertaken with the objective to understand the magnetite ± apatite mineralization in the Singhbhum Shear Zone and additionally to grow the current understanding of the ore genesis in order to make more robust and all-encompassing ore-genetic models. In this work "magnetite ± apatite mineralization" refers to the visible presence of either magnetite or both magnetite and apatite in the outcrop and hand specimen scale without any specific reference to their economic potential although some of the deposits described in this study were (are being) mined for either of the minerals. The overall objective of the present research work is to understand the magnetite ± apatite mineralization in the SSZ with the central focus on magnetite, to examine the utility of magnetite geochemistry in deciphering the physicochemical conditions, ore-forming process, and

deposit types and to investigate the possibility of using magnetite geochemistry in identifying critical metals-mineralized systems.

The objectives can be outlined as follows:

A. To understand the origin of magnetite ± apatite mineralization in the Singhbhum Shear Zone from a number of geological environments such as magmatic, hydrothermal and sedimentary, integrating mode of occurrences, textures and geochemistry (major and trace element) of magnetite coupled with that of accessory minerals wherever available/required.

B. To check the utility and efficiency of various discriminators based on magnetite geochemistry in understanding the deposit affiliation or to fingerprint the underlying physicochemical process (e.g. temperature, fO_2, hydrothermal alteration) of magnetite ± apatite and U mineralization in the backdrop of earlier proposed ore-genetic models integrating geochemistry of magnetite ± apatite and associated gangue minerals (biotite and chlorite) and whole rock geochemistry.

C. Examining the suitability of trace element geochemistry of magnetite in order to understand the putative (?) relationship between critical metal mineralization and geochemistry of accessory minerals and in vectoring uranium mineralized “pay-zones”.

To fulfill the objectives, the following methods have been adopted although not always injective, described broadly in a systematic pattern -

A. *Field study and sampling:* Field investigation was carried out in a stretch of approximately 70 km from Mohuldih in the west to Bagjata in the east, all are located within or close to the SSZ. Magnetite samples are collected from some key locations where the mineralization is hosted in a variety of rocks ranging from metamorphosed-sedimentary rock (Turamdih and Mohuldih) and extensively hydrothermally altered rocks (Bagjata and Pathargora). Separate samples were collected from U-mineralized (uraninite-bearing ore zone) and non-mineralized rocks from the Bagjata uranium deposits.

B. *Microscopic investigation*: Optical and scanning electron microscopic (SEM) investigations were carried out to identify the constituent minerals, decipher the textural relations of magnetite with other minerals and examine intra-grain compositional variations in magnetite, if any.

C. *Geochemical investigation*: Field study and microscopic studies were followed by geochemical characterization of magnetite and associated accessory minerals using Electron Probe Micro Analyzer (EPMA) and Laser Ablation Inductively Coupled Plasma Mass Spectrometer (LA-ICPMS). In addition to utilize the geochemistry of magnetite in some instances the geochemistry of accessory minerals and whole rock geochemical data of the variably altered host rocks of various magnetite-bearing assemblages have been used to decipher the alteration signature and ore-forming process.

1.5. Outline of the thesis

After the present introductory chapter incorporating a brief review about the regional geology vis-à-vis the polymetallic mineralization in Singhbhum Shear zone along with the historical use of magnetite geochemistry as a petrogenetic tool, Chapter 2 describes the magnetite samples collected from Bagjata U deposit. Integrating mode of occurrence, textural relations and geochemical differences the origin of the magnetite mineralization have been discussed. Physicochemical conditions (Temperature and fO_2) of the ore formation are inferred combining geochemistry and thermometric calculations based on the compositions of accessory biotite and chlorite. Whole rock geochemistry of different rocks hosting magnetite mineralization has been utilized along with the geochemistry of magnetite to understand the nature of hydrothermal alterations. The prime intent is to understand how far the signature of physicochemical formation condition evolving from magnetite trace element geochemistry correlates with the associated hydrothermal alteration pattern. Various trace element-based discriminators for both process-type identification and deposit-type identification have been used which is common to all the chapters as one of the prime intent of the present thesis work being the evaluation/utilization of trace-element-based discrimination using magnetite geochemistry. Most of the widely used trace element-based identification diagrams for process and the deposit-types are revisited in this chapter and also an alternative identification diagram have been suggested and tested on the globally compiled dataset. This chapter holds special significance because of the close spatial relation of magnetite with U-REE mineralization in this deposit.

In Chapter 3, magnetite mineralization is discussed focusing on two magnetite-bearing assemblages and these two assemblages are identified by their marked difference in mode of occurrence during field study and the chapter encircles around the detailed petrographic as well as geochemical characterization followed by the interpretations about

the origin and the nature of magnetite mineralization in those units. One of the assemblages being subjected to various types of post-depositional disturbances extending the limit of this chapter to further check the robustness of the existing trace element based discriminators for magnetite when the pristine composition is changed. The processes which are responsible for textural and geochemical changes in magnetite since formation will be investigated and the mechanisms and the chemical changes coming with it will be inferred. The trace element based discrimination of depositional environment being one of the central themes of this thesis work, Cehapter 3 exclusively focuses on the applicability of discriminating criteriaons in a deposit where the records of the original formation conditions might be altered. Additionally a brief commentary will be made on the nature of the ore-forming fluid using magnetite composition and accessory mineral phase chemistry.

Chapter 4 introduces magnetite samples from the Turamdih (approximately 6 kKm. East to Mohuldih) and Mohuldih U deposits which is hosted in the same banded quartzite unit. The chapter describes the mode of occurrence of magnetite in the banded sedimentary rock unit and comparison will be made with the typical sedimentary rocks from the closely located IOG groups and with some typical reference sample from other banded iron formation deposits in order to know about the origin of this banded rock units which is unlike the typical rocks of banded iron formations as has been described by the previous researchers.

In Cehapter 5 all of the observations of the present study will be briefly summarized about the magnetite mineralization in Singhbhum Shear Zone in the context of the nature of the magnetite mineralization and the variations of the physicochemical conditions for magnetite mineralization in the selected 4 locations of the present study. In addition to this, the results of the various discriminatory diagrams which have been used in different chapters will be evaluated critically and the chapter will end describing the limitations and the future scopes of the present study.

Chapter 2: Magnetite in the Bagjata Uranium deposit: implications for alteration, mineralization and trace elements-based discrimination

2.1. Introduction:

Bagjata deposit located at the eastern flank of the Singhbhum Shear Zone, approximately 25 km west of Jaduguda U mine (Fig. 2.1), is one of the most important locales of U mineralization which also contains elevated concentrations of rare earth elements (REEs) (Pal et al., 2011, 2021). The total reserve of the deposit is about 1860 tons of U_3O_8 with a cutoff grade of 0.047 % U_3O_8 (Patel et al., 2021 and reference therein). The previous

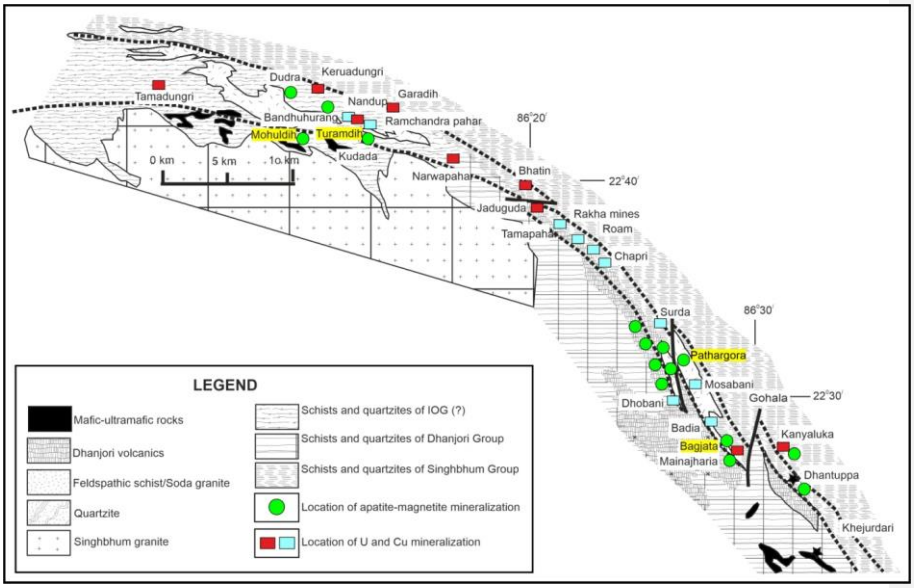

Figure 2. 1 Geological map of Singhbhum Shear Zone

The Map of Singbhum Shear Zone showing the location of the Bagjata U deposit and the major litho units in and around the study area and also around the shear zone. Pathargora (from the Eastern sector) and Mohuldih and Turamdih (from the Western sector) areas which are also part of the present study are highlighted in this map as well.

studies based on Bagjata U deposit, broadly focused on the chemical evolution of REE mineralization (Pal et al., 2011) and U mineralization (Patel et al., 2021), recognized multiple fluid flux/superimposed hydrothermal alterations in the deposit using the mode of occurrence and in situ dating of LREE-bearing phase allanite and by using textural/chemical characterization with B isotope measurement of different generations of tourmaline. Although both the studies agreed upon the timing of the major hydrothermal alteration events occurring at 1.8-1.9 Ga, 1.66-1.56 Ga, and ca. 1.0 Ga, they largely differ in detail (e.g. nature of the fluid related to those hydrothermal alteration events) of those three events. Considering the characteristic mineral assemblage (Fe oxide, U-REE bearing phases) and the extremely altered nature of the host rocks Pal et al.(2011) suggested Bagjata U deposit bears close similarities with IOCG-type of deposits whereas Patel et al.(2021) holds back from commenting about the affiliation of the Bagjata deposit, but stated that the B isotope values of tourmaline from Bagjata falls in the recommended range for IOCG-type deposits (Barton, 2014~~3~~). It's worth mentioning that Pal et al. (2010) previously reported strongly positive B isotope composition of tourmaline from Jaduguda U deposit and linked that with evaporate-derived fluids akin to many IOCG deposits over the globe. It is known that magnetite is one of the key mineral in IOCG deposits which can be utilized to fingerprint the nature of the deposit-type (Dupuis and Beaudoin, 2011; Huang et al., 2019, 2022; Hong et al., 2021). In case of Bagjata deposit magnetite is a common accessory phase found in most of the different mineralogical associations (and also both in U-REE-bearing assemblages and in U-REE-devoid assemblages) present in the deposit yet no previous study utilizes magnetite for getting insight about the ore-forming process. Considering the above mentioned gaps in knowledge the objectives of this chapter are as following:

A. Understanding the difference in mode of occurrence, texture and geochemistry of magnetite from different magnetite-bearing mineral associations from hydrothermally altered host rocks.

B. Utilizing the host rock geochemical data and corresponding magnetite composition to understand the nature of the hydrothermal alteration processes

C. Use of magnetite geochemistry to know about the physicochemical parameters (T, fO_2, nature of the ore-forming fluid) of the ore-forming process along with the efficacy of magnetite composition to differentiate between different types of ore deposits/ore forming processes and thus trying to resolve the ore genesis dilemma

D. Magnetite occurs in the U- and REE-mineralized rocks and apatite-magnetite veins/breccia in this deposit and thus offers a unique opportunity to explore the suitability of using magnetite geochemistry in discriminating the U-mineralized vs. barren systems± REE mineralized vs. barren system and deciphering the deposit type and associated alterations.

To work on the aforementioned objectives this chapter integrates mode of occurrence, texture, mineralogical assemblage of magnetite vis-à-vis geochemistry of magnetite and selected gangue minerals (e.g. apatite, biotite and chlorite) along with the whole rock compositions of variably altered hydrothermal host rocks.

2.2. Geology of Bagjata U deposit

2.2.1 Deposit-scale geology

The Bagjata uranium deposit is located close to the contact between the Singbhum group siliciclastic rocks of the Chaibasa Formation and the meta-volcanic rocks of Dhanjori Group (Fig. 2.1 and 2.2).The major rock types that occur in and around the Bagjata U deposit are “soda granite”/albite schist, garnetiferous muscovite schist, kyanite-bearing quartzite, Dhanjori meta-volcanic rocks and Dhanjori quartzite. Quartz and albite are the main components of the albite schist with occasional presence of biotite, chlorite, muscovite and sericite. The garnetiferous muscovite schist is composed predominantly of quartz and muscovite with occasional presence of garnet porphyroblasts, Kyanite-bearing quartzite occurs as discontinuous bands or pockets in muscovite-sericite schist. The fine-grained Dhanjori metavolcanic rock is composed of amphibole, plagioclase, chlorite, and epidote. The rock at places is altered to biotite schist and chlorite schist. Although biotite schist and chlorite schist do not form large continuous mappable units on the surface (See Fig. 2.2.A), they are at places extensive in occurrence in the form of bands/veins. In Fig. 2.2A the term Dhanjori volcanics has been used to include the unaltered meta-volcanic rocks and their altered equivalents. Close to the mineralized zone, the unaltered Dhanjori rocks are largely replaced by biotite schist and chlorite schist as seen in the underground mine (Fig. 2.2B).

2.2.2 Description of host rocks of magnetite (± U mineralization)

Systematic samples for this study were collected from the vertical shaft (during the lowering of the cage) and two working levels at 60 m and 100 m. Magnetite is present in variable modal proportion in all the different lithological units shown in the vertical

shaft (Fig. 2.2B). Magnetite samples are collected from magnetite-apatite breccia, biotite schist and

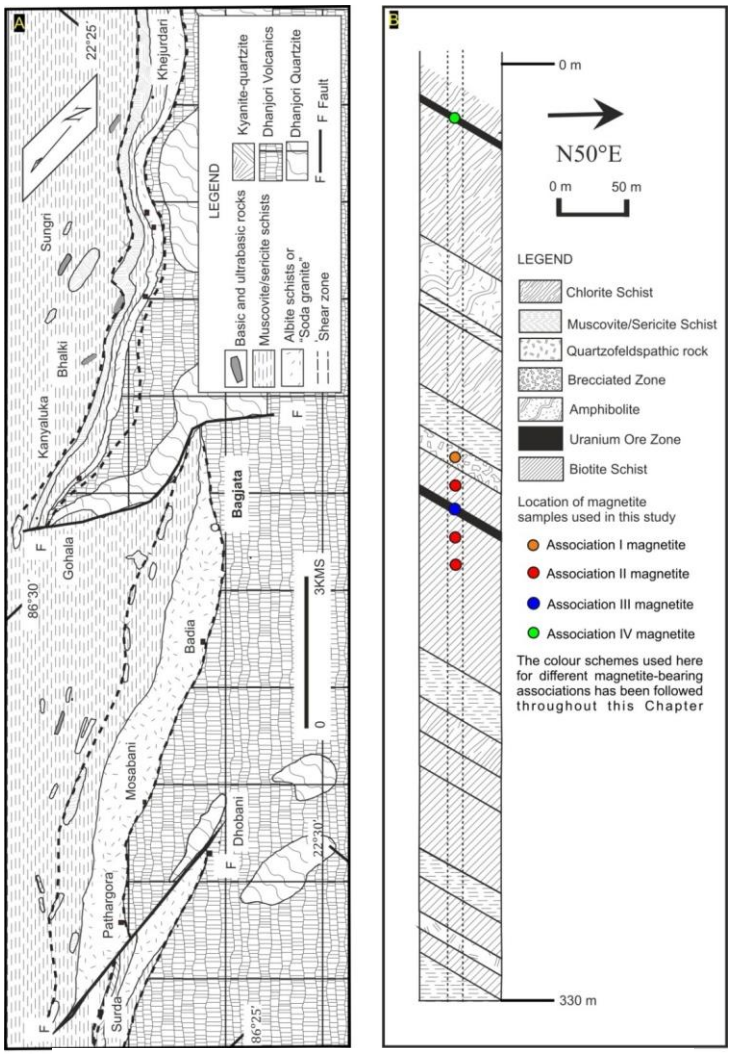

Figure 2.2 Distribution of lithological units in and around Bagjata area and in vertical shaft

(A) Lithological map showing the distribution of different rocks types around the Bagjata U deposit (adapted from Talapatra, 1968); (B) Distribution of different rock types and the locations of magnetite-bearing samples used for this study is shown along a part of the vertical shaft in the Bagjata uranium mine. Note that Magnetite samples are collected from all the major lithological units and both from ore zone and non-ore zone. The width of the vertical shaft is not to scale.

chlorite schist with samples belonging to both barren and fertile assemblage (in terms of U mineralization).

The mineralogy of magnetite-apatite rich rock is dominated by apatite grains with the presence of magnetite and biotite in interstitial spaces along with the occasional presence of recrystallized aggregates of smaller apatite grains. The Majority of the apatite grains are large in size ranging from 500-1000 µm and often exceeding >1000 µm except the recrystallized granular aggregates of apatite grains. The modal abundance of the constituent minerals in magnetite-apatite rich rocks varies in this order – apatite >> magnetite ≈ biotite

The modal abundances of the constituent minerals in biotite schist and chlorite schist are strongly variable; the respective names are given based on the abundant mineral. The biotite schist comprises biotite, quartz, chlorite, sericite, allanite, apatite, albite, magnetite and tourmaline. Chlorite schist has the similar mineralogy with chlorite dominating over biotite. A common feature in chlorite schist is the extensive replacement of biotite along grain boundaries and cleavages. The muscovite-sericite schist comprises predominantly of quartz and muscovite occasionally with garnet porphyroblast. It has been observed that magnetite from biotite schist show large variations in grain size. The magnetite from uraninite-bearing ore assemblage in the biotite schist is associated with ubiquitous fluorite.

Two uranium ore lodes are present in the deposit (Fig. 2.2B). The U-ores are hosted mainly in biotite schist and chlorite schist whereas muscovite/sericite schist host low grade U mineralization (Bhola, 1972; Pal et al., 2011). Uraninite is the primary hypogene ore mineral of U in the Bagjata deposit and elsewhere in the SSZ. Allanite is the dominant LREE-bearing mineral along with occasional presence of monazite. Chalcopyrite is the predominant Cu-sulfide mineral.

2.3. Analytical Protocol

2.3.1 SEM and EPMA

The polished thin sections of the magnetite samples were examined thoroughly using optical microscope followed by Scanning Electron Microscope (SEM). A JEOL JSM 6490 scanning electron microscope was used to generate backscattered electrons images and to select spots for EPMA and LA-ICPMS analysis free of any visible inclusion phases which can perturb the geochemical data.

The major element concentrations of magnetite and some of the accessory ore minerals (apatite, biotite and chlorite) were obtained using a Cameca SX 100 electron probe micro analyzer (EPMA) equipped with four wavelength dispersive spectrometers at the Department of Geology and Geophysics, Indian Institute of Technology (IIT), Kharagpur. The EPMA analyses were done at an acceleration voltage of 15 kV and a beam current of 20 nA. The dwell time was set at 10s on the peak. The following standard and emission lines were used to calibrate the instrument - jadeite (Na-Ka), fluor-apatite (F-Ka, P-Ka), orthoclase (Si-Ka, K-Ka), MgO (Mg-Ka), Al_2O_3 (Al-Ka), NaCl (Cl-Ka), hematite (Fe-Ka), rhodonite (Mn-Ka), TiO_2 (Ti-Ka), barite (Ba-La), sphalerite (Zn-Ka), Cr_2O_3 (Cr-Ka), wollastonite (Ca-Ka) and Vanadium metal (V-Ka). A TAP crystal was used to analyze Na, F, Mg, Al, Si; PET for K, Ca, Ti; LPET for Cl, P, Ba; LIF

for Cr, Mn, Zn and Fe. The ZAF matrix corrections were performed by the Cameca-supplied PAPSIL software. Fluorine was calibrated with fluor-apatite using a spot size of 5 mm to minimize its excitation. The major element data are provided in Table 1.

2.3.2 LA-ICPMS

The ~~T~~race element concentrations in magnetite, apatite, biotite and chlorite were measured using the laser ablation inductively coupled mass spectrometer (LA-ICP-MS) at the Radiogenic Isotope facility of the Department of Geology and Geophysics, IIT Kharagpur. The setup comprised of Thermo fisher Scientifici CAP-Q quadrupole ICPMS coupled with a New Wave Research 193 ArF Excimer laser ablation system. The ablations were done at a 10 Hz repetition rate, 5 J/cm^{2}fluence and 40 μm spot size. The ICPMS was optimized for maximum sensitivity on Li, Co, In, Pb, Th and U by ablating the NIST 612 reference glass. The oxide production rate (monitored on $^{232}Th^{16}O$) was always <2 %. The analyses were performed in time-resolved mode, with each analysis consisting of 30s measurement of gas blank and 40s peak signal measurementwith the laser ablating on the sample. Correction for instrumental mass-bias and drift was done using external standardization by bracketing groups of ten unknowns with two NIST 612 reference glass measurements. The data quality was monitored by analyzing NIST 610 reference glass as unknown interspersed with the measurement of the samples. The data was reduced offline using the GLITTER® software (Griffin, 2008). The time-resolved signals were observed carefully to check whether micro–inclusion phases are ablated or not, and if detected, the specific spot is either dropped or the concentrations are calculated based on the clean segment of the time-resolved spectra. Concentrations of Si for biotite and Fe for magnetite measured in EPMA were used as an internal standard. In most of the case the ablated areas were selected from the same spots where the EPMA analyses were initially done to get the best calibrated results. Accuracy and precision as determined

from repeat analyses of the NIST 610 reference glasses are in the range of 5–10 % for most elements. The representative trace element data are provided in respective tables (magnetite: Table 2 and biotite: Table 4, apatite: Table 7). The whole rock analyses of 9 samples for 4 different magnetite-bearing assemblages were done in Actlabs, Canada. The Actlabs code 4LITHORES was used for all the analyses. Major elements were analyzed by Fusion ICP (WRA) and the trace elements were analyzed by Fusion ICP/MS (WRA4B2). The whole rock geochemistry data are provided in Table 8.

2.4. Results

2.4.1 Petrography: mode of occurrences and textures of different Magnetite-bearing assemblages

Magnetite is present in all the major rock types mentioned in Section 2.2.2. Magnetite-bearing samples have been collected from different associations and assigned corresponding number to each of the assemblages. Association I magnetite belongs to apatite-magnetite-rich brecciated rock. Association II magnetite occurs in allanite (LREE-rich epidote group mineral) and biotite-bearing veins and pockets in biotite schist. Association III and IV magnetite are present in U-ore zone occurring in biotite schist (Association III) and chlorite schist (Association IV) respectively. All the magnetite-bearing samples were collected from the vertical shaft, well below the zone of weathering and none of the studied magnetite record significant low-temperature alteration which could alter the original compositions (Ovalle et al., 2018; La Cruz et al., 2020).

In the apatite-magnetite breccia of association I, subhedral to anhedral magnetite along with biotite occurs in the interstitial spaces of large apatite grains (Fig. 2.3A) appearing as biotite-magnetite-cemented brecciated apatite. Xenotime is present as inclusion in apatite (Fig. 2.3B).

Magnetite grains of association II occur in two different ranges of grain size. Subhedral to anhedral magnetite in biotite-allanite rich band (Fig. 2.3C-D) generally ranges in size between 20 and 200 μm, with few oversized grains (≥ 2000 μm; Fig. 2.3F) at places. Some of the magnetite grains of this association contain micro-inclusions at the central part of the grain (these inclusions are too small to successfully analyze in EPMA and are avoided during ICPMS) whereas the boundary of these grains are free of these inclusions (Fig. 2.3E). The rock is schistose and often schistosity defined by biotite warps around large magnetite grain (inset of Fig. 2.3F) hinting that some of the magnetite of association II formed prior to or at the early stage of the shearing event. Biotite grains are chloritized at places.

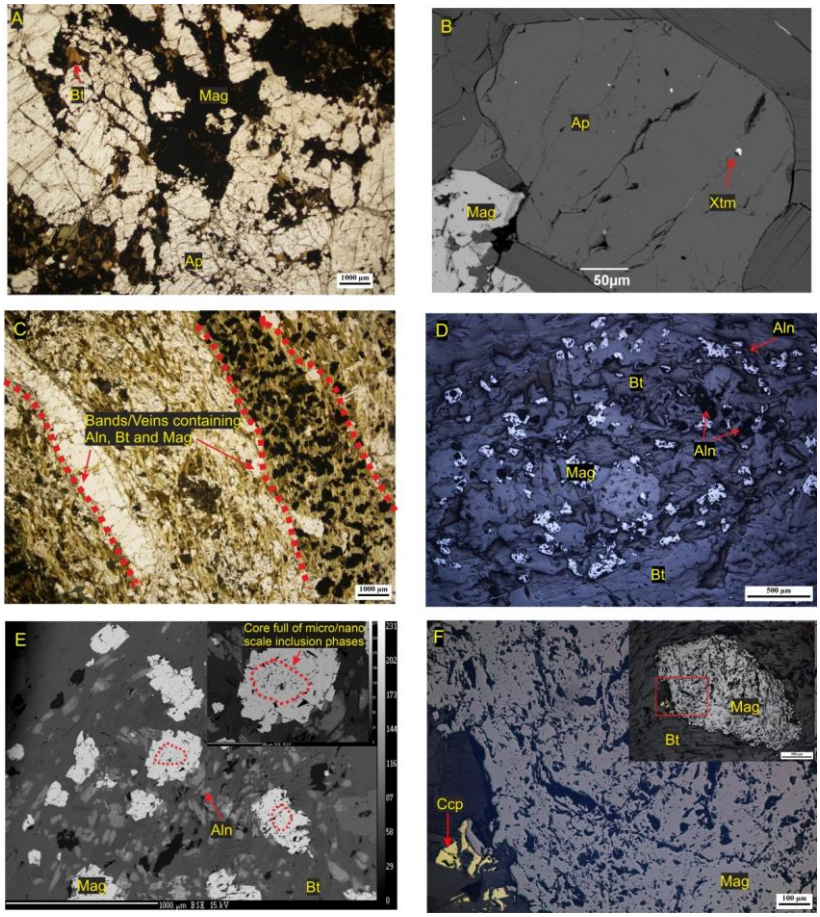

Figure 2.3 Mode of occurrence of magnetite samples from Association I and II

Plane polarized light (A and C) and reflected light (D, F and inset of F) photomicrographs and back-scattered electron images (B, E and inset of E) of association I (Fig. A-B) and association II (Fig. C-F) showing magnetite hosted in magnetite-apatite brecciated rock and magnetite associated with biotite and allanite - (A) Magnetite and biotite occur along the intergranular spaces between large-sized apatite grains (B) Apatite grain with xenotime inclusion. (C) Magnetite occurs along bands containing allanite-biotite and magnetite. (D) Reflected light image showing disseminated magnetite in the biotite-allanite-bearing zone. (E) BSE image showing occurrence of magnetite with allanite and biotite. Note the presence of tiny inclusion phases present in central part of magnetite magnified and marked in the inset. (F) Large magnetite grain with biotite warps around the boundary of the grain. The main figure is an enlargement of the red squared box in the inset. Mineral abbreviations used in this figure and whenever used in the present study followed Whitney and Evans (2010).

Magnetite grains of association III and IV are different than other associations in terms of containing uraninite inclusions within magnetite (both association III and IV)

and uraninite-ilmenite intergrowths (only in association III). The host rock of association III is biotite schist comprised mainly of biotite, magnetite, quartz, albite (Fig. 2.4A) In association III, some magnetite grains are disseminated in the host rocks but the majority of the magnetite grains occur along with biotite in the form of veins/bands (Fig. 2.4A-C). Fluorite is intricately associated with magnetite-ilmenite intergrowths and biotite (Fig. 2.4B) in this association. Previously similar kind of texture was reported from Jaduguda and Bhatin U-

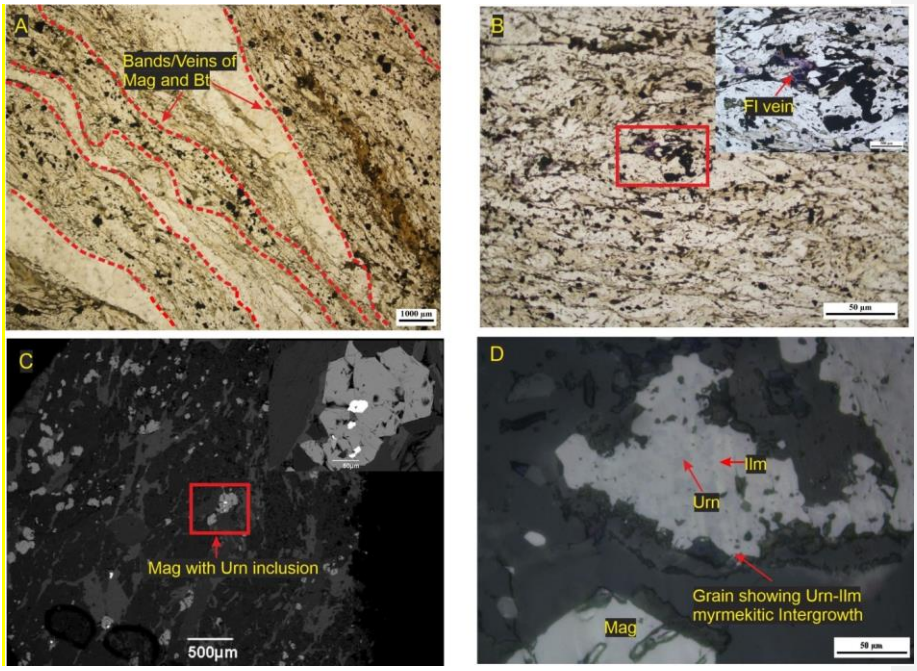

Figure 2.4 Mode of occurrence of magnetite samples from Association III

Plane polarized light (A, B and E) and reflected light (D and F) photomicrographs ~~microphotographs~~ and back scattered electron images (C and inset of C and F) of association III (Fig. 4A-D) and association IV (Fig. 4E-F) magnetite and associated minerals; (A) and (B) Magnetite occurring in bands/veins along with biotite and uraninite. In (B) presence of fluorite in this association is shown. The inset in (B) is of higher magnified version of the area marked in red square. (C) BSE image showing mode of occurrence of magnetite and inclusions of uraninite in magnetite which is zoomed in inset.

deposits by Rao and Rao (1983) and interpreted to be the result of interaction between U-bearing solution and ilmenite.

Contrary to biotite schist host rock of association III, magnetite grains of association IV are hosted in chlorite schist (Fig.2.5A). Another notable difference is that the magnetite grains of association IV are larger in size and also the size of the uraninite inclusions are somewhat larger (Fig. 2.5B) compared to what has been observed in case of association III. The host rock comprises predominantly of chlorite, biotite, quartz and magnetite. Biotite in this rock is extensively replaced by chlorite and only relics of biotite are seen.

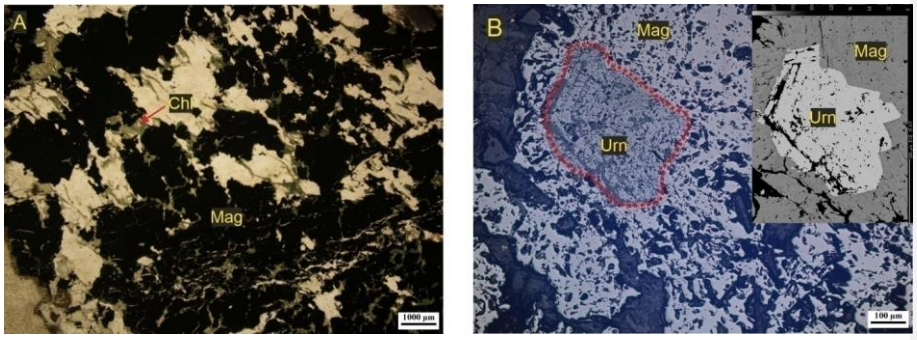

Figure 2.5 Mode of occurrence of magnetite samples from Association IV

Plane polarized light (A) Reflected light (B) ~~microphotographs~~ photomicrographs and back scattered electron image (inset of B) of association IV hosted in chlorite schist. Uraninite inclusion present within magnetite grain shown in magnified BSE image of (B).

2.4.2 Geochemistry: Composition of magnetite and associated phases

Notable differences are observed in major and trace element concentrations of magnetite and associated mineral phases from 4 different magnetite associations. The major element and trace elements concentrations of magnetite and different associated phases are provided in respective tables.

2.4.2.1 Composition of magnetite

Significant differences are seen in the concentrations of spinel elements such as Ti, V, Cr, Mn, and Al in magnetite of different associations (Fig. 2.6 & Tables 1 and Table 2). Box and whisker plots in Fig. 2.6 show the variation in concentrations of trace elements where Si, Mg, Al, Sn and Cr show most wide range of intra-sample variations (Fig. 2.6) and large inter-quartile range.

Highest average concentration of V (average 2.0 wt. %) is seen in association I magnetite and the lowest in association IV (average 621.32 ppm). Magnetite from association II and III contains 0.5 wt%, 0.18 wt% V on an average respectively. Association I magnetite contains highest Ti with an average of 600 ppm Ti. Lowest average concentration of Ti is present in association IV magnetite, the average being 255 ppm. Association II and III magnetite contains very close average concentration of Ti – 342 ppm and 326 ppm respectively. The average concentration of Cr is very low (average 16 ppm) in association IV magnetite and very high (average 905 ppm) in association III magnetite. On the other hand association I and II magnetite contain nearly similar concentrations of Cr and the average values are146 and 133.8 ppm Cr respectively. Concentration of Mn is highest in association I, averaging 235 ppm, and lowest in case of association IV, averaging 59 ppm. Concentration of Al also shows similar trend like Mn (Fig. 2.6B); highest average concentration of Al (0.42 wt%) is present in association I magnetite and lowest average concentration (779 ppm) is recorded in association IV magnetite.

Concentration of transition metals such as Co and Ni also vary significantly among different assemblages. Concentrations of Ni and Co are highest in association I magnetite (average – 700 ppm and 92 ppm respectively). Association III and IV

(uraninite-bearing assemblages) magnetite contain higher concentration of Ni than magnetite of association II (lowest average concentration of Ni – ~~315.52~~316 ppm). On the other hand, magnetite from

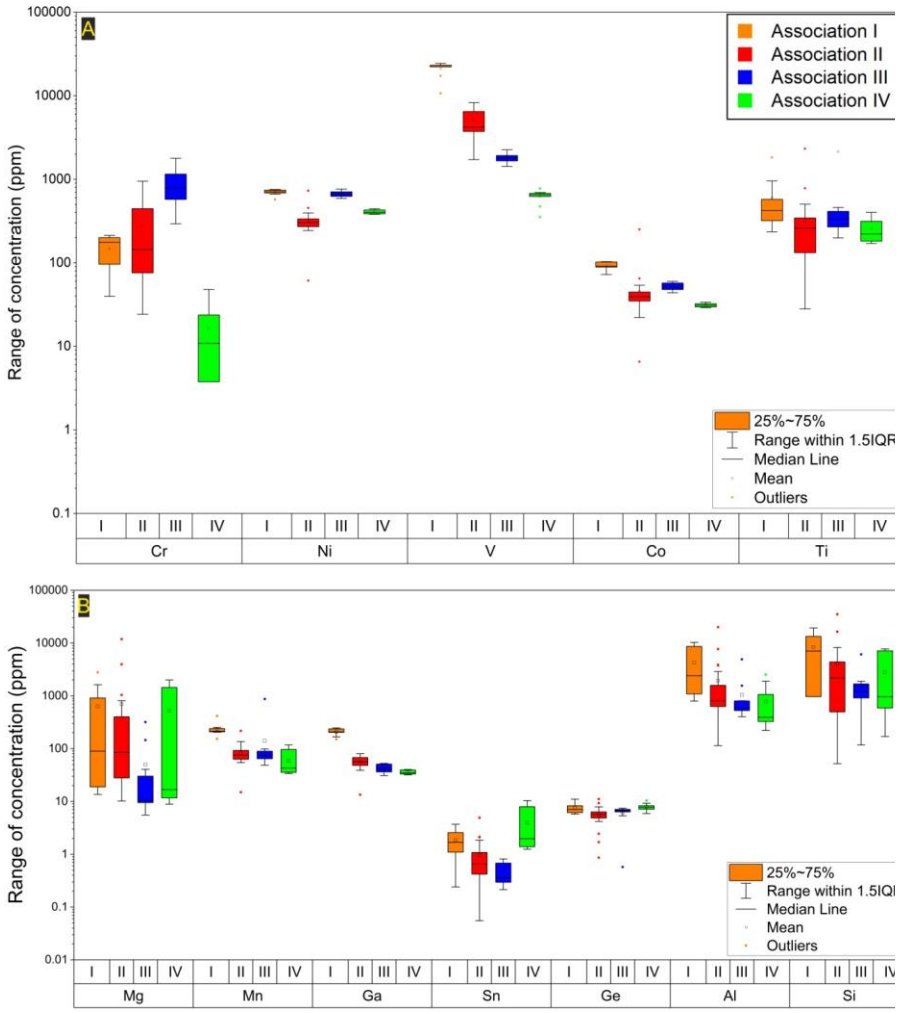

Figure 2.6 Compositional variations in selected spinel elements of magnetite samples from 4 different associations from Bagjata U deposit

Note that the elements are arranged in a way that in both (A) and (B) and from (A) to (B) the compatibility of each element in magnetite decreases from left to right. Legends are shown in Fig. A. The symbol and the colour schemes used in this

figure for different magnetite associations will be followed throughout this chapter.

association IV contains lowest concentration of Co (averaging 31 ppm) and higher concentration of Ni than magnetite of association II (lowest average concentration of Ni – 31~~65.52~~ ppm).

Concentration of Ga is highest in association I magnetite with the average being 209 ppm and lowest in association IV magnetite (average 35 ppm). The highest concentration of Ge is present in association IV (average 7.8 ppm) and lowest average concentration in association II (average 5.5 ppm), although in case of association II outliers present both below and above the mean and median line. Concentration of Sn is highest in associate IV magnetite averaging 3.96 ppm and association III magnetite is most depleted in concentration of Sn with the average being 0.45 ppm.

Highest concentrations of Si is observed in association I magnetite (average value - 0.84 wt%) and the lowest average concentration of Si is observed in association III magnetite (average - 1560 ppm). Lowest concentration of Mg is also found in magnetite of association III (average – 50 ppm), whereas highest average concentration of Mg is found in association II magnetite (average – 788 ppm) and magnetite of association I have very close average concentration of Mg with association II magnetite (average – 633 ppm). Although during major element (by EPMA) and trace element analysis (by LA-ICPMS) analysis spots were selected with great caution to avoid the inclusion of other mineral phases, the concentration of Si, Al and Mg showed somewhat abrupt increment in case of those magnetite grains which contains visible inclusion in optical and BSE images. Also note the presence of significant no. of outliers along with high intra-sample and inter-sample quartile range of these elements (Fig. 2.6B).

2.4.2.2 Composition of biotite and chlorite

Major element composition of biotite (Table 3) and chlorite (Table 5) and selected trace element composition of biotite is given in Table 4. All the biotites of Bagjata from 3 different associations (Association I, II and III) are of intermediate composition between Mg-rich (phlogopite) and Fe-rich end members (annite). However the average values of the Mg/(Mg + Fe) ratios are higher in association I (average 0.32) and association II (average 0.31) biotite compared to biotite of association III (average 0.26). Apart from the differences in major element composition, variation in trace element compositions are also noted among associations I, II and III (Table 4). Although Ni and Co both are enriched in association III biotite, these biotite grains show consistently higher Ni/Co ratio than the biotite samples of association I and II. The Ni/Co ratios are 8.7, 8.2 and 11.72 (average values) for association I, II and III respectively. Biotite of association III is most depleted in Ga (average 34 ppm), but enriched in Mn (average 501 ppm) compared to biotite of association I and II.

All the chlorites associated with magnetite from association IV are chamositic in composition. The average Mg/(Mg + Fe) ratios calculated from EPMA compositions of chlorite grains of this association is 0.27. The Major element compositions of chlorite are is given in Table 5.

2.4.2.3 Composition of apatite

Apatite samples from association I and II are not significantly different in terms of most of the major element analyzed in EPMA (Table 6.). The average concentration of Ca is 40.47 wt% vs. 40.62 wt% for association I and II respectively. The only notable difference has been observed in terms of P content. Association I apatites are

comparatively more enriched in P (average concentration 18.27 wt%) than the apatite samples from association I (average concentration 17.77 wt%).

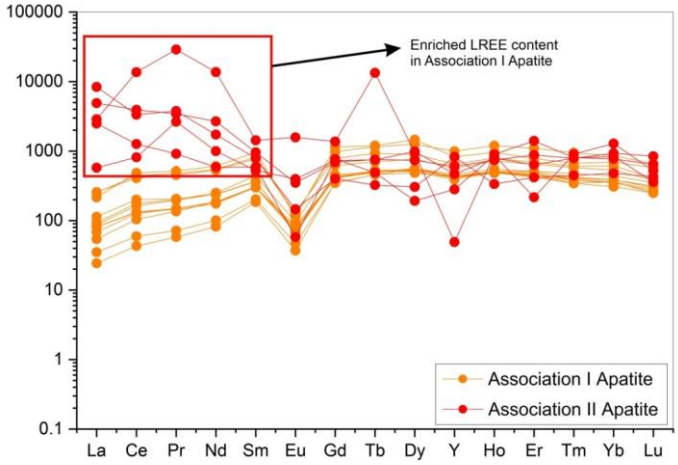

Figure 2.7 Compositional variation between apatite samples of Association I and II

Note the difference in LREE content between Association I and Association II apatite, higher in case of association I apatite samples shown in the chondrite normalized REE diagram

On the other hand, the apatite samples from association II which are associated with magnetite, biotite and allanite showing significant enrichment in LREE content (average concentration of ∑LREE ≈ 6400 ppm) than the apatite samples from association I apatite (average concentration of ∑LREE ≈ 367 ppm). Note that although association I samples are enriched in LREE, concentration of HREE remains almost invariable between apatites from these 2 associations (Fig. 2.7). The cumulative average concentration in case association I and II apatite is ∑HREE ≈ 752 ppm vs. 538 ppm respectively.

Apart from the compositional enrichment in LREE content, association II apatite is also relatively enriched in V (average concentration ≈ 236 ppm) compare-d to the apatite s of association I (average concentration - 5.3 ppm).

2.4.2.4 Composition of host rocks

One rock sample is from magnetite-apatite ± biotite-bearing brecciated rock hosting association I magnetite, 3 of the rock samples are from biotite schist rock hosting association II and III magnetite and 5 other rock samples are from chlorite schist hosting association IV magnetite and similar rocks. The major element and REE concentrations of the representative host rocks used in this study are given in Table 8.

Magnetite-apatite rich rock are significantly enriched in P, Ca and Fe and depleted in Na, K and Si compared to the biotite and chlorite schist (Fig. 2.8A) plotted in the

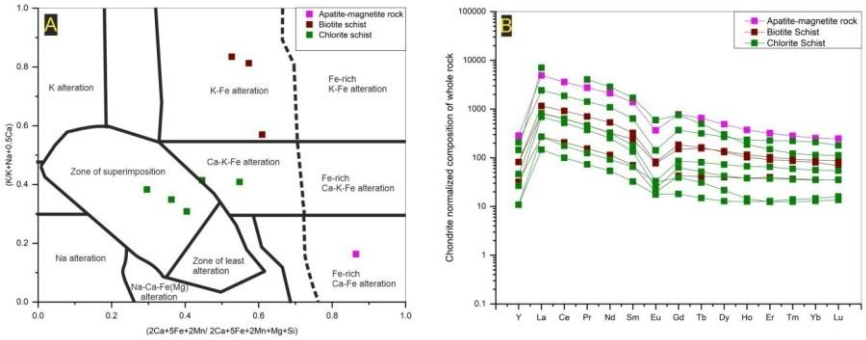

Figure 2. 8 Compositional variation of different host rocks in Major element and REEs shown in aAlteration index dDiagram and cChondrite--normalized REE Diagram

(A) IOCG alteration diagram from different alteration types based on the whole rock composition of rocks hosting magnetite (after Montreuil et al. (2013). See text (section 2.5.1) for discussion. (B) Chondrite (values from McDonough and Sun, 1995) normalized plot of whole rock compositions of the different rock units (Apatite-magnetite rock, biotite schist and chlorite schist) hosting magnetite in Bagjata deposit. Note the similar REE pattern for all rock types.

alteration index diagram suggested by Montreuil et al. (2013) and the implications of this alteration diagram has been discussed in detail in section 2.5.1. This extreme enrichment in P, Ca and Fe in magnetite-apatite-rich brecciated rock is due to the abundance of

apatite and magnetite. The biotite schists are obviously enriched in K than the other two types of rock hosting magnetite. No notable difference has been observed between biotite schist hosting U-mineralized unit and barren unit. These rocks are also enriched in Fe than chlorite schist. On the other hand, the chlorite schists are enriched in Si, Al and depleted in K in comparison to biotite schist.

All the studied rocks have very similar chondrite-normalized REE-pattern with LREE-enriched and HREE-depleted trends and significant negative Eu anomaly albeit variable enrichments of REEs (Fig. 2.8B). The REE enrichment ranges from ~100 to up to ~10000 times. Chlorite schist has wide range of enrichment overlapping with biotite schist. Importantly, the chondrite-normalized pattern remains consistently similar across all the host rocks of different magnetite-bearing assemblages.

2.5. Discussion

2.5.1 Nature of the magnetite mineralization from mode of occurrence, whole rock composition and mineral thermometry

In this section mode of occurrence of magnetite samples from Bagjata U mine along with their textural relationship with the associated gangue mineral phases and host rocks will be explored to get an insight of the underlying physicochemical process which was responsible for magnetite mineralization in this deposit. The geochemical composition of the rock hosting magnetite mineralization will also be used in addition to calculated temperature range from different thermometric calculations based on magnetite, biotite and chlorite compositions in order to understand the formation process.

2.5.1.1 Origin/Nature of the magnetite mineralization: constraints from mode of occurrence and whole rock composition

The magnetite-bearing assemblages described in this study essentially occur as veins, pockets and stringers with grain size of the constituent minerals being larger than those in the host rocks, which provide *prima facie* evidences for their epigenetic hydrothermal origin. The host rocks are also variably altered as evidenced by large variations in the modal abundances of the constituent minerals in different scales. The occurrence of magnetite of association I in the form of magnetite-cemented breccia closely resemble with Ca-Fe ± K metasomatism (Coriveau et al., 2016). The magnetite grains of association II are ~~associated~~ with allanite and biotite in pockets and veins and therefore, are interpreted to be the product of K-Fe metasomatism with accompanying LREE mineralization (cf. Pal et al. 2011). Pal et al. (2011) proposed that the Ca-K-Fe metasomatism was accompanied by influx of LREE evidenced by the abundant presence of allanite in some samples as described in our study. In a more recent study on Jaduguda deposit, Pal et al. (2021) suggested that Ca for allanite could be derived from the Ca-rich mafic protolith. It therefore stands to reason that the alteration assemblage of association II at Bagjata may also represent K-Fe alteration, Ca being derived locally. Magnetite of association III formed along with the biotite and is interpreted to be the product of K-Fe metasomatism. Association IV magnetite grains are accompanied by abundant chlorite in the assemblage. Replacement of biotite by chlorite is ubiquitously present close to this association in the host rock implying their formation by hydrolytic alteration (H^+-metasomatism with accompanying alkali-/K-removal).

Montreuil et al. (2013) (further developed by Corriveau et al. (2016)) proposed a novel method of deciphering alteration types in IOAA (Iron-oxide alkali altered) systems using whole rock compositions that can potentially distinguish different alteration types

in metamorphosed hydrothermally altered rocks. Because the mineralization in the SSZ has many characters akin to IOCG style mineralization, in order to understand the nature of alteration types of different magnetite-bearing assemblages of Bagjata, whole rock compositions of the host rocks are plotted in alteration index diagram of Montreuil et al. (2013). The authors proposed an alteration index diagram that distinguishes Na, Na-Ca-Fe, Ca-Fe, Ca-K-Fe, K-Fe and K alteration types from a wide range of protoliths following the alteration sequencing model of Corriveau et al. (2010). The first index constructed as Na/(Na+K+0.5Ca) (all elements in molar proportions) to differentiate Na, K and Ca-Fe alterations (designated as AIOCG1) and the other index is constructed as (2Ca+5Fe+2Mn)/(2Ca+5Fe+2Mn+Mg+Si) to discriminate Na-K, Ca-Fe, K-Fe and Fe alterations (designated as AIOCG2). The magnetite-apatite-rich brecciated rock which hosts the association I magnetite is plotted in the Fe-rich Ca-Fe alteration region in the diagram (Fig. 2.8A). The biotite schist hosting magnetite of association II and association III plotted in the domain of K-Fe alteration. On the other hand, chlorite schist hosting association IV magnetite mostly plotted in the 'zone of superimposition' with two samples falling in Ca-K-Fe region (Fig. 2.8A). It is to be noted that in chlorite schist, relics of biotite replaced by chlorite, is present which testifies superimposition of acidic/hydrolytic alteration (H^+) of an earlier K-Fe altered rock with accompanying removal of K. Thus the vein assemblages, mineral alterations and whole rock compositions collectively suggest that the rocks in the Bagjata deposit were subjected to Ca-Fe ± K, K-Fe ± LREE and H^+ metasomatism all of which were accompanied by magnetite formation with (association III and IV) or without (association I and II) uranium mineralization. Although the alteration index diagram does successfully discriminate the broad variation in corresponding hydrothermal alterations based on the whole rock composition, advanced attributes like association of LREE component with

K-Fe alterations comes from accessory mineral composition. The corresponding fluid responsible for K-Fe alterations (Association II) was enriched in LREE as evidenced by the abundant presence of allanite in the mineralogical association and further attested by the apatite chemistry. Chondrite-normalized REE plot of apatite composition from association I and II (Fig. 2.7) shows all the LREE are enriched in case of association I apatite compared to association II. This implies that although the very similar REE patterns of the variably altered rocks suggest that they formed from the same/similar protolith (Fig. 2.8B), each hydrothermal alteration types has key individual characteristics.

The major types of alterations in the SSZ, described by previous worker include Na, K, H^+ and B metasomatism (Pal et al., 2010; Pal et al., 2021a; Pal et al. 2021b, *in press*; Pal and Chaudhuri, 2016; Sarkar, 1984; Sengupta et al., 2005). The quartz-albite bearing albite schist have been considered to be the Na-metasomatized product of mafic as well as felsic protolith (Sarkar, 1984). The K-metasomatism in the SSZ is represented by the presence of biotite schist that at places contain more than 60-70 vol. % of biotite and the acidic/hydrolytic alteration is culminated in the formation of chlorite schist and the sericite schist. In addition to this, presence of abundant tourmalinite bears the evidence of B-metasomatism in the shear zone rocks (Pal et al., 2010; Sengupta et al., 2011, 2005). Considering broadly from regional scale to small micro-domain-scales, a recursive pattern of B→ Na (-Ca)→K(-Fe)→H^+ metasomatism is recognized in the SSZ (Pal and Chaudhuri, 2016; Pal et al., 2021). The alteration types described in this study are in consonance with the alteration types described in earlier studies and have commonalities with the different variants of IOCG-type alterations. Thus combining the mode of occurrence of magnetite in different alteration assemblages and host rocks along with the whole rock geochemical data the present study proposes that all the magnetite

from different mineralogical association are essentially formed by hydrothermal ore-forming process and the alteration signatures reflected from the whole rock composition strongly resembles with what have been observed in IOCG-type deposits elsewhere in the globe (Barton, 2014; Huang et al., 2019).

2.5.1.2 Temperature of hydrothermal alterations associated with magnetite mineralization: A mineral thermometry based approach

In order to get an estimation about the formation temperature of various magnetite-bearing assemblages associated with specific alteration patterns as described in the foregoing section, temperature form biotite thermometry (for association I, II and III), chlorite thermometry (for association IV), and magnetite-thermometry (for all the associations) are calculated. This integrative approach would provide the temperature of magnetite formation vis. a. vis. the temperature of the hydrothermal alteration.

The temperature dependence of Ti-incorporation in biotite structure has long been used by petrologists to derive the temperature of the assemblages (Henry and Guidotti, 2002; Henry et al., 2005). In the present study biotite temperature was calculated (results given in Table 3) following the methods suggested by (Wu and Chen, 2014) using the formula calculation suggested by (Li et al., 2021). The temperature calculation requires idea about pressure. Mishra et al. (2003) obtained a maximum pressure of 2.6 kb from their fluid inclusion studies of mineralized sulfide veins from Mosabani and Rakha deposits. As the depth of mineralization is uncertain, in this study the temperatures are calculated using 3.0 kb (0.3 GPa) and 0.6 kb (0.06 GPa) corresponding to depths of 10 km and 2 km respectively considering the most hydrothermal mineralization takes place within the brittle crust in this depth range. It may be noted that the calculated temperatures using two different pressures differ only by ~15°C. In the following discussion the temperature obtained with 3.0 kb is used as it is more realistic and close to

the pressure reported for sulfide mineralization (*op cit*). The highest temperature is obtained from association III, followed by association I and association II (Fig. 2.9A). The average temperature for association III biotite is ~ 500ºC (average is 498~~7.83~~°C), and the average temperatures for association I and II are ~453°C and ~439°C respectively. Distinct temperature ranges obtained from different associations suggest that biotite compositions did not re-equilibrate during metamorphism because the analyzed biotite comes from biotite-rich zones unlike disseminated biotite of typical metamorphic origin. The high temperature, close to and in excess of 450^0C is in good agreement with homogenization temperatures of fluid inclusion in apatite associated with U and REE mineralization and tourmaline associated with sodic alteration (Pal et al., 2008; Pal and Bhowmick, 2015) reported from this shear zone.

In case of association IV temperature was calculated using the chlorite thermometry based on empirical/semi-empirical models and thermodynamic models (Kranidiotis and MacLean, 1987; Cathelineau, 1988; Jowett, 1991; Zang and Fyfe, 1995; Vidal et al., 2001, 2005). Although the range of temperature from different thermometers is variable to certain extent (Fig.2.9B), chlorite grains of association IV yields significantly lower temperature than

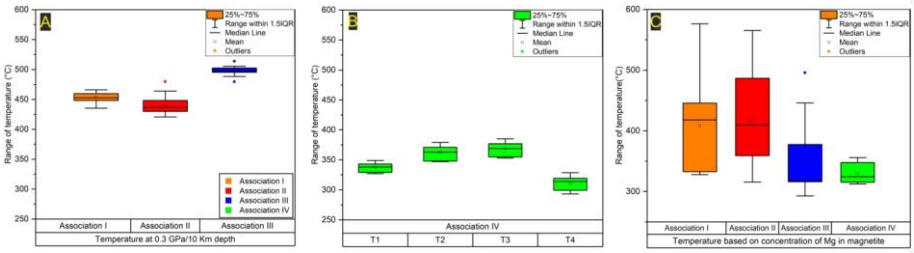

Figure 2.9 Range of formation temperature of different magnetite bearing associations by biotite, chlorite and magnetite based thermometric calculations

Box and whisker plots (A-C) of temperature range from Ti in biotite thermometry for association I, II and III (A), calculated after Wu and Chen, (2014). Temperature range from chlorite thermometry for association IV (B) – T1, T2, T3are based on empirical equation calculated after Kranidiotis and MacLean (1987), Cathelineau (1988), Jowett (1991) respectively and T4 is based on thermodynamic model by Vidal et al. (2001). Temperature range from magnetite thermometry for association I-IV (C) are calculated following the method by Canil and Lacourse (2020). The legends for all the diagrams are shown in Fig. A.

those obtained from biotite of association I, II and III. In the present study, the range of temperature obtained for hydrothermal chlorite from association IV is 310°-370°C broadly in similar range as reported by Pant et al., (2019) for hydrothermal chlorite. It is evident from the above discussion that Ca-K-Fe and K-Fe alteration related to apatite-magnetite, REE and one stage of U mineralization (association III) took place at higher temperature (≥ ~450ºC) than the hydrolytic alteration related to U mineralization of association IV(~350ºC).

From experimental observations Canil and Lacourse (2020) demonstrated that the $X_{Mg} = [Mg/(Mg + Fe_{total})]$ of magnetite is strongly dependent on temperature and the concentration of Mg in magnetite is comparatively fO_2-independent than some other commonly incorporated trace elements like Cr, Al, Mn etc. and proposed a geothermometer based on X_{Mg} values. Temperatures were calculated here by using the Fe and Mg concentrations of magnetite determined by EPMA~~EMPA~~ and LA-ICP-MS (Table

1 and Table 2), following the suggested empirical calibration, which considers an uncertainty of ± 50 °C

$$TMg(°C) = -8344(\pm 322)lnXMg - 2.12(\pm 0.28) - 273$$

All calculated temperatures except those spots that contain unusually high Mg (> 1000 ppm Mg) using this method for Bagjata magnetite fall in the sub-solidus temperature range (< 600ºC) supporting our earlier interpretation of hydrothermal origin (not magmatic) of all studied magnetite types (Fig. 2.9C). The mean temperatures for all associations exceed 300ºC. Association I and II (Ca-Fe ± K and K-Fe alteration respectively, the latter related to REE mineralization) yield higher temperature than association IV (hydrolytic alteration associated with U-mineralization) consistent with biotite and chlorite thermometer whereas association III (K-Fe alteration associated with U-mineralization) yields lower temperature than association I and II contrary to biotite thermometer. Magnetite of association I and association II which are the product of Ca-Fe-K alteration and K-Fe-LREE alteration types formed at relatively higher T than magnetite samples of association III and IV which are the product of K-Fe and H+ metasomatism according to Mg based thermometry from magnetite composition. Textural evidence along with the whole rock composition of magnetite-hosting strata indicate although physicochemical conditions are variable to certain extent between different magnetite-bearing assemblages reflected in the thermometric measurement, occurrence of magnetite in form of veins, pockets testifies that magnetite samples from the Bagjata U-deposits are essentially the product of hydrothermal alteration processes.

2.5.2 Physicochemical condition of ore forming processes: Implication of trace element geochemistry of magnetite

The classification of magnetite into different associations based on mineralogical association and accompanying alteration broadly correlates with the compositional variations of magnetite from different associations. The composition of hydrothermal magnetite is influenced by intrinsic parameters such as crystallographic controls (ionic radius), temperature (T) and oxygen fugacity (fO_2) along with the controls of co-crystallizing phases, host rock and fluid compositions (Dare et al., 2014; Nadoll et al., 2014). In the following sections the viability of correlating the trace element composition of magnetite with fO_2 and T range, with the thermometric measurement for the latter one, is explored. Additionally, concentration of some specific trace elements will be used to get some insights about the fluid composition associated with different hydrothermal alterations.

2.5.2.1 Temperature

Titanium and V have long been regarded as important spinel element for their high partition coefficient in favor of magnetite, and as an indicator of formation temperature (Dare et al., 2014; Nadoll et al., 2014; Deditius et al., 2018). This qualitative measurement of formation temperature mainly stems from the understanding that in magmatic condition and during cooling, partitioning of these elements is directly linked to change in T (Turnock and Eugster, 1962; Butcher and Merkle, 1987) as the partition coefficients are largely dependent on T (McIntire, 1963). The magnetite compositions of this study is used in the proposed (Ti + V) vs. (Al + Mn) (Nadoll et al., 2014) diagram to check whether it discriminate different associations of magnetite formed at different temperatures associated with specific type of alteration (Fig. 2.10A). Most of the data cluster around the >500°C and 300°C-500°C field. Although this diagram does not distinctly discriminate magnetite formed during different alteration (higher temperature)

it is in broad agreement with decreasing temperature from association I and association II to association III and association IV as obtained from different mineral thermometer. Importantly, magnetite of different associations has distinctive and restricted Ti + V concentrations but more variable Al + Mn concentrations suggesting greater reliability of Ti and V in deciphering relative temperature of formation.

Nadoll et al. (2014) suggested Ti/V as an effective tool to discriminate high Ti-igneous magnetite from Henderson Climax-type Mo deposit from high vanadium bearing igneous magnetite from inner zone batholiths and mentioned that Ti/V ratio remains constant even with decreasing T and decreasing total abundance of (Ti + V) content. In our study, the cumulative concentrations of (Ti + V) roughly decreases and Ti/V ratios increases with decreasing temperature (Fig. 2.10B), wherein the high temperature Ca-Fe ± K (association I) and K-Fe ± LREE alteration assemblages (association II) have higher (Ti + V) and lower Ti/V ratios than hydrolytic alteration assemblages(association IV). Perhaps comparison of Ti/V ratio of magnetite from different deposits (as done in Nadoll et al. 2014) is not applicable in case of comparison of magnetite from the same deposit with varying temperature and alteration(Fig. 2.10C). Observations in this study indicate that cumulative incorporation of Ti + V and Ti/V ratios in magnetite are better indicator of overall temperature trends (Fig. 2.10D). It is important to note that the interpretation on overall trend in temperature is consistent with magnetite thermometry of all associations, biotite thermometry of association I and association II and chlorite thermometry of association IV. It is not known at the moment why association III stands out as an exception in biotite thermometry. The association III is characterized by ilmenite-uraninite intergrowth and ubiquitous presence of fluorite (Fig. 2.4B). Extreme solubility of Ti in F-rich fluid is now well-known (Ryzhenko et al., 2006; Rapp et al., 2010). It is possible that high content of Ti in the fluid resulted in higher enrichment of Ti in the biotite leading to unusually high temperature obtained from biotite thermometry. The possibility that association III

formed by a different process whereas association I, II and IV might have formed as a continuum of the same process also cannot be ruled out.

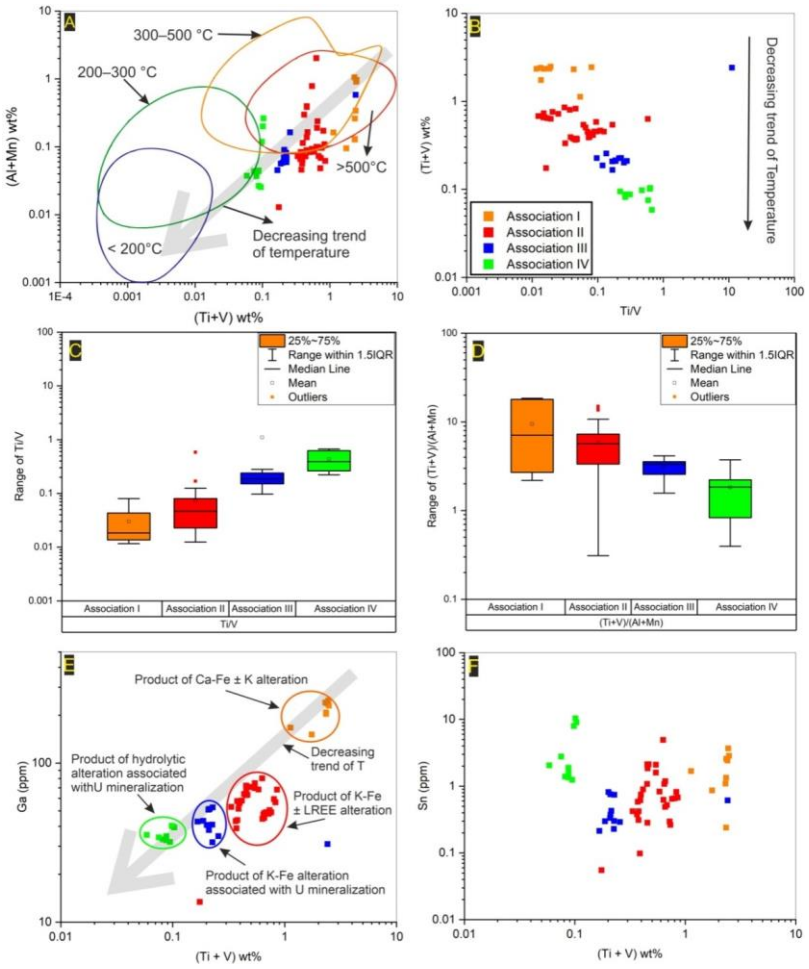

Figure 2. 10 Variation of trace elements in magnetite as a function of temperature

Bivariate (A, B, E and F)) and Box and Whisker plots (C and D) of magnetite samples from different associations; (A) (Ti + V) vs. (Al + Mn) plots (all in wt%) redrawn from Deditius et al. (2018) showing most of the magnetite samples plotted in the >500°C and 300°-500°C field. with some of the samples plotted outside of the designated fields. (B) Ti/V vs. (Ti + V) plots are shown with the possible decreasing trend of T. (C) and (D) are Box and whisker plots of Ti/V and (Ti + V)/(Al + Mn) respectively. Ga vs. (Ti + V) (E) and Sn vs. (Ti + V) (F) plots for magnetite of different associations. The legends are shown in Fig. B. See text for discussion.

Considering that Sn and Ga are often cited for their T dependence, with higher concentration in higher temperature environments (Nadoll et al., 2014; Knipping et al., 2015b), the applicability of concentrations of these elements with respect to Ti + V is examined as the latter works reasonably well with our sample. Despite overlap of magnetite data from association III with those from association II and IV, Ga concentrations mimic the overall decreasing temperature trend from association I, to association II to association III (Fig. 2.10E). The concentrations of Sn do not vary accordingly with temperature of the alteration types (Fig. 2.10F).

2.5.2.2 Oxygen fugacity

Partitioning of elements with variable valence state proved to be an effective monitor of oxygen fugacity (fO_2).Elements such as V, Cr, Sn, Mn, Ge etc. with variable valence states have previously been linked to their dependency on prevailing oxygen fugacity (Acosta-Góngora et al., 2014; Chen et al., 2015a; Huang et al., 2019). Several previous studies reported systematic correlation between fO_2 and concentration of multivalent element such as V and Sn and no effect of fO_2 on partitioning of homovalent element like Co, Ni and Ga (Mallmann and O'Neill, 2009) in magnetite (Toplis and Corgne, 2002; Sievwright et al., 2017).

The most common valence state of V varies between +3 to +5. Vanadium in +3 state is most compatible in magnetite structure (Righter et al., 2006). Slight increase in fO_2 drives the valence state to +4 or +5 and V becomes incompatible in magnetite structure. On the contrary the valence-dependent incorporation of Sn in magnetite structure is the opposite. The two most common valence state of Sn is +2 and +4 and the more oxidized state i.e. Sn in +4 state is more compatible in magnetite structure compared to Sn in +2 state (Huang et al. 2019 and reference therein). Therefore, in order to check

the role of *f*O2_and amplify the effect of fO_2 component Sn vs. V/Sn ratios are plotted (Fig. 2.11A). It can be inferred from the graph that magnetite of association I, II and III with very high V/Sn ratios most likely formed in lower fO_2 condition whereas magnetite from association IV with lower V/Sn ratios formed in comparatively more oxidized condition. In another plot to check the effect of increasing fO_2 on magnetite composition is examined taking into account the well-established correlation between V and oxygen fugacity by trying a combination of V/Ga and (Ge + Sn) as partitioning of homovalent cation such as Ga is known to be independent of fO_2 (Mallmann and O'Neill, 2009; Nadoll et al., 2014) and partitioning of Ge in magnetite has been suggested to be favorable at higher fO_2 (Meng et al., 2017). However, in the studied magnetite no variation is seen in the Ge content (Fig. 2.11B).

Interestingly the composition of apatite from association I and association II shed further light about the relative fO_2 condition between these 2 associations, if the incorporation of V in magnetite and apatite is considered. V in +5 state is most compatible in apatite structure whereas +3 is the most compatible state of V in magnetite. Increase in V content in association I magnetite compared to association II magnetite corresponds well with relatively lower concentration of V in apatite of association I and implies the fO_2condition was comparatively more reducing in case of association I than association II magnetite samples.

Carew (2004) reported the interrelation between Vanadium and Sn concentration in the context of changing fO_2 in Ernest Henry deposit where the consistent decrease in V and corresponding increase in concentration of Sn was attributed to the increase in fO_2 of the fluid as the system moved towards potassic alteration from the earlier sodic alteration with accompanying decrease in T and increase in oxygen fugacity (Carew, 2004). On the other hand, there are also reports of no correlation between V and Sn based on

geochemistry of magnetite from Proterozoic Fe-Cu deposits of Kangdian province of SW China albeit

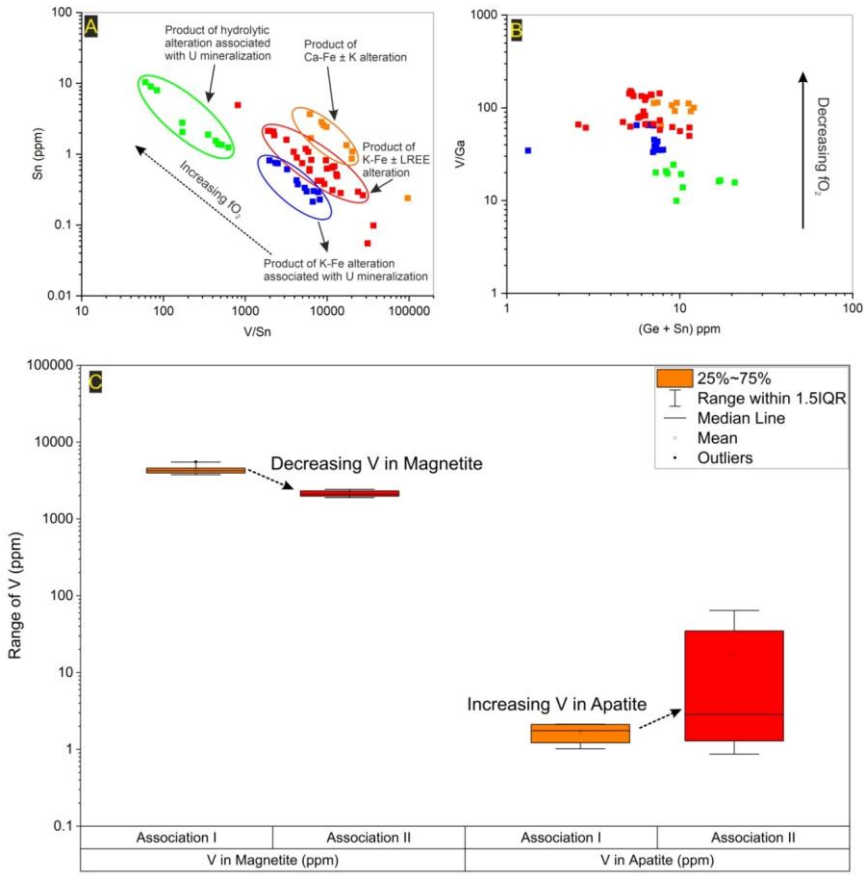

Figure 2.11 Variation in concentrations of trace elements in magnetite and apatite as a function of oxygen fugacity (*f*O2)

Bivariate V/Sn (A) and V/Ga vs. (Ge + Sn) (B) and Box and whisker plot of V concentration in magnetite vs. apatite (C) plots for magnetite of different associations. The legends are same as preceding Figures for (A) and (B). See text for discussion.

Formatted: Font: 11 pt, Italic, Font color: Text 1, Expanded by 0.25 pt, Kern at 14 pt

different study reported that the fluids of the Cu-sulfide stage were more oxidized compared to fluids of the Fe-oxide stages (Chen et al. 2015 and reference therein). The latter authors have suggested that variable concentrations of V and Sn in corresponding

fluid are the major controlling factor, not fO_2. However, considering the consistent decrease in temperature from Ca-Fe ± K, K-Fe ± LREE and H^+ metasomatized rocks (association I, II and IV), barring the exception of association III, it is possible that these alteration assemblages stemmed from the same but evolving fluid. Therefore, it is proposed that V/Sn ratio vs. Sn concentration of magnetite can be an effective tool to decipher the relative fO_2 of the mineralizing fluids, consistent with obvious negative correlation between Sn vs. V/Sn. Other elemental ratios involving Vanadium such as V/Ga can also be useful in this regard.

2.5.3 Trace element systematic of magnetite: implications for discriminators

As discussed in the preceding section that magnetite chemistry can reflect the physicochemical parameters related to the environment it grows in, numerous studies tried to utilize this by suggesting diagrams/plots based on well-characterized dataset to identify the process and deposit-type affiliation. In case of Bagjata U deposit the information derived from mode of occurrence, textures and alteration patterns put to further test by application of these discriminators.

2.5.3.1 Implications of trace element based process discriminator

The trace element compositions of Bagjata magnetite are compared with bulk continental crust normalized multi-element variation diagram (Fig. 2.12A) proposed by Dare et al., (2014). These authors selected 25 elements and arrange them in order of increasing compatibility in magnetite. The concentration of different elements are normalized to bulk continental crust to reflect the variation of the pattern caused either by the composition of the hydrothermal fluid and/or the compatibility of the element in magnetite structure (Dare et al., 2014). It has been observed that there is a general increasing trend in elemental concentrations from left to right in case of magmatic magnetite, primarily controlled by partitioning between melt and magnetite. On the

contrary, hydrothermal magnetite does not often follow this pattern because of a greater control of fluid composition compared to partitioning of elements in magnetite structure. For comparing the compositional difference between magnetite formed from relatively high T hydrothermal fluid with those formed from low T hydrothermal fluid inferred from thermometric calculations, some of the extreme end members of our studied samples in terms of formation temperature are selected–

a) Magnetite associated with apatite ± biotite and biotite ± allanite (association I and II respectively associated with high T Ca-Fe ± K and K-Fe ± LREE alterations) and

b) Magnetite which are the product of chloritic alteration (association IV).

The reason behind selecting these associations is to get idea about the relative differences in physicochemical parameters (mainly temperature) and the composition of the fluid (Fig. (2.12A). The observed differences are in partial accordance with the differences shown by Dare et al. (2014, 2015) to discriminate between high temperature and low temperature hydrothermal magnetite. Magnetite formed from high T hydrothermal fluid (association I and II) are enriched in more magnetite compatible elements (V, Cr, Zn, Ga etc) perhaps indicating T as primary control for incorporation of these elements (Canil and Lacourse, 2020) whereas significant overlap is observed between association I, II and association IV magnetite in case of W and Ge concentrations which is often enriched in magnetite formed from low T hydrothermal fluid and magnetite from low T BIF (Dare et al., 2014 and reference therein). In Bagjata both association I and II magnetites are generally enriched in magnetite-compatible elements than association IV magnetite (Fig 2.12A) where compatibility increase from left to right of the diagram) barring some exceptions which is largely in agreement with the proposition by Dare et al. (2014) that

low T fluids (both in case of low T hydrothermal environment and in case of Banded Iron Formation) are depleted in magnetite-compatible elements probably due to decrease in solubility of these elements with decrease in temperature, resulted in overall low abundance of compatible trace elements (Dare et al., 2014 and reference therein).

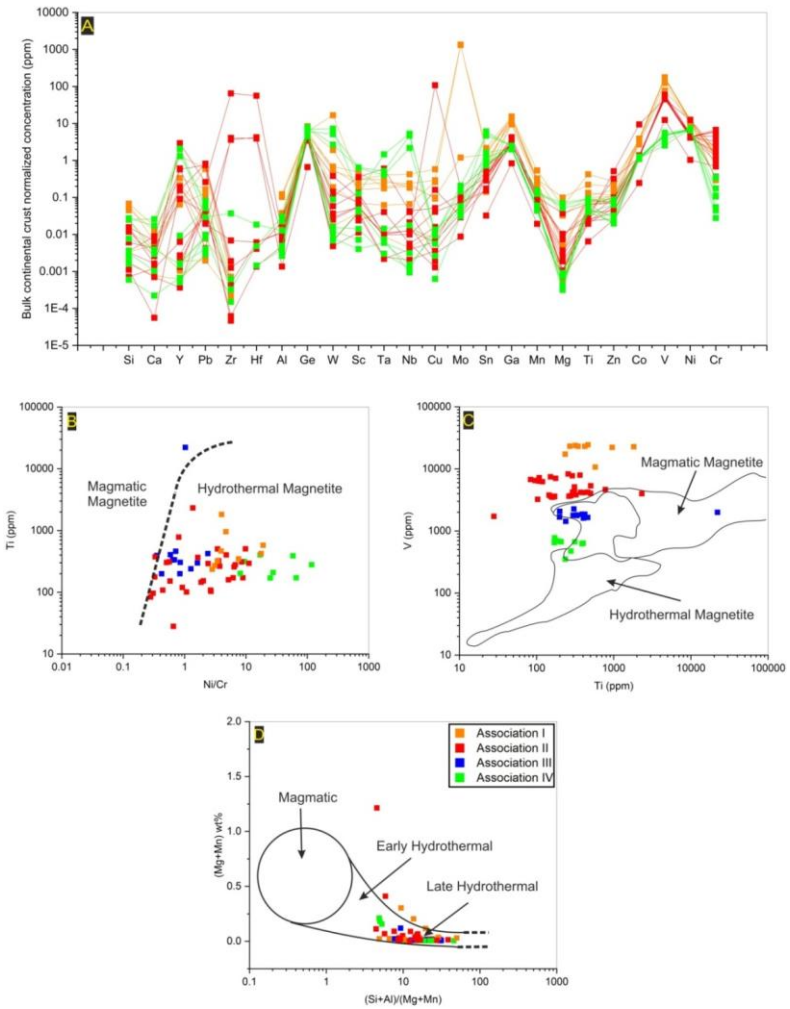

Figure 2.12 Trace element geochemistry of magnetite as an indicator of process of formation

Bulk continental crust (values from Rudnick and Gao, 2003) normalized magnetite composition of association I, II and IV(A) and bivariate plots (B-D)) of magnetite; (A) Enrichment of specific elements in association I and II vs. IV showing relative difference in formation temperature of magnetite samples of respective associations.(B) Ti vs. Ni/Cr plot after Dare et al. (2014) to discriminate magmatic magnetite from hydrothermal magnetite. Note that all the Bagjata magnetite samples are plotted in the hydrothermal magnetite field with minor exceptions. (C) V vs. Ti plot to discriminate hydrothermal and magmatic magnetite after Knipping et al. (2015) and the fields are drawn based on the dataset of Nadoll et al. (2014). (D) (Mg + Mn) vs. (Si + Al) / (Mg + Mn) plot after Deditius et al. (2018), proposed to show the compositional changes of magnetite from magmatic to hydrothermal

environment. Legends are shown in (D).

In addition to the multi-component diagram the magnetite data is tested in the now widely used Ti vs. Ni/Cr discriminator (Dare et al., 2014). All the magnetite grains plotted in hydrothermal field with minor exceptions (Fig. 2.12B). This diagram was proposed on the basis of coupled behavior of Ni and Cr in magmatic environment and the decoupling of Ni from Cr in hydrothermal environment (Ni is considered to be more mobile than Cr). The discrimination diagram suggested by Dare et al. (2014) clearly decipher the hydrothermal origin of Bagjata magnetite. The hydrothermal origin of magnetite samples from Bagjata U deposit has been demonstrated, in an earlier section, based on mode of occurrence and associated hydrothermal alteration.

The Ti and V concentrations of Bagjata magnetite are plotted in another discrimination diagram proposed by Knipping et al. (2015). Most of the magnetites fall beyond the assigned field for either hydrothermal or magmatic magnetite (Fig. 2.12C). On the contrary the discrimination diagram ((Si + Al)/(Mg + Mn) vs. (Mg + Mn) in wt. %)) suggested by Deditius et al. (2018) based on the study of Los Colorado hydrothermal magnetite works well to discriminate hydrothermal magnetite of Bagjata U deposit from magmatic magnetite (Fig. 2.12D). However, it is not possible to comment on the fields provided in an attempt to discriminate early hydrothermal from late hydrothermal fluid for our studied samples.

2.5.3.2 Implications of trace element based deposit type discriminator

Trace element concentrations have been used to fingerprint the deposit types and applied in numerous previous studies (Dupuis and Beaudoin, 2011; Nadoll et al., 2014; Chen et al., 2015b, 2015a; Knipping et al., 2015b; Heidarian et al., 2016; Huang et al., 2019; Huang and Beaudoin, 2019). Dupuis and Beaudoin (2011) proposed several empirical discrimination diagrams based on trace element concentrations of magnetite

from a range of ore deposits including iron oxide-copper-gold (IOCG), Kiruna apatite–magnetite, banded iron formation (BIF), porphyry Cu, Fe- Cu skarn, Fe-Ti, V, Cr, Ni-Cu-PGE, Cu-Zn-Pb volcanogenic massive sulfide (VMS) and Archean Au-Cu porphyry and Opemiska Cu veins (reviewed in Chapter 1). Characteristic compositional trends of different variants of magnetite are suggested to be connected to respective styles of mineralization and thus might provide important insights for geochemical/mineral explorations (Dupuis and Beaudoin, 2011). Two bivariate diagrams of the proposed discriminators based on concentrations/ratios of Ti, V, Al, Mn, Ca, Cr and Ni are used here. The discriminator used in this study excludes the Ca component due to its negligible concentration in EPMA and LA-ICPMS analysis (Fig. 2.13A-B) following the modification suggested by Nadoll et al. (2014). Most of the magnetite from different associations plot within and around the fields allocated for IOCG-Porphyry and Kiruna-type deposits with some samples from association I magnetite extended to Fe-Ti, V deposit field. Magnetite from association II form major clusters in Kiruna-type fielled and some of the samples extends to porphyry field and in unspecified areas in both the (Ti + V) vs. (Al + Mn) and (Ti + V) vs. Ni/ (Cr + Mn) plots.

Magnetites from association I plot in the field of Fe-Ti, V in both the diagrams owing to their very high concentration of V. Magnetite from association III belongs to both Kiruna-type and Porphyry in one plot and mainly remain restricted to Kiruna-type and unspecified area in other whereas association IV magnetite cluster in and around IOCG field in (Ti + V) vs. (Al + Mn) plot but beyond any specified fields in (Ti + V) vs. Ni/(Cr + Mn) plot. For our studied samples there is a significant mismatch between the outcomes of the two discriminatory diagrams and similar discrepancy have been reported by Broughm et al. (2017) based on their study on magnetite from magnetite-apatite ore body and the magnetite from the host rocks from Kiruna and El Laco. Although, these discrimination diagrams clearly distinguish Bagjata magnetite from sedimentary (BIF) and skarn magnetite, lack of uniformity restricts further interpretations using these

discriminators. One of the problems in using these discriminators for our samples is that at least one or more data from the same association plot in more than one of the specified deposit fields even after taking into account

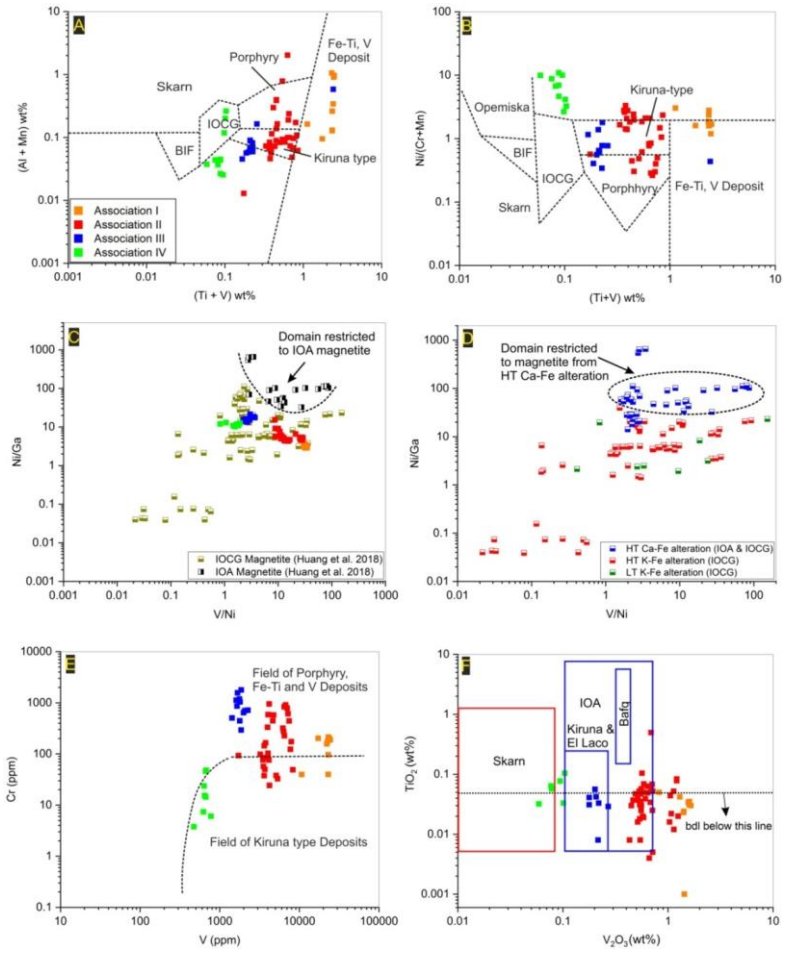

Figure 2.13 Trace element geochemistry of magnetite as deposit-type indicator

Discrimination diagram for using magnetite chemistry to separate different types of deposits: (A) and (B) suggested by Dupuis and Beaudoin (2011) and (A) modified by Nadoll et al. (2014), (C) and (D) are suggested by the present study to discriminate IOA-magnetite from IOCG-magnetite and to recognize the compositional contrast between HT Ca-Fe alteration vs. HT and LT K-Fe alterations

respectively (dataset compiled from Huang et al., (2019) and references therein); (E) and (F) are discrimination diagrams suggested by Knipping et al. (2015) and Hu et al. (2020) respectively. Note that in (A) and (B) most of the magnetite samples of this study plotted in Kiruna-IOCG and Porphyry field with the magnetite deciphered to be formed at high T (Association I and II) form clusters in Kiruna and Porphyry field with some samples from association I even extended to Fe-Ti, V deposit. Also note that in (E) majority of the sample falls below the detection limit of Ti. Legends are as shown in Fig . (A), (C) and (D).

the possibility of anomalous concentrations of Al due to invisible micro-inclusion which are found in a broad spectrum of deposit types like IOA, IOCG, Skarn (Heidarian et al., 2016; Hu et al., 2015, 2014; Huang and Beaudoin, 2021, 2019).

In an attempt to discriminate magnetite of variable mineralogical association/host rock/alteration types based on trace element geochemistry it is proposed that Ni/Ga vs. V/Ni plot can be used with further ~~more~~ reliance compared to the previously mentioned plots (Fig. 2.13C). This new discriminator successfully discriminates magnetite from a number of IOCG and IOA deposits over the globe. Compositional data of magnetite from IOCG deposits (Igrape Bahia, Alemao, Alvo, Salobo and Sossego from Carajás province, Brazil; Ernest Henry and Olympic dam from Australia; Candelaria from Chile, and Kwyjibo from Canada) and IOA deposits (Kiruna and Rektorn from Sweden; El Romeral from Chile; Pilot Knob; Pea Ridge and Lyon mountain from USA and Savage river deposit) are taken from the dataset by (Huang et al., (2019) and references therein). Magnetites from IOA deposits are restricted to the domain marked in Fig. 2.13C and bulk of the IOA-magnetite compositions are consistent with the general proposition of higher concentration of V (thereby high V/Ni ratios) than magnetite samples from IOCG deposits worldwide (Huang et al., 2019). Note that magnetite samples of the present study irrespective of their U-bearing lineage plot in the domain of IOCG-magnetite. Furthermore, our proposed discriminator effectively discriminates magnetite samples belonging to different alteration types relevant to IOA and IOCG deposits (Fig. 2.13D).

Although the result might seem intuitive to some extent from the previous diagram based on deposit type, but it is worth mentioning as the alteration types are not exclusive to ~~the~~ types of deposits. To maintain consistency in magnetite samples the same dataset (Huang et al., 2019) is used in both of these diagrams to check the variation between alteration types. The plot shows that despite overlap in V/Ni ratios between different alteration types, what separates the HT Ca-Fe alterations from that of HT and LT K-Fe alteration related magnetite samples is their anomalously high Ni/Ga ratio consistent with relatively higher concentrations of Ni generally associated with HT Ca-Fe alterations irrespective of the deposit types except some of the Kiruna samples.

In addition to ~~this~~ several other available discriminators are tested on Bagjata-magnetite samples. To distinguish Kiruna type deposits from all other high T deposit types (Porphyry, IOCG, Fe-Ti, V/P deposits), Knipping et al. (2015) proposed V vs. Cr plot where the authors assign Cr <100 ppm and V >500 ppm to Kiruna-type. Bagjata magnetite falls in both field and even the magnetites from the same association plot in two different fields for some of the associations although Bagjata does not belong to either of the deposit types (Fig. 2.13E). Broughm et al. (2017) reported higher Cr concentrations (Cr >100 ppm) from Kiruna, which questions the rationale behind this discrimination diagram. Magnetite data are also tested in the discriminator proposed by Hu et al. (2020) in order to differentiate IOA samples from Skarn deposits (Fig. 2.13F). Assignment of most of the magnetite samples in respective fields in this discriminator are not considered as majority of them falls below the detection limit of Ti. Rest of the magnetites from Bagjata lie mainly in the IOA field with magnetites from association IV straddling the boundary between IOA and skarn field probably because of their formation at comparatively low T and high fO_2 environments (leading to lower concentrations of V) as discussed in previous section (Section 2.5.1 and 2.5.2). Some of the association I and

association II magnetite samples are ~~seen to be~~ scattered outside the specified fields of this diagram both in cases where TiO_2 value is above and below detection limit.

Further attempt is made to discriminate the Bagjata hydrothermal magnetite from sedimentary BIF iron ore and magmatic Fe-Ti deposits based on concentration of V, Ni, Ti and Fe (Fig. 2.14) (after Loberg and Horndahl,1983). All these discriminators discriminate

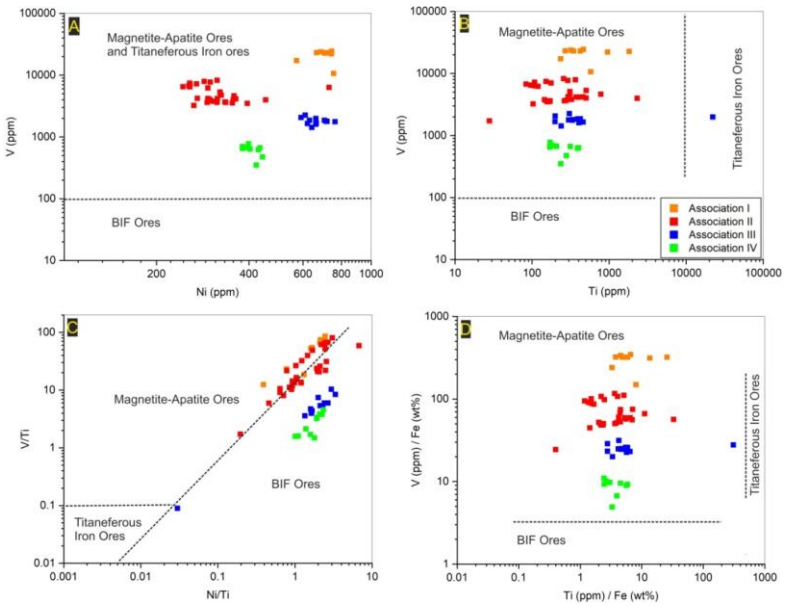

Figure 2.14 Trace element geochemistry of magnetite as deposit-type indicator

Magnetite samples of this study plotted in discriminator diagram proposed by Loberg and Horndahl (1983) to discriminate titaneferous iron ore and BIF iron ore from magnetite-apatite iron ore based on (A) V vs. Ni, (B) V vs. Ti, (C) V/Ti vs. Ni/Ti and (D) V (ppm)/Fe (wt%) vs. Ti (ppm)/Fe (wt%). Note that except in (C), all other discriminators effectively separate magnetite from Bagjata U deposit from Titaneferous iron ore and BIF iron ores. Legends are as shown in B.

Bagjata magnetite from BIF iron ore and magmatic Fe-Ti deposits except the V/Ti vs. Ni/Ti plots. Although these discriminators are based on whole rock composition and

therefore presumed to be less precise compared to other types of deposit discriminators which are largely based on *in situ* EPMA/LA-ICPMS data (Dupuis and Beaudoin, 2011; Knipping et al., 2015b) of magnetite, they work reasonably well to discriminate Bagjata hydrothermal magnetite from typical sedimentary and magmatic magnetite because of the individual large field allocated for individual deposit types compared to the narrow fields in other discriminators and because of their selection of discriminating elements. It has been pointed out by Huang and Beaudoin (2019) that these discriminators efficiently distinguish IOA-magnetite samples from magmatic Fe-Ti deposits and BIF even if the samples were altered/re-equilibrated. Although the deposit discriminators suggested by (Loberg and Horndahl, 1983) works reasonably well (Fig. 2.14) to discriminate Bagjata hydrothermal magnetite from magmatic and sedimentary magnetite, all magnetite, irrespective of apatite association and despite their IOCG affinity fall in the field of magnetite-apatite ore (except in Fig. 2.14C). Based on the comparison of trace element composition of Bagjata magnetite with proposed discriminators by several authors, it is suggested that all discrimination diagrams may not always straightforwardly and unambiguously fingerprint deposit types. Such an exercise must be corroborated with geological context, field observations, mineral assemblages and textural (intra- and inter-grain) criterions, the latter has been emphasized by Huang and Beaudoin (2021, 2019) particularly in deposits where multiple hydrothermal events and metamorphic overprints are evident.

Formatted: Font: Italic

2.5.4 Magnetite Vis a. Vis Critical metal (U and REE) mineralization

Rusk et al. (2010) suggested that Mn/V vs. Mn/Ti ratios of magnetite can discriminate between mineralized and barren iron oxide breccias in the context of IOCG mineralization from Ernest Henry Fe-oxide-Cu-Au deposit. They've shown that Mn/Ti ratios in Ernest Henry and some other regional IOCG deposits are invariably higher

compared to unmineralized magnetite-matrix breccias. Our attempt to differentiate magnetite from uranium ores (association III and IV) from the other non-fertile associations (association I and II) based on Mn/V and Mn/Ti ratios (Fig. 2.15A) shows significant overlapping of Mn/Ti values between U-mineralized and non-mineralized samples. On the contrary high Mn/V ratios are associated with magnetite from U-ores. In this study a new discriminator is proposed to separate the magnetite associated with uraninite-bearing fertile associations from the magnetite in uraninite-absent non-fertile associations based on elemental ratios involving V, Ni, and Ga. Additionally, concentration

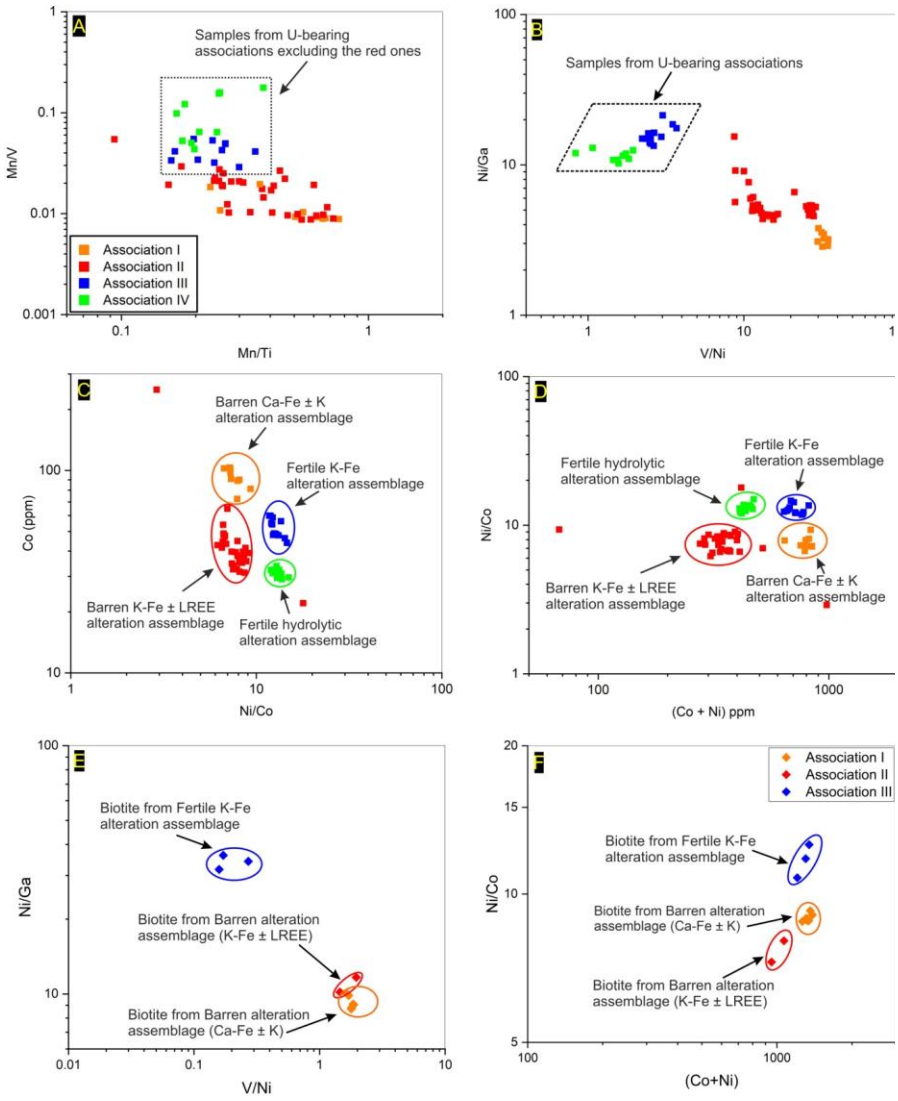

Figure 2.15 Trace element geochemistry of magnetite as fertility discriminator

Bivariate plots of Mn/V vs. Mn/Ti (A), Ni/Ga vs. V/Ni (B), Co vs. Ni/Co (C), Ni/Co vs. (Co + Ni) (D) based on magnetite composition; Ni/Ga vs. V/Ni (E) and Ni/Co vs. (Co + Ni) (F) based on biotite composition. Plot (A) was suggested by Rusk et al., (2010) and plot (B) and (E) are suggested by the present study and used to discriminate U-bearing samples from non-ore samples of the Bagjata uranium deposit. Magnetite samples are marked in terms of visible presence/absence of uraninite. Legends are as shown in Fig. A (magnetite) and F (biotite).

of Co and Ni and their ratios also observed to separate the U-fertile associations from barren associations All of these elements are readily compatible in magnetite structure. The discrimination plot of Ni/Ga vs. V/Ni effectively separates the uraninite-bearing samples from barren associations (Fig.2.15B). It has been observed that high Ni/Ga and high Ni/Co ratio can be used as an indicator of U mineralization for our studied samples. Further the potential differences between concentrations of Ni, Co, cumulative Co + Ni and Ni/Co ratios of magnetite from different associations are examined in an attempt to understand whether magnetite chemistry can be used as a tracer for mineralizing systems (Fig. 2.15C-D). Overall, association I and III have the highest, association IV has intermediate and association III has the lowest Ni contents. On the other hand, with significant overlap, Co concentrations generally decrease from association I → association III→ association II→ association IV. The cumulative Co + Ni concentrations show significant overlap with a general decreasing trend from association I and III → association II and IV. Therefore, the absolute concentrations of Co and Ni cannot unequivocally differentiate between U-mineralized (association III and IV) from the non-mineralized systems (association I, II). The Ni/Co ratios of all the studied magnetite are more than 1. However, interestingly, magnetite associated with U-mineralized fertile alterations can be discriminated on the basis of having distinctly higher Ni/Co ratios (and therefore lower Co/Ni ratio) compared to non-mineralized associations. It is important to note that biotite of U-mineralized association III also has higher Ni/Co ratios compared to biotite from non-mineralized association I and II (Fig. 2.15F). The discriminator suggested in this study to trace U mineralization based on the concentrations of V, Ni and Ga in magnetite has been tested for associated biotite composition and it has been observed that biotite samples from the U-bearing assemblage can be traced using the same discriminator suggested for magnetite (Fig. 2.15E).

It's worth mentioning that although 'fertile' assemblages are referred to visible presence of uraninite throughout this chapter, the discriminator(s) suggested in this study additionally discriminates association II (magnetite associated with REEs) from the association devoid of REEs/REE-bearing phases and thus can also be tested as a tracer for REE mineralization. Amalgamating all of the observations based in Bagjata U deposit, it is suggested that although fertility discriminators perhaps work best when used in a regional context, ratios of some key first row transition and post transition metals such as V, Mn, Co, Ni and Ga are key to the success (also in discriminating deposit and alteration types as discussed in Section 2.5.3.2). The possibility of getting a discriminator relevant universally in the context of IOCG mineralization is still under scrutiny. Applicability of these new discriminators for differentiating non-ore zone magnetite or biotite from ore-zone magnetite/biotite in the context of IOCG-type mineralization is yet to be globally-tested awaiting future studies on other deposits to evaluate the usefulness of these diagrams.

2.6. Concluding Remarks/Summary

Mode of occurrence and geochemistry of magnetite from four different associations have been studied from the Bagjata U-deposit in the Singhbhum Shear Zone (SSZ), eastern India. Magnetite in all of these associations are interpreted to be hydrothermal in origin and associated with Ca-Fe ± K (association I), K-Fe (association II & III) and H^+ metasomatism (association IV) and bear similarities with what have been observed in IOCG-type deposits around the globe. In IOCG alteration index diagram, whole rock compositions of the rocks hosting different magnetite fall in Ca-Fe-, K-Fe-alteration field and in the field of superimposition validating the interpretations on alteration. Based on the concentrations of temperature- and fO_2-sensitive trace elements it is proposed that magnetite of Ca-Fe and K-Fe alteration (association I, II and III) formed

at relatively higher T and lower fO_2 condition than magnetite of hydrolytic alteration (association IV). The interpretation about relative formation temperatures is in agreement with Mg in magnetite thermometry, Ti in biotite thermometry and chlorite thermometry based on different empirical equations and thermodynamic modeling. Various trace element-based discriminators are revisited which are widely used in recent literatures to fingerprint the deposit type or underlying formation process. Hydrothermal magnetite of Bagjata deposit can be discriminated from magmatic magnetite using Ti vs. Ni/Cr and (Mg + Mn) vs. (Si + Al) / (Mg + Mn) plot. The widely used deposit-type discriminators such as (Ti + V) vs. (Mn + Al) or (Ti + V) vs. Ni/(Cr + Mn) or Cr vs. V plot do not unequivocally identify the type of deposit Bagjata belongs to. The present study recommends the use of a new discriminator of V/Ni vs. Ni/Ga plot, which successfully identify and assign different clusters to magnetite samples from IOA and IOCG deposits tested in magnetite samples of Bagjata deposit and also from other deposits all around the globe. Additionally, the present study also advocates the use of the same V/Ni vs. Ni/Ga plot to be used as a tracer for critical metal (U-REE) mineralization based on the trace element geochemistry of associated magnetite and biotite.

Chapter 3: Magnetite in Fe-Ti oxide pods and magnetite ± apatite veins from Pathargora: post-crystallization modifications and their implications

3.1. Introduction

Titaniferous spinels (titanomagnetite, magnetite, ulvöspinel) and ilmenite ($FeTiO_3$) are common Fe-Ti oxide phases in many igneous and metamorphic rocks. Their textural relations and compositional variations provide important insights about various physicochemical constraints such as temperature, oxygen fugacity, and cooling rate of the system (Turner et al., 2008; Pang et al., 2008b; Mollo et al., 2013; Liu et al., 2015). Consequently the chemical composition of magnetite has~~ve~~ been utilized in previous studies to provide some typically selected trace element-based diagrams that discriminate between magmatic vs. hydrothermal ore-forming processes (Dare et al., 2014; Knipping et al., 2015b) and also identifies magnetite samples from a variety of deposit-types (Dupuis and Beaudoin, 2011) including BIF, Skarn, IOCG, Kiruna-type, Porphyry and Fe-Ti, V deposits. Although these diagrams are not well-characterized in terms of alteration (partly/completely altered) history (Wen et al., 2017) when proposed, they have been used extensively in many recently published literatures (Broughm et al., 2017; Mukherjee et al., 2017; Salazar et al., 2020; La Cruz et al., 2020; Palma et al., 2020) to trace the evidence of formation process or to identify the deposit-type. However, magnetite is prone to post-depositional changes in textures as well as chemistry by various processes (Hu et al., 2014, 2015; Makvandi et al., 2016a; Wen et al., 2017) than previously assumed. Despite that fact there are only limited number of studies (Wen et al., 2017; Huang and Beaudoin, 2019) address the issue of the textural and chemical reequilibration and its effect on process/deposit identifier diagrams. To understand the mechanism and effect due to post-depositional changes proper integration of magnetite composition and their subsequent changes with detailed textural characterization is needed.

This can provide useful insights to interpret the results of the discriminator diagrams more meaningfully and may help to refine the existing discriminators to make them more robust.

In the present chapter magnetite samples from two strikingly different assemblages from Pathargora in the Singhbhum Shear Zone (the location of the Pathargora as shown in Fig. 2.1 of the previous chapter) have been studied. The objectives of this chapter are following –

A. Understanding the difference in mode of occurrence, texture and geochemistry of magnetite from different mineral assemblages with or without impacted by post-crystallization processes.

B. Decipher the origin of the magnetite mineralization having different mode of occurrences, mineralogical associations, textural attributes and geochemistry with caveats of using magnetite trace element-based discriminatory diagrams alone as a discriminating criterion if not blended with the textural aspects.

C. Use of magnetite geochemistry along with the other associated phases to know about the physicochemical parameters (T, fO_2, fFluid) of the mineralizing processes and also how the post-mineralization changes influence the records of the original formation condition.

D. To unravel the nature and mechanism of the post-depositional processes and how they modify the pristine signatures.

3.2. Geology of Pathargora

3.2.1 Deposit scale Geology

The present study is conducted in Pathargora (22º 32' 32.1" N 86º 26' 22.4" E) area located close to the boundary between the rocks belonging to the Dhanjori Group and the Singhbhum Group (To note the location of the albite schist between Dhanjori volcanics belonging to Dhanjori Group and garnetiferous muscovite/sericite schist belonging to Singhbhum Group, the reader is advised to check the Fig. 2.2A of the previous chapter 2). The rocks in and around the study area, from south to north, are broadly represented by Dhanjori quartzite, Dhanjori meta-volcanic rocks, feldspathic schist/ "Soda granite" and garnetiferous quartzite/sericite schist, the last one belongs to the Singhbhum Group. The feldspathic schist at Pathargora occurs at the upper fringe of the Dhanjori meta-igneous rocks. Patches of kyanite-bearing quartzite/kyanite-bearing sericite schist often mark the northern boundary of the shear zone. The magnetite-ilmenite–bearing ore body and the magnetite-apatite bearing veins described in this study are located within the feldspathic schist.

3.2.2 Description of the host rock of magnetite-ilmenite and magnetite+ apatite mineralization

Two distinct mineral associations of magnetite-ilmenite and magnetite-apatite ± biotite ± chlorite have been observed in Pathargora. Both of these associations are hosted in feldspathic schist/ "Soda granite". The origin of this host rock is strongly debated; theories range from magmatic (Dunn and Dey, 1942) to product of Na-metasomatism of a sedimentary (Banerji and Talapatra, 1966) or a mafic (Sarkar, 1984; Pal et al., 2008) protolith. The term 'albite schist' will be used henceforth to highlight the mineralogy without any obvious connotation to origin. We have collected the samples from the magnetite-ilmenite pod and magnetite-apatite veins hosted in albite schist. One such vein and the

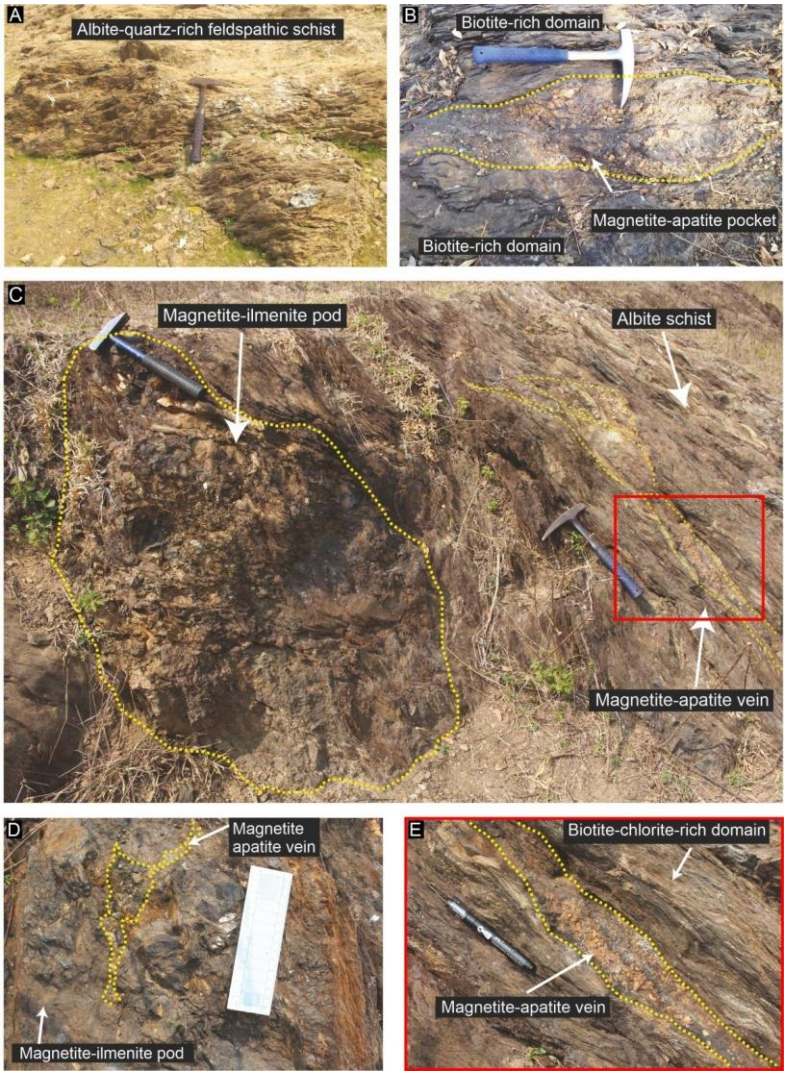

Figure 3.1 Field photographs of magnetite-ilmenite ore body and magnetite-apatite veins hosted in the albite schist

A. Typical light-colored albite schist comprising predominantly of albite and quartz. Magnetite-ilmenite pods (C-D) and magnetite-apatite veins (B-E) are hosted in the unit. Note the presence of magnetite-apatite veins in the vicinity of the pods (C) and also within the magnetite-ilmenite pod (D).The red square in (C) is magnified in (E).The presence of biotite-rich (B) and biotite-chlorite-rich (E) domains often associated with the magnetite-apatite veins.

magnetite-ilmenite bearing pod are shown in Fig. 3.1C-E, where magnetite-apatite vein surrounds the magnetite-ilmenite pod. These veins/pockets contain varying proportion of magnetite, apatite and biotite and are commonly surrounded by foliated biotite-rich zones. The host rock is also schistose and sheared as evidenced by the presence of intense and ubiquitous mylonitic foliations defined by stretched quartz grains and pressure fringes on apatite, magnetite and tourmaline, cChlorite and biotite (mainly chlorite) define the pervasive schistosity (Fig. 3.1). The feldspathic schist is locally characterized by alternative dark and light colored bands; the light colored band is composed of quartz, albite, and sericite with minor apatite and tourmaline whereas the dark colored band is dominated by biotite, chlorite, magnetite, fine-grained tourmaline and apatite. Apatite-magnetite-biotite veins and pockets (few millimeters to tens of centimeters) are commonly seen in the feldspathic schist (Fig 3.1B-C). Large disseminated clots of tourmaline and tourmaline-bearing veins and pockets are also commonly seen in the rock. The rock is also compositionally heterogeneous with locally high FeO + MgO (up to ~ 23 wt. %) and highly variable Na_2O and K_2O content (~3-5 wt. % of each).

3.3. Analytical Protocol

3.3.1 SEM &EPMA

The Back Scattered Electron (BSE) images of the samples and semi-quantitative analyses of the minerals were obtained using a JEOL JSM 6490 Scanning Electron Microscope (SEM) hosted at the Indian Institute of Technology, Kharagpur. Major element compositions were obtained using Cameca SX 100 electron probe equipped with four wavelength dispersive spectrometers (WDS). The EPMA was operated at acceleration voltage of 15 kv and beam current of 20 nA. EPMA analyses were performed with great

caution to avoid incorporation of any exsolved ilmenite lamellae during the analysis of magnetite and vice versa followed by the preliminary characterization by optical and scanning electron microscopy. The standards and emission line used to calibrate the instrument are same as has been described in Chapter 2.

3.3.2 LA-ICPMS

Trace element concentrations were measured *in-situ* in thin sections using a Thermo Fisher Scientific iCap-Q quadrupole inductively coupled plasma mass spectrometer (ICPMS) coupled to a New Wave Research 193 nm ArF excimer laser ablation (LA) system at the Department of Geology and Geophysics, IIT Kharagpur. The laser was operated at 5 Hz repetition rate and ca. 5 J/cm^2 fluence at a spot size of 45–50 μm. The instrument was optimized for maximum sensitivity on Li, Co, In, Pb, Th, and U by ablating the NIST 612 reference glass. The raw counts for each isotope were measured in time-resolved mode with 35s of gas blank measurement with the laser turned off and 45s of peak signal measurement with the laser ablating on the sample. Correction for instrumental mass-bias and drift was done using external standardization by bracketing groups of ten unknowns with two measurement of the NIST SRM 610 reference glass. The data quality was monitored by analyzing the NIST SRM 612 reference glass as unknown interspersed with the measurements of the samples. The data was reduced off-line using the GLITTER® program (Griffin, 2008). The time-resolved signals were carefully monitored to avoid the mixing of magnetite and ilmenite during ablation. Spot analyses suspected of mixing (identified through inflexions or changes in the slopes of the time-resolved ablation patterns) were either discarded or clean segments of the time-resolved spectra were used for the calculation of concentrations. Accuracy and precision as determined from repeat analyses of the NIST 612 and 610 reference glasses are in the range of 5–10 % for most elements.

Formatted: Font: Italic

3.4. Results

3.4.1 Petrography

Petrographic observations have been described in broadly two sections – one section deals with the magnetite samples from the pods. Based on the intensity of hematitization of magnetite, the pod samples are further classified into association I and association IA. The other section deals with the samples from the magnetite-apatite–bearing veins (association II).

3.4.1.1 Petrography of samples from the pod (Association I and IA)

3.4.1.1.1 Host magnetite and hematitized magnetite

Magnetite in the studied ore body occurs as coarse massive aggregate interwoven with texturally and morphologically different ilmenite. Magnetite grains are variably hematitized. In association I magnetite is partly hematitized along grain-boundaries, micro-cracks and it is important to note that hematite along crystallographic planes is cleaner, rarely having minor micro-pores in the vicinity (Fig. 3.2A). On the other hand, hematite associated with micro-cracks is highly porous (Fig. 3.3B-C) in case of association IA. In association IA the hematitization process almost completely and pseudomorphically transformed the magnetite grains to hematite. This hematitized magnetite is extremely porous and cloudy (Fig. 3.3C). Association IA bears evidences of deformation in the presence of fractures, micro-shear planes and deformed/kinked ilmenite lamellae (Fig. 3.3D–E). Xenotime (Y-HREE-phosphate) and biotite are frequently present along the shear planes and micro-fractures in this assemblage (Fig. 3.3A and D-E).

3.4.1.1.2 Textural relations of ilmenite with the host

The association I and IA are characterized by texturally and morphologically different types of ilmenite. Also, the volume proportions of ilmenite in both association I and association IA

assemblages vary significantly within a single grain, within a thin section and in different thin sections. The area proportion of ilmenite, in some cases equals or much exceeds that of host in a thin section (Fig. 3.3A-B). Based on variations in micro-textural features, ilmenite lamellae/intergrowths are classified into 3 major categories and described briefly here.

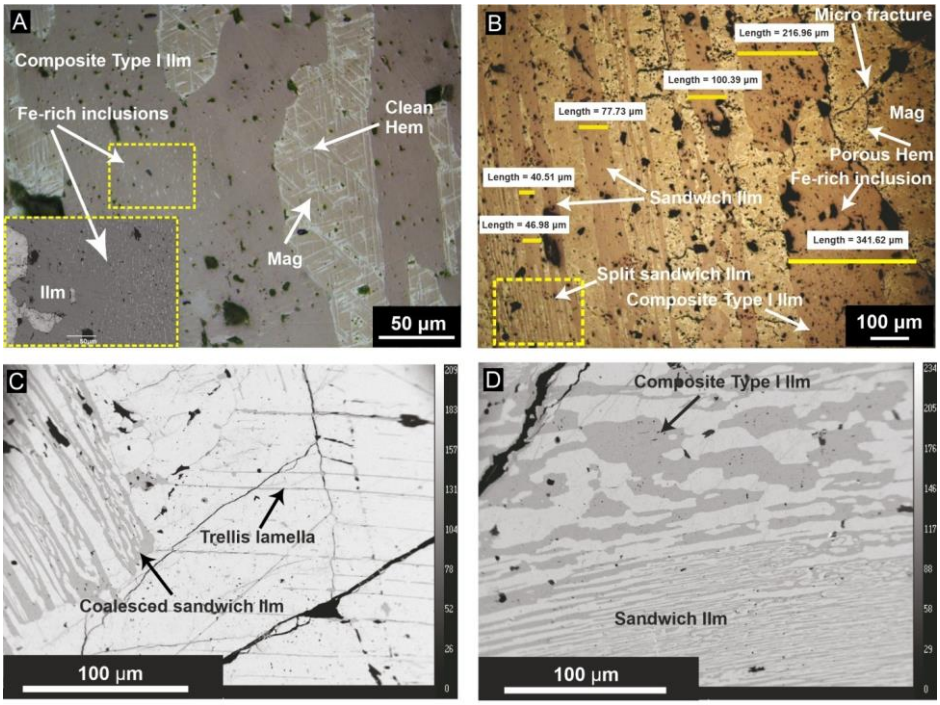

Figure 3.2 Mode of occurrence of magnetite and ilmenite lamellae in association I

Reflected light photomicrographs (A-B) and back-scattered electrons images (C-D, inset of A) of different magnetite-ilmenite intergrowth from association I – (A) Intergrowth of magnetite and composite Type I ilmenite containing elliptical, oriented Fe-rich inclusions (brighter spots in magnetite). Hematite along crystallographic planes is clean/non porous; (B) Sandwich and composite Type I ilmenite lamellae. Porous hematite (bright) along anastomosing micro-fractures in magnetite, this feature is more common in association IA; (C) Trellis-type ilmenite lamella along with sandwich lamella; (D) Irregular anhedral composite Type I ilmenite lamellae in close association with Sandwich lamellae and splitting of Sandwich lamellae in thin lamellae

Trellis and Sandwich type ilmenite lamellae

Fine lamellae of ilmenite, with widths generally less than 10 μm occur along all three {111} crystallographic planes of the host (Fig. 3.2C). Trellis-type ilmenite lamellae is extremely rare and observed mainly in association I in close association with other type of lamellae such as with Sandwich lamellae in Fig. 3.2C. Similar associations are also noted

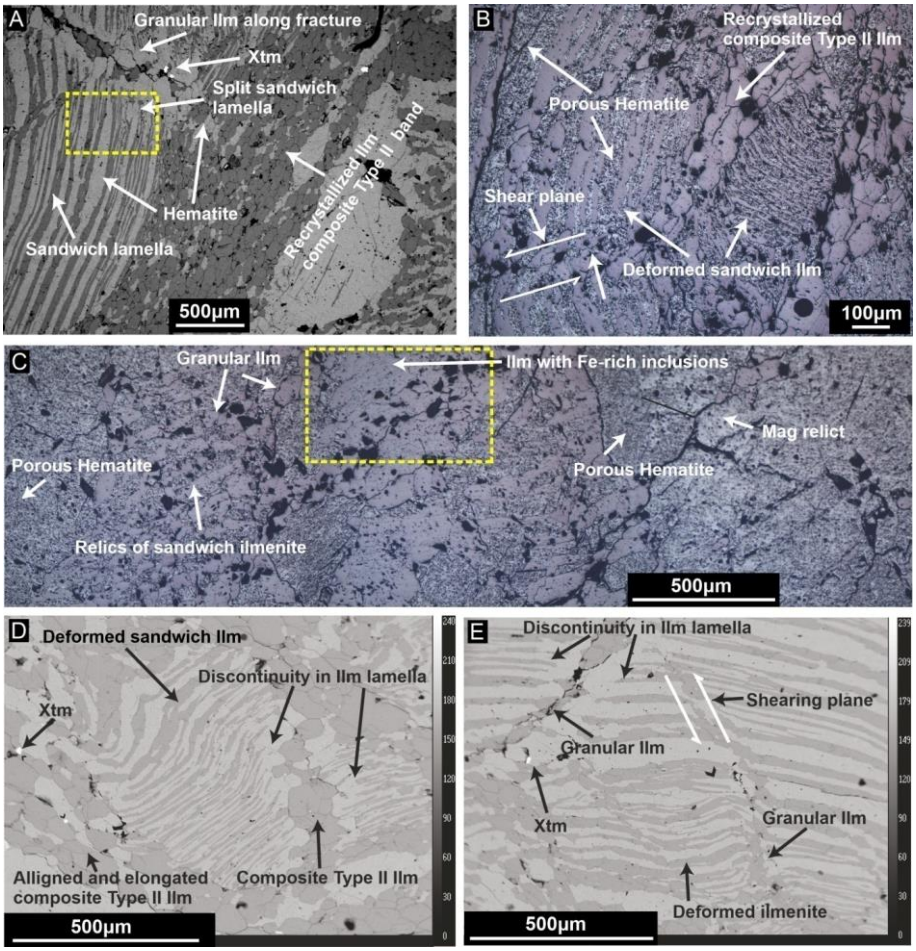

Figure 3.3 Mode of occurrence of magnetite and ilmenite lamellae in association IA

BSE images (A, D-E) and reflected light photomicrographs (B and E) of different hematite (hematitized magnetite) – ilmenite intergrowths from association IA – (A) and (B) Sandwich and composite Type II ilmenite lamellae in highly porous hematite of association IA; note the

abundant presence of ilmenite (A-B) and splitting of sandwich lamella (A); sandwich lamella grades to granular ilmenite along shear planes and fractures (A); elongate and oriented composite Type II ilmenite locally occurs as thick bands comprising predominantly of ilmenite and minor hematite (A); (C) Intergrowth between highly porous hematite and ilmenite; (D) Granular composite Type II ilmenite surrounding hematitized magnetite containing deformed/kinked sandwich ilmenite lamella; ilmenite grains are locally aligned (lower left);note the variable inter-granular angles; (E)Occurrence of granular ilmenite along shear planes and fractures (E); sandwich lamellae are discontinuous close to the magnetite g rain boundary (D) and fracture (E); also note the presence of xenotime; The yellow box in Fig. C is magnified in Fig. 3.4A

from other Fe-Ti oxide rich assemblages (Pang et al., 2008a; Tan et al., 2016). The sandwich ilmenite lamellae are comparatively thicker (between 25 μm and 85 μm wide) (Fig. 3.2B-D and 3.3A-B). They are oriented along one of the major {111} crystallographic planes of the host. At places, these lamellae thicken near the grain boundary and merge with nearby lamellae (Fig. 3.2C). Occasionally, the thick lamellae are split into numerous thinner lamellae (Fig. 3.2B and 3.3A). The split lamellae have variable thickness between 5 μm and 25 μm and are aligned parallel to the thicker lamellae (Fig. 3.2B). The sandwich lamellae in association I a~~A~~re commonly deformed/kinked, and disrupted along fractures and micro-shear planes (Fig. 3.3D–E). The lamella and host are often seen to transform into granular aggregate of ilmenite and magnetite along these micro-shear planes and fractures (Fig. 3.3B and E).

Composite type ilmenite lamellae

Based on morphology and textural relation with host, this type of ilmenite is classified into: 1) composite Type I or internal granular ilmenite that occurs within and is intricately interwoven with the host magnetite, 2) composite Type II or external granular ilmenite that occurs outside the grain boundary of the host (Fig. 3.4). Composite Type I lamella are common in both association I and IA whereas the composite Type II lamella is present exclusively in association IA.

Composite Type I intergrowth (internal granular intergrowth)

Composite Type I ilmenite commonly occurs as granular aggregates of anhedral grains having highly variable thickness even within a single grain; width varies between 70 μm and 450 μm (Fig. 3.2A-B and D and 3.3C). They characteristically have highly irregular grain boundaries unlike the straight to curvilinear contact of trellis type and sandwich type lamella. Similar ilmenite intergrowths have been described as "internal granular exsolution" by Buddington and Lindsley, (1964). Unlike the previously reported internal granular aggregate, some of the composite Type I ilmenite grains described in this study show somewhat crude crystallographic orientations (Fig. 3.2B and D). Composite Type I ilmenite is distinctive from composite Type II ilmenite and sandwich and trellis type ilmenite lamella

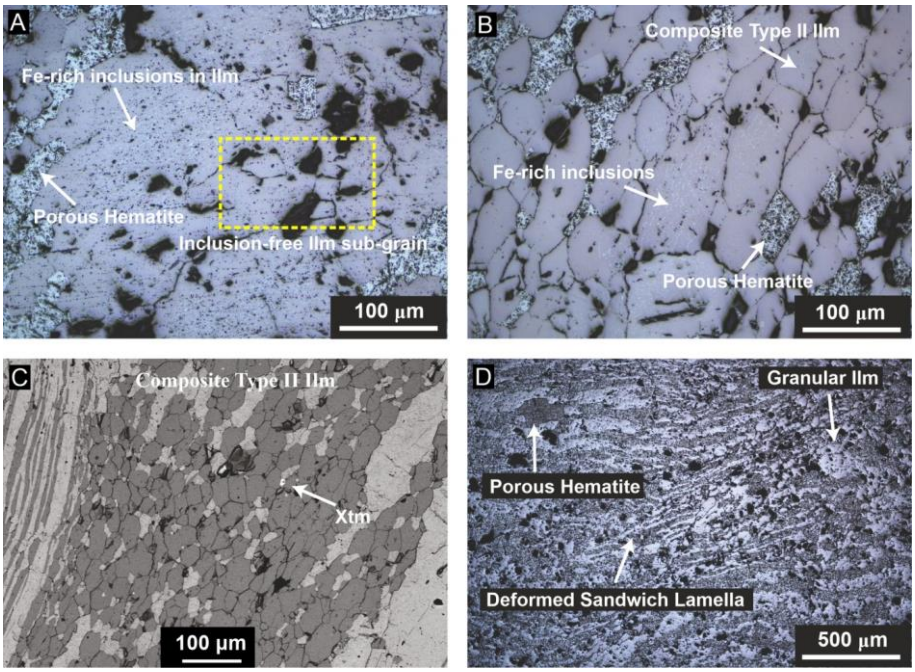

Figure 3.4 Mode of occurrence of composite type II ilmenite in association IA

Reflected light photomicrographs (A, B and D) and BSE image (C) showing different textures of composite Type II ilmenite. Fe-rich inclusion-bearing ilmenite (similar to composite Type I ilmenite) occurring outside magnetite (A and B). The ilmenite is partly recrystallized to form inclusion-free sub-grains (A); C) Recrystallized nature of the composite Type II ilmenite; Note the variable inter-granular angles, occasionally up to 120◦.

Also note the presence of xenotime. D) Relics of deformed sandwich lamella present in a groundmass of granular ilmenite and porous hematite. (A) displays the magnified version of yellow box in Fig. 3.3C

in having abundant oriented, elliptical, tiny (<1 μm) unidentified Fe-rich inclusions which are absent in other ilmenite types (Fig. 3.2A-B and 3.3 C). These Fe-rich phases are present in the core part and are often aligned along the long axis of the host composite Type I ilmenite (Fig. 3.2C). Although less abundant, similar Fe-rich inclusion-bearing anhedral to subhedral ilmenite, partly or completely recrystallized, are also present outside the host (Fig. 3.3C and 3.4A-B).

Composite Type II intergrowth (external granular intergrowth)

Euhedral to subhedral granular aggregates of ilmenite which are at places elongated, occur at the boundary of the hematitized magnetite grains, along micro-fractures and micro-shear planes and as closely packed thick ilmenite-rich bands (Fig. 3.3A-B, D-E, 3.4C). Similar granules of ilmenite grains at the external border of the host magnetite have been described as "external granular exsolution" in the seminal work of Buddington and Lindsley(1964). In some cases, hematitized magnetite grains containing deformed sandwich ilmenite lamellae are partly or completely surrounded by intergrowth of coarser (than the lamella) subhedral/euhedral composite Type II ilmenite and hematitized magnetite granules, producing a heterogeneous core-mantle-like structure, similar to what is known as 'necklace structure' or 'corona structure' (Fig. 3.3D). Such hematitized magnetite grains are impoverished in ilmenite lamellae close to the grain boundary. Large, anhedral ilmenite grains in closely packed bands occasionally contains Fe-rich inclusions similar to composite Type I ilmenite (Fig. 3.3C and 3.4A--B). Partial to near complete transformation of such inclusion-bearing large grains to inclusion-free sub-grains is also seen (Fig. 3.4A). The granules of composite Type II ilmenite show variable ilmenite-ilmenite and ilmenite-hematitized magnetite inter-granular angles, often 120° (in case of ilmenite-ilmenite-ilmenite

contacts), both in the necklace structure and in the bands (Fig. 3.3Dand 3.4C). Relics of deformed sandwich lamella occur in a groundmass of recrystallized granular ilmenite and magnetite (Fig. 3.3C and 3.4D). A very common feature is the presence of secondary xenotime (Y-phosphate) in close association with this composite Type II ilmenite (Fig. 3.3A and D-E, and 3.4C).

3.4.1.2 Petrography of samples from the magnetite-apatite vein

Unlike the magnetite samples in the pods, magnetite samples of association II from the magnetite-apatite veins is devoid of any magnetite-ilmenite intergrowths and especially variable in terms of associated mineralogy if compared to the magnetite-ilmenite dominated mineralogy in association I. Apatite-magnetite ± biotite veins (few millimeters to tens of centimeters) are extremely heterogeneous with varying proportions of magnetite, apatite, biotite, chlorite etc. Variation in modal abundance of magnetite and apatite often leads to almost monominerallic bands composed of apatite and one such occurrence has been shown in Fig. 3.5A. The grain-size of the apatite is smaller in the mixed bands (Fig. 3.5.B) where the band mineralogy is also comprised of magnetite ± biotite ± chlorite. Subhedral to anhedral magnetite observed to occur alongside biotite where bands of biotite penetrates the host albite-schist rock (Fig. 3.5.D) or occur at the grain margin/within the fractures of the large-sized apatite grains (Fig. 3.5E). The size of the apatite grains are usually large compared to the magnetite (Fig. 3.5B-F) and the size of the magnetite grains are hugely variable ranging from ≤50 μm to as large as >1000 μm. Large-sized grains of both magnetite and apatite (generally ≥1000 μm) locally show preferred orientation along the schistosity (Fig. 3.5C and G). Warping of schistosity around the large grains probably indicates the magnetite-apatite mineralization might predate the shearing event or syn-genetic with the shear deformation event. Micro-inclusions of both LREE-bearing phases (monazite) and HREE-bearing (xenotime) phases are seen within the apatite grain (Fig. 3.5F).

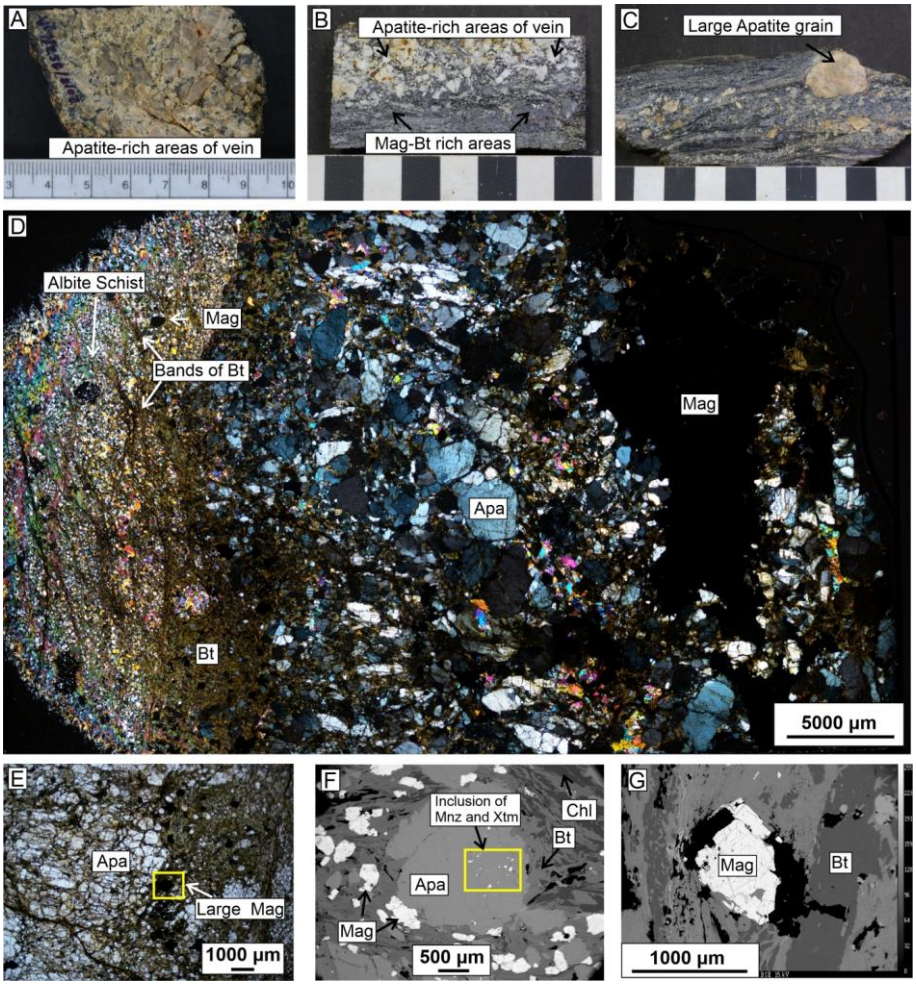

Figure 3.5 Mode of occurrence of magnetite and apatite from association II at various scales

Hand specimen photographs (A-C), cross polarized light (D), plane polarized light (E) photomicrographs and BSE images (F and G) showing magnetite from the magnetite-apatite veins and textural relation with the associated phases – (A-C) Variation in relative modal abundance with apatite dominated band (A); Mixed band with distinct apatite-rich areas and magnetite-rich areas (B) and presence of extremely large-sized apatite grain compared to other phases in the bands within the vein (C); (D) Pockets of magnetite-apatite within the biotite-rich dark bands and their textural relations with the host albite schist; (E) Magnetite with biotite along the fractures at the grain margin of apatite; (F) Apatite containing

inclusions of LREE-bearing phase monazite and Y-HREE bearing phase xenotime; (G) Large magnetite and apatite (in C and F) grains warped by schistosity defining biotite/chlorite

3.4.2 Geochemistry: Composition of magnetite and associated phases

Discernible differences are observed in major and trace element concentrations between magnetite host and sandwich ilmenite lamella, sandwich lamella and composite Type I ilmenite and between magnetite of association I vs. association II and the hematite (hematitized magnetite) of association IA assemblages. Due to very small size of trellis type lamella, reliable geochemical data could not be generated either by EPMA or LA-ICPMS. The major and trace element compositions of magnetite (association I and II) and hematite (association IA) are given in Table 9 (major element composition) and in Table 10 (trace element composition). The major and trace element composition of ilmenite (of association I and IA), apatite (of association II) and biotite (of association II) are given in Table 12, Table 13 and Table 14 (major element and trace elements in apatite, respectively) and in Table 15, respectively.

3.4.2.1 Magnetite vs. Ilmenite lamellae of association I

Because the magnetite of association IA assemblage is pervasively hematitized, the comparison between ilmenite and magnetite is done based on observations from association I. Among the major and minor elements which commonly occur in Fe-Ti oxides, all ilmenite types are depleted in V and Cr, and except composite Type I ilmenite of association I they are also depleted in Al compared to magnetite (Fig. 3.6A and C). Ilmenite is enriched in Mg and Mn compared to magnetite (Fig. 3.6B). Among the transition elements, ilmenite is enriched in Sc, Co, Cu and Zn and depleted in Ni (Fig. 3.6D–F). Magnetite is significantly enriched in Ga compared to ilmenite (Fig. 3.6F). The concentrations of high field strength elements

(HFSE) such as U, Th, Zr and Hf are low both in ilmenite and magnetite of association IA (below 1 ppm) and overlap (Fig. 3.6G and H). In contrast, the concentrations of Nb and Ta are much higher in ilmenite compared to magnetite (Fig. 3.6I). Similarly, ilmenite is significantly enriched in Sn and W compared to magnetite (Fig. 3.6J). The concentrations of light rare earth elements (LREE) are mostly below detection limit to less than 1 ppm both in magnetite and ilmenite of association I; concentrations of heavy rare earth elements (HREE) plus Y (HREEY) are slightly higher than LREEs in ilmenite (Fig. 3.6K).

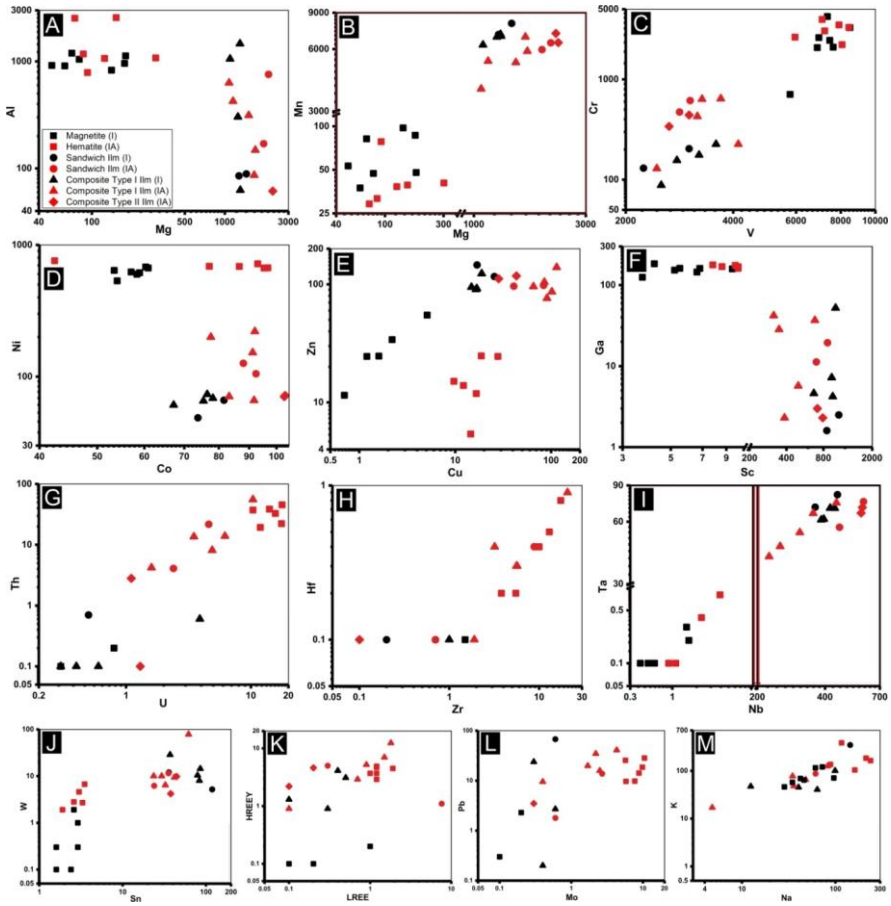

Figure 3.6 Compositional variations in magnetite, hematite and different types of ilmenite

Bivariate plots of various elements showing the compositional differences between magnetite (association I), hematite (association IA), sandwich and composite Type I ilmenite (Association I and IA) and composite type II ilmenite (Association IA). The colour schemes used in this figure for association I and IA will be followed throughout this chapter

3.4.2.2 Magnetite of association I vs. hematite of association IA

The concentrations of Mg, Al, Mn, V and Cr are similar in magnetite and hematite (Fig. 3.6A–C) and that of Ti is highly variable both in magnetite and hematite (Table 9 and 10). While P is below detection limit in most magnetite grains, it is detected in all hematite and the mean concentration of P in hematite is ~154 ppm. Hematite generally contains higher concentrations of Na and K compared to magnetite (Fig. 3.6M). Among the transition elements, hematite is notably enriched in Cu and Co whereas the concentrations of Ni and Zn in magnetite and hematite overlap (Fig. 3.6D and E). Hematite and magnetite have similar concentrations of Nb and Ta but hematite is notably enriched in U and Th (Fig. 3.6G, I and L). While the U and Th concentrations never exceed 1 ppm (values on individual spots often are below the detection limits) in magnetite, the mean concentrations of U and Th in hematite are 15 and 33 ppm respectively. The U/Th ratios in magnetite are always >1.0 whereas that of hematite is always <1.0. Concentrations of Sn in association I magnetite are similar to that of association IA hematite but hematite is enriched in W (Fig. 3.6J). Although Zr and Hf are below detection limits in most spot analyses in magnetite, both Zr and Hf are detected and the concentrations are notably higher in hematite (Fig. 3.6H). Hematite is also enriched in LREEs, Y-HREEs, Mo and Pb compared to magnetite (Fig. 3.6K and L).

3.4.2.3 Composition of Magnetite of association I vs. II and composition of apatite and biotite of association II

Significant compositional variations are present between magnetite from magnetite-ilmenite bearing pod and magnetite samples from magnetite-apatite vein (Table 9 and Table 10). Magnetites from these 2 associations are compared together in Box and Whisker plot which shows the difference in concentration of some important spinel element between these 2 associations. Magnetite samples from association I show clear enrichment of Cr, Vanadium and Ga and on the other hand association II samples have elevated Ti, Mg, Mn and Ge, whereas Co and Ni concentrations are comparatively similar with slight enrichment of Ni in magnetite from association II (Fig. 3.7). Average concentrations of Cr, V and Ga as measured

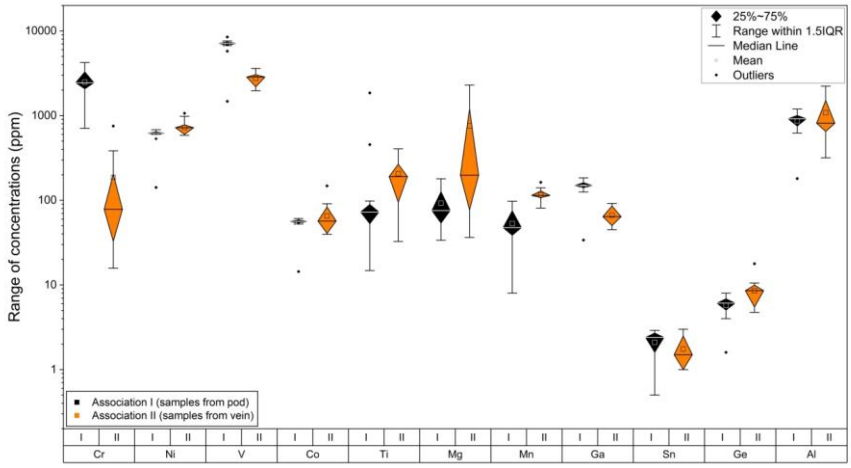

Figure 3.7 Compositional variation in selected spinel elements between magnetite samples from association I and II

Selected multi-element Diamond-filled Box and Whisker plots for trace elements in magnetite from the pod (association I) and the vein (association II). Diamonds outline the 25th to 75th percentiles and whiskers extend to the minimum and maximum values. Line within the diamonds represents the median values, whereas the hollow square represents the average values. The colour schemes used in this figure for association I and II will be followed throughout this chapter.

in LA-ICPMS for association I vs. association II are 2490.9 vs. 186.59 ppm, 7212.9 ppm vs. 2764 ppm and 155.44 vs. 66.67 ppm respectively. Beside that the average concentrations of Ti, Mg, Mn and Ge are 73.52 vs. 205.92 ppm (excluding the outlier); 108.57 vs. 757.68 ppm; 64.529 vs. 115.81 ppm; 6.3 vs. 8.53 ppm respectively, displaying consistently lower concentrations for association I in comparison with magnetite samples from association II. Concentration of Co and Ni are relatively similar with the mean concentrations of 57.54 vs. 65.36 ppm and 623.2 vs. 725.76 ppm respectively for association I and association II magnetite. Aluminium is one of the elements which is of comparable mean concentrations in both the assemblage (996.88 vs. 1080.6 ppm in association I and II respectively) with association II magnetite samples displaying large variance and association I magnetite samples displaying slightly elevated median line (Fig. 3.7). Magnetite samples of association I do not contain REEs (most of the spot analyses are below the detection limit of LA-ICPMS) whereas association II magnetite samples have REES measured at significantly higher concentrations.

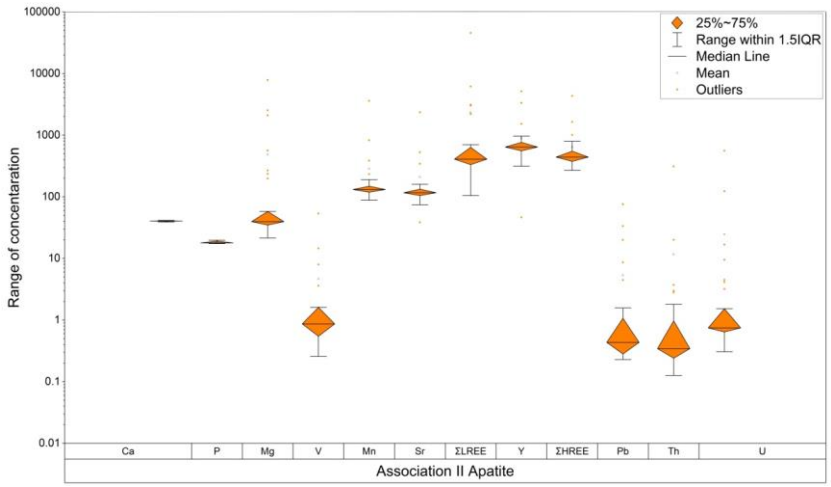

Figure 3.8 Compositional range of selected elements in apatite samples from association II

Multi-element Diamond-filled Box and Whisker plots showing concentration range of some selected elements in apatite from the magnetite-apatite veins (association II). Diamonds outline the 25th to 75th percentiles and whiskers extend to the minimum and maximum values. Line within the box represents the median values, hollow square represents the average values, whereas the solid circles display the outliers. Concentration of Ca and P are in wt% and other elements are showing ranges in ppm. Note that the concentration of Y is higher than all the REEsS.

Apatite samples from the magnetite-apatite veins contain on an average 40.44 wt% Ca and 18.08 wt% of P measured in EPMA. The average concentrations of some other important elements measured in EPMA/LA-ICPMS are Mg (487 ppm), V (5 ppm), Sr (209 ppm), Y (890 ppm), Pb (5.33 ppm), Th (11.7 ppm), U (24.62 ppm) (Fig. 3.8).Note that all the apatite from association II show higher concentrations along with the higher inter-quartile range of Y in comparison with the cumulative concentrations of both the LREEs and HREEs (excluding the extreme outliers). The mean concentrations of Y vs. ∑LREE vs. ∑HREE are 890 ppm vs. 608 ppm vs. 640 ppm (Fig. 3.8)

All of the biotite analyzed in EPMA are intermediate in composition between the Mg-rich end member (phlogopite) and Fe-rich end member (annite) with slightly elevated concentrations of Fe (average ≈ 12 wt%) than Mg (average of ≈ 9 wt%). The Mg/ (Mg + Fe) ratios vary between 0.41-0.45 with the mean value of 0.43. The average concentration of Ti is close to 0.5 wt%.

3.5. Discussion:

3.5.1 Origin of magnetite in pod and magnetite-apatite mineralization in vein

It has long been considered that the crystallographically oriented un-mixing is characteristic of slow cooling (Buddington and Lindsley, 1964). The magnetite-ilmenite intergrowths at Pathargora are indicative of slow cooling and slow ascent as most of the grains show extensive crystallographically-oriented intergrowth of magnetite and ilmenite. In case of slow-ascent, 25%-50% of titanomagnetite grains show exsolution/oxy-exsolution features comprising a Ti-poor magnetite host and Ti-rich exsolved phases, whereas in case of rapid-ascent the assemblage is dominated by homogeneous titanomagnetite grains with only 1% - 2% grains containing exsolutions (Turner et al., 2008). The mineralogy of the pod sample (association I) is solely dominated by the presence of minerals like magnetite and ilmenite of mafic lineage and presence of various types of magnetite-ilmenite intergrowths bearing the signature of oxy-exsolution process at sub-solidus temperature range (Buddington and Lindsley, 1964; Pang et al., 2008b; Tan et al., 2016) as described in the petrography section (section 3.4.1.1.2) Fe-rich exsolution bearing composite type I ilmenite (Figs. 3.2. A-B and 3.3C), which have been frequently observed in Pathargora is generally found in primary ilmenite crystallized simultaneously with magnetite both in natural settings and in experimental synthesis (Buddington and Lindsley, 1964) and is consistent with what have been observed in case of some Fe-Ti oxide bearing mafic-ultramafic intrusions (Bijigou, Panzhihua, and Xinjie) from various locations of SW China (Tan et al., 2016). The mode of occurrence of the magnetite-ilmenite body and the textural attributes collectively indicate the mineralogical assemblage of association I possibly represents magmatic segregation of titanomagnetite from a basaltic magma and subsequent compositional and textural re-equilibration thereafter.

On the other hand the magnetite samples from association II are formed inside vein, which often surrounds or penetrates the magmatic magnetite-ilmenite bearing ore body (Fig. 3.1). Magnetite samples from this association are characterized by the presence of common hydrothermal minerals such as biotite, chlorite etc., and large variation in grain-size of the constituent minerals (Fig. 3.5C). The highly variable mineralogy, heterogeneous distribution of minerals, presence of a biotite-rich selvages surrounding the veins and also the evidence of the variable fluid-induced alteration of the host albite schist rock (Pal et al., 2008) indicates the formation of magnetite of association II by hydrothermal ore-forming processes.

It is worth noting that some of the recent studies (Canil et al., 2016; Huang and Beaudoin, 2019; Wu et al., 2019; Rodriguez-Mustafa et al., 2020; Zeng et al., 2022)have reported the presence of ilmenite exsolution textures with the high Ti-magnetite (generally >1 wt% and ranges in between 1-3 wt%) found in magmatic-hydrothermal settings and thereby reconsidering the common notion of considering the magnetite-ilmenite exsolution textures considered to be the hallmark of an igneous origin followed by sub-solidus reequilibration with decreasing T and increasing fO_2 (Buddington and Lindsley, 1964; Von Gruenewaldt et al., 1985). The difference between the Pathargora and these previously mentioned scenarios are as following –

A. Ti content is always higher (≥1 wt% to 3 wt%) in the host magnetite (*op cit.)* in these magmatic-hydrothermal system compared to typical low-T hydrothermal magnetite (≤0.1 wt%), whereas in Pathargora the magmatic magnetite is impoverished in Ti (most of the grains have <100 ppm Ti).

B. Unlike Pathargora, in most of the previously reported cases, magnetite-ilmenite exsolution are accompanied by the presence of hydrothermally

formed diopside, albite, garnet, fluor-apatite, quartz, biotite, and chlorite (Hu et al., 2015; Zeng et al., 2022).

C. The absence of Fe-rich exsolution phases in earlier study (of magnetite-ilmenite intergrowth in magmatic-hydrothermal mineralization) and the absence of composite type I ilmenite lamellae which have been interpreted as primary magmatic in origin in this study and in some Fe-Ti-oxide bearing intrusions of ELIP (SW China).

D. Ilmenite lamellae of considerable thickness (i.e. Sandwich ilmenite lamellae or Composite type I ilmenite lamellae) are rarely reported/not reported at all. This seems enigmatic considering that solid state diffusion is much slower than CDRP (Coupled Dissolution Reprecipitation, one of the commonly suggested mechanisms in those studies).

Some researcher have suggested high-Ti magnetite with ilmenite exsolution can be formed from high T hydrothermal fluid in magmatic-hydrothermal settings (Hu et al., 2015; Duan et al., 2019) with one of the studies assigning very specific term to the type of fluid "high-temperature hydrosaline liquids" (Zeng et al., 2022 and references therein) whereas other have suggested the high Ti magnetite is of magmatic decent but were overprinted by later-stage hydrothermal alteration (Huang and Beaudoin, 2019; Wu et al., 2019).

3.5.2 Mechanism and impact of post-depositional processes

In the following sections we discuss the possible mechanisms by which different types of magnetite-ilmenite intergrowth might have formed in association I samples collected from the pod followed by the discussion about how the mineral assemblage of association I transformed later which leads to the formation of association IA assemblage along with the

associated changes in the chemical composition of the sample from the magnetite-ilmenite-bearing pod.

3.5.2.1 Mechanism of post-depositional processes

3.5.2.1.1 Formation Mechanism of magnetite-ilmenite textures (Association I)

Formation mechanism: Trellis-type and Sandwich-type lamella

The exsolution of ulvöspinel in magnetite below the magnetite-ulvöspinel solvus (600ºC) forms characteristic cloth-textured ulvöspinel in magnetite. But the exsolution textures in the studied samples comprise nearly-pure trellis and sandwich ilmenite lamellae. Buddington and Lindsley (1964) concluded that most ilmenite lamella exsolves from titanomagnetite by the oxidation of the ulvöspinel component of the magnetite-ulvöspinel solid solution at temperature above the magnetite-ulvöspinel solvus through the reaction

$$6Fe_2TiO_{4(\text{magnetite-ulvöspinel solid solution})} + O_2 = 6FeTiO_{3(\text{ilmenite lamellae})} + 2Fe_3O_{4(\text{magnetite host})} \ldots. (1)$$

The ilmenite lamella in magnetites from Pathargora is therefore best explained by the oxy-exsolution of magnetite-ulvöspinel solid solution above the solvus.

Ilmenite exsolution lamellae in magnetite can also be the result of exsolution of ilmenite from cation-deficient spinel solid solution (Lattard, 1995; Tan et al., 2016). In this process ilmenite lamella does not constitute more than ca. 16 vol. % of the Ti-rich magnetite crystals (Tan et al., 2016). Cation-deficient spinel can form by substitution of Fe^{2+} by high valence cations such as Ti^{4+}, Al^{3+}, and Cr^{3+} as per reactions 2 and 3 below.

$$2Fe^{2+} = Ti^{4+} + \square \ldots.(2) \qquad 3Fe^{2+} = 2X + \square \ldots (3)$$ [where, $X=Fe^{3+}$, Al^{3+}, Ga^{3+} Cr^{3+}, V^{3+}]

However, the large volume of ilmenite lamellae (>> 16 vol. %) relative to that of magnetite suggests that this mechanism of direct exsolution from cation-deficient spinel was not operative in the magnetite of Pathargora.

Splitting of thick ilmenite lamella into thinner lamella and ilmenite granules which coarsen towards the grain boundary of magnetite to form patchy ilmenite is most likely due to recrystallization of lamellar ilmenite similar to what is seen in some feldspar (Mondal et al., 2017). Disruption and depletion of ilmenite lamella near fractures and presence of granular ilmenite and magnetite intergrowth and xenotime in the fractures and shear planes suggest deformation-induced, fluid-mediated recrystallization of lamellar ilmenite to granular ilmenite (Fig. 3.3A and D-E).

Formation mechanism: Composite Type I ilmenite (internal granular aggregate)

The formation of different types of lamellae has been linked to variable degree of diffusion and oxidation wherein increasing degree of oxidation and diffusion thought to result in trellis type → sandwich type → internal granules of ilmenite in host magnetite →external granules of ilmenite at the magnetite grain boundary (Buddington and Lindsley, 1964). Although the trellis lamellae and sandwich lamella are most likely the products of advanced stages of oxidation (Haggerty, 1976), converging evidences suggest that the composite Type I ilmenite (internal granules) may not be the product of oxidation-exsolution of ulvospinel component of magnetite-ulvospinel solid solution at increased degree of oxidation and diffusion. Only the composite Type I ilmenite contain Fe-rich inclusions. Similar Fe-rich phases are reported to occur only in primary ilmenite (not in the exsolved ilmenite) from Xinjie intrusion of Emeishan Large Igneous Province, SW China (Tan et al., 2016). In Pathargora, occurrence of Fe-rich inclusion-bearing anhedral ilmenite in granular aggregate outside magnetite (Fig. 3.3C, 3.4A-B) further suggests that oxidation of ulvospinel component of magnetite-ulvospinel solid solution and exsolution of ilmenite in magnetite cannot be the sole mechanism of formation of such ilmenite. If the area proportion of ilmenite and magnetite (as seen in polished thin sections) are taken to represent their volume proportions, then the abundant presence of ilmenite, locally significantly exceeding the

volume proportion of magnetite (Fig. 3.3A-B), although not conclusive, may also suggest that not all the ilmenites in the studied rock assemblage are product of oxidation-exsolution from titanomagnetite and some ilmenites probably are primary in origin, crystallizing directly from the melt. The possibility of formation of primary ilmenite grains prior to the crystallization of titanomagnetite from a basaltic magma is not uncommon (Buddington and Lindsley, 1964; Wright and Weiblen, 1968; Tan et al., 2016).

Formation mechanism: Composite Type II ilmenite (external granular aggregate)

The intergranular angle often reaching to 120º (Section 3.4.1.1.2) suggests that euhedral to subhedral granular composite Type II ilmenite or external granules are essentially the product of recrystallization (Fig. 3.3A-E). The discontinuity of sandwich lamella close to the grain boundary of host magnetite grains and presence of coarse external granular ilmenite surrounding the host suggests that lamellar ilmenite migrated to and coalesced at the grain boundary of magnetite (Fig. 3.3D). The relics of deformed sandwich lamella in a groundmass of granular ilmenite also indicate that a part of composite Type II external ilmenite formed via recrystallization of deformed sandwich ilmenite lamella (Fig. 3.4D). Moreover, the partial to complete recrystallization and formation of clean sub-grains from Fe-rich inclusion-bearing large anhedral ilmenite grains outside magnetite (similar to composite Type I ilmenite; Section 3.4.1.1.2) is *prima facie* evidence of formation of some of the composite Type II ilmenite through recrystallization of composite Type I ilmenite (those occurring outside magnetite), which has been interpreted to be primary magmatic in origin (Fig. 3.4A-B). We therefore, propose that the composite Type II ilmenite is largely the product of recrystallization of exsolved lamellar ilmenite and primary magmatic ilmenite.

The composite Type II granular ilmenite is present exclusively in the deformed association IA assemblage (evidenced by the presence of deformed ilmenite lamella and

micro-shear planes), which suggests deformation played important role in recrystallization of existing ilmenite and formation of external granules. Strain-induced nucleation and new grain formation is a common phenomenon in geological environments (Valcke et al., 2015). Several lines of textural evidences such as: 1) transformation of ilmenite laths to granular ilmenite along shear planes (Fig. 3.3B and E), 2) elongated nature of ilmenite defining linear patterns in core-mantle structure and ilmenite-rich massive bands (Fig. 3.3A-B and D), and 3) relics of deformed ilmenite lamella in a groundmass of recrystallized granular ilmenite and magnetite (Fig. 3.4D) all suggest deformation-induced dynamic recrystallization was the primary mechanism of formation of composite Type II ilmenite in Pathargora. Evidence of sub-grain formation, high angle grain boundary, often reaching to 120^{o}, and polygonized nature of ilmenite (± magnetite) suggests sub-grain formation and rotation was the most likely mechanism of dynamic recrystallization (Valcke et al., 2015; Huang and Logé, 2016). The coarsening of ilmenite grains (the coarser grain size of recrystallized ilmenite grains compared to the width of sandwich ilmenite lamella from which the granules have formed; Fig. 3.3D) at places may be due to fluid-assisted recrystallization that promoted better nucleation and coarser grain size. The rarity of thin trellis-type lamellae in association IA which are extremely prone to disruption/elimination by fluid-induced events (Verdugo-Ihl 2021) along with the presence of hydrothermal xenotime and biotite at places in the zone of recrystallization lends support to post-magmatic fluid invasion.

3.5.2.1.2 Mechanism of hematitization (Association IA)

Two mechanisms have been proposed for the hematitization of magnetite: a) redox-controlled oxidation of magnetite (called martitization), and b) non-redox fluid-induced hematitization of magnetite (Lagoeiro, 1998; Ohmoto, 2003; Mücke and Cabral, 2005; Zhao et al., 2019). The redox-controlled transformation of magnetite to hematite can be expressed by the following reaction:

$$2Fe_3O_4 + 0.5\ O_2 \rightarrow 3Fe_2O_3 \ldots\ldots\ldots\ldots\ldots\ldots\ldots\ldots\ (4)$$

On the other hand, in the absence of O_2 the transformation can take place via the following reactions involving low pH acidic fluid:

$$Fe_3O_4 + 2H^+ \rightarrow Fe_2O_3 + Fe^{2+} + H_2O \ldots\ldots\ldots\ldots\ldots\ (5)$$

The molar volume of hematite and magnetite are 30.274 cm^3 and 44.524 cm^3 respectively (Robie and Hemingway, 1995; Ohmoto, 2003). The transformation of magnetite to hematite via redox reaction results in ~ 2% volume increase whereas transformation via non-redox process results in ~ 32-33 % volume reduction and significant loss of Fe in the interacting fluid (Ohmoto, 2003; Zhao et al., 2019). Unlike the redox reaction, significant volume reduction in the non-redox process will result in the formation of highly porous hematite (Ohmoto, 2003; Mücke and Cabral, 2005). The clean hematite, with/without minor pores along crystallographic planes, is indicative of oxidation of magnetite to hematite. On the other hand abundant pores in hematite that pseudomorph magnetite in association IA assemblage and abundant pores along anastomosing cracks in partly hematitized magnetite in association I are suggestive of significant volume reduction/porosity generation and redox-independent hematitization. Pseudomorphic replacement most likely took place by dissolution-precipitation mechanism via advective mass transport along advancing reaction fronts facilitated by continued generations of pores resulting in increased fluid pathways (Putnis, 2002; Ruiz-Agudo et al., 2014). The volume proportions (assumed to be identical to their area proportion; *cf* Baidya et al., 2019) of pores in pseudomorphic hematite of association IA were calculated using the NIS-ELEMENTS-D image analysis software of Nikon®. The calculated volume proportions at multiple places from different thin sections yield a porosity range of 24 to 28 %, which is close to what is predicted for redox-independent hematitization of magnetite. Based on the presence of abundant porous hematite

and minor clean hematite and the calculated porosity, –we propose that redox-independent acidic fluid-induced process of hematitization was most significant, –whereas the role of redox reaction was much less important. Mass balance calculation also shows substantial loss of Fe (~ 28 %) during hematitization (discussed in section 3.5.2.2.2), which is in accordance with the proposed redox-independent hematitization of magnetite.

Another important aspect to consider is that the ilmenite-rutile buffer lies at lower fO_2 than the hematite-magnetite buffer. Therefore, if abundant hematite was formed by redox process due to increase in fO_2 above the hematite-magnetite buffer then ilmenite is expected to be transformed to rutile. No such oxidative transformation of ilmenite to rutile is seen in the samples, which lends support to the proposition of redox-independent fluid-induced hematitization of magnetite without significant increase in fO_2. Supporting evidences come from the geochemistry of magnetite and hematite. Elevated concentrations and significant enrichment of several elements, including REEs, transition metals and HFS elements in hematite compared to magnetite (Section 3.5.2.2.2) cannot be explained by simple oxidation of magnetite. Such enrichments can be best explained by derivation of these elements from extraneous sources and transport to the alteration site by hydrothermal fluid that was responsible for hematitization. Additional geochemical evidences on the nature of this fluid are elaborated in section 3.5.3.2.2.

Based on studies in shear zone rocks (Beach, 1976; Sinha et al., 1986; O'Hara, 1988) it has been proposed that large compositional (and volume) changes are invariably related to zones of high strain which leads to local high fluid/rock ratio. Presence of deformed ilmenite lamellae, micro-shear planes, fractures and presence of hydrothermal minerals such as xenotime in association IA assemblage are in accord with the proposition that shearing most likely localized the fluid flow in some parts of the magnetite-ilmenite body resulting in

localized hematitization of magnetite (Beach, 1976; Sinha et al., 1986; O'Hara, 1988; Tobisch et al., 1991).

3.5.2.2 Impact of the post-depositional processes: redistribution of the elements

3.5.2.2.1 Element redistribution during Subsolidus oxy-exsolution

Oxidation-exsolution of titanomagnetite involves redistribution of Ti, Al, Mg, Mn, Nb, Ta, Sc, Ga, Sn, W etc. according to their compatibility in magnetite and/or ilmenite (Buddington and Lindsley, 1964; Liu et al., 2015). For deciphering the partitioning of different elements between ilmenite and magnetite during exsolution, we have used the data from association I assemblage, because unlike association IA assemblage it is not pervasively altered and therefore likely to reflect the element distribution/redistribution pattern between magnetite and ilmenite due to the oxy-exsolution process. The higher concentration of Ti, Mg and Mn in ilmenite compared to their host magnetite is consistent with the greater ~~better~~ compatibility and higher partitioning of these elements in ilmenite compared to magnetite (Haggerty, 1976; Liu et al., 2015). On the other hand, higher concentration of Al and Cr and V in magnetite is in agreement with the known preferences of these elements for magnetite compared to ilmenite (Haggerty, 1976; Knecht et al., 1977; Lattard, 1995; Tan et al., 2016). Notably higher concentrations of HFS elements such as Nb and Ta, transition elements such as Sc, Co, Cu and Zn and gran~~i~~ophile elements such as Sn and W in ilmenite lamellae compared to their host magnetite suggest that these elements are more compatible in ilmenite and preferentially partition in ilmenite during the oxidation-exsolution process. On the contrary, Ga is highly compatible in magnetite compared to ilmenite and retained in magnetite structure during element redistribution.

3.5.2.2.2 Change in elemental concentrations due to hematitization of magnetite

Mass balance calculations were carried out to quantify the loss and gain of different elements during hematitization of magnetite. Any mass balance calculation requires a reference frame relative to which exchange of elements can be estimated. The pseudomorphic replacement of magnetite by hematite is suggestive of the isovolumetric (volume of magnetite = volume of hematite + volume of pores) nature of the replacement process. Therefore, the mass balance estimates were done factoring the calculated volume reduction (ca. 26 %)in the ISOCON reaction (Grant, 1986, 2005).The average concentrations of individual elements in unaltered magnetite in association I are considered to represent the compositions of magmatic magnetite and those from the hematite in association IA (hematite containing similar ilmenite lamellae as that of association I) are taken to represent the final composition after alteration (hematitization of magnetite). The results of mass balance calculation are given in Table 11 and shown in Fig. 3.9.

Mass balance calculations using EPMA and LA-ICPMS data show consistent patterns (though at varying degree) of loss of Cr, Fe, V and gain of Al, and contrasting pattern for Ti (loss and gain for EPMA and LA-ICPMS data respectively (Fig. 3.9 A-B). It is evident that Mg, V and Cr, which are usually compatible in spinel structure, were substantially lost during hematitization. Iron is usually conserved during oxidation of hematite. The substantial loss of Fe (~ 28 % both using EPMA and LA-ICPMS data) therefore, lends support to redox-independent hematitization of magnetite by acidic fluid (see section 3.5.2.1.2). The highly variable concentrations of Ti and contrasting loss and gain may be due to local re-precipitation of Ti. The mass balance calculation also demonstrates significant gain of Na, K and P and loss of Mn during hematitization (Fig. 3.9A-B).

Among the transition elements, there was substantial gain of Cu, minor gain of Co, minor loss of Zn and substantial loss of Ni suggesting that large amount of Cu was brought in by the interacting fluid;, Co might have been redistributed without major loss, and Ni was lost in the interacting fluid (Fig. 3.9B).

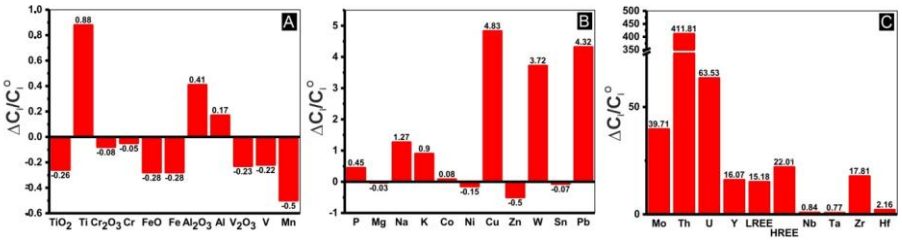

Figure 3.9 Results of mass balance calculations showing change in concentrations of different elements in hematite samples from association IA

Mass balance calculations display loss and gain of different elements in hematite; Values corresponding to oxides and elements are results based on calculation using EPMA and LA-ICPMS data respectively; (A) Results shows loss of Cr, Fe, Mn and V and gain of Al; Contrasting results obtained for Ti using EPMA and LA-ICPMS data. (B) Substantial gain of P, Na, K, Cu, W and Pb, minor gain of Co, and loss of Ni, Zn and Sn; (C) Significant gain of Mo, Th, U, Y, LREE, HREE and Zr. Note the much higher gain of Th than U, HREE than LREE and Zr than Hf. There is substantial and similar gain of both Nb and Ta.

The hematitization was accompanied by substantial gain of U, Th, Pb, W and Mo (Fig. 3.9B-C). Such consistent gains suggest that these elements were brought in by the interacting fluid and immobilized by hematite. Selective enrichment of U, W and Mo at constant Sn in hematite during pseudomorphic replacement of magnetite by hematite has been explained by transport of these elements (U, W and Mo) in common hexavalent state in oxidized fluid and greater capacity of hematite crystal structure to incorporate hexavalent cations (Courtney-Davies et al., 2019). Although Sn was largely conserved (minor loss is noted) it has been argued above and discussed in section 3.5.3.2.2 below that the hematite formed due to interaction of reduced acidic fluid with magnetite and U was most likely transported as U^{4+}. Consistently higher concentration of Th than U in hematite and much higher gain of Th than U suggest greater availability of Th than U in the fluid that caused hematitization (Fig. 3.9C).

While both LREEs and HREEs are mostly below detection limits in magnetite, they were consistently detected in hematite suggesting substantial gain of REEs in hematite. It is also likely that the fluid carried more HREE than LREE as indicated by ≥ 1 HREE/LREE ratios in hematite and higher gain of HREEs (and Y) compared to LREEs (Fig. 3.9C). Similar gains of Nb and Ta in hematite, similar Nb/Ta ratios in magnetite and hematite and excellent positive correlations between Nb and Ta suggest these elements were brought in by the alteration fluid and they behaved similarly during hematitization. The results of mass balance calculation suggest that Zr and Hf were gained by hematite and brought in by the alteration fluid. However, because concentrations of Zr and Hf in magnetite are below detection limits in most spots, mass balance results does not provide actual quantification of gain.

3.5.3 Physicochemical Parameters: Records and modifications

3.5.3.1 Temperature

Temperature known to be one of the most important of several parameters such as fO_2, host rock chemistry, co-crystallizing phases, fluid composition (for hydrothermal magnetite) etc. for controlling the composition of magnetite. Elements such as Ti, V, Ga which are generally considered to be T-sensitive wherein higher formation T results in higher concentrations of these elements have been used in previous studies to get an idea about the formation T (Dare et al., 2012, 2014; Nadoll et al., 2014; Knipping et al., 2015a, 2015b; Salazar et al., 2020). In this present chapter we couple the variation in magnetite chemistry of T-sensitive elements by incorporating T-sensitive ratios/plots (Nadoll et al., 2014; Deditius et al., 2018) along with the Mg-based magnetite thermometry (Canil and Lacourse, 2020) and Ti in biotite thermometry (Wu and Chen, 2014; Li et al., 2020, 2021) similar to the previous chapter (Chapter 2). This multi-proxy-based approach is useful to interpret the results from thermometric calculations which often lead to underestimation/overestimation of T for numerous reasons. In the (Ti + V) wt% vs. (Al + Mn) wt% magmatic magnetite samples of

association I plotted near the boundary of the 300 – 500°C and >500°C field, whereas most of the hydrothermal magnetite samples falls in the field of 300 – 500°C with some of the magnetites plotting outside any designated field (Fig. 3.10A). The Ti/V ratio also proposed by (Nadoll et al., 2014), which deemed to remain unchanged even with the decreasing cumulative concentration of Ti and V, shows consistently higher values in hydrothermal magnetite from the magnetite-apatite veins (Fig. 3.10B). On the contrary in Ga/Ni vs. V/Ni plot, magmatic magnetite samples plot distant than hydrothermal magnetite and consistent with the T trend (Fig. 3.10C) This V/Ni vs. Ga/Ni plot is a slightly twisted form of the discriminator we have suggested in chapter 2 to utilize the T-sensitivity of Ga as there are reports of Ga-enrichment with increasing crystallization T (Nadoll et al., 2014 and references therein) and as we know Ga is enriched in magmatic melts (0.47 and 495 ppm with average of 18 ppm) (+4.2/–3.4)compared to natural (average is 1.6 ppm) (Prokof'ev et al., 2016). Instead of the effect of oxy-exsolution the reflection of increasing T trend can be seen in Fig. 3.10C, based on V, Ga and Ni based elemental ratios.

Temperature of magnetite (association I and association II) formation were calculated using the magnetite thermometer by Canil and Lacourse (2020) and from biotite thermometry using associated biotite chemistry and the methodology followed in both the cases are as discussed in chapter 2.

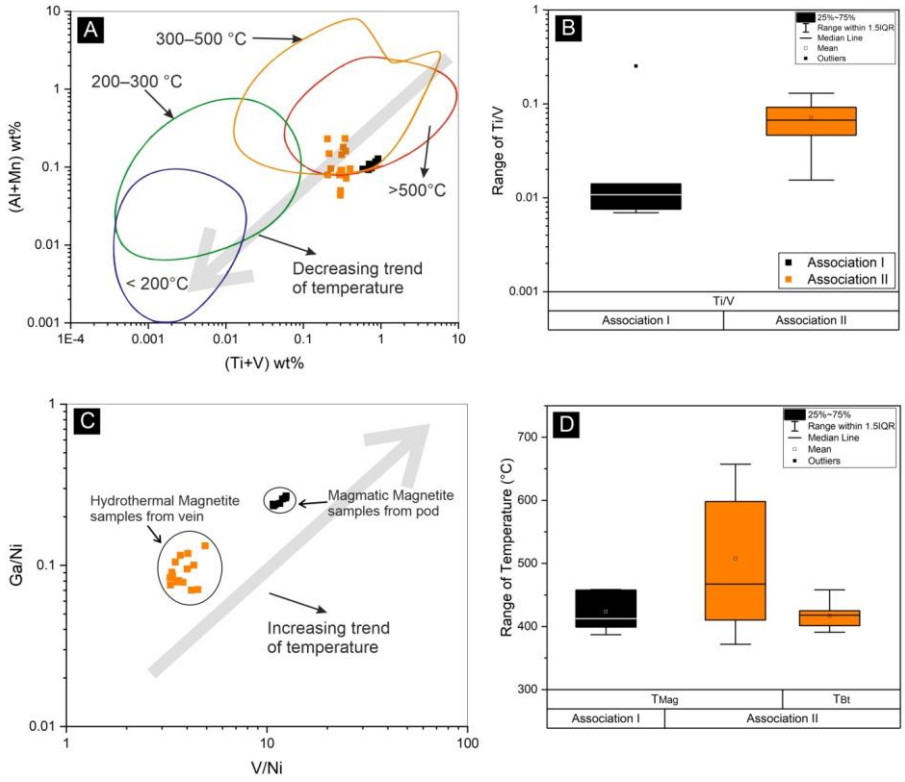

Figure 3.10 Range of formation temperature for association I and II magnetite samples as a function of T-sensitive trace elements and by biotite and magnetite-based thermometry

Bivariate plots (A and C) and Box and Whisker plots (B and D) showing the T range/trend based on cumulative concentrations of (Ti + V) vs. (Al + Mn) (A); ratios of Ti/V (B); based on V/Ni and Ga/Ni ratios (C) and (D) as a result of Mg in magnetite and Ti in biotite thermometry. The T fields in (A) redrawn from Deditius et al. (2018) and Ti/V ratio as suggested by Nadoll et al. (2014) and references there in. Ti in biotite thermometry for association II samples (D) are calculated after Wu and Chen, (2014). Temperature range from magnetite thermometry for association I and II (D) are calculated following the method by Canil and Lacourse (2020). Legends for all the diagrams are shown in Fig. B.

The T range from biotite of association II varies between 390°C - 458°C with the average of 416°C (Table 15). However the "Mg in magnetite" thermometry yields higher and variable T for hydrothermal magnetite from vein samples compared to magmatic magnetite from the pod (Fig. 3.10D). The average value of the T_{Mg} of magnetite from association I is ≈

425°C and for association II magnetite the average T_{Mg} is ≈ 500°C with the median value close to ≈ 450°C for the later. It is important to note that although the T for magmatic magnetite in Pathargora derived through magnetite thermometry is disputable, the thermometry yields reasonable T range (≈ 450°C - 500°C) for magnetite samples from the magnetite ± apatite vein assemblage which is consistent with the range suggested by (Pal and Bhowmick, 2015), based on micro-thermometric measurement in fluid inclusion hosted in apatite from Turamdih. In case of magmatic magnetite of association I the reason behind getting lower T trend or range (Fig. 3.10A-B) close to hydrothermal magnetite (Fig. 3.10A) is mainly due to the fact that all of these diagrams involve either Ti or Mn (Fig. 3.10A) or Mg (Fig. 3.10B), which get preferentially partitioned into ilmenite structure during oxy-exsolution as have been demonstrated in section 3.5.2.2.1.

3.5.3.2 Nature of the fluid

3.5.3.2.1 Nature of the fluid in hematitization (association IA)

Many of the observed trace element enrichment patterns in hematite can be explained by the involvement of a reduced and acidic fluid during the hematitization of magnetite, which is in agreement with the proposed redox-independent hematitization of magnetite (Section 3.5.2.1.2 and 3.5.2.2.2). Manganese is a redox sensitive element and in oxidizing environment, such as that prevails in low temperature weathering environment, may re-precipitate locally as oxides/hydroxides due to oxidation of Mn^{2+} to Mn^{3+}/Mn^{4+} often resulting in localized high concentration of Mn (van der Weijden and van der Weijden, 1995; Koppi et al., 1996; Baidya et al., 2019). Loss of Mn during hematitization (no localized high concentration is seen in hematite as evident from LA-ICPMS data) thus lends support to our proposition that hematitization of magnetite was mainly redox-independent. It is known that uranium in oxidized low-temperature fluids is better transported as U^{6+} than $Th^{4+}$and thereby U is decoupled from Th resulting in greater availability of U in the oxidized fluid. Baidya et

al., 2019 demonstrated greater mobility of U in low temperature oxidized weathering fluid and better retention/immobilization of U than Th by hematite. Therefore, if U and Th are transported in low temperature oxidized fluid, the value of U/Th ratios would increase significantly in hematite compared to the ratios in original magnetite. Although U and Th content in magnetite is very low or below detection limit, wherever detected, U content is higher than Th in magnetite. Despite the higher concentration of U than Th in magnetite (and U/Th ratios being > 1), the much higher concentration of Th (U/Th ratios being << 1), and much higher enrichment of Th than U in hematite (which is known to retain more U than Th; *op cit.*) are *prima facie* evidences that the fluid involved in hematitization of magnetite was not oxidized. Although U^{6+} is more soluble in common hydrothermal fluid than U^{4+}, experimental study (Keppler and Wyllie, 1990; Timofeev et al., 2018) and thermodynamic calculations (Xing et al., 2019) indicate that in reduced acidic fluid U can be transported as U^{4+} as chloride and fluoride complexes whereas in such fluid Th is commonly transported as F^- complexes as it does not form Cl^- complexes (Keppler and Wyllie, 1990; Kovalenko et al., 2012; Nisbet et al., 2018). Additionally high Y/Ho ratio in all the hematites (average ≈ 18) indicates the fluid was rich in F^- as decoupled behaviour of Y and Ho in F- dominated fluid is now known (also discussed in the following section). The highly porous nature and the signatures of trace element enrichment of hematite, and some of the trace element enrichment/depletion patterns therefore collectively suggest redox-independent hematitization of magnetite by a reduced and acidic fluid which might have been F-bearing.

3.5.3.2.2 Nature of the fluid in magnetite-apatite mineralized vein (Association II)

The chondrite–normalized Y-REE pattern of magnetite and apatite samples from association II are shown in Fig 3.11A-B (Table 14). Both magnetite and apatite show positive Ce anomaly and negative Eu anomaly.

Apart from these, magnetite also shows overall flat pattern with some of the analyzed grain are characterized by negative Dy anomaly. REEs rarely get incorporated in magnetite due to their lower partition coefficient. The average partition coefficients of Lu, Gd and Y in magmatic systems are 0.15, 0.031 and 0.026, respectively (Dare et al., 2012) and similarly in hydrothermal system REEs rarely get partitioned into magnetite (Huang et al., 2015). Therefore most of the hydrothermal magnetite of association II showing enrichment of REEs with respect to the chondrite values indicates that the hydrothermal fluid was extremely enriched in REEs, as a minor amount of REEs in magnetite implies REE enrichment in the respective hydrothermal fluid (Huang et al., 2015). Apatite samples are characterized by conspicuous MREE enrichment and also show strong negative Eu anomaly (average value of Eu/Eu* is 0.17) and moderately positive Ce anomaly (average value of Ce/Ce* is 1.17) and moderately negative Y anomaly. Cao et al. (2012) and Pan et al.(2016) demonstrated that apatite crystallizing in oxidizing condition have higher Eu and low Ce (thereby positive Eu and negative Ce anomaly compared to reducing condition, as Eu and Ce are most compatible in apatite structure in +3 state, because of the compatibility in radius with Ca^{2+} (Sha and Chappell, 1999). Considering that Eu and Ce occur in +2 and +3 state in a reducing fluid the observed Eu and Ce anomaly can be explained. Converging evidence comes from the plot suggested by Mercer et al. (2020) where the calculated Eu/Eu* vs. Ce/Ce* of the apatite samples clustered mostly in the region of 'moderately reducing' field (Fig. 3.11D), based on compilation of fluor-apatite data from a broad spectrum of environments ranging from mafic-intermediate to rhyolite suite as well as incorporating apatite samples from IOA-IOCG deposits. The value of Eu/Eu* ≥ 0.5 is generally associated with the oxidizing condition and Mercer et al. (2020) showed that apatites belonging to hematite zone are associated with ≥ 0.5 and sometimes ≥1, whereas in the present case the fluor-apatite samples from Pathargora lies in between 0.08 – 0.33.

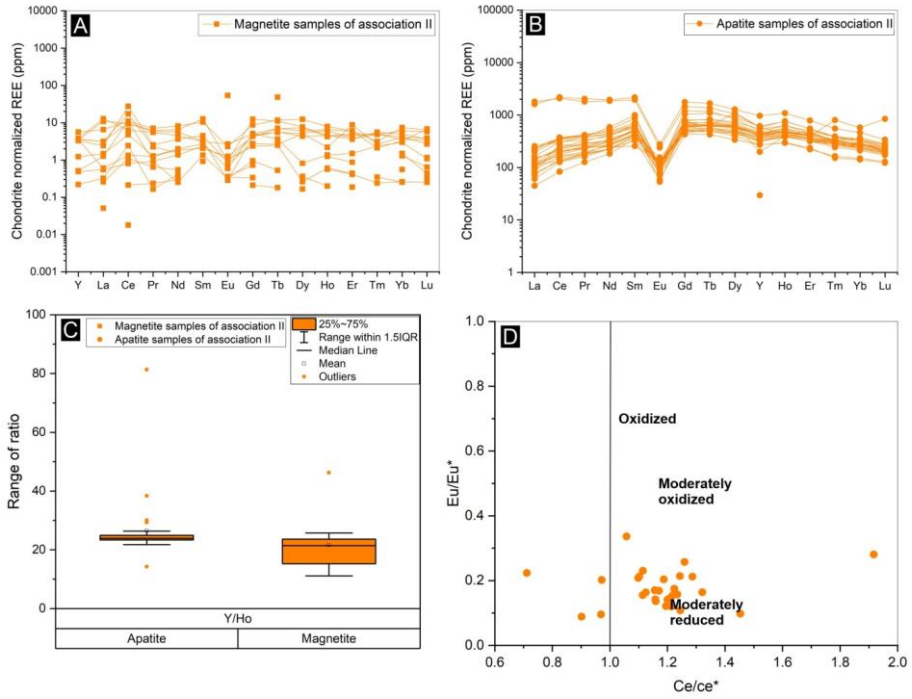

Figure 3.11 Compositional variations of magnetite and apatite in REEsS and REE-based ratios

Chondrite–normalized REE (A-B), Box and Whisker (C) and Bivariate (D) plots based on composition of magnetite and apatite from the magnetite-apatite –bearing veins of association II;- nNote the overall flat but enrichment of REEsS in magnetite (A) and MREE-enriched but LREE and HREE depleted pattern of apatite samples (B). Y/Ho ratios in magnetite and apatite where consistent higher ratios (≈ 20) indicating decoupled behavior between Y-Ho (C) and (D) Concentration of Eu and Ce in fluor-apatite samples from association II plotted in the diagram suggestive of redox condition (redrawn from Mercer et al.(2020) and references therein) which shows most of the fluor-apatite samples from Pathargora cluster around the "moderately reduced" zone. In A-B, cChondrite values are taken from McDonough and Sun, (1995). The legends for all the diagrams are shown in respective figures and the legends for (C) and (D) are given in (C).

Although the degree of reducing nature being moderate or not cannot be confirmed, the higher concentration of V in associated magnetite samples (ranges between 1966 ppm - 3604

ppm) considering the global references further supports the interpretation about the nature of the fluid being reducing in nature as V in +3 state has been found to be most compatible in magnetite structure than the other higher valence states (Toplis and Carroll, 1995; Carew, 2004; Righter et al., 2006). On the contrary Sn (most compatible in magnetite in +4 state compared to the reduced +2 state), which is mostly below the detection limit of LA-ICPMS further hints at the reducing nature of the fluid (Carew, 2004; Chen et al., 2015b). Apart from the characteristic enrichment of MREE, the depletion in LREE-HREE might also be the result of localized REE leaching from fluor-apatite, ~~(leading to the formation of secondary monazite and xenotime),~~ which leads to the formation of secondary REE-bearing phases and these observations are consistent both from natural occurrence in deposit-scale and from experimental results (Harlov, 2015; Normandeau et al., 2018).

The ratios of Y/Ho for all the magnetite and apatite samples of association II are generally ≥10 and ≥20 respectively (Fig. 3.11C). The average value of Y/ho ratio in case of magnetite samples is 21.62 while in case of apatite the average value is 26.48. It is well-known that Y shows similarity in geochemical nature with the HREEs although their complexing behaviour in F^{-} ligand-rich fluid differs largely from all the HREEs including Ho despite the close similarity in radius of Y^{3+} and Ho^{3+}(Luo and Byrne, 2000; Tanis et al., 2012). All the apatite samples from association II are fluor-apatite (F ranges between 3.5 - 4 wt %) with negligible content of Cl (≤0.05 wt %). Loges et al., (2013) showed that in a F^{-} rich fluid Y preferentially fractionate over all the lanthanides including Ho as a result of the higher stability constant of YF^{2+}. The decoupling of Y from Ho as envisaged in the Y/Ho ratios magnetite and apatite samples perhaps indicate that the hydrothermal fluid which precipitates them are probably dominated by the presence of F^{-} ligand. Thus combining all observations, it seems reasonable to state that the hydrothermal fluid that precipitated magnetite and apatite was enriched in REEs as evidenced from the enhanced concentration of

REEs in magnetite, probably reducing in nature and rich in F^- ligand compared to other commonly found ligands in hydrothermal system.

3.5.4 Discriminator diagram: implications and impact of post-depositional changes

3.5.4.1 Deposit-type discriminator

The magnetite samples from the pod (association I) and the vein (association II) have been plotted in the deposit-type discriminators proposed by Dupuis and Beaudoin, (2011) and modified by (Nadoll et al., 2014). The two diagrams based on (Ti + V) wt% vs. (Al + Mn) wt% and Ni/(Cr + Mn) wt% identified the magmatic magnetite of association I and hydrothermal magnetite of association II of different origin and thereby plotted in different clusters (Fig. 3.12A-B). In the (Ti + V) vs. (Al + Mn) plot, the magmatic magnetites of association I plotted at the Fe-Ti, V-Kiruna-porphyry junction and the hydrothermal magnetite of association II are plotted in both the Kiruna and porphyry field. In Ti + V vs. Ni/ (Cr + Mn) plot, the magmatic magnetite mostly plots in the porphyry field and at the boundary between the porphyry and Fe-Ti, V deposit, whereas the hydrothermal magnetite plots close to the Kiruna field and beyond any designated field areas. The similar impact of changes in magnetite chemistry due to oxy-exsolution have been observed (as shown in section 3.5.3.1) in case of these deposit-type identification diagrams as an artifact of partitioning of Ti in ilmenite in case of association I. In fact the first of the two deposit diagrams actually uses the same component of (Ti + V) and (Al + Mn) as shown in the diagram drawn with different T field (Nadoll et al., 2014; Deditius et al., 2018). If magnetite samples were not subjected to elemental redistribution and if Ti not fractionated in ilmenite, the magmatic samples perhaps would plot in the domain of Fe-Ti, V ore (Fig. 3.12A-B). In fact, some of the studies approximated the composition of original magmatic magnetite by reintegrating the composition of exsolved ilmenite lamellae into the host magnetite (Sun et

al., 2019) and showed the resulting composition plotted in the field of Fe-Ti, V deposit (Sun et al., 2019; Rodriguez-Mustafa et al., 2020) in similar scenarios.

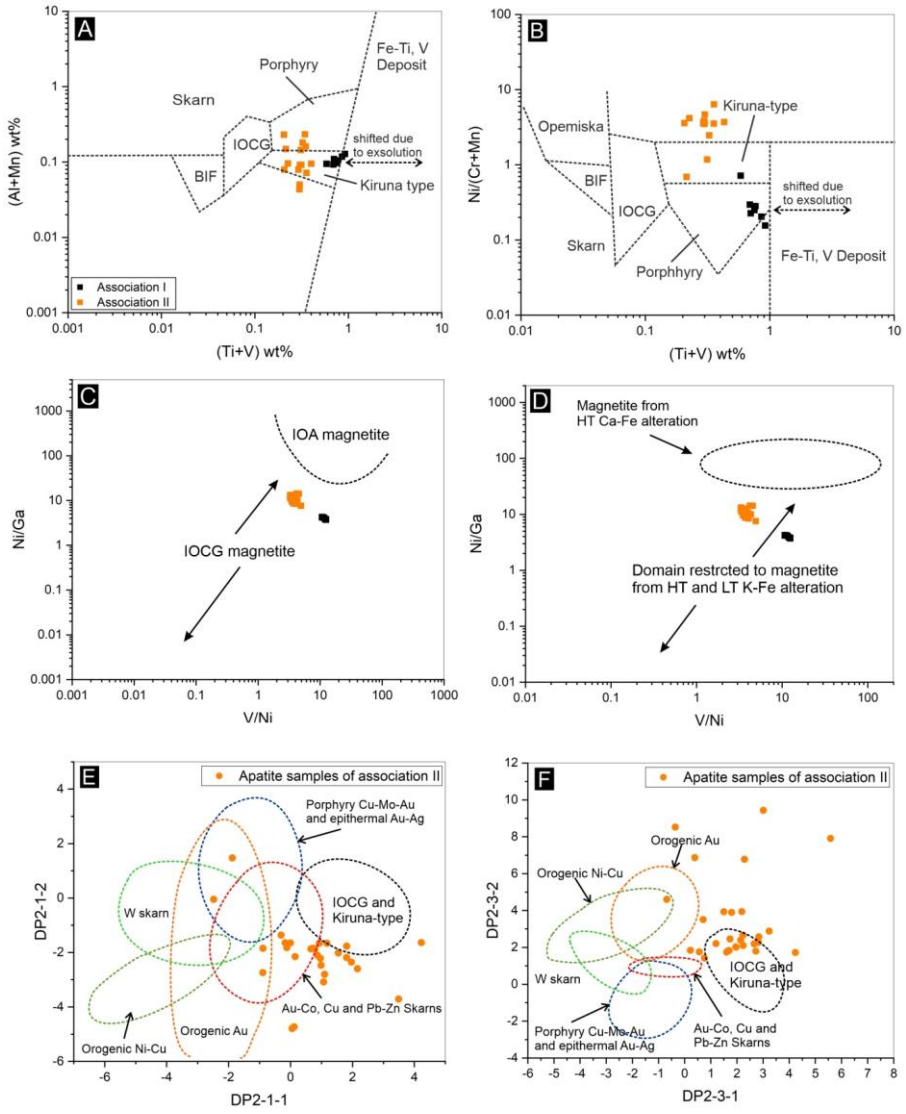

Figure 3.12 Geochemistry of magnetite-apatite as indicator for deposit types and alteration types

Discrimination diagrams for using magnetite (A-D) and apatite (E-F) composition to separate different types of deposits (A-F excluding D) and associated alteration types (D) : (A-B) suggested by Dupuis and Beaudoin (2011), (C-D) suggested by the

present study and (E-F) suggested by Mao et al. (2016). The legends for magnetite-based plots (A-D) is given in (A) and for apatite in the respective diagrams. See text for details.

Additionally the magnetite compositions are plotted in the V/Ni vs. Ni/Ga plot which have been suggested by the present study in the previous chapter (Chapter 2) to discriminate between magnetite samples from IOCG deposits from IOA deposits and also to identify the associated alteration types common to these deposits, namely K-Fe and Ca-K-Fe alterations (in Chapter 2, Fig. 2.13C-D). All the magnetite samples of Pathargora remain restricted to IOCG domain including the magmatic magnetite samples from the pod. Additionally all the magnetite samples plotted in the zone restricted to K-Fe alteration in the suggested identification diagram (Fig. 3. 12C-D). It needs to be highlighted that the plotting of magnetite geochemical data within the designated area doesn't mandate the deposit-type affiliation and also deviation/not plotting in the designated area doesn't necessitate not belonging to that specific deposit-type. As in the present case, all of the magnetite samples from the pod and the vein are plot very closely and within the IOCG domain (Fig. 3.12C) but our field-based observations coupled with textural and geochemical study demonstrate the difference in their formation as discussed in the earlier sections.

The geochemistry of apatite which is also known to be robust (Bouzari et al., 2011) and ubiquitous in presence in most of the magmatic/hydrothermal/metamorphic/sedimentary environment (Sha and Chappell, 1999; Webster and Piccoli, 2015; Pan et al., 2016; Liu et al., 2017) like magnetite and has also been used to gainget insights about the formation process or differentiating between different types of deposit (Belousova et al., 2001, 2002; Mao et al., 2016; Mercer et al., 2020a). In Pathargora in case of association II, apatite are consistently associated with magnetite in the magnetite-apatite-bearing veins and therfore the composition of apatite can also provide valuable insights about the deposit-type affiliations in addition to

depoit-type discriminator, based on magnetite geochemistry. We have used two of the several discriminators suggested by Mao et al. (2016) where the DPA (Discriminant Projection Analysis) function is designed to discriminate apatites from orogenic Ni-Cu, orogenic Au, v~~V~~arious types of porphyries, skarn, IOCG, and Kiruna-type deposits . In DP2-1-2 vs. DP2-1-1 and in DP2-3-1 vs. DP2-3-2 diagram all the apatite samples from association II are plotted within or close (Fig. 3.12E-F) to the IOCG and Kiruna-type field. Integrating the results from the aforementioned discriminators for different deposit types (Fig. 3.12A-F, excluding D) and discrminator for alteration types (Fig. 3.12D); it seems reasonable to assume the magnetite samples of association I belongs to the 'Fe-Ti, V deposit' if we corroborate the loss of Ti due to oxy-exsolution and the shifting comes with it. In case of association II, magnetite samples plotting in the compositional domain common to the magnetite samples from IOCG deposits (Fig. 3.12C) and the associated apatite plotting in the IOA-IOCG domain (Fig. 3.12F) (the discriminators suggested ~~by~~ (see Mao et al., 2016) do not discriminates between apatite samples from IOA and IOCG deposits) or close to the domain (Fig. 3.12E) may indicate a similar depositional environment. Association II magnetite samples from the magnetite-apatite vein, occurs within the biotite-rich domain in the field (Fig. 3.1B), in hand specimen (Fig. 3.5B) and in micro-scale (Fig. 3.5D-E) and the magnetite samples also shows compositional similarity with the compiled magnetite samples from the K-Fe alteration assemblages from IOCG deposits, may thus indicate the formation of magnetite might be associated with the K-Fe type alteration-type~~s~~ similar to what has been observed in case of IOCG deposits. This similarity should not be treated conclusively as the present study also demonstrated that apatite samples from the same association shows compositional similarity with both the apatite samples from IOA and IOCG deposits. Further scrutiny is warranted to precisely confirm about the deposit-type affinity.

3.5.4.2 Process Discriminator

The most widely used and well-known diagram used in recent literature to identify the origin of magnetite (magmatic vs. hydrothermal) based on the concentration of Ti, Ni and Cr (suggested by Dare et al.~~in~~ 2014) appropriately identifies the formation process of association II magnetite of hydrothermal descent but in case of magmatic magnetite samples of association I some of the samples fall over the boundary between magmatic and hydrothermal field with some of the samples even plotted inside the hydrothermal field due to decreased concentration of Ti (Fig. 3.13A). The Ni/Cr ratio that~~which~~ has been suggested to be ≤1 for magmatic magnetite and ≥1 for hydrothermal magnetite holds true for the magmatic and hydrothermal magnetite samples from Pathargora. Some of the studies tried to deal with the issues of getting more reliable compositional data by using large spot size during LA-ICPMS , secondary ion mass spectrometry (SIMS) and also in electron microprobe analyzer (EPMA) assuming it reflects the composition of the mineral before exsolution (Dare et al., 2012). On the other hand, some other studies mentioned the possibility of getting mixed analysis/ "averaging" (Deditius et al., 2018) of the trace elements in magnetite by doing so. The identification diagram based on concentration of V and Ti suggested by Knipping et al. (2015b), where the different fields are drawn based on the dataset of Nadoll et al. (2014), does not yield explainable result where most of the magnetite samples are plotted outside any of the designated area and some of the hydrothermal magnetite samples of association II plotted in the intersectional area (Fig. 3.13B) between 'magmatic magnetite' and 'hydrothermal magnetite'.

One of the main reasons behind getting conflicting results with our petrographic and field-based observations in most of the discriminators that have been used in the present study is that most of the discriminators use~~ds~~ Ti concentration as an important discriminating factor. The rationale behind these discriminators is understandable considering the long-

standing notion of Ti being largely immobile under~~in~~ hydrothermal conditions and also explainable in the present case behind the improper shifting of the magmatic magnetite towards the hydrothermal field or from the Fe-Ti, V field to other areas in case of deposit-type discriminators. Although no intersectional/designated space for magmatic-hydrothermal deposit was suggested in the identification diagram suggested by Dare et al. (2014) unlike Knipping et al. (2015b), there are recent reports of high Ti content (1-3 wt%) in many magmatic-hydrothermal and also in hydrothermal settings (Hu et al., 2015; Canil et al., 2016; Wu et al., 2019), which often exceeds or falls very close to the assigned range of the concentration of Ti used in the diagram. The present study emphasizes that trace element geochemistry-based process discriminator might not be the sufficient alone to discriminate between the different ore-forming processes. Meaningful insights into ore genesis can be gained only when coupled with detailed petrographic observations (Deditius et al., 2018; Huang and Beaudoin, 2021) in order to address the dynamic variability in most geological systems .

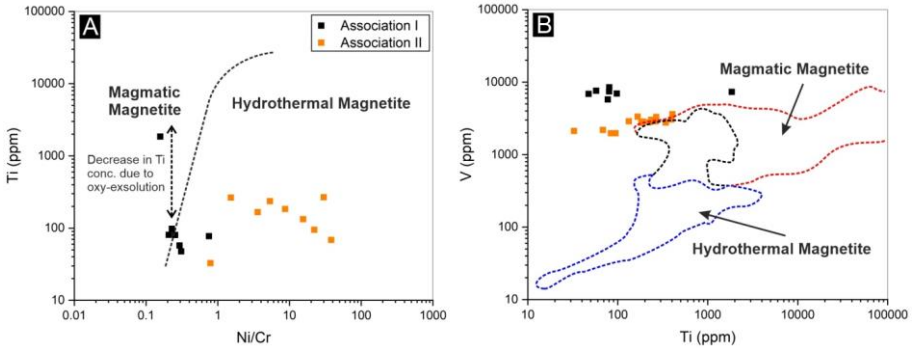

Figure 3.13 Geochemistry of magnetite as an indicator of formation process

Bivariate plots based on concentrations of Cr, Ni, Ti (A) and Ti, V (B) to distinguish magmatic magnetite from hydrothermal magnetite showing magmatic

magnetite samples (association I) from Pathargora plotted over the boundary and in both magmatic and hydrothermal field, whereas hydrothermal magnetite (association II) remain restricted within the designated hydrothermal field (A) (after Dare et al. (2014)) and in (B) most of the magmatic and hydrothermal magnetite samples are plotted outside the suggested field (after Knipping et al. (2015) and the fields are drawn based on the dataset of Nadoll et al. (2014)). The legends are as shown in (A).

3.6. Concluding Remarks/Summary

Field-based observations coupled with micro-scale textural and geochemical characterization of two strikingly different mineral associations from Pathargora area shows evidences of magnetite mineralization by both magmatic and hydrothermal ore-forming processes. Magmatic magnetite from magnetite-ilmenite-bearing samples from the pod displayed significant impact of post-formational changes involving oxidation-exsolution followed by deformation-induced recrystallization and textural re-equilibration and hydrothermal fluid-induced hematitization. On the contrary magnetite samples from the magnetite-apatite-bearing veins are not affected by such processes. Using T and redox-sensitive trace elements and REEs in magnetite and associated apatite and biotite samples attempt has been made to understand the physicochemical conditions of the ore-forming processes. Flat but overall enrichment of REEs except Eu in magnetite, decoupling of Y/Ho along with the typical values of Eu/Eu* and Ce/Ce* collectively indicates involvement of reducing and REE-rich mineralizing fluid responsible for hydrothermal magnetite mineralization in veins/pockets. Presence of fluor-apatite with negligible Cl^- content possibly hints the mineralizing fluid was F^- dominated. High V and negligible concentration of Sn in magnetite further validates the reducing nature of the fluid. Commonly used indicator diagrams for formation T, formation process and deposit-type discriminator yield more or

less results with significance for hydrothermal magnetite, but in case of magmatic magnetite results are often misleading if the results were not corroborated with textural criterions. In most of the cases ambiguity arises because most of these diagrams include elements, such as Mg (in temperature indicator), Mn (in deposit type indicator) or Ti (in temperature, formation process and deposit-type indicator), which got partitioned into ilmenite due to more compatibility. However, Ga/Ni vs. V/Ni plot which is used in this study shows consistency with the invoked T trend albeit the effect of oxy-exsolution. The post-depositional processes modifying the magmatic magnetite has been deconstructed through understanding the mechanism and elemental reorganization associated with it by using petrography and geochemical characterization and also by using mass-balance calculation. Formation of deformed composite type II ilmenite bears evidence of strain-induced, fluid-mediated dynamic recrystallization process that transforms magmatic magnetite to highly porous, trace-element rich hematite with distinct chemical signature from the predecessor. Hematitization was accompanied by significant gain of U, Th, Pb, Cu, Mo, W and REEs in hematite and depletion of Ni, Cr, V from hematite. Significant reductions in volume which generated porous hematite, absence of rutile in the altered assemblage along with the loss of Mn, enrichment of Th over U in hematite all as a whole if taken into consideration, indicates redox-independent nature of the hematitization and involvement of a reduced, F^--bearing acidic, metal-enriched fluid in the process. Understanding the mechanism and the reorganization of element distribution associated with the oxy-exsolution and fluid-induced hematitization allows to exclude (hematite samples are not incorporated to be discriminated via process/deposit type discriminator) or to explain the results of the discriminator diagrams. The present study recommends that mode of occurrence and trace element geochemistry of magnetite can be an effective tool to discriminate magnetite formed by different processes in

multiply deformed and metamorphosed terrains like SSZ, but only if combined with field-based observations and petrography and other available proxies.

Chapter 4: Magnetite in Banded Magnetite Quartzite from Turamdih and Mohuldih: the textural and geochemical conflicts

4.1. Introduction:

In Turamdih and Mohuldih area, located in the western segment of the Singhbhum shear zone, magnetite ± apatite ± ilmenite and magnetite ± apatite ± rutile occurs in banded magnetite quartzite with alternating quartz-rich and Fe ± Ti-oxide-rich bands which *sensu lato* resembles the Banded Iron Formation (BIF)/rocks formed by syn-sedimentary processes. BIFs are chemically/biochemically precipitated sedimentary rocks. The major constituents of the BIF rocks come from the seawater and hence these rocks are considered to be one of the major source to get insights about the chemistry of the ancient ocean (Klein, 2005; Bekker et al., 2010; Planavsky et al., 2010; Posth et al., 2011) and also the cycling of Fe being attached to other important biogeochemical elements like Carbon, BIF chemistry has been utilized to know about the biological processes as well (Bekker et al., 2010). In the present chapter the mode of occurrence, texture and trace element geochemistry of magnetite from the banded rock in and around Turamdih and Mohuldih is discussed which occurs in alternating bands composed of quartz keeping in mind the following objectives –

A. To understand the possible origin of magnetite samples from Turamdih and Mohuldih by comparing the compositions with BIF-magnetite from eastern India and some selected metamorphosed/un-metamorphosed BIFs from other parts of the globe.

B. To know about the physicochemical parameters (T, fO_2) and the variation of these parameters (if any) related to magnetite mineralization between Turamdih and Mohuldih hosted in the same banded rock by making use of textural and geochemical observations.

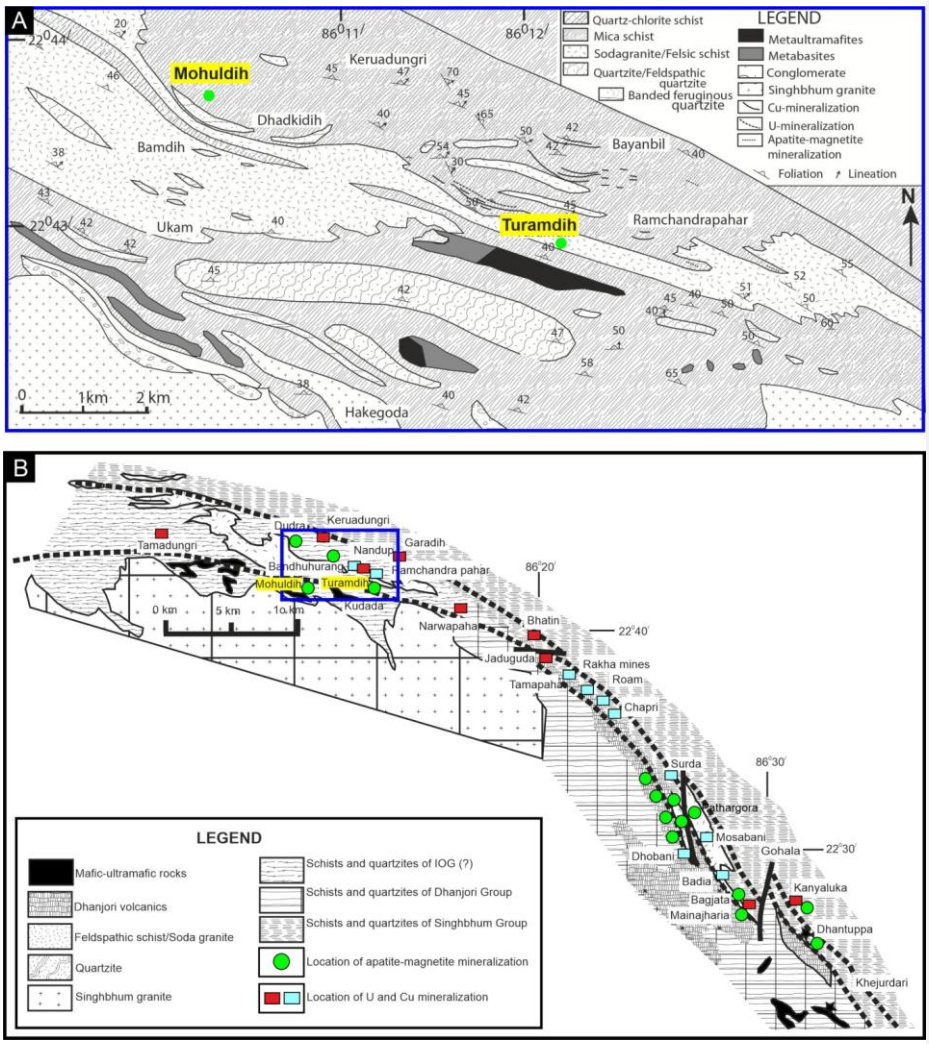

Figure 4.1 Distribution of lithologicunits in and around Turamdih and Mohuldih area

The major lithologic units are shown in (A). The blue coloured box in the figure (B) showing the location of Turamdih and Mohuldih area in the western part of the SSZ which has been magnified in the figure above (A). Note the occurrence of Banded magnetite quartzite in (A) in Turamdih and Mohuldih.

4.2. Local Geology and host rock of magnetite

4.2.1 Local Geology

The Turamdih and Mohuldih areas are located on the northern fringe of the Archaean western Iron Ore Basin whereas Bagjata and Pathargora (discussed in earlier chapters) are spatially associated with Proterozoic Dhanjori Basin as per published map. (Fig. 4.1).The rock types in and around the Mohuldih U mine and Turamdih areas are roughly similar. The rocks exposed in and around Turamdih-Mohuldih, from north to south, are represented mainly by mica schist, chlorite schist, feldspathic schist/soda granite and Singhbhum granite. Impersistent bands of quartzite and conglomerate occur within the chlorite schist. Small outcrops of meta-ultramafic/meta-mafic rocks are also seen within the chlorite schist. The mica schist that crops out on the north of the study area is composed predominantly of muscovite and quartz with subordinate chlorite and common garnet porphyroblasts. This rock is interpreted to belong to the Singhbhum Group. The chlorite schist is composed predominantly of chlorite, quartz, muscovite/sericite and variable proportion of apatite and magnetite. The feldspathic schist is composed predominantly of quartz and albite with subordinate chlorite, sericite, and biotite. Discontinuous bands of quartzite are commonly ferruginous with alternating bands of quartz and magnetite. The lithological assemblage dominated by chlorite schist has been interpreted to be matasomatized/metamorphosed products of mafic igneous rocks and likely belong to the Iron Ore Group (Pal et al., 2009).

In both Turamdih and Mohuldih the main host of U-Cu mineralization is quartz-chlorite-sericite schist (Pal et al., 2009) but in case of Mohuldih sparse U mineralization is also hosted in banded quartzite in the footwall lode (Patel et al., 2021). Magnetite samples from Mohuldih are collected from the underground mine whereas in case of Turamdih, samples are collected from surface exposure outside the mine. Magnetite-apatite occurrences in these two areas found in various ore assemblages including the U-Cu mineralization

hosting quartz-chlorite schists and banded quartzite but in the present chapter the occurrence of magnetite in banded and variably deformed quartzite rock unit is described (Fig. 4.2).

4.2.2 Host rock of magnetite

As described in the previous section (section 4.2.1) magnetite occurs in various lithologies in Turamdih and in Mohuldih area, but the focus of this chapter is on the magnetite hosted in the banded magnetite quartzite.

The rock is banded to thinly laminated to nearly massive. The banded magnetite-quartzite units are characterized by pervasive alternate bands of light and dark coloured units (Fig 4.2A). The light-colored bands are composed predominantly of quartz and the dark-colored bands are composed mainly of magnetite. The quartzite unit is weakly magnetic to non-magnetic. It has been noted in the field as well as during hand specimen study that the thickness of these alternating dark vs. light-coloured bands is highly variable with the dark bands rarely exceeding the thickness of more than a centimeter. The rock is highly folded and quartz veins often cross-cut the bands (Fig. 4.2B-C). Displacement of these bands along the veins is common. The quartz veins often show pinch and swell structure. Considering the Fe-rich nature and the presence of alternating Si- rich and Fe-rich bands/laminae Sarkar (1984) termed this rock as "*Banded ferruginous quartzite*", deviant from the typical Banded Iron Formation (*sensu stricto*).

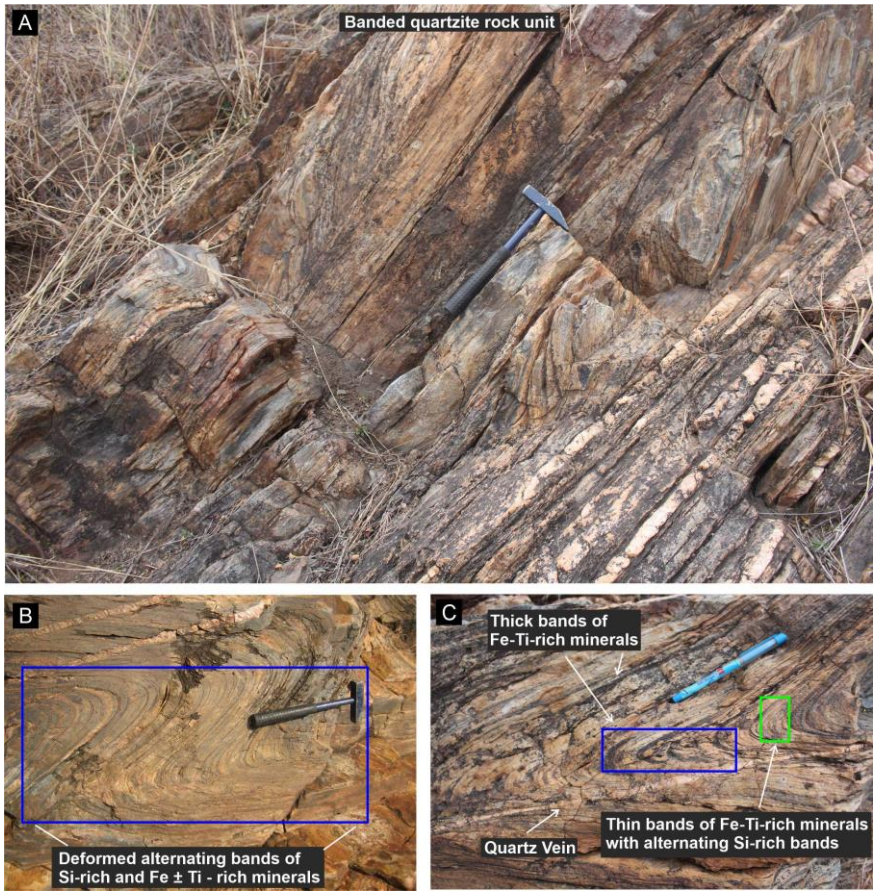

Figure 4.2 Field photographs of the banded magnetite quartzite unit

Alternating dark and light coloured bands in the banded magnetite quartzite from Turamdih area (A-C). Note the folded nature of the bands and the variations in thickness of the bands (B-C) with quartz vein cross-cutting the banded unit (C).

4.3. Analytical Conditions

The polished thin sections of the magnetite samples were examined thoroughly using optical microscope followed by Scanning Electron Microscope. A JEOL JSM 6490 scanning electron microscope was used to generate backscattered electrons images and to select spots for EPMA and LA-ICPMS analysis free of any visible inclusion phase which can perturb the

geochemical data. Magnetite samples are observed to be variably hematitized in both the samples collected from the Turamdih area and Mohuldih U deposit. Grains that show only slight to moderate martitization may be easily analyzed with the small EMPMA beam size (<2 μm). Laser ablation ICP-MS on the other hand, with considerably larger analytical spot sizes (commonly >10 μm), can be adversely affected by martite and ilmenite in magnetite. However, data collected in the present study demonstrate that magnetite with a low degree of martitization (< 10% of the grain surface) will not negatively affect LA-ICP-MS analyses To avoid the influence in trace element analysis when the samples are ablated by ICPMS, core of the magnetite samples are chosen. This hematitization has no relation with the ore-forming event/events described here and will not be discussed further. The analytical protocol used to get the major element composition of magnetite and apatite in EPMA and the trace element composition by LAICPMS are similar to what have been used in Chapter 3. The mMajor and trace element composition of magnetite is given in Table 17 and the major element composition and concentrations of V of associated apatite is given in Table 18.

4.4. Results

4.4.1 Petrography:

Although there is no visible difference in field and in hand specimen, petrographic observations suggest that Magnetite in Turamdih (Association T) and Mohuldih (Association M) is different with respect to associated Fe-Ti oxide phases and described in two different sections.

4.4.1.1 Petrography: Samples from Turamdih (association T)

The studied rocks are composed predominantly of quartz with variable proportions of Fe-Ti-oxide minerals and other silicate minerals such as chlorite and biotite. The most common Fe-

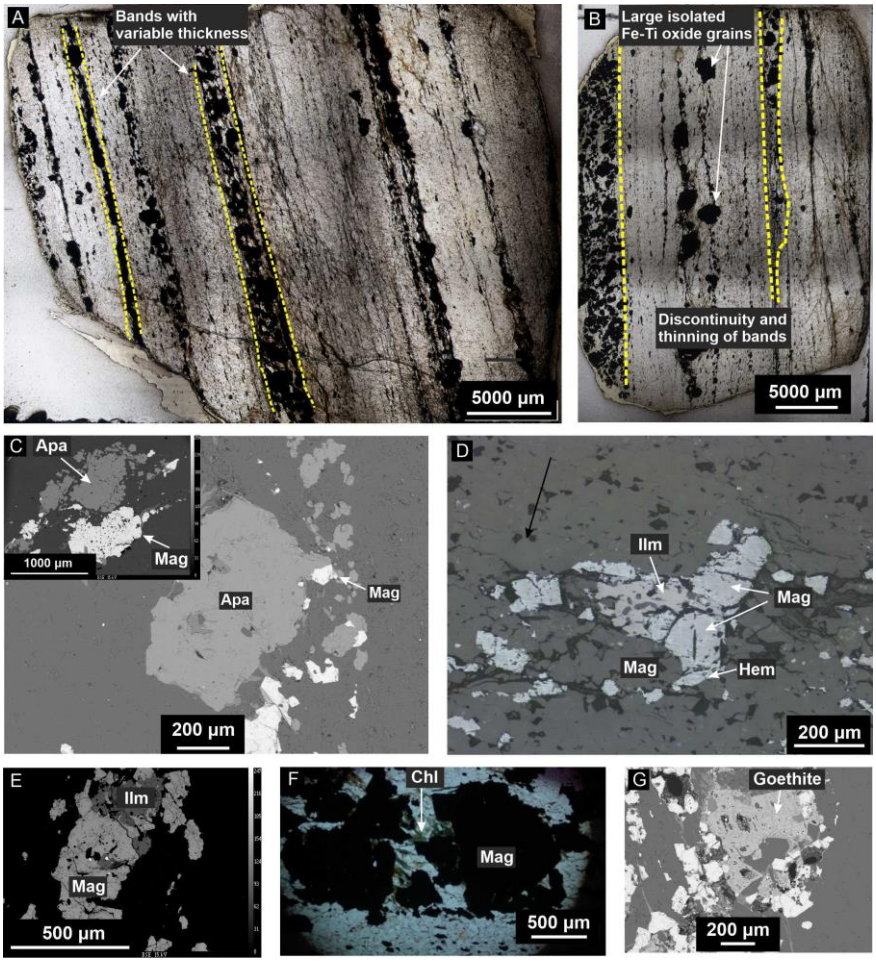

Figure 4.3 Mode of occurrence of magnetite and associated mineralogy in association T

Plane polarized light (A-B and F), backscattered electrons images (C, E, G and inset of C), reflected light (D) photomicrographs showing the magnetite from the banded quartzite rocks of Turamdih and the textural relation with associated apatite and ilmenite. Note the variable thickness (A) and discontinuation of the banded structure (B). Magnetite is showing sharp grain boundary contact with apatite (C and inset of C). Also note the presence of chlorite (F) associated with magnetite in the assemblage and presence of goethite (G).

Ti-oxide minerals are magnetite and ilmenite. The dark-coloured micro-bands is dominated by the presence of magnetite ± ilmenite ± apatite in Turamdih. Variations in band thickness

have been observed between the bands and also within the stretch of a single band in thin section scale (Fig. 4.3A). Also the bands are not always continuous. Often the ingredient minerals popbulge out (Fig. 4.3B) from the non-linear stretches of different bands. Bifurcations Splitting of the bands have been observed. Ilmenite is commonly closely associated with magnetite and when magnetite-apatite and magnetite-ilmenite occur together, they share straight boundary contact or one mineral is partly included in the other (Fig. 4.3C-D). Magnetite and ilmenite also show intergrowth texture where angular magnetite is interwoven with ilmenite (Fig. 4.3D-E). Abundant patchy ilmenite is also seen within magnetite. The size of the isolated magnetite grains often exceeds >1000 μm (Fig.4.3B and inset of C). Magnetite grains are variably hemaetitized along grain boundaries and crystallographic planes (Fig. 4.3D). Fe-hydroxide such as goethite usually occurs in micro-fractures in the silicate matrix and in magnetite, as irregular patches and partly replacing and overgrowing magnetite (Fig. 4.3G).Poorly developed foliation, defined by chamositic chlorite generally warps around the coarse grains of Fe ± Ti oxides (Fig. 4.3F).

4.4.1.2 Petrography: Samples from Mohuldih

The Mohuldih samples are similar in containing the alternating Si-rich vs. Fe ± Ti rich layers (Fig. 4.4A-B). But the dark-coloured micro-bands are mainly composed of magnetite ± rutile ± apatite (Fig. 4.4D) instead of ilmenite which is commonly observed in case of Turamdih samples. The bands in some of the Mohuldih samples are found to be poorly ill-formed. Allanite patches at high angle with the bands are seen at places (Fig. 4.4B and G). Magnetite also occurs as disseminated grains in the quartz-rich matrix. Extreme variations in grain size are common for both magnetite and apatite (Fig. 4.4D-F). The smaller grains of magnetite and apatite are generally elongated or directed along the band or direction of foliation, however the large anhedral grains of magnetite and apatite are not always so, and at

some places apatite grains contain monazite-xenotime inclusions (Fig. 4.4 C-D and F). Some

Magnetite also occurs as disseminated grains in the quartz-rich matrix. Extreme variations in

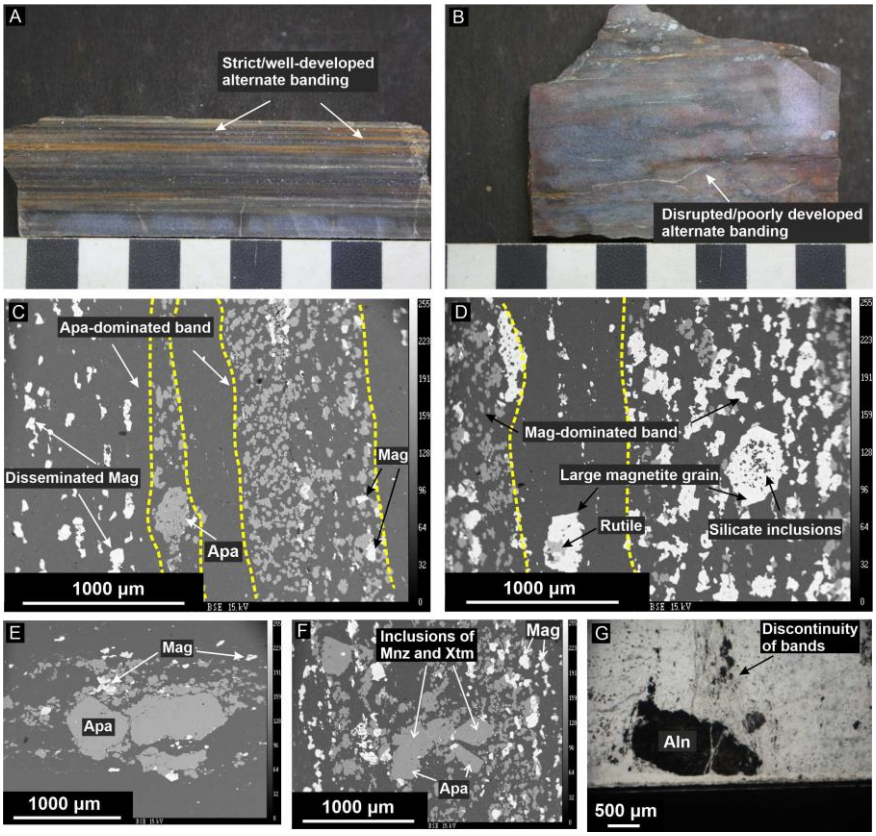

Figure 4.4 Mode of occurrence of magnetite in Association M

Hand specimen photographs (A-B), backscattered electrons images (C-F) and plane polarized light (G) ~~micro~~photomicrographs of magnetite samples from Mohuldih U deposit. Bands are variably enriched in magnetite and apatite (C-D) and disruption in the alternating banded structure (B) vs. well-developed bands (A). Note the presence of rutile (D) with magnetite in this assemblage. Apatite grains often contain inclusions of monazite and xenotime (F) and at places devoid of the inclusions (E). Presence of allanite has been observed in this association (G).

grain size are common for both magnetite and apatite (Fig. 4.4D-F). The smaller grains of magnetite and apatite are generally elongated or directed along the band or direction of foliation, however the large anhedral grains of magnetite and apatite are not always so, and at some places apatite grains contain monazite-xenotime inclusions (Fig. 4.4 C-D and F). Sharp mutual boundaries between magnetite-apatite and rutile are present (Fig. 4.4D and F). Some of the bands are largely composed of apatite whereas magnetite dominated bands and the presence of disseminated magnetite in the groundmass has also been observed (Fig. 4.4C-D).

4.4.2 Geochemistry

4.4.2.1 Composition of magnetite

The magnetite samples from Turamdih area (association T) have higher concentrations of Vanadium (average V in association T – 4342 ppm vs. average V in association M magnetite – 2125 ppm)~~,~~ ~~)~~ whereas the magnetite samples from the Mohuldih U deposit are enriched in Cr (average Cr in association T magnetite – 54 ppm vs. average Cr in association M magnetite – 436 ppm)) and the variations in concentrations of other important spinel elements have been shown in the Box and W~~w~~hisker diagram in Fig. 4.5A-B). Concentrations of Ti is slightly higher in association T magnetite than the association M magnetite (average Ti in association T magnetite – 181 ppm vs. average Ti in association M magnetite – 173 ppm). Concentration of U is higher in Mohuldih magnetite samples which were~~are~~ collected from the underground U mine than the magnetite samples of Turamdih (average U in association M magnetite ≈ 5 ppm vs. average U in association T magnetite ≈ 1 ppm).

4.4.2.2 Composition of apatite

The major element composition of apatite associated with the magnetite of Turamdih and Mohuldih is almost similar. The average concentration of Ca and P in apatite samples

from Turamdih is 40.18 ~~wt%~~ and 18.55 wt%, whereas in case of Mohuldih U deposit the average concentrations of Ca and P is 40.24 and 18.33 wt% respectively (Table 18). There are significant differences in trace elements of apatite between Turamdih and Mohuldih and Vanadium is one such element with the average concentrations of 1.66 ppm for apatite of Turamdih vs. 7.44 ppm in case of apatite from Mohuldih.

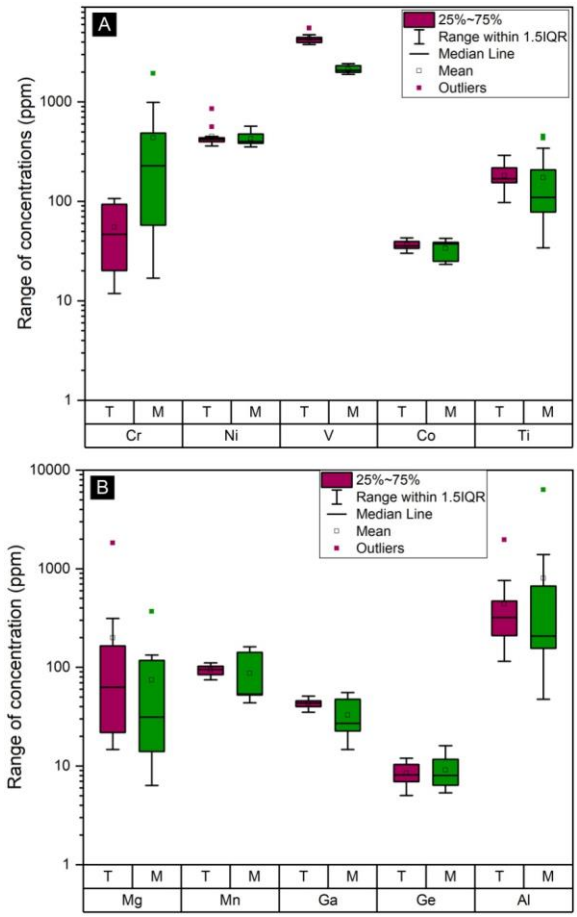

Figure 4.5 Compositional variations between magnetite samples from Association T vs. M

Multi-element Box and Whisker plots are showing concentrations of various trace elements in magnetite from Turamdih and Mohuldih U deposit. The boxes outline the 25th to 75th percentiles and whiskers extend to the minimum and maximum values. Line within the box represents the median value, hollow square represents the average value, whereas the solid squares displays the outliers. The colour schemes used in this figure for Association T and M will be followed throughout this chapter.

4.5. Discussion

4.5.1 Physicochemical condition of magnetite formation in Mohuldih and Turamdih

The variations in (Ti + V)/(Al + Mn) ratios have been shown to scale with the temperature of formation between magnetite samples from high T igneous, high T hydrothermal to low T hydrothermal environment (Nadoll et al., 2014). Magnetite samples from Mohuldih and Turamdih both show consistent and very high values (always ≥1) of the ratios of cumulative concentrations of (Ti + V) and (Al + Mn) (Fig. 4.6B), which are comparable to magnetite formed in high T hydrothermal/igneous system (such as Porphyry deposit - Nadoll et al. (2014) and references therein). Also it is important to note that, magnetite samples from Turamdih are characterized by comparatively higher values of this ratio with corresponding higher inter-quartile ranges compared to the samples from Mohuldih. The results from Mg-based thermometry (Canil and Lacourse, 2020) are also consistent with the T trend from the (Ti + V)/(Al + Mn) ratios with the bulk of the magnetite showing T range of 400°C or close to 400°C (Fig. 4.6A). Magnetites from Turamdih area are also enriched in Ga compared to most of the magnetite from Mohuldih U deposit with some of the magnetite samples from Mohuldih shows similarity in concentrations of Ga with magnetite samples from Turamdih (Fig. 4.6C). Concentrations of Vanadium in magnetite (Carew, 2004) and apatite (Mao et al., 2016) scales to fluctuations in fO_2 as have been shown

and used in the previous studies and previous chapter (Chapter 2) of the present thesis work. The consistently higher concentration of Vanadium (average value ≈ 4500 ppm) in magnetite samples from Turamdih in comparison with magnetite samples from Mohuldih (average value ≈ 2000 ppm if considered in conjunction with the increasing concentrations of Vanadium in associated Mohuldih apatite (Fig. 4.6D), implies the formation of Turamdih

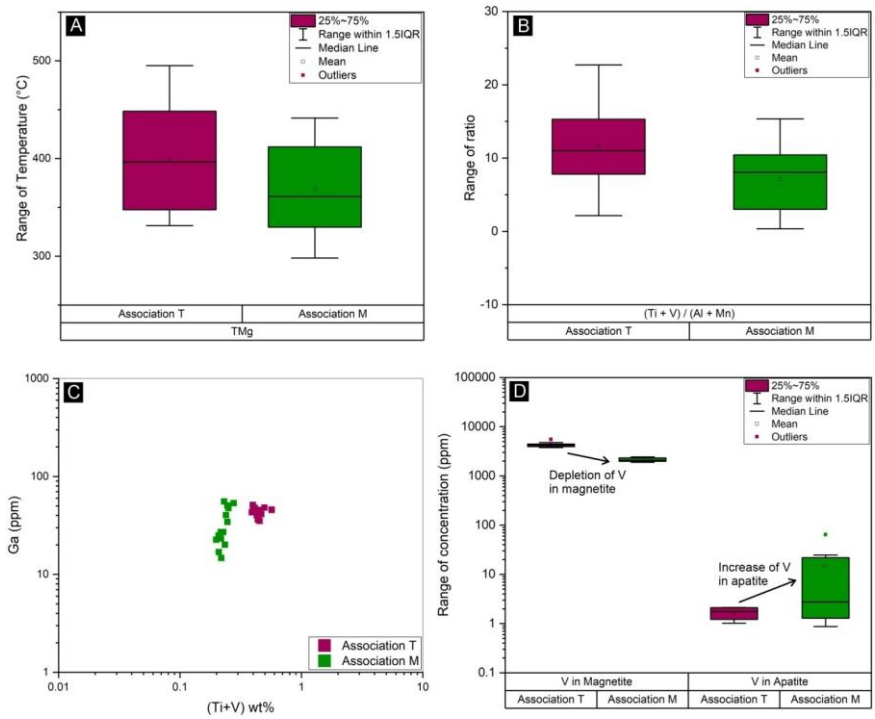

Figure 4.6 Range of formation temperature as a function of concentrations of specific trace elements and by magnetite-based thermometry

Box and Whisker plots (A-B and D) and bivariate plot (C) showing the T range/trend and compositional difference between magnetite and apatite based on Mg in magnetite thermometry (A), Concentrations of (Ti + V) and (Al + Mn) (B); based on concentrations of Ga, Ti and V (C). Temperature range from magnetite thermometry for association T and M (A) are calculated following the method by Canil and Lacourse (2020). The legends for all the diagrams are shown in Fig. C

magnetite in relatively lower fO_2 condition than Mohuldih. The relatively higher fO_2 condition prevailed in case of Mohuldih is also consistent with association of rutile with

magnetite in this association; ~~and~~ the higher values/ranges of Cr in magnetite samples from Mohuldih (Fig. 4.5A), as Cr in +6 state is most mobile and most available and due to a possible reduction from +6 to +3 state get incorporated in magnetite structure (Knipping et al., 2015a, 2015b and references therein).

Based on the concentrations of some critical trace elements which are typically sensitive to fluctuations in physicochemical conditions and the results from the Mg-based thermometry the following inferences can be drawn –

A. Enrichment of T-sensitive trace elements, such as Ti, V, Ga etc. indicates very high formation T (≈ 400°C) for magnetite from both Turamdih and Mohuldih.

B. Despite hosted in the similar banded quartzite unit, there are certain/subtle differences in physicochemical conditions between Turamdih and Mohuldih. The higher concentration of Ti, Ga and particularly Mg concentrations of which are relatively independent of the fO_2 condition and strongly controlled by the prevailing temperature hinting that magnetite samples of Turamdih formed at relatively higher T compared magnetite samples from Mohuldih U deposit. .

C. There is almost no resemblance in the concentrations of the aforementioned T- fO_2sensitive trace elements in magnetite samples from Turamdih and Mohuldih with what typically observed in case of BIF magnetite albeit the textural similarity in occurrence in form of alternating Si-rich and Fe-rich alternating layers. It has been noted by numerous previous studies that magnetite samples from the BIF generally contains extremely less Ti, V, Cr, Ga (≤10 ppm in most of

the cases) (Angerer et al., 2012; Nadoll et al., 2014; Gourcerol et al., 2016; Ghosh and Baidya, 2017), which is opposed to the typical trace element-enriched nature of magnetite of the present study.

4.5.2. Comparison of REE chemistry: Mohuldih-Turamdih vs. BIF

Considering the contrasting composition between magnetite samples of the present study and magnetite samples formed in low T BIF in terms of concentrations of certain specific trace elements in magnetite, the concentrations of REE, which is known to be one of the most robust proxies of depositional environment (Busigny et al., 2013; Gourcerol et al., 2016; Gatsé Ebotehouna et al., 2021; She et al., 2021), are put to the comparison between magnetite samples from banded magnetite quartzite of the present study vs. magnetite from BIF *sensu stricto*. . The REE compositions of magnetites of the present study are compared with BIF samples from the IOG group of rocks in Singhbhum (Ghosh and Baidya, 2017) and from Meliadine and Meadowbank BIF deposits (Canada) (Gourcerol et al., 2016 and references therein). All the magnetites used as proxy for BIF magnetite belong to Algoma-type BIF. The concentrations of REEs were normalized using the latest published values of PAAS (Post Archean Australian Shale) (Pourmand et al., (2012) instead of the most widely used one by Taylor and McLennan (1985), as in the latest published values measured abundance of Tb and Yb were added whereas in the previously published case the values were derived by interpolation between neighbor REEs. Also no significant differences were seen in the REE patterns normalized to PAAS values by Taylor and McLennan (1985) (not included in the chapter) vs. (Pourmand et al., (2012). Therefore, in the present chapter normalization was done using the values given by Pourmand et al., (2012).

The PAAS-normalized REE patterns show broadly similar range of enrichment/depletion of the REEsS for magnetite from Turamdih (association T) and

Mohuldih (association M) and samples from IOG group of rocks (Badampahar deposit and Jashipur deposit – reference in Ghosh and Baidya (2017) with clear differences in Eu anomaly (negative in the Turamdih-Mohuldih magnetite and positive in case of Badampahar and Jashipur), Y anomaly (negative to positive in the Turamdih-Mohuldih magnetite and positive in case of Badampahar and Jashipur) (Fig. 4.7A-C). Additionally, the ∑LREE/∑HREE, Sm/Yb ratios and PAAS-normalized Eu/Eu* values are compared with the BIF samples of Meadowbank and Meliadine deposits with magnetite from Turamdih and Mohuldih. Depletion of LREEs relative to HREEs along with associated positive La, Y and especially Eu anomalies are often cited and accepted as an evidence of precipitation from

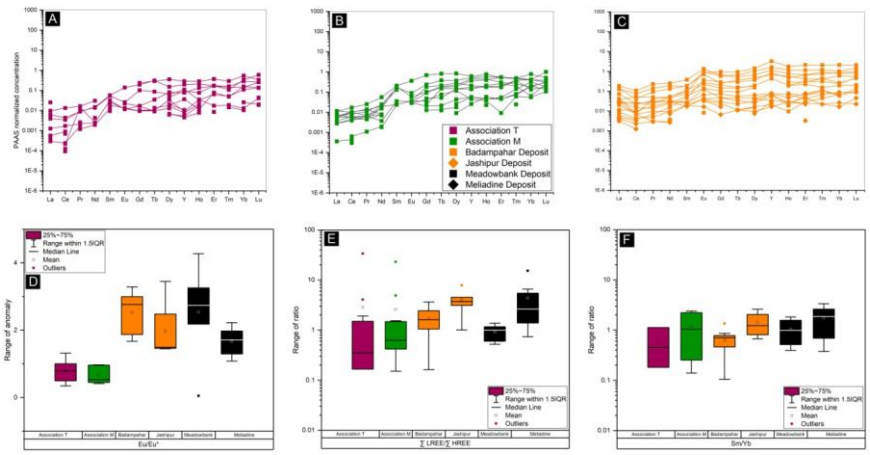

Figure 4.7 Variation in composition of magnetite samples from association T and M vs. BIF

PAAS normalized REE diagrams (A-C) and Box and whisker plots (D-F) for magnetite samples from association T, association M and compiled magnetite geochemical data (Gourcerol et al., 2016; Ghosh and Baidya, 2017). Note the similarity in absolute concentration of REEs (A-C) and the presence of negative Eu anomaly in magnetite samples of the present study (A-B) and positive Eu anomaly in the BIF magnetite (C).

Archean seawater with modifications by moderate T (<250°C) hydrothermal/vent-sourced fluids (Bau and Dulski, 1996; Thurston et al., 2012; Gourcerol et al., 2016). The magnetites from both Mohuldih and Turamdih areas are relatively more depleted in LREE compared to the BIF samples (Fig. 4.7E), but is not associated with positive Eu anomaly with only one of the magnetite samples from Turamdih area showing feeble positive Eu anomaly (Fig. 4.7A-B and D), which is considered to be a benchmark for hydrothermal component in chemical sediments (Cox et al., 2013; Ghosh and Baidya, 2017). Absence of Eu anomaly or decreasing Eu/Eu* often reported in case of low T hydrothermal fluid (Sverjensky, 1984; Danielson et al., 1992; Mcmanus et al., 2002; Alexander et al., 2008), which is perhaps not valid for the present case considering the high temperature of formation and exceptionally high concentrations of specific trace elements like Ti, V, Ga etc. The comparison of Sm/Yb ratios which are often used to measure the proportion of fluid-mixing components between hydrothermal vent fluid and seawater shows consistently lower values than the reference BIF samples and increase in Sm/Yb and Eu/Sm often indicates the involvement of high T fluid (Gatsé Ebotehouna et al., 2021).

To summarize, the magnetite samples of the present study shows some key difference such as absence of Eu anomaly vis à vis some key similarities such as depletion in LREE (even more depleted compared to the reference BIF samples) or overall similar range of absolute concentration of the REEs with the BIF magnetite samples regardless of their diagenetic, later metamorphic or hydrothermal (Gourcerol et al., 2016) histories. However, high concentrations of temperature sensitive elements in the studied samples are in stark contrast to what is commonly observed in BIF.

4.5.3 Atypical chemistry: imprint of high T hydrothermal fluid or later modification?

The T calculated from oxygen isotopic compositions of phosphates in sediments from the 3.2–3.5-billion-year-old Barberton Greenstone Belt in South Africa, shows the Archean ocean T ranges between 26°C to 35°C from highest $\delta^{18}O_P$ values and assuming equilibrium with sea water with $\delta^{18}O_p = 0‰$ (Blake et al., 2010). The magnetite samples from typical BIF may have subtle variations in formation T due to their difference in origin within the realm of BIF-like environment. It is now established from the oxygen isotopic compositions that the earliest magnetite in BIF records the T range between 50°C-100°C and magnetite formed slightly later records the T range of 250°C (Konhauser et al., 2017). Composition of Turamdih and Mohuldih magnetite are somewhat cryptic in this context as discussed in section 4.5.1 and 4.5.2 and as manifested in the mixed signals from the enrichment of key T-sensitive elements and involvement of hydrothermal component from the concentrations of REEs. Based on the established upper threshold concentrations for the suite of typical spinel elements (commonly present at detectable levels in magnetite), the main discriminator elements for magnetite are selected and the elements are Mg, Al, Ti, V, Cr, Mn, Co, Ni, Zn, and Ga where magnetite from BIF is characterized by low Al, Ti, V, Cr, Mn, Co, Ni, Zn, Ga and Sn (Nadoll et al., 2014). On the contrary most of these elements are enriched in magnetite samples of the present study (Fig. 4.5A-B).

4.5.3.1 Imprint of hydrothermal input

Ti/V vs. Mn plot shows that the Mohuldih and Turamdih magnetite plot in close space (Fig. 4.8A) and apart from the reference BIF samples. Using the magnetite from the unaltered and hydrothermally altered magnetite samples Nadoll et al., (2014) stated that a trend of decreasing Mn and decreasing Ti/V ratios can be ascribed to hydrothermally altered samples. Positive Eu anomaly are the hallmark of hydrothermal component in chemically precipitated sediments (Ohmoto et al., 2006; Condie, 2022). However the negative Eu anomaly present in

the magnetite samples of the present study is in contradiction with significant hydrothermal component. Absence of positive Eu anomaly may not indicate the absence of hydrothermal component as hydrothermal plumes may interact with various reservoirs such as basalt ~~basalt~~ (no Eu^*_{CHUR}) and terriginous sediments (negative Eu^*_{CHUR}) that might change the signature (Cox et al., 2013). So, presence of positive Eu anomaly might be indicative of a hydrothermal source, but absence of the anomaly is not sufficient enough to rule out the possibility of the involvement of a hydrothermal source.

The result from the (Ti +V) vs. (Al + Mn) plots with defined T fields (*op cit.)* shows that the magnetite samples from Turamdih and Mohuldih formed at comparatively higher range of T (300~~°C~~-500°C) than the reference BIF samples (Fig. 4.8B) although the bulk of the samples plot outside the defined area. This indicates that despite somewhat similar concentrations of REEs or LREE/HREE depletion pattern, the fluid responsible for magnetite crystallization in Turamdih and Mohuldih are not same as observed in case of BIF magnetite. Fig. 4.8B shows that all of the reference BIF magnetite samples plot in lower T-regime

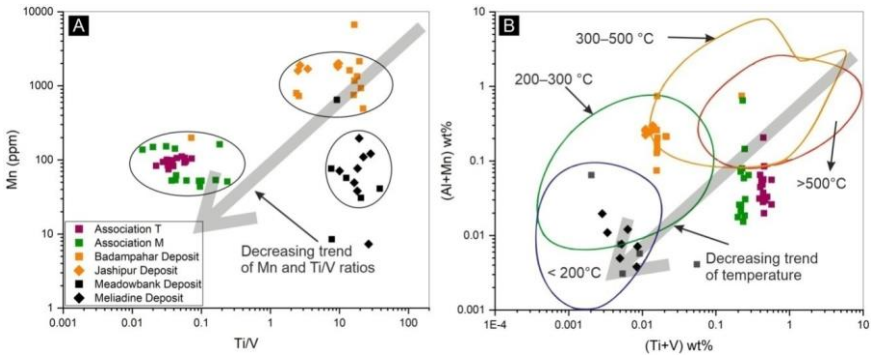

Figure 4. 8 Bivariate plots of Mn vs. Ti/V and (Ti + V) wt% vs. (Al + Mn) wt%

Magnetite samples from Turamdih and Mohuldih are showing lower Mn concentrations and higher (Ti + V) concentrations than the BIF magnetite samples. Note that the BIF magnetites are plotted in lower T field compared to the magnetite samples from association T and M.

(magnetite from Badampahar and Jashipur - 200°C-300°C and magnetite samples from Meliadine and Meadowbank - 200°C-300°C and in <200°C field) consistent with their lower formation T. Although BIF actually formed at much lower T than the fields suggested in this diagram, but the diagram indicates that the T associated with the formation of the magnetite samples from Turamdih and Mohuldih areas are higher compared to the reference BIF samples. The higher formation T as evident from the enrichment of specific trace elements like Ti, V and Ga are also consistent with the petrographic observation where magnetite and ilmenite (Association T– Fig. 4.3D-E) and magnetite and rutile Association M – Fig. 4.4D) have been shown to share grain boundaries reflecting that these minerals crystallized together. Elements like Ti known to have low solubility and therefore immobile in low T fluid, whereas in case of fluids with considerably higher T, Ti becomes mobile (Nadoll et al., 2012).

4.5.3.2 Imprint/element mobility related to metamorphism

The age of the studied magnetite-bearing rocks is not known for sure. If they belong to IOG, the age must be Paleoarchaean and if they belong to Dhanjori volcanics the age must be Paleoproterozoic. Archean and the early Paleoproterozoic BIF are commonly subjected to various grades of metamorphism ranging from 200 °C to 800 °C after diagenesis (Konhauser et al., 2017), therefore the composition of magnetite may get changed due to element mobility or element exchange with associated phases during metamorphism. The Turamdih and Mohuldih U deposit are located within the Singbhum Shear Zone (SSZ) which underwent two different phases of metamorphim (also discussed in the Chapter 1). In Singhbhum Shear Zone, tThe prograde metamorphism accompanied and outlasted the ductile shearing which peaks at the metamorphic temperature-pressure calculated from the garnet-biotite thermometer and the garnet-muscovite-plagioclase-biotite geobarometer respectively were 480 ± 40°C and 6.4 ± 0.4 kbar (Sengupta et al., 2005 and the references therein) in

epidote-amphibolite facies. On the other hand the retrograde metamorphism took place at similar temperature range calculated via garnet-chlorite thermometry (Sengupta et al., 2005). Chloritization of biotite, muscovitization of kyanite are some of the features associated with the retrograde metamorphism and the event postdates the ductile shearing event.

To check the extent of modification, if any, due to element exchange during such metamorphism, the magnetite compositional data of the present study is plotted in the V vs. Cr diagram ~~suggested by~~ (see Lan et al., 2019). In that plot the magnetite composition from the Xuchang and Xincai BIFs which have undergone amphibolite-facies metamorphism snd the Wuyang BIF which has undergone granulite-facies metamorphism with metamorphic temperatures ranging from 650 °C to 810 °C (Lu et al., 2013) is used along with the unmetamorphosed magnetite (Dai 2014) samples from South China as a basic frame of reference (Fig. 4.9.A).

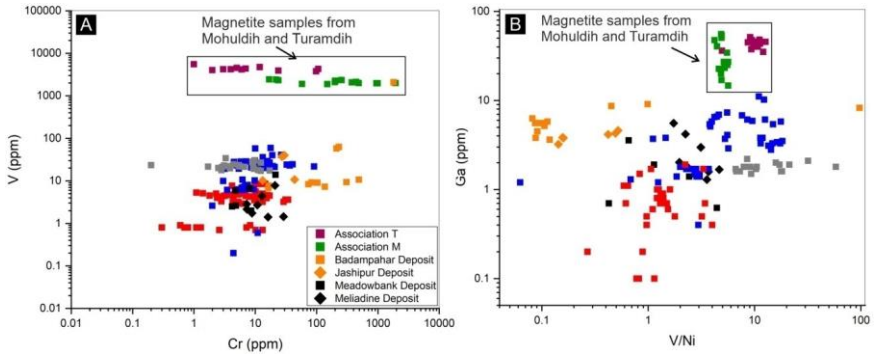

Figure 4.9 Compositional variation between magnetite samples from association T and M vs. metamorphosed/unmetamorphosed BIF magnetite

Bivariate plots of V vs. Cr (A) and Ga vs. V/Ni (B) showing that the magnetite samples from the present study are compositionally distinct from the magnetite samples metamorphosed at various grade and also from the BIF magnetite in terms of V, Cr, Ga and Ni concentrations. (compiled dataset from (Lan et al., 2019)

Magnetite from both Turamdih and Mohuldih plots way apart from the unmetamorphosed magnetite and also from the magnetite samples which are variably metamorphosed (Lan et al., ~~(~~2019). It is also important to note that the reference BIF samples plot either within the clusters of metamorphosed and unmetamorphosed magnetite samples or close to the cluster. From the results of the trace elemental mapping Lan et al. (2019) further showed that the rim of the magnetite grains are enriched in Mg, Mn, Al, Si, Na compared to the grain core and linked that with elemental exchange between magnetite and coexisting mineral phases during metamorphism. Lan et al. (2019) mentioned specifically that elements such as Vanadium, Cr, Co, Ni, Zn and Ga do not change significantly during metamorphism of various grades and can be used as 'genetic discriminator'. The composition of the magnetite samples of the present study are also plotted with the metamorphosed and unmetamorphosed BIF magnetite compositional data compiled by Lan et al. (2019) along with reference BIF magnetite composition, in the V/Ni vs. Ga plot (Fig. 4.9B). Similar results can be observed as that from V vs. Cr plot. All the magnetite samples of the present study have distinguishable V and Ga concentrations. Additionally, this plot to some extent differentiates between the magnetite samples thatwhich are variably metamorphosed, although overlapping concentrations have been observed between metamorphosed and unmetamorphosed samples. These two plots collectively indicate that the enrichment of the specific trace elements, such as V, Cr, Ga, Zn, Ni etc can't be explained through the elemental exchange during metamorphism. Also, the most abundant co-existing phase in the case of magnetite is quartz, which is not known to contain these trace elements in elevated concentrations. Therefore, all the data collectively indicate that the enrichment of trace elements in the studied magnetite that resemble what is commonly observed in case of high T hydrothermal magnetite, were contributed from an external source, most possibly hydrothermal fluids.

4.5.4 Implications of trace-element based discriminators

In order to get further insights into the formation of the magnetite from Turamdih and Mohuldih some the process- identifiers, based on trace element geochemistry of magnetite, are produced. The utility of these elements have already been discussed in the previous chapters and not repeated here.

4.5.4.1 Process type discriminator

Most of the reference samples are plotted either over the magmatic-hydrothermal boundary with the bulk of the Badampahar and Jashipur magnetite plotted in the hydrothermal domain whereas bulk of the Meadowbank and Meliadine magnetite samples are plotted in the domain of magmatic magnetite (Fig. 4.10A). The Turamdih samples are

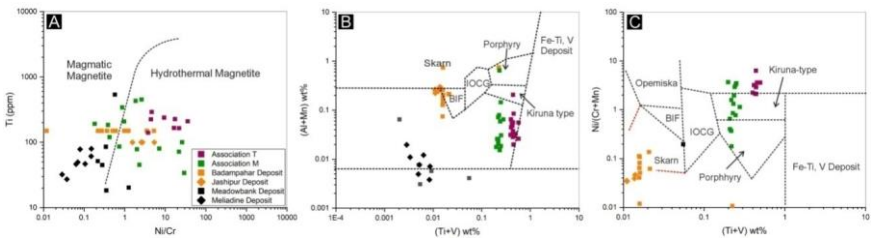

Figure 4.10 Process-type and deposit-type discriminator diagrams based on trace element geochemistry of magnetite

Bivariate plots based on concentrations of Cr, Ni, Ti (A) and Ti, V, Al, Mn (B) and Ti, V, Ni, Cr and Mn (C) to distinguish magmatic magnetite from hydrothermal magnetite (A) showing most of the magnetite samples from association T and M plotted in the hydrothermal field (after Dare et al. (2014); to distinguish deposit-type (B and C) showing magnetite samples from the present study plotted in both Porphyry and Kiruna-type field (C) and in no particular field (B).

restricted to hydrothermal domain but some of the Mohuldih magnetite samples are plotted close to the boundary and some even plotted inside the domain of magmatic magnetite. The plotting of the studied magnetite on the right of BIF field is primarily due to the higher concentration of Ti and V. It likely indicates that the fluid involved in the formation of the magnetites leached Ti and V from mafic protolith. The availability of high Ti in the fluid

during magnetite crystallization is evident from the ubiquitous presence of ilmenite/rutile in association with magnetite Although the Algoma--type BIF used in the present study as reference do not plot invariably in the hydrothermal field, which would have been consistent with the genesis, there are reports that this Ti vs. Ni/Cr plot can effectively identify the underlying formation process for Algoma-type BIF in case of other Archean metamorphosed sedimentary rocks (Duparc et al., 2016).

4.5.4.2: Deposit-type discriminator

In the present study the petrographic and field-based observations seemed to poorly correlate with the magnetite chemistry reflective of high T formation environment. Although most of the previous studies based on magnetite samples do not use (Ti + V) vs. (Al + Mn) plot (Duparc et al., 2016; Gourcerol et al., 2016), instead utilized the (Ti + V) vs. Ni/(Cr + Mn) plot, both these diagrams are used for the magnetite samples from Turamdih and Mohuldih along with our reference BIF samples to decipher possible deposit type (Fig. 4.10B-C). The Turamdih and Mohuldih magnetite in both these diagrams plot either within the Kiruna-field/Porphyry Field/outside of the designated areas for different types of deposits. The high T chemistry of Mohuldih and Turamdih is probably responsible for the unexplainable closeness to these deposit types. The reference samples also do not fall in the designated areas for the BIF deposits, rather fall closely to Skarn-field in both of these deposit-type identifiers. As the magnetite from Algoma-type BIF do not correspond to either magmatic/hydrothermal sources, but rather incorporates various degrees of interactions between seawater and hydrothermal vent fluids and these diagrams are ideally based on temperature gradient. Gourcerol et al., (2016) mentioned the chemical space for BIF in the (Ti + V) vs. Ni/(Cr + Mn) diagram as 'controversial' and suggested to extends the diagram to more lower values of (Ti + V) and Ni/(Cr + Mn). In fact the reference BIF samples fall in the extended BIF suggested by Gourcerol et al., (2016) (Fig. 4.10.B). Gatsé Ebotehouna et al.

(2021), based on the studied magnetite samples from Nabeba high-grade iron deposit (Republic of the Congo) hosted in banded iron formation (BIF) in the Ivindo Basement Complex suggested to extend the BIF field again to lesser values of (Ti + V) and Ni/(Cr + Mn). The results which seemed significant in the context is that although the origin is inconclusive based on the discriminators, the Turamdih and Mohuldih magnetite are remarkably different, in terms of composition, from both metamorphosed and un-metamorphosed BIF-hosted magnetite reported from different parts of the globe.

4.6. Concluding Remarks

The present study based on magnetite samples hosted in banded quartzite/ "fFerruginous quartzite" unit from Mohuldih U mine and Turamdih area indicates that mode of occurrence and textural criterions can often be illusive if not integrated with geochemistry. Magnetite associated with ilmenite ± apatite at Turamdih and magnetite associated with apatite ± rutile at Mohuldih occur in rock characterized by alternating dark and light coloured Fe-rich and Si-rich bands having the appearance similar to BIF or sedimentary iron formations, but is chemically distinct. Alternating Si-rich and Fe-rich bands as seen in banded iron formation are often considered to be the *prima facie* evidence of chemical or biochemical sedimentation. However, the geochemical characterization of magnetite and in this study highlights that presence of alternating silica and iron-rich banding may not unequivocally indicate formation via chemical/biochemical sedimentary process, which has widely been used as a proxy for ancient sea-water chemistry and periodic changes therein due to change in feedback of climate-ocean interactions over time. Although the present state of the work is not conclusive about the origin of magnetite in banded quartzite samples but it is important to note that the key transition and post transition elements (V, Ni, Ga) in magnetite structure thatwhich remain relatively unaffected during post-depositional changes (Huang

and Beaudoin, 2019, 2021) and chondrite-normalized REE pattern show no/minor resemblance with BIF-hosted magnetite samples reported from the Iron Ore Group from eastern India (Ghosh and Baidya, 2017) and with magnetite samples collected from typical BIF from Canada (Gourcerol et al., 2016). It is possible that the magnetite-rich bands formed in localized environment with significant input from hot hydrothermal vents. In this regard it is also need to be mentioned that the debate surrounding the formation of alternate banding about whether it is a depositional feature reflecting precipitation from different water masses or whether it has formed from an initially homogeneous Fe-Si precipitate during diagenesis or metamorphism is not resolved yet. Some author suggested the banding to be a primary depositional feature supported by the results from the short-lived ^{182}Hf-^{182}W radiogenic isotope system, which revealed a systematic difference between the μ182W values of magnetite and metachert bands in BIF samples from Temagami (Bau et al., 2022), while some other opposed that notion (Rasmussen et al., 2014). Also the rhythmic and alternating Fe- and Si-rich banding via metasomatism or oxidation and mobility of Fe during metamorphism has been proposed to generate rocks having similar appearance as that of BIF and is described as 'pseudo-BIF' in recent studies (Hinsberg and Szilas, 2021). However in the present study we can state that perhaps the metals were derived from mafic protolith via hydrothermal/metamorphic fluid-induced processes during the formation of magnetite without getting into the debate regarding the formation of the alternating bands considering the mineralogy of the Fe-rich band in case of Turamdih and Mohuldih being dominated by magnetite-ilmenite/magnetite-rutile.

Chapter 5: Summary

5.1 Magnetite in magnetite ± apatite mineralization in Singhbhum Shear Zone (SSZ)

The present study describes magnetite ± apatite mineralization in the Singhbhum Shear Zone spanning two locations from the eastern part of the shear zone (Bagjata and Pathargora), and two locations from the western part (Mohuldih and Turamdih). Multiple styles/types of mineralization are noted. Field-based study coupled with geochemistry and petrographic observations demonstrate close juxtaposition of magmatic magnetite and hydrothermal magnetite + apatite mineralization in Pathargora, hosted in albite schist. In Bagjata U deposit, magnetite is hosted in biotite schist, chlorite schist and apatite-magnetite brecciated rocks. In each of the cases, the rocks hosting magnetite mineralization are subjected to extensive hydrothermal alterations/superimposed multiple stages of hydrothermal alterations. Magnetite is classified on the basis of the associated hydrothermal alteration assemblages. Magnetite in magnetite-apatite rich brecciated rock is interpreted to be the product of Ca-Fe ± K alterations. Magnetite associated with uraninite-biotite and allanite-biotite is interpreted as the products of fertile (U-mineralization) K-Fe alteration and K-Fe ± LREE alteration whereas the magnetite associated with chlorite and uraninite is the product of hydrolytic/H^+ alteration. Magnetites in the western sector (Turamdih and Mohuldih), hosted in banded quartzite unit and texturally being similar to magnetite hosted in BIF rocks, are apparently different from the magnetite in Pathargora and Bagjata in the eastern sector. In both Pathargora and Bagjata, the magnetite occurring in veins and pocket with extreme variations in grain size and their restricted occurrence within the veins bear the evidence of their formation by hydrothermal ore-forming processes. On the other hand, in Mohuldih and Turamdih the occurrence of magnetite in Fe-rich bands with alternating Si-rich layer is akin to sedimentary magnetite but the geochemistry of magnetite defies such an interpretation.

Multiple-proxy based approaches are adopted to estimate the temperature of magnetite mineralization in the studied areas as temperature is one of the important criterions to decipher the process of formation (viz. sedimentary vs. hydrothermal vs. magmatic). Concentrations of T-sensitive trace elements in magnetite are compared with the results of Mg-in-magnetite thermometry along with the Ti-in-biotite thermometry and chlorite thermometry based on empirical/semi-empirical equations or thermodynamic modeling (wherever applicable). The present study makes use of some selected trace elements with higher partition coefficient/affinity for magnetite commonly known as 'spinel elements'. In Bagjata, the thermometric measurements, elemental concentrations and selected elemental ratios in conjunction with diagrams with defined T-field indicate that the temperature decreases from Ca-Fe ± K alteration to K-Fe ± LREE to hydrolytic alterations for the magnetite-bearing assemblages. The temperature ranges obtained for Ca-Fe ± K (biotite thermometry: ≈ 450°C and magnetite thermometry ~ 410°C), K-Fe ± LREE (biotite thermometry: ~ 440°C and magnetite thermometry: ~ 420°C), fertile K-Fe alteration (biotite thermometry: ≈ 500°C and magnetite thermometry: ≈ 350°C) and fertile hydrolytic alterations (chlorite thermometry: 310 - 370 °C - average T range provided by different chlorite thermometers and magnetite thermometry: ≈ 330°C) are in crude convergence with typical enrichment of T-sensitive elements such as V, Ga in case of magnetite associated with Ca-Fe ± K and K-Fe ± LREE alteration assemblage. This enrichment pattern is also reflected in high V/Ni ratios and Ga concentration of magnetite of these respective associations (Fig. 5.1 B) barring the exception of magnetite from K-Fe alteration associated with uraninite. The magmatic magnetite of Pathargora was subjected to oxy-exsolution and therefore, yields lower T range in Mg-based thermometry owing to the post-crystallization of original magmatic composition, the details are discussed in Chapter 3. However, the T range for hydrothermal magnetite in magnetite + apatite veins from the same area formed at ~ 450°C

(biotite thermometry: ranges between 390°C - 458°C with the average ≈ 416°C and magnetite thermometry: average T_{Mg} is ≈ 500°C with the median value close to ≈ 450°C). The magnetite in the banded magnetite quartzite from Turamdih and Mohuldih U deposits yields significantly higher T range than the magnetite formed in low T sedimentary environment and thus challenges sedimentary origin inferred from mode of occurrence bearing similarity with typical Banded Iron Formation.

In Chapter 3 it has been shown that the fluid which is responsible for magnetite mineralization in veins/pockets (in Pathargora) was rich in F^- ion and REEs as evident from the composition of magnetite and associated fluorapatite and decoupled behaviour of Y and Ho. In addition to this, the reducing nature of the ore-forming fluid has been suggested based on typical/restricted values of Eu/Eu* and Ce/Ce* and enrichment/depletion of redox-sensitive trace elements such asV and Sn using corresponding composition in magnetite and apatite. In case of Bagjata, the ore-forming fluid related to magnetite without uraninite(association I and II) and magnetite associated with uraninite (association III and IV) vary in nature as envisaged from the corresponding magnetite composition from the respective associations by their distinct difference in Ni/Co ratios, difference in vanadium content.For U-barren vs. U-fertile assemblage, it has been noted in the present study that the concentration of elements either of restricted valence state (Mg) or of variable valence state (Mn) which can be incorporated in magnetite structure substituting Fe^{2+} in reduced condition are generally higher in barren assemblage suggesting the corresponding fluid is reducing in nature than the U-mineralizing fluid not precluding the effect of redox condition. The higher content of vanadium in U-barren assemblage than U-fertile assemblages further validated that the Ca-Fe and K-Fe ± LREE alteration (association I and association II) formed at relatively lower fO_2 condition than magnetite of fertile hydrolytic/K-Fe type of alteration. In chapter 4, the relative variance in fO_2 between Turamdih and Mohuldih has been interpreted based on

the concentrations of redox-sensitive elements and also by the difference in associated mineralogy. Lower concentrations of elements which get incorporated in magnetite preferentially in low fO_2 condition is lower in case of magnetite from Mohuldih U deposit and is in accord with the association being characterized by the presence of rutile instead of ilmenite which is noted in Turamdih .

5.2 Geochemistry of magnetite: implications for trace element-based discriminations

5.2.1 Trace element based discrimination

The present study deciphers the ore-forming process in most of the cases primarily from the field observations and petrographic study. As in case of magnetite from the Bagjata U deposit, the interpretation about the nature of the ore forming process responsible for magnetite mineralization is drawn based on multiple lines of evidences: A. The rocks hosting the magnetite mineralization in the Bagjata deposit are extensively hydrothermally altered. The biotite schist and chlorite schist which host magnetite mineralization both in U-bearing ore zone and non-ore zone are known to be the products of hydrothermal alteration of Dhanjori volcanic rocks (Sarkar, 1984; Pal et al., 2011). B. Occurrence of magnetite which shows extreme variation in size and invariably formed inside the veins with accompanying hydrothermal phase such as biotite and chlorite. C. The bulk rock geochemistry plotted in the alteration index diagram (Montreuil et al., 2013; Corriveau et al., 2016) further justifies the involvement of hydrothermal process in the magnetite mineralization. Similarly in case of Pathargora the magnetite which formed by the hydrothermal process are identified on the basis of their mode of occurrence and associated mineralogical assemblages by field-based and microscopic study. The magmatic magnetites are discriminated from the hydrothermal variety through petrographic observations of mineralogy dominated by magnetite and ilmenite and the occurrence of various complex magnetite-ilmenite intergrowths formed by

the well-known subsolidus oxy-exsolution process. However, the results of Ti vs. Ni/Cr discriminator, suggested to differentiate between hydrothermal and magmatic process (Dare et al., 2014), do not yield consistent results in all the cases. It has been noted in the present study that in case of hydrothermal magnetite samples, the suggested discriminator identifies the process aptly both in case of hydrothermal magnetite samples from Pathargora and in case of Bagjata U deposit. The reason behind this might be the comparatively broad space designated for the hydrothermal variety than the restricted areas for magmatic magnetite. Field-based knowledge and petrographic characterization although seems necessary and sufficient to have preliminary ideas about the ore-forming processes and works in case of Pathargora and Bagjata, seems inadequate to give conclusive/all-inclusive insights about the magnetites from the banded magnetite quartzite in case of Turamdih and Mohuldih. Ti vs. Ni/Cr diagram do not designate any space for magnetite formed by syn-sedimentary process but the banded magnetite samples plot in the zone designated for 'hydrothermal magnetite' samples probably because of the involvement of hydrothermal fluid during the formation of those magnetite as discussed in chapter 4. The present study suggests that the identification of the underlying physicochemical process using identification diagrams certainly provides meaningful insights as we have observed in case of hydrothermal magnetites of Bagjata and Pathargora (chapter 2 and chapter 3), but if not correlated with the textural studies can lead to improper identification as basic/as trivial the suggestion of coupling petrographic and geochemical knowledge may sound and as have been shown in case of magmatic magnetite in chapter 3.

Discrimination of magnetite from different types of deposit namely iron oxide-copper-gold (IOCG), Kiruna apatite– magnetite, banded iron formation (BIF), porphyry, skarn, Fe-Ti, V deposits (reviewed in Chapter 1) depends necessarily on assuming that the compositional trend of magnetite remains unique and restricted to each of the deposit-types.

However, the generalization about the compositional trend and its specificity to each deposit variants broadly seems valid but the fields drawn for each deposit types in the discriminator suggested by (Dupuis and Beaudoin, 2011) were based on the dataset for different types of deposit-incorporated in the diagram when the diagram has been proposed. Later, it has been noted that magnetites from Kiruna-type deposits (Knipping et al., 2015b; Broughm et al., 2017) plot in the Porphyry field, IOCG-deposit field, and beyond any specified area and there were suggestions (by the referred authors) of removing the 'Kiruna-Field' from the discriminator or modifications of the designated space. In the Bagjata U deposits magnetite is associated with Ca-Fe ± K (association I), K-Fe (association II & III) and H^+ metasomatism (association IV) akin to IOCG-style alteration. However, magnetite samples mostly plot beyond the IOCG field except some of the association IV magnetite in the (Ti + V) vs. (Al + Mn) plot (Fig. 2.13A). In case of Pathargora the effect of exsolution changed the composition otherwise the diagram would have worked. In the banded magnetite quartzite, the magnetite are plotted away from the BIF field because of the higher Ti and V content which is not common for the low-T sedimentary environment. Also, in the present work, it is noted that the reference BIF magnetite plot away from the BIF-field. Some authors (Gourcerol et al., 2016; Gatsé Ebotehouna et al., 2021) recommended that BIF field needs to be expanded in that diagram. Importantly, the magnetites from Turamdih and Mohuldih have much higher trace element concentrations proposed in the diagram and compared to the magnetites from the reference BIF samples. The present study recommends that using trace element geochemistry of magnetite without considering other relevant criterions may lead to improper identification of the deposit-types as envisaged from the results of the present study and the literatures.

Apart from using magnetite geochemistry in identifying the formation process/ deposit-type affiliation by the existing discriminators from the recent literatures, the present

study also tested the possibility of using magnetite geochemistry as a tracer for critical metal (U-REE) mineralization. The V/Ni vs. Ni/Ga plot which is suggested to differentiate magnetite samples from IOA and IOCG deposits and also discriminate between HT Ca-Fe and HT K-Fe alteration associated magnetite, separate the magnetite samples associated with uraninite from the magnetite samples where uraninite is absent in the assemblage in case of Bagjata U deposit (Fig. 2.15B). Additionally, the same holds true for biotite as well (Fig. 2.15E). It was however, not possible to test whether the 'high Ni/Ga and low V/Ni' (observed in case both biotite and magnetite from the U-ore-bearing assemblages) criterion is valid for other U-REE bearing IOCG deposits due to lack of U-ore related magnetite compositional data in literature.

5.2.2 Importance of some critical elements in discrimination

The present study in all of the chapters utilizes the Ti vs. Ni/Cr and the (Ti + V) wt% vs. (Al + Mn) wt% diagram to decipher the origin/deposit-type affinity for magnetite from the SSZ. It has also been noted that concentrations of some selected trace elements such as Vanadium, Ga, Ni, Co etc. shows characteristic values with respect to the specific mineralogical association the magnetite belongs to. It should be noted that that the discrimination plot suggested in this work to separate magnetite from IOA and IOCG deposits, magnetite associated with HT K-Fe alteration vs. magnetite from HT Ca-Fe

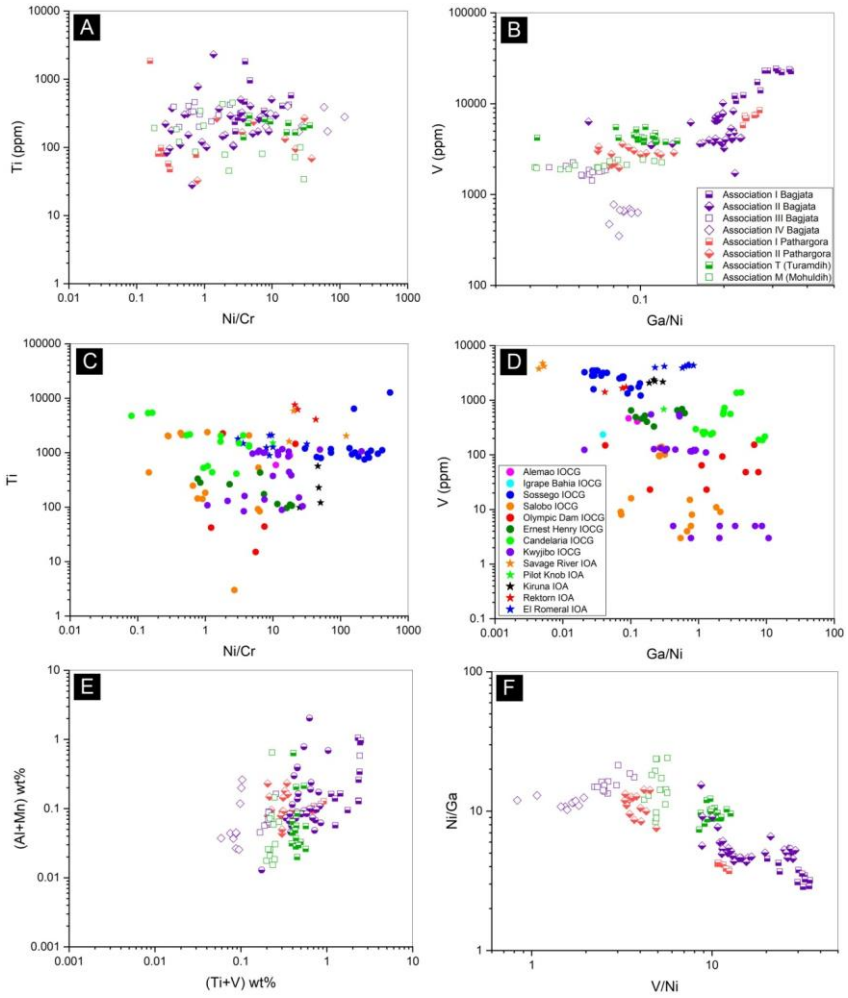

Figure 5.1 Bivariate plots of magnetite composition of the present study and magnetite from IOA and IOCG deposits

Bivariate plots of Ti vs. Ni/Cr (A and C), V vs. Ga/Ni (B and D), (Ti +V) vs. (Al +Mn) and V/Ni vs. Ni/Ga (F). SSZ magnetites are plotted in A, B, E and F and IOA-IOCG magnetites are plotted in C and D (compiled from Huang et al., (2019)).Legends for A, B, E and F (samples of the present study) is as shown in Band legends for IOA-IOCG magnetite samples are as shown in D. The IOCG magnetites are assigned solid circles and the IOA magnetites are assigned star symbol and the samples collected from different deposits are colour coded accordingly.

alteration and also for discriminating magnetite from U-bearing associations from U-barren associations (discussed in Chapter 2) all shares commonality in elements which were used for discrimination i.~~-~~e. V, Ni and Ga. In Fig. 5.1 all the SSZ samples are plotted in the Ti vs. Ni/Cr (Fig. 5.1A), (Ti + V) wt% vs. (Al + Mn) wt% (Fig. 5.1E), V vs. Ni/Ga (Fig. 5.1B), V/Ni vs. Ni/Ga (Fig. 5.1F) plot. The magnetite incorporated in the diagrams and as described in the respective chapters and as summarized in the section 5.1 in the present chapter are characterized by certain difference in formation processes and also in some cases the ore forming mechanisms are different. However, in most of the cases the ratios involving V, Ni and Ga remains characteristic to magnetite samples with respect to the association they belong and thereby lacks significant overlapping compared to the other plots. Also it has been noted by previous studies that the concentration of V and Ni remains unchanged or less prone to change compared to the other commonly incorporated trace elements in magnetite (Deditius et al., 2018; Huang and Beaudoin, 2021). Selection of elements that~~which~~ remain characteristic of the deposit types during subsequent alterations/re-equilibrations and retains the original composition (Deditius et al. 2018; Huang and Beaudoin 2019) might be key to the success of these discriminators or discriminations. The present study recommends the use of first row transition metals like V, Ni ± Co and post-transition metals like Ga as it has ~~been~~ proved to be more useful compared to the other elements already established in case of mineral petrogenetic studies from an economic perspective (Dupuis and Beaudoin, 2011; Dare et al., 2014; Nadoll et al., 2014) and in broad scale petrogenesis (Polat and Hofmann, 2003; Ordóñez-Calderón et al., 2008). The magnetite from IOA and IOCG deposits are plotted in Ti vs. Ni/Cr (Fig. 5.1C) and V vs. Ga/Ni plot (Fig. 5.1D). Ti vs. Ni/Cr (after Dare et al. (2014) is not a discriminator suggested to differentiate between different types of deposits and neither the V vs. Ni/Ga plot claims to separate magnetite from IOA and IOCG deposits. But on the premise of what has been discussed previously in the current section, it is

worth noting that in the V vs. Ga/Ni plot comparatively less superimposition is noted between magnetite samples from different deposits compared to the discrimination diagrams based on the concentrations of Ti, Ni and Cr. Also the magnetite samples from the same deposit plot more or less closely except the magnetite sample from Kwyojibo and Salobo IOCG deposit. The present study thus recommends that some of the elements are more useful in terms of discrimination potential compared to the elements used in the existing discriminators.

5.3. Limitations and future scopes

Numerous previous studies helped making great strides in understanding the polymetallic mineralization in Singhbhum Shear Zone, which provides important perspectives on the complex geological history of this shear zone. Although the mineralization of U, Cu and REEs has been previously dated, the present study lacks absolute age data, which might prove helpful to correlate with the regional and global tectonic events. An extensive study based on the *in situ* isotope age data would provide comprehensive insights about the metallogeny in general. Also it has been noted in the present study that monazite and xenotime, which are ideal mineral to get chronological data are frequently associated with the magnetite mineralization in most of the mineral assemblages studied in the present work and can be utilized in this purpose. The integration of geochemistry with chronology would provide better insight into the evolution of the polymetallic mineralization in the SSZ. In the present study the fO_2 conditions associated with the magnetite mineralization has been attempted to understand in a qualitative way based on thhe concentrations of selected trace elements that~~which~~ are sensitive to the change in fO_2. Although this qualitative approach provides some useful information, quantification of fO_2 will perhaps enhance the precision in understanding the physicochemical conditions of

Formatted: Font: Italic

mineralization. The present study based on the geochemistry of magnetite tested the most widely used trace element based discriminators and in some cases suggest alternatives integrating magnetite composition from previous literature and magnetite analyzed in the present study. However, a data-driven approach integrating a large data base needs to be attempted to confirm the applicability of trace element discriminators proposed in this study. Also, the more fundamental aspect of addressing the complexity of relating the geochemistry of accessory minerals to the ore genesis requires more focus on why some of the discriminators worked and some other fails to yield meaningful results rather than what result we are getting using the existing discriminators.

References

Acharyya, S.K., Gupta, A., and Orihashi, Y., 2010, Neoarchean–Paleoproterozoic stratigraphy of the Dhanjori basin, Singhbhum Craton, Eastern India: And recording of a few U–Pb zircon dates from its basal part: Journal of Asian Earth Sciences, v. 39, p. 527–536, doi:https://doi.org/10.1016/j.jseaes.2010.04.023.

Acosta-Góngora, P., Gleeson, S.A., Samson, I.M., Ootes, L., and Corriveau, L., 2014, Trace element geochemistry of magnetite and its relationship to Cu-Bi-Co-Au-Ag-U-W mineralization in the great bear magmatic zone, NWT, Canada: Economic Geology, v. 109, p. 1901–1928, doi:10.2113/econgeo.109.7.1901.

Aleinikoff, J.N., Selby, D., Slack, J.F., Day, W.C., Pillers, R.M., Cosca, M.A., Seeger, C.M., Fanning, C.M., and Samson, I.M., 2016, U-Pb, Re-Os, and Ar/Ar geochronology of rare earth element (REE)-Rich breccia pipes and associated host rocks from the mesoproterozoic pea ridge Fe-REE-Au deposit, St. Francois Mountains, Missouri: Economic Geology, v. 111, p. 1883–1914, doi:10.2113/econgeo.111.8.1883.

Alexander, B.W., Bau, M., Andersson, P., and Dulski, P., 2008, Continentally-derived solutes in shallow Archean seawater: Rare earth element and Nd isotope evidence in iron formation from the 2.9 Ga Pongola Supergroup, South Africa: Geochimica et Cosmochimica Acta, v. 72, p. 378–394, doi:10.1016/J.GCA.2007.10.028.

Angerer, T., Hagemann, S.G., and Danyushevsky, L. V., 2012, Geochemical evolution of the banded iron formation-hosted high-grade iron ore system in the Koolyanobbing greenstone belt, Western Australia: Economic Geology, v. 107, p. 599–644, doi:10.2113/econgeo.107.4.599.

Baidya, A.S., Pal, D.C., and Upadhyay, D., 2019, Chemical weathering of garnet in Banded

Iron Formation: Implications for the mechanism and sequence of secondary mineral formation and mobility of elements: Geochimica et Cosmochimica Acta, v. 265, p. 198–220, doi:10.1016/j.gca.2019.08.037.

Banerji, A.K., 1981, Ore genesis and its relationship to volcanism, tectonism, granitic activity, and metasomatism along the Singhbhum shear zone, eastern India: Economic Geology, v. 76, p. 905–912, doi:10.2113/gsecongeo.76.4.905.

Banerji, A.K., and Talapatra, A.K., 1966, Soda-granites from South of Tatanagar, Bihar, India: Geological Magazine, v. 103, p. 340–351, doi:10.1017/S0016756800053012.

Banerji, A.K., Tatapatra, A., Sankaran, A. V., and Bhattacharyya, T.K., 1972, Ore Genetic Significance of Geochemical Trends During Progressive Migmatisation Within Part of the Singhbhum Shear Zone: Journal of the Geological Society of India, v. 13, p. 39–50.

Barnes, S.J., Maier, W.D., and Ashwal, L.D., 2004, Platinum-group element distribution in the Main Zone and Upper Zone of the Bushveld Complex, South Africa, *in* Chemical Geology, Elsevier, v. 208, p. 293–317, doi:10.1016/j.chemgeo.2004.04.018.

Barnes, S.J., and Roeder, P.L., 2001, The range of spinel compositions in terrestrial mafic and ultramafic rocks: Journal of Petrology, v. 42, p. 2279–2302, doi:10.1093/petrology/42.12.2279.

Barton, M.D., 2014, Iron Oxide(-Cu-Au-REE-P-Ag-U-Co) Systems, *in* Treatise on Geochemistry: Second Edition, Elsevier Inc., v. 13, p. 515–541, doi:10.1016/B978-0-08-095975-7.01123-2.

Barton, M.D., 2013, Iron Oxide(-Cu-Au-REE-P-Ag-U-Co) Systems, *in* Treatise on Geochemistry: Second Edition, Elsevier Inc., v. 13, p. 515–541, doi:10.1016/B978-0-08-095975-7.01123-2.

Bau, M., and Dulski, P., 1996, Distribution of yttrium and rare-earth elements in the Penge and Kuruman iron-formations, Transvaal Supergroup, South Africa: Precambrian Research, v. 79, p. 37–55, doi:10.1016/0301-9268(95)00087-9.

Bau, M., Frei, R., Garbe-Schönberg, D., and Viehmann, S., 2022, High-resolution Ge-Si-Fe, Cr isotope and Th-U data for the Neoarchean Temagami BIF, Canada, suggest primary origin of BIF bands and oxidative terrestrial weathering 2.7 Ga ago: Earth and Planetary Science Letters, v. 589, p. 117579, doi:10.1016/j.epsl.2022.117579.

Beach, A., 1976, The interrelationships of fluid transport, deformation and geochemistry and heat flow in early Proterozoic shear zones in the Lewisian complex.: Philos. Trans. R. Soc. London, v. A280, p. 529- 604.

Bekker, A., Slack, J.F., Planavsky, N., Krapež, B., Hofmann, A., Konhauser, K.O., and Rouxel, O.J., 2010, Iron Formation: The Sedimentary Product of a Complex Interplay among Mantle, Tectonic, Oceanic, and Biospheric Processes: Economic Geology, v. 105, p. 467–508, doi:10.2113/GSECONGEO.105.3.467.

Belousova, E.A., Griffin, W.L., O'Reilly, S.Y., and Fisher, N.I., 2002, Apatite as an indicator mineral for mineral exploration: Trace-element compositions and their relationship to host rock type: Journal of Geochemical Exploration, v. 76, p. 45–69, doi:10.1016/S0375-6742(02)00204-2.

Belousova, E.A., Walters, S., Griffin, W.L., and O'Reilly, S.Y., 2001, Trace-element signatures of apatites in granitoids from the Mt Isa Inlier, Northwestern Queensland: Australian Journal of Earth Sciences, v. 48, p. 603–619, doi:10.1046/j.1440-0952.2001.00879.x.

Bhattacharya, H.N., Nelson, D.R., Thern, E.R., and Altermann, W., 2015, Petrogenesis and

geochronology of the Arkasani Granophyre and felsic Dalma volcanic rocks: Implications for the evolution of the Proterozoic North Singhbhum Mobile Belt, east India: Geological Magazine, v. 152, p. 492–503, doi:10.1017/S0016756814000442.

Bhola, K.L., 1972, Uranium deposits in Singhbhum and their development for use in the nuclear power programme in India: Proceedings of the Indian National Science Academy, v. 37A, p. 277–296.

Bhola, K.L., Rama Rao, Y.N., Suri Sastry, C., and Mehta, N.R., 1966, Uranium mineralization in Singbhum thrust belt, Bihar, India: Economic Geology, v. 61, p. 162–173, doi:10.2113/gsecongeo.61.1.162.

Bilenker, L.D., Simon, A.C., Reich, M., Lundstrom, C.C., Gajos, N., Bindeman, I., Barra, F., and Munizaga, R., 2016, Fe-O stable isotope pairs elucidate a high-temperature origin of Chilean iron oxide-apatite deposits: Geochimica et Cosmochimica Acta, v. 177, p. 94–104, doi:10.1016/j.gca.2016.01.009.

Blake, R.E., Chang, S.J., and Lepland, A., 2010, Phosphate oxygen isotopic evidence for a temperate and biologically active Archaean ocean: Nature, v. 464, p. 1029–1032, doi:10.1038/nature08952.

Bouzari, F., Hart, C.J.R., Barker, S., and Bissig, T., 2011, Exploration for concealed deposits using porphyry indicator minerals (PIMs): Application of apatite texture and chemistry, *in* 25th International Applied Geochemistry Symposium, p. 89–90.

Bowles, J.A., Gee, J.S., Burgess, K., and Cooper, R.F., 2011, Timing of magnetite formation in basaltic glass: Insights from synthetic analogs and relevance for geomagnetic paleointensity analyses: Geochemistry, Geophysics, Geosystems, v. 12, p. 2001, doi:10.1029/2010GC003404.

Bragg, W.H., 1915, The structure of the spinel group of crystals: The London, Edinburgh, and Dublin Philosophical Magazine and Journal of Science, v. 30, p. 305–315, doi:10.1080/14786440808635400.

Broughm, S.G., Hanchar, J.M., Tornos, F., Westhues, A., and Attersley, S., 2017, Mineral chemistry of magnetite from magnetite-apatite mineralization and their host rocks: examples from Kiruna, Sweden, and El Laco, Chile: Mineralium Deposita, v. 52, p. 1223–1244, doi:10.1007/s00126-017-0718-8.

Buddington, A.F., and Lindsley, D.H., 1964, Iron-Titanium Oxide Minerals and Synthetic Equivalents: Journal of Petrology, v. 5, p. 310–357, doi:10.1093/petrology/5.2.310.

Busigny, V., Lebeau, O., Ader, M., Krapež, B., and Bekker, A., 2013, Nitrogen cycle in the Late Archean ferruginous ocean: Chemical Geology, v. 362, p. 115–130, doi:10.1016/J.CHEMGEO.2013.06.023.

Butcher, A.R., and Merkle, R.K.W., 1987, Postcumulus modification of magnetite grains in the upper zone of the Bushveld Complex, South Africa: Lithos, v. 20, p. 247–260, doi:10.1016/0024-4937(87)90012-0.

Canil, D., Grondahl, C., Lacourse, T., and Pisiak, L.K., 2016, Trace elements in magnetite from porphyry Cu-Mo-Au deposits in British Columbia, Canada: Ore Geology Reviews, v. 72, p. 1116–1128, doi:10.1016/j.oregeorev.2015.10.007.

Canil, D., and Lacourse, T., 2020, Geothermometry using minor and trace elements in igneous and hydrothermal magnetite: Chemical Geology, v. 541, p. 119576, doi:10.1016/j.chemgeo.2020.119576.

Cao, M., Li, G., Qin, K., Seitmuratova, E.Y., and Liu, Y., 2012, Major and trace element characteristics of apatites in granitoids from central Kazakhstan: Implications for

petrogenesis and mineralization: Resource Geology, v. 62, p. 63–83, doi:10.1111/j.1751-3928.2011.00180.x.

Carew, M.J., 2004, Controls on Cu-Au mineralisation and Fe oxide metasomatism in the Eastern Fold Belt, N.W. Queensland, Australia: undefined-undefined p., https://www.mendeley.com/catalogue/6c102ed7-4c73-3364-9300-6b440ea3cbff/?utm_source=desktop&utm_medium=1.19.4&utm_campaign=open_catalog&userDocumentId=%7Bd806d020-3206-3983-9c24-70ecada3594b%7D (accessed January 2021).

Cathelineau, M., 1988, Cation site occupancy in chlorites and illites as a function of temperature: Clay Minerals, v. 23, p. 471–485, doi:10.1180/CLAYMIN.1988.023.4.13.

Chaudhuri, T., Wan, Y., Mazumder, R., Ma, M., and Liu, D., 2018, Evidence of Enriched, Hadean Mantle Reservoir from 4.2-4.0 Ga zircon xenocrysts from Paleoarchean TTGs of the Singhbhum Craton, Eastern India: Scientific Reports, v. 8, p. 1–12, doi:10.1038/s41598-018-25494-6.

Chen, W.T., Zhou, M.F., Gao, J.F., and Hu, R., 2015a, Geochemistry of magnetite from Proterozoic Fe-Cu deposits in the Kangdian metallogenic province, SW China: Mineralium Deposita, v. 50, p. 795–809, doi:10.1007/s00126-014-0575-7.

Chen, W.T., Zhou, M.F., Li, X., Gao, J.F., and Hou, K., 2015b, In-situ LA-ICP-MS trace elemental analyses of magnetite: Cu-(Au, Fe) deposits in the Khetri copper belt in Rajasthan Province, NW India: Ore Geology Reviews, v. 65, p. 929–939, doi:10.1016/j.oregeorev.2014.09.035.

Chowdhury, P., Mulder, J.A., Cawood, P.A., Bhattacharjee, S., Roy, S., Wainwright, A.N., Nebel, O., and Mukherjee, S., 2021, Magmatic thickening of crust in non-plate tectonic

settings initiated the subaerial rise of Earth's first continents 3.3 to 3.2 billion years ago: Proceedings of the National Academy of Sciences of the United States of America, v. 118, doi:10.1073/pnas.2105746118.

Condie, K.C., 2022, The atmosphere and hydrosphere, *in* Earth as an Evolving Planetary System, Academic Press, p. 229–268, doi:10.1016/b978-0-12-819914-5.00006-8.

Corriveau, L., Montreuil, J.F., and Potter, E.G., 2016, Alteration facies linkages among iron oxide copper-gold, iron oxide-apatite, and affiliated deposits in the great bear magmatic zone, Northwest Territories, Canada: Economic Geology, v. 111, p. 2045–2072, doi:10.2113/econgeo.111.8.2045.

Corriveau, L., Williams, P.J., and Mumin, A.H., 2010, Alteration vectors to IOCG mineralization : from uncharted terranes to deposits: Geological Association of Canada, v. 20, 89–110 p., https://ci.nii.ac.jp/naid/10030932892 (accessed September 2021).

Courtney-Davies, L., Ciobanu, C.L., Verdugo-Ihl, M.R., Dmitrijeva, M., Cook, N.J., Ehrig, K., and Wade, B.P., 2019, Hematite geochemistry and geochronology resolve genetic and temporal links among iron-oxide copper gold systems, Olympic Dam district, South Australia: Precambrian Research, v. 335, p. 105480, doi:10.1016/j.precamres.2019.105480.

Cox, G.M., Halverson, G.P., Minarik, W.G., Le Heron, D.P., Macdonald, F.A., Bellefroid, E.J., and Strauss, J. V., 2013, Neoproterozoic iron formation: An evaluation of its temporal, environmental and tectonic significance: Chemical Geology, v. 362, p. 232–249, doi:10.1016/j.chemgeo.2013.08.002.

La Cruz, N.L., Ovalle, J.T., Simon, A.C., Konecke, B.A., Barra, F., Reich, M., Leisen, M., and Childress, T.M., 2020, The Geochemistry of Magnetite and Apatite from the El

Laco Iron Oxide-Apatite Deposit, Chile: Implications for Ore Genesis: Economic Geology, v. 115, p. 1461–1491, doi:10.5382/econgeo.4753.

Danielson, A., Möller, P., and Dulski, P., 1992, The europium anomalies in banded iron formations and the thermal history of the oceanic crust: Chemical Geology, v. 97, p. 89–100, doi:10.1016/0009-2541(92)90137-T.

Dare, S.A.S., Barnes, S.J., and Beaudoin, G., 2015, Did the massive magnetite "lava flows" of El Laco (Chile) form by magmatic or hydrothermal processes? New constraints from magnetite composition by LA-ICP-MS: Mineralium Deposita, v. 50, p. 607–617, doi:10.1007/s00126-014-0560-1.

Dare, S.A.S., Barnes, S.J., and Beaudoin, G., 2012, Variation in trace element content of magnetite crystallized from a fractionating sulfide liquid, Sudbury, Canada: Implications for provenance discrimination: Geochimica et Cosmochimica Acta, v. 88, p. 27–50, doi:10.1016/j.gca.2012.04.032.

Dare, S.A.S., Barnes, S.J., Beaudoin, G., Méric, J., Boutroy, E., and Potvin-Doucet, C., 2014, Trace elements in magnetite as petrogenetic indicators: Mineralium Deposita, v. 49, p. 785–796, doi:10.1007/s00126-014-0529-0.

Das, K., Bose, S., and Ghosh, G., 2017, The Neoarchean-Paleoproterozoic basin development and growth of the Singhbhum Craton, eastern India and its global implications: Insights from detrital zircon U-Pb data: Precambrian Research, v. 298, p. 123–145, doi:10.1016/j.precamres.2017.06.008.

De, S., Mazumder, R., Ohta, T., Hegner, E., Yamada, K., Bhattacharyya, T., Chiarenzelli, J., Altermann, W., and Arima, M., 2015, Geochemical and Sm-Nd isotopic characteristics of the Late Archaean-Palaeoproterozoic Dhanjori and Chaibasa metasedimentary rocks,

Singhbhum craton, E. India: Implications for provenance, and contemporary basin tectonics: Precambrian Research, v. 256, p. 62–78, doi:10.1016/j.precamres.2014.10.020.

Deb, M., and Sarkar, S.C., 2017, Minerals and allied natural resources and their sustainable development: Springer Geology, v. 10, p. 978–981, doi:10.1007/978-981-10-4564-6.

Deditius, A.P., Reich, M., Simon, A.C., Suvorova, A., Knipping, J., Roberts, M.P., Rubanov, S., Dodd, A., and Saunders, M., 2018, Nanogeochemistry of hydrothermal magnetite: Contributions to Mineralogy and Petrology, v. 173, p. 1–20, doi:10.1007/s00410-018-1474-1.

Dey, S., Topno, A., Liu, Y., and Zong, K., 2017, Generation and evolution of Palaeoarchaean continental crust in the central part of the Singhbhum craton, eastern India: Precambrian Research, v. 298, p. 268–291, doi:10.1016/j.precamres.2017.06.009.

Duan, C., Li, Y., Mao, J., Hou, K., Wang, C., Yang, B., Wang, Q., and Li, W., 2019, Ore formation at the Washan iron oxide–apatite deposit in the Ningwu Ore District, eastern China: Insights from in situ LA-ICP-MS magnetite trace element geochemistry: Ore Geology Reviews, v. 112, p. 103064, doi:10.1016/j.oregeorev.2019.103064.

Dunn, J.A., and Dey, A.K., 1942, Geology and petrology of Eastern Singhbhum and surrounding areas, *in* Memoirs of the Geological Survey of India, v. 69, p. 176.

Duparc, Q., Dare, S.A.S., Cousineau, P.A., and Goutier, J., 2016, Magnetite chemistry as a provenance indicator in Archean metamorphosed sedimentary rocks: Journal of Sedimentary Research, v. 86, p. 542–563, doi:10.2110/jsr.2016.36.

Dupuis, C., and Beaudoin, G., 2011, Discriminant diagrams for iron oxide trace element fingerprinting of mineral deposit types: Mineralium Deposita, v. 46, p. 319–335,

doi:10.1007/s00126-011-0334-y.

Evans, B.W., and Frost, B.R., 1976, Chrome-spinel in progressive metamorphism—a preliminary analysis, *in* Chromium: its Physicochemical Behavior and Petrologic Significance, Pergamon, p. 959–972, doi:10.1016/b978-0-08-019954-2.50020-2.

Fleet, M.E., 1981, The structure of magnetite: Acta Crystallographica Section B Structural Crystallography and Crystal Chemistry, v. 37, p. 917–920, doi:10.1107/s0567740881004597.

Frost, B.R., 1990, Chapter 13. Stability of Oxide Minerals in Metamorphic Rocks: Oxide Minerals, p. 469–488, doi:10.1515/9781501508684-016.

Gatsé Ebotehouna, C., Xie, Y., Adomako-Ansah, K., Gourcerol, B., and Qu, Y., 2021, Depositional Environment and Genesis of the Nabeba Banded Iron Formation (BIF) in the Ivindo Basement Complex, Republic of the Congo: Perspective from Whole-Rock and Magnetite Geochemistry: Minerals 2021, Vol. 11, Page 579, v. 11, p. 579, doi:10.3390/MIN11060579.

Ghosh, R., and Baidya, T.K., 2017, Using BIF magnetite of the Badampahar greenstone belt, Iron Ore Group, East Indian Shield to reconstruct the water chemistry of a 3.3–3.1 Ga sea during iron oxyhydroxides precipitation: Precambrian Research, v. 301, p. 102–112, doi:10.1016/j.precamres.2017.09.006.

Ghosh, D., Dutta, T., Samanta, S.K., and Pal, D.C., 2013, Texture, microstructure and geochemistry of magnetite from the Banduhurang uranium mine, Singhbhum Shear Zone, India - Implications for physico-chemical evolution of magnetite mineralization: Journal of the Geological Society of India, v. 81, p. 101–112, doi:10.1007/s12594-013-0009-7.

Ghosh, S.., and Sengupta, S., 1987, Progressive development of structures in a ductile shear zone: Journal of Structural Geology, v. 9, p. 277–287, doi:10.1016/0191-8141(87)90052-6.

Goldschmidt, V.M., 1954, Geochemistry:

Goswami, J.N., Mishra, S., Wiedenbeck, M., Ray, S.L., and Saha, A.K., 1995, 3.55 Ga old zircon from Singhbhum–Orissa Iron Ore Craton, eastern India: Current Science, v. 69, p. 1008–1012.

Gourcerol, B., Kontak, D.J., Thurston, P.C., and Duparc, Q., 2016, Do magnetite layers in algoma-type banded iron formations (BIF) preserve their primary geochemical signature? A case study of samples from three archean BIF-hosted gold deposits: Canadian Mineralogist, v. 54, p. 605–624, doi:10.3749/canmin.1500090.

Grant, J.A., 2005, Isocon analysis: A brief review of the method and applications: Physics and Chemistry of the Earth, Parts A/B/C, v. 30, p. 997–1004, doi:https://doi.org/10.1016/j.pce.2004.11.003.

Grant, J.A., 1986, The isocon diagram; a simple solution to Gresens' equation for metasomatic alteration: Economic Geology, v. 81, p. 1976–1982, doi:10.2113/gsecongeo.81.8.1976.

Griffin, W.L., 2008, GLITTER : Data reduction software for laser ablation ICP-MS: Mineralogical Association of Canada, 308–311 p.

Grigsby, J.D., 1990, Detrital magnetite as a provenance indicator: Journal of Sedimentary Petrology, v. 60, p. 940–951, doi:10.1306/d426764f-2b26-11d7-8648000102c1865d.

Groves, D.I., Bierlein, F.P., Meinert, L.D., and Hitzman, M.W., 2010, Iron oxide copper-gold

(IOCG) deposits through earth histoiy: Implications for origin, lithospheric setting, and distinction from other epigenetic iron oxide deposits: Economic Geology, v. 105, p. 641–654, doi:10.2113/gsecongeo.105.3.641.

Von Gruenewaldt, G., Klemm, D.D., Henckel, J., and Dehm, R.M., 1985, Exsolution features in titanomagnetites from massive magnetite layers and their host rocks of the upper zone, eastern Bushveld complex.: Economic Geology, v. 80, p. 1049–1061, doi:10.2113/gsecongeo.80.4.1049.

Haggerty, S.E., 1976, Oxidation of opaque mineral oxides in basalts, *in* Oxide Minerals, Mineralogical Society of America, v. 3, p. Hg1–Hg100.

Harlov, D.E., 2015, Apatite: A fingerprint for metasomatic processes: Elements, v. 11, p. 171–176, doi:10.2113/gselements.11.3.171.

Heidarian, H., Lentz, D., Alirezaei, S., Peighambari, S., and Hall, D., 2016, Using the chemical analysis of magnetite to constrain various stages in the formation and genesis of the Kiruna-type chadormalu magnetite-apatite deposit, Bafq district, Central Iran: Mineralogy and Petrology, v. 110, p. 927–942, doi:10.1007/s00710-016-0440-8.

Henry, D.J., and Guidotti, C. V., 2002, Titanium in biotite from metapelitic rocks: Temperature effects, crystal-chemical controls, and petrologic applications: American Mineralogist, v. 87, p. 375–382, doi:10.2138/AM-2002-0401.

Henry, D.J., Guidotti, C. V., and Thomson, J.A., 2005, The Ti-saturation surface for low-to-medium pressure metapelitic biotites: Implications for geothermometry and Ti-substitution mechanisms: American Mineralogist, v. 90, p. 316–328, doi:10.2138/AM.2005.1498.

Hinsberg, V. van, and Szilas, K., 2021, BIF or MIF? Using trace elements to identify the

nature of iron formations.:, https://2021.goldschmidt.info/goldschmidt/2021/meetingapp.cgi/Paper/6087 (accessed January 2022).

Hong, S., Zuo, R., Huang, X., and Xiong, Y., 2021, Distinguishing IOCG and IOA deposits via random forest algorithm based on magnetite composition: Journal of Geochemical Exploration, v. 230, p. 106859, doi:10.1016/j.gexplo.2021.106859.

Hu, H., Lentz, D., Li, J.W., McCarron, T., Zhao, X.F., and Hall, D., 2015, Reequilibration processes in magnetite from iron skarn deposits: Economic Geology, v. 110, p. 1–8, doi:10.2113/econgeo.110.1.1.

Hu, H., Li, J.W., Harlov, D.E., Lentz, D.R., McFarlane, C.R.M., and Yang, Y.H., 2020, A genetic link between iron oxide-apatite and iron skarn mineralization in the Jinniu volcanic basin, Daye district, eastern China: Evidence from magnetite geochemistry and multi-mineral U-Pb geochronology: Bulletin of the Geological Society of America, v. 132, p. 899–917, doi:10.1130/B35180.1.

Hu, H., Li, J.W., Lentz, D., Ren, Z., Zhao, X.F., Deng, X.D., and Hall, D., 2014, Dissolution-reprecipitation process of magnetite from the Chengchao iron deposit: Insights into ore genesis and implication for in-situ chemical analysis of magnetite: Ore Geology Reviews, v. 57, p. 393–405, doi:10.1016/j.oregeorev.2013.07.008.

Huang, X.W., and Beaudoin, G., 2021, Nanoinclusions in zoned magnetite from the Sossego IOCG deposit, Carajás, Brazil: Implication for mineral zoning and magnetite origin discrimination: Ore Geology Reviews, v. 139, p. 104453, doi:10.1016/J.OREGEOREV.2021.104453.

Huang, X.W., and Beaudoin, G., 2019, Textures and chemical compositions of magnetite

from iron oxide copper-gold (IOCG) and kiruna-type iron oxide-apatite (IOA) deposits and their implications for ore genesis and magnetite classification schemes: Economic Geology, v. 114, p. 953–979, doi:10.5382/econgeo.4651.

Huang, X.-W., Beaudoin, G., and Yang, Y., 2022, A HR-TEM study on two generations of magnetite from the Alemao IOCG deposit, Carajás, Brazil: Implication for Fe-Cu mineralization: Ore Geology Reviews, v. 146, p. 104934, doi:10.1016/J.OREGEOREV.2022.104934.

Huang, X.W., Boutroy, É., Makvandi, S., Beaudoin, G., Corriveau, L., and De Toni, A.F., 2019, Trace element composition of iron oxides from iocg and ioa deposits: Relationship to hydrothermal alteration and deposit subtypes: Mineralium Deposita, v. 54, p. 525–552, doi:10.1007/s00126-018-0825-1.

Huang, X.W., Gao, J.F., Qi, L., Meng, Y.M., Wang, Y.C., and Dai, Z.H., 2016, In-situ LA-ICP-MS trace elements analysis of magnetite: The Fenghuangshan Cu-Fe-Au deposit, Tongling, Eastern China: Ore Geology Reviews, v. 72, p. 746–759, doi:10.1016/j.oregeorev.2015.09.012.

Huang, K., and Logé, R.E., 2016, A review of dynamic recrystallization phenomena in metallic materials: Materials and Design, v. 111, p. 548–574, doi:10.1016/j.matdes.2016.09.012.

Huang, X., Qi, L., and Meng, Y., 2014, Trace element geochemistry of magnetite from the Fe(-Cu) deposits in the Hami Region, Eastern Tianshan Orogenic Belt, NW China: Acta Geologica Sinica, v. 88, p. 176–195, doi:10.1111/1755-6724.12190.

Huang, X.W., Zhou, M.F., Qiu, Y.Z., and Qi, L., 2015, In-situ LA-ICP-MS trace elemental analyses of magnetite: The Bayan Obo Fe-REE-Nb deposit, North China: Ore Geology

Reviews, v. 65, p. 884–899, doi:10.1016/j.oregeorev.2014.09.010.

Jain, A.K., Banerjee, D.M., and Kale, V.S., 2020, Tectonics of the Indian subcontinent: Journal of Earth System Science, v. 129, doi:10.1007/s12040-020-01501-1.

Johnson, D.A., and Barton, M.D., 2006, Iron-oxide±Cu-Au-REE deposits and their by-product potential:

Johnson, P.T., Dasgupta, D., and Smith, A.D., 1993, Pb-Pb systematic of copper sulphide mineralization, Singhbhum area, Bihar: Indian Journal of Geology, v. 65, p. 211–213.

Jowett, E.C., 1991, Fitting Iron and Magnesium into the Hydrothermal Chlorite Geothermometer, *in* In Proceedings of the GAC/MAC/SEG Joint Annual Meeting, Toronto, Canada, Elsevier BV, doi:10.2139/SSRN.3863523.

Keppler, H., and Wyllie, P.J., 1990, Role of fluids in transport and fractionation of uranium and thorium in magmatic processes: Nature, v. 348, p. 531–533, doi:10.1038/348531a0.

Klein, C., 2005, Some Precambrian banded iron-formations (BIFs) from around the world: Their age, geologic setting, mineralogy, metamorphism, geochemistry, and origins: American Mineralogist, v. 90, p. 1473–1499, doi:10.2138/AM.2005.1871.

Knecht, B., Simons, B., and Woermann, E., 1977, Phase relations in the system Fe-Cr-Ti-O and their application in lunar thermometry, *in* Lunar Science Conference, v. 2, http://adsabs.harvard.edu/full/1977LPSC....8.2125K (accessed April 2020).

Knipping, J.L., Bilenker, L.D., Simon, A.C., Reich, M., Barra, F., Deditius, A.P., Lundstrom, C., Bindeman, I., and Munizaga, R., 2015a, Giant Kiruna-type deposits form by efficient flotation of magmatic magnetite suspensions: Geology, v. 43, p. 591–594, doi:10.1130/G36650.1.

Knipping, J.L., Bilenker, L.D., Simon, A.C., Reich, M., Barra, F., Deditius, A.P., Wälle, M., Heinrich, C.A., Holtz, F., and Munizaga, R., 2015b, Trace elements in magnetite from massive iron oxide-apatite deposits indicate a combined formation by igneous and magmatic-hydrothermal processes: Geochimica et Cosmochimica Acta, v. 171, p. 15–38, doi:10.1016/j.gca.2015.08.010.

Konhauser, K.O. et al., 2017, Iron formations: A global record of Neoarchaean to Palaeoproterozoic environmental history: Earth-Science Reviews, v. 172, p. 140–177, doi:10.1016/j.earscirev.2017.06.012.

Koppi, A.J., Edis, R., Field, D.J., Geering, H.R., Klessa, D.A., and Cockayne, D.J.H., 1996, Rare earth element trends and cerium-uranium-manganese associations in weathered rock from Koongarra, Northern Territory, Australia: Geochimica et Cosmochimica Acta, v. 60, p. 1695–1707, doi:10.1016/0016-7037(96)00047-6.

Kovalenko, N.I., Ryzhenko, B.N., Prisyagina, N.I., and Bychkova, Y. V., 2012, Experimental determination of uranium (IV) speciation in HF solutions at 500°C and 1000 bar: Geochemistry International, v. 50, p. 18–25, doi:10.1134/S0016702912010053.

Kranidiotis, P., and MacLean, W.H., 1987, Systematics of chlorite alteration at the Phelps Dodge massive sulfide deposit, Matagami, Quebec: Economic Geology, v. 82, p. 1898–1911, doi:10.2113/GSECONGEO.82.7.1898.

Kumar, A., Parashuramulu, V., Shankar, R., and Besse, J., 2017, Evidence for a Neoarchean LIP in the Singhbhum craton, eastern India: Implications to Vaalbara supercontinent: Precambrian Research, v. 292, p. 163–174, doi:10.1016/j.precamres.2017.01.018.

Lagoeiro, L.E., 1998, Transformation of magnetite to hematite and its influence on the dissolution of iron oxide minerals: Journal of Metamorphic Geology, v. 16, p. 415–423,

doi:10.1111/j.1525-1314.1998.00144.x.

Lan, C., Zhao, T., Chen, W.T., and Long, X., 2019, Trace elemental modification in magnetite from high-grade metamorphosed BIFs in the southern North China Craton: Ore Geology Reviews, v. 112, p. 103019, doi:10.1016/j.oregeorev.2019.103019.

Lattard, D., 1995, Experimental evidence for the exsolution of ilmenite from titaniferous spinel: American Mineralogist, v. 80, p. 968–981, doi:10.2138/am-1995-9-1013.

Li, X., Zhang, C., Behrens, H., and Holtz, F., 2020, Calculating biotite formula from electron microprobe analysis data using a machine learning method based on principal components regression: Lithos, v. 356–357, p. 105371, doi:10.1016/J.LITHOS.2020.105371.

Li, X., Zhang, C., Behrens, H., and Holtz, F., 2021, On the improvement of calculating biotite formula from EPMA data: Reexamination of the methods of Dymek (1983), Yavuz and Öztas (1997), Li et al. (2020) and reply to the discussion of Baidya and Das: Lithos, p. 106403, doi:10.1016/J.LITHOS.2021.106403.

Lindsley, D.H., 2018, The crystal chemistry and structure of oxide minerals as exemplified by the Fe-Ti oxides, *in* Oxide Minerals, p. 1–60, https://cir.nii.ac.jp/crid/1574231874843450240 (accessed May 2022).

Liu, W. et al., 2017, Arsenic in hydrothermal apatite: Oxidation state, mechanism of uptake, and comparison between experiments and nature: Geochimica et Cosmochimica Acta, v. 196, p. 144–159, doi:10.1016/j.gca.2016.09.023.

Liu, P.P., Liang, J., Zhou, M.F., and Chen, W.T., 2020, Micro-textures and chemical compositions of metamorphic magnetite and ilmenite: Insights from the Mianhuadi mafic complex in SW China: Journal of Asian Earth Sciences, v. 192, p. 104264,

doi:10.1016/j.jseaes.2020.104264.

Liu, P.P., Zhou, M.F., Chen, W.T., Gao, J.F., and Huang, X.W., 2015, In-situ LA-ICP-MS trace elemental analyses of magnetite: Fe-Ti-(V) oxide-bearing mafic-ultramafic layered intrusions of the Emeishan Large Igneous Province, SW China: Ore Geology Reviews, v. 65, p. 853–871, doi:10.1016/j.oregeorev.2014.09.002.

Loberg, B.E.H., and Horndahl, A.K., 1983, Ferride geochemistry of Swedish precambrian iron ores: Mineralium Deposita, v. 18, p. 487–504, doi:10.1007/BF00204493.

Loges, A., Migdisov, A.A., Wagner, T., Williams-Jones, A.E., and Markl, G., 2013, An experimental study of the aqueous solubility and speciation of Y(III) fluoride at temperatures up to 250°C: Geochimica et Cosmochimica Acta, v. 123, p. 403–415, doi:10.1016/j.gca.2013.07.031.

Lu, J.S., Wang, G.D., Wang, H., Chen, H.X., and Wu, C.M., 2013, Metamorphic P-T-t paths retrieved from the amphibolites, Lushan terrane, Henan Province and reappraisal of the Paleoproterozoic tectonic evolution of the Trans-North China Orogen: Precambrian Research, v. 238, p. 61–77, doi:10.1016/j.precamres.2013.09.019.

Luo, Y.R., and Byrne, R.H., 2000, The ionic strength dependence of rare earth and yttrium fluoride complexation at 25°C: Journal of Solution Chemistry, v. 29, p. 1089–1099, doi:10.1023/A:1005186932126.

Makvandi, S., Ghasemzadeh-Barvarz, M., Beaudoin, G., Grunsky, E.C., Beth McClenaghan, M., and Duchesne, C., 2016a, Principal component analysis of magnetite composition from volcanogenic massive sulfide deposits: Case studies from the Izok Lake (Nunavut, Canada) and Halfmile Lake (New Brunswick, Canada) deposits: Ore Geology Reviews, v. 72, p. 60–85, doi:10.1016/j.oregeorev.2015.06.023.

Makvandi, S., Ghasemzadeh-Barvarz, M., Beaudoin, G., Grunsky, E.C., McClenaghan, M.B., Duchesne, C., and Boutroy, E., 2016b, Partial least squares-discriminant analysis of trace element compositions of magnetite from various VMS deposit subtypes: Application to mineral exploration: Ore Geology Reviews, v. 78, p. 388–408, doi:10.1016/j.oregeorev.2016.04.014.

Mallmann, G., and O'Neill, H.S.C., 2009, The Crystal/Melt Partitioning of V during Mantle Melting as a Function of Oxygen Fugacity Compared with some other Elements (Al, P, Ca, Sc, Ti, Cr, Fe, Ga, Y, Zr and Nb): Journal of Petrology, v. 50, p. 1765–1794, doi:10.1093/petrology/egp053.

Mao, M., Rukhlov, A.S., Rowins, S.M., Spence, J., and Coogan, L.A., 2016, Apatite trace element compositions: A robust new tool for mineral exploration: Economic Geology, v. 111, p. 1187–1222, doi:10.2113/econgeo.111.5.1187.

Mazumder, R., De, S., Ohta, T., Flannery, D., Mallik, L., Chaudhury, T., Chatterjee, P., Ranaivoson, M.A., and Arima, M., 2015, Palaeo-Mesoproterozoic sedimentation and tectonics of the Singhbhum Craton, eastern India, and implications for global and craton-specific geological events: Geological Society, London, Memoirs, v. 43, p. 139 LP – 149, doi:10.1144/M43.10.

Mazumder, R., and Sarkar, S., 2004, Sedimentation history of the Palaeoproterozoic Dhanjori Formation, Singhbhum, eastern India: Precambrian Research, v. 130, p. 267–287, doi:https://doi.org/10.1016/j.precamres.2003.12.005.

McClenaghan, M.B., 2005, Indicator mineral methods in mineral exploration: Geochemistry: Exploration, Environment, Analysis, v. 5, p. 233–245, doi:10.1144/1467-7873/03-066.

McDonough, W.F., and Sun, S. s., 1995, The composition of the Earth: Chemical Geology, v.

120, p. 223–253, doi:10.1016/0009-2541(94)00140-4.

McIntire, W.L., 1963, Trace element partition coefficients-a review of theory and applications to geology: Geochimica et Cosmochimica Acta, v. 27, p. 1209–1264, doi:10.1016/0016-7037(63)90049-8.

Mcmanus, J., Nägler, T.F., Siebert, C., Wheat, C.G., Hammond, D.E., and Letter, R., 2002, Oceanic molybdenum isotope fractionation: Diagenesis and hydrothermal ridge-flank alteration: Geochemistry, Geophysics, Geosystems, v. 3, p. 1–9, doi:10.1029/2002GC000356.

Meinert, L.D., 1987, Skarn zonation and fluid evolution in the Groundhog mine, central mining district, New Mexico (USA).: Economic Geology, v. 82, p. 523–545, doi:10.2113/gsecongeo.82.3.523.

Meng, Y., Ruizhong, H.U., Huang, X., and Gao, J., 2017, Germanium in Magnetite: A Preliminary Review: Acta Geologica Sinica, v. 91, p. 711–726, doi:10.1111/1755-6724.13127.

Mercer, C.N., Watts, K.E., and Gross, J., 2020a, Apatite trace element geochemistry and cathodoluminescent textures—A comparison between regional magmatism and the Pea Ridge IOAREE and Boss IOCG deposits, southeastern Missouri iron metallogenic province, USA: Ore Geology Reviews, v. 116, p. 103129, doi:10.1016/j.oregeorev.2019.103129.

Mercer, C.N., Watts, K.E., and Gross, J., 2020b, Apatite trace element geochemistry and cathodoluminescent textures—A comparison between regional magmatism and the Pea Ridge IOAREE and Boss IOCG deposits, southeastern Missouri iron metallogenic province, USA: Ore Geology Reviews, v. 116, doi:10.1016/j.oregeorev.2019.103129.

Miller, S.R., Mueller, P.A., Meert, J.G., Kamenov, G.D., Pivarunas, A.F., Sinha, A.K., and Pandit, M.K., 2018, Detrital zircons reveal evidence of Hadean crust in the Singhbhum Craton, India: Journal of Geology, v. 126, p. 541–552, doi:10.1086/698844.

Mishra, S., Deomurari, M.P., Wiedenbeck, M., Goswami, J.N., Ray, S., and Saha, A.K., 1999, 207Pb/206Pb zircon ages and the evolution of the Singhbhum Craton, eastern India: An ion microprobe study: Precambrian Research, v. 93, p. 139–151, doi:10.1016/S0301-9268(98)00085-0.

Mishra, B., Pal, N., and Ghosh, S., 2003, Fluid Evolution of the Mosabani and Rakha Copper Deposits, Singhbhum District, Jharkhand: Evidence from Fluid Inclusion Study of Mineralized Quartz Veins: Journal of Geological Society of India, v. 61, p. 51–60, http://ischolar.info/index.php/JGSI/article/view/83797 (accessed September 2021).

Mollo, S., Putirka, K., Iezzi, G., and Scarlato, P., 2013, The control of cooling rate on titanomagnetite composition: Implications for a geospeedometry model applicable to alkaline rocks from Mt. Etna volcano: Contributions to Mineralogy and Petrology, v. 165, p. 457–475, doi:10.1007/s00410-012-0817-6.

Mondal, S., Upadhyay, D., and Banerjee, A., 2017, The Origin of Rapakivi Feldspar by a Fluid-induced Coupled Dissolution–Reprecipitation Process: Journal of Petrology, v. 58, p. 1393–1418, doi:10.1093/petrology/egx058.

Montreuil, J.F., Corriveau, L., and Grunsky, E.C., 2013, Compositional data analysis of hydrothermal alteration in IOCG systems, Great Bear magmatic zone, Canada: To each alteration type its own geochemical signature: Geochemistry: Exploration, Environment, Analysis, v. 13, p. 229–247, doi:10.1144/geochem2011-101.

Moorbath, S., Taylor, P.N., and Jones, N.W., 1986, Dating the oldest terrestrial rocks — fact

and fiction: Chemical Geology, v. 57, p. 63–86, doi:https://doi.org/10.1016/0009-2541(86)90094-X.

Mücke, A., and Cabral, A.R., 2005, Redox and nonredox reactions of magnetite and hematite in rocks: Chemie der Erde, v. 65, p. 271–278, doi:10.1016/j.chemer.2005.01.002.

Mukherjee, R., Venkatesh, A.S., and Fareeduddin, 2017, Chemistry of magnetite-apatite from albitite and carbonate-hosted Bhukia Gold Deposit, Rajasthan, western India – An IOCG-IOA analogue from Paleoproterozoic Aravalli Supergroup: Evidence from petrographic, LA-ICP-MS and EPMA studies: Ore Geology Reviews, v. 91, p. 509–529, doi:10.1016/j.oregeorev.2017.09.005.

Mukhopadhyay, J., Beukes, N.J., Armstrong, R.A., Zimmermann, U., Ghosh, G., and Medda, R.A., 2008, Dating the oldest greenstone in India: A 3.51-Ga precise U-Pb SHRIMP zircon age for dacitic lava of the southern Iron Ore Group, Singhbhum craton: Journal of Geology, v. 116, p. 449–461, doi:10.1086/590133.

Mukhopadhyay, J., Crowley, Q.G., Ghosh, S., Ghosh, G., Chakrabarti, K., Misra, B., Heron, K., and Bose, S., 2014, Oxygenation of the Archean atmosphere: New paleosol constraints from eastern India: Geology, v. 42, p. 923–926, doi:10.1130/G36091.1.

Nadoll, P., Angerer, T., Mauk, J.L., French, D., and Walshe, J., 2014, The chemistry of hydrothermal magnetite: A review: Ore Geology Reviews, v. 61, p. 1–32, doi:10.1016/j.oregeorev.2013.12.013.

Nadoll, P., and Mauk, J.L., 2011, Wüstite in a hydrothermal silver-lead-zinc vein, Lucky Friday mine, Coeur d'Alene mining district, U.S.A.: American Mineralogist, v. 96, p. 261–267, doi:10.2138/am.2011.3553.

Nadoll, P., Mauk, J.L., Hayes, T.S., Koenig, A.E., and Box, S.E., 2012, Geochemistry of

magnetite from hydrothermal ore deposits and host rocks of the mesoproterozoic Belt Supergroup, United States: Economic Geology, v. 107, p. 1275–1292, doi:10.2113/econgeo.107.6.1275.

Nadoll, P., Mauk, J.L., Leveille, R.A., and Koenig, A.E., 2015, Geochemistry of magnetite from porphyry Cu and skarn deposits in the southwestern United States: Mineralium Deposita, v. 50, p. 493–515, doi:10.1007/s00126-014-0539-y.

Nelson, D.R., Bhattacharya, H.N., Thern, E.R., and Altermann, W., 2014, Geochemical and ion-microprobe U-Pb zircon constraints on the Archaean evolution of Singhbhum Craton, eastern India: Precambrian Research, v. 255, p. 412–432, doi:10.1016/j.precamres.2014.09.024.

Neymark, L.A., Holm-Denoma, C.S., Pietruszka, A.J., Aleinikoff, J.N., Fanning, C.M., Pillers, R.M., and Moscati, R.J., 2016, High spatial resolution U-Pb geochronology and Pb isotope geochemistry of magnetite-apatite ore from the pea ridge iron oxide-apatite deposit, St. Francois Mountains, Southeast Missouri, USA: Economic Geology, v. 111, p. 1915–1933, doi:10.2113/econgeo.111.8.1915.

Nisbet, H., Migdisov, A., Xu, H., Guo, X., van Hinsberg, V., Williams-Jones, A.E., Boukhalfa, H., and Roback, R., 2018, An experimental study of the solubility and speciation of thorium in chloride-bearing aqueous solutions at temperatures up to 250 °C: Geochimica et Cosmochimica Acta, v. 239, p. 363–373, doi:10.1016/j.gca.2018.08.001.

Normandeau, P.X., Harlov, D.E., Corriveau, L., Paquette, J., and McMartin, I., 2018, Characterization of fluorapatite within iron oxide alkali-calcic alteration systems of the great bear magmatic zone: A potential metasomatic process record: Canadian

Mineralogist, v. 56, p. 167–187, doi:10.3749/canmin.1700035.

O'Hara, K., 1988, Fluid flow and volume loss during mylonitization: an origin for phyllonite in an overthrust setting, North Carolina U.S.A.: Tectonophysics, v. 156, p. 21–36, doi:10.1016/0040-1951(88)90280-6.

Ohmoto, H., 2003, Nonredox transformations of magnetite-hematite in hydrothermal systems: Economic Geology, v. 98, p. 157–161, doi:10.2113/gsecongeo.98.1.157.

Ohmoto, H., Watanabe, Y., Yamaguchi, K.E., Naraoka, H., Haruna, M., Kakegawa, T., Hayashi, K.I., and Kato, Y., 2006, Chemical and biological evolution of early Earth: Constraints from banded iron formations: Memoir of the Geological Society of America, v. 198, p. 291–333, doi:10.1130/2006.1198(17).

Olierook, H.K.H., Clark, C., Reddy, S.M., Mazumder, R., Jourdan, F., and Evans, N.J., 2019, Evolution of the Singhbhum Craton and supracrustal provinces from age, isotopic and chemical constraints: Earth-Science Reviews, v. 193, p. 237–259, doi:https://doi.org/10.1016/j.earscirev.2019.04.020.

Ordóñez-Calderón, J.C., Polat, A., Fryer, B.J., Gagnon, J.E., Raith, J.G., and Appel, P.W.U., 2008, Evidence for HFSE and REE mobility during calc-silicate metasomatism, Mesoarchean (~3075 Ma) Ivisaartoq greenstone belt, southern West Greenland: Precambrian Research, v. 161, p. 317–340, doi:10.1016/j.precamres.2007.09.004.

Ovalle, J.T., La Cruz, N.L., Reich, M., Barra, F., Simon, A.C., Konecke, B.A., Rodriguez-Mustafa, M.A., Deditius, A.P., Childress, T.M., and Morata, D., 2018, Formation of massive iron deposits linked to explosive volcanic eruptions: Scientific Reports 2018 8:1, v. 8, p. 1–11, doi:10.1038/s41598-018-33206-3.

Pal, D.C., Banerjee, A., Dutta, A., and Sarangi, A.K., 2022, Hydrothermal alterations and U-

REE mineralisation in the Narwapahar uranium deposit, Singhbhum shear zone, India: Journal of Earth System Science, v. 131, doi:10.1007/s12040-021-01782-0.

Pal, D.C., Barton, M.D., and Sarangi, A.K., 2009, Deciphering a multistage history affecting U-Cu(-Fe) mineralization in the Singhbhum Shear Zone, eastern India, using pyrite textures and compositions in the Turamdih U-Cu(-Fe) deposit: Mineralium Deposita, v. 44, p. 61–80, doi:10.1007/s00126-007-0165-z.

Pal, D.C., Basak, S., McFarlane, C., and Sarangi, A.K., 2021, EPMA geochemistry and LA-ICPMS dating of allanite, epidote, monazite, florencite and titanite from the Jaduguda uranium deposit, Singhbhum Shear Zone, eastern India: Implications for REE mineralization vis-à-vis tectonothermal events in the Proterozoic Mo: Precambrian Research, v. 359, p. 106208, doi:10.1016/j.precamres.2021.106208.

Pal, D.C., and Bhowmick, T., 2015, Petrography and microthermometry of fluid inclusions in apatite in the Turamdih uranium deposit, Singhbhum shear zone, eastern India - An insight into ore forming Fluid: Journal of the Geological Society of India, v. 86, p. 253–262, doi:10.1007/s12594-015-0310-8.

Pal, D.C., and Chaudhuri, T., 2016, Radiation damage-controlled localization of alteration haloes in albite: implications for alteration types and patterns vis-à-vis mineralization and element mobilization: Mineralogy and Petrology, v. 110, p. 823–843, doi:10.1007/s00710-016-0453-3.

Pal, D.C., Chaudhuri, T., McFarlane, C., Mukherjee, A., and Sarangi, A.K., 2011, Mineral chemistry and in situ dating of allanite, and geochemistry of its host rocks in the Bagjata uranium mine, Singhbhum shear zone, India-implications for the chemical evolution of REE mineralization and mobilization: Economic Geology, v. 106, p. 1155–1171,

doi:10.2113/econgeo.106.7.1155.

Pal, D.C., and Rhede, D., 2013, Geochemistry and chemical dating of uraninite in the Jaduguda uranium deposit, Singhbhum shear zone, India-implications for uranium mineralization and geochemical evolution of uraninite: Economic Geology, v. 108, p. 1499–1515, doi:10.2113/econgeo.108.6.1499.

Pal, D.C., Saravanan, C.S., and Mishra, B., 2008, Involvement of high temperature oxidized brine in pre-shearing hydrothermal alteration : evidence from fluid inclusions in tourmaline in feldspathic schist , Pathargora area , Singhbhum shear zone , eastern India: Abstracts with program of the second meeting of the Asian Current Research on Fluid Inclusions (ACROFI-2), p. 1–6.

Pal, D.C., Trumbull, R.B., and Wiedenbeck, M., 2010, Chemical and boron isotope compositions of tourmaline from the Jaduguda U (–Cu–Fe) deposit, Singhbhum shear zone, India: Implications for the sources and evolution of mineralizing fluids: Chemical Geology, v. 277, p. 245–260, doi:10.1016/J.CHEMGEO.2010.08.008.

Palma, G., Barra, F., Reich, M., Simon, A.C., and Romero, R., 2020, A review of magnetite geochemistry of Chilean iron oxide-apatite (IOA) deposits and its implications for ore-forming processes: Ore Geology Reviews, v. 126, p. 103748, doi:10.1016/j.oregeorev.2020.103748.

Palma, G., Reich, M., Barra, F., Ovalle, J.T., del Real, I., and Simon, A.C., 2021, Thermal evolution of Andean iron oxide–apatite (IOA) deposits as revealed by magnetite thermometry: Scientific Reports, v. 11, p. 1–9, doi:10.1038/s41598-021-97883-3.

Pan, L.C., Hu, R.Z., Wang, X.S., Bi, X.W., Zhu, J.J., and Li, C., 2016, Apatite trace element and halogen compositions as petrogenetic-metallogenic indicators: Examples from four

granite plutons in the Sanjiang region, SW China: Lithos, v. 254–255, p. 118–130, doi:10.1016/j.lithos.2016.03.010.

Pandey, O.P., Mezger, K., Ranjan, S., Upadhyay, D., Villa, I.M., Nägler, T.F., and Vollstaedt, H., 2019, Genesis of the Singhbhum Craton, eastern India; implications for Archean crust-mantle evolution of the Earth: Chemical Geology, v. 512, p. 85–106, doi:10.1016/j.chemgeo.2019.02.040.

Pang, K.N., Zhou, M.F., Lindsley, D., Zhao, D., and Malpas, J., 2008a, Origin of Fe-Ti oxide ores in mafic intrusions: Evidence from the Panzhihua intrusion, SW China: Journal of Petrology, v. 49, p. 295–313, doi:10.1093/petrology/egm082.

Pang, K.-N., Zhou, M.-F., Lindsley, D., Zhao, D., and Malpas, J., 2008b, Origin of Fe–Ti Oxide Ores in Mafic Intrusions: Evidence from the Panzhihua Intrusion, SW China: Journal of Petrology, v. 49, p. 295–313, doi:10.1093/petrology/egm082.

Pant, S., Singh, S., Sahoo, P.R., Kumar, A., Saravanan, B., Venkatesh, A.S., Yadav, G.S., and Kumar, P., 2019, Mineral chemistry and geothermometry of chlorites in relation to physico-chemical conditions of uranium mineralization in the central part of the Singhbhum Shear Zone, eastern India: Ore Geology Reviews, v. 112, p. 102997, doi:10.1016/j.oregeorev.2019.102997.

Patel, S., Upadhyay, D., Mishra, B., Abhinay, K., and Sarangi, A.K., 2021, Multiple episodes of hydrothermal alteration and uranium mineralization in the Singhbhum Shear Zone, eastern India: constraints from chemical and boron isotope composition of tourmaline: Lithos, v. 388–389, p. 106084, doi:10.1016/j.lithos.2021.106084.

Planavsky, N., Bekker, A., Rouxel, O.J., Kamber, B., Hofmann, A., Knudsen, A., and Lyons, T.W., 2010, Rare Earth Element and yttrium compositions of Archean and

Paleoproterozoic Fe formations revisited: New perspectives on the significance and mechanisms of deposition: Geochimica et Cosmochimica Acta, v. 74, p. 6387–6405, doi:10.1016/j.gca.2010.07.021.

Polat, A., and Hofmann, A.W., 2003, Alteration and geochemical patterns in the 3.7-3.8 Ga Isua greenstone belt, West Greenland: Precambrian Research, v. 126, p. 197–218, doi:10.1016/S0301-9268(03)00095-0.

Posth, N.R., Konhauser, K.O., and Kappler, A., 2011, Banded iron formations: Encyclopedia of Earth Sciences Series, p. 92–103, doi:10.1007/978-1-4020-9212-1_19/COVER/.

Pourmand, A., Dauphas, N., and Ireland, T.J., 2012, A novel extraction chromatography and MC-ICP-MS technique for rapid analysis of REE, Sc and Y: Revising CI-chondrite and Post-Archean Australian Shale (PAAS) abundances: Chemical Geology, v. 291, p. 38–54, doi:10.1016/J.CHEMGEO.2011.08.011.

Prokof'ev, V.Y., Naumov, V.B., and Dorofeeva, V.A., 2016, Gallium concentration in natural melts and fluids: Geochemistry International, v. 54, p. 691–705, doi:10.1134/S0016702916080097.

Putnis, A., 2002, Mineral replacement reactions: from macroscopic observations to microscopic mechanisms: Mineralogical Magazine, v. 66, p. 689–708, doi:10.1180/0026461026650056.

Ramachandran, S., Parthasarathy, T.N., and Saraswat, A.C., 1989, Xenotime from Kanyaluka, Singhbhum district, Bihar, India: rare-earth element abundances and economic potentiality: Explor Res At Miner 2, p. 177–182.

Rao, N.K., Aggarwal, S.K., and Rao, G.V.U., 1979, Lead Isotopic Ratios of Uraninites and the Age of Uranium Mineralization in Singhbhum Shear Zone, Bihar: Jour. Geol. Soc.

India, v. 20, p. 124–127, https://www.osti.gov/etdeweb/biblio/5601273 (accessed May 2022).

Rao, N.K., and Rao, G.V.U., 1980, Uraninite in the uranium deposits of Singhbhum Shear Zone, Bihar: Journal of the Geological Society of India, v. 21, p. 387–397, https://inis.iaea.org/search/search.aspx?orig_q=RN:13647572 (accessed February 2021).

Rao, N.K., and Rao, G.V.U., 1983a, Uranium mineralization in Singhbhum shear zone, Bihar: I Ore Mineralogy and Petrography: Journal of Geological Society of India, v. 24, p. 437–453, https://inis.iaea.org/search/search.aspx?orig_q=RN:17067938.

Rao, N.K., and Rao, G.V.U., 1983b, Uranium Mineralization in Singhbhum Shear Zone, Bihar: III. Nature of Occurrence of Uranium in Apatite-Magnetite Rocks: Journal of the Geological Society of India, v. 24, p. 555–561, http://www.geosocindia.org/index.php/jgsi/article/view/65196.

Rao, N.K., and Rao, G.V.U., 1983c, Uranium Mineralization in Singhbhum Shear Zone, Bihar: IV Origin and Geological Time Frame: Journal of the Geological Society of India, v. 24, p. 615–627, http://www.geosocindia.org/index.php/jgsi/article/view/65288.

Rao, N.K., and Rao, G.V.U., 1983d, Uranium Mineralization In Singhbhum Shear Zone, Bihar II. Occurence of “Brannerite”: JOURNAL GEOLOGICAL SOCIETY OF INDIA, v. 24, p. 489–501.

Rapp, J.F., Klemme, S., Butler, I.B., and Harley, S.L., 2010, Extremely high solubility of rutile in chloride and fluoride-bearing metamorphic fluids: An experimental investigation: Geology, v. 38, p. 323–326, doi:10.1130/G30753.1.

Rasmussen, B., Krapež, B., and Meier, D.B., 2014, Replacement origin for hematite in 2.5 Ga banded iron formation: Evidence for postdepositional oxidation of iron-bearing

minerals: GSA Bulletin, v. 126, p. 438–446, doi:10.1130/B30944.1.

Reguir, E.P., Chakhmouradian, A.R., Halden, N.M., Yang, P., and Zaitsev, A.N., 2008, Early magmatic and reaction-induced trends in magnetite from the carbonatites of Kerimasi, Tanzania: Canadian Mineralogist, v. 46, p. 879–900, doi:10.3749/canmin.46.4.879.

Righter, K., Leeman, W.P., and Hervig, R.L., 2006, Partitioning of Ni, Co and V between spinel-structured oxides and silicate melts: Importance of spinel composition: Chemical Geology, v. 227, p. 1–25, doi:10.1016/j.chemgeo.2005.05.011.

Robie, R.A., and Hemingway, B.S., 1995, Thermodynamic properties of minerals and related substances at 298.15 K and 1 bar (105 Pascals) pressure and at higher temperatures: US Geological Survey Bulletin, v. 2131, p. 456, doi:10.1016/0016-7037(79)90232-1.

Rodriguez-Mustafa, M.A., Simon, A.C., del Real, I., Thompson, J.F.H., Bilenker, L.D., Barra, F., Bindeman, I., and Cadwell, D., 2020, A Continuum from Iron Oxide Copper-Gold to Iron Oxide-Apatite Deposits: Evidence from Fe and O Stable Isotopes and Trace Element Chemistry of Magnetite: Economic Geology, v. 115, p. 1443–1459, doi:10.5382/ECONGEO.4752.

Rudnick, R.L., and Gao, S., 2003, Composition of the Continental Crust, *in* Treatise on Geochemistry, Elsevier Inc., v. 3–9, p. 1–64, doi:10.1016/B0-08-043751-6/03016-4.

Ruiz-Agudo, E., Putnis, C. V., and Putnis, A., 2014, Coupled dissolution and precipitation at mineral-fluid interfaces: Chemical Geology, v. 383, p. 132–146, doi:10.1016/j.chemgeo.2014.06.007.

Rusk, B., Oliver, N., Cleverley, J., Blenkinsop, T., Zhang, D., Williams, P., and Habermann, P., 2010, Physical and chemical characteristics of the Ernest Henry iron oxide copper gold deposit, Australia; implications for IOGC genesis, *in* Hydrothermal Iron Oxide

Copper-Gold & Related Deposits: a global perspective - advances in the understanding of IOCG deposits. Global Perspective Series, 3, PGC Publishing, Linden Park, SA, Australia, v. 3, p. 201–218, https://www.mendeley.com/catalogue/38b23464-fbec-3792-b4b6-6aeb83c6ab50/?utm_source=desktop&utm_medium=1.19.4&utm_campaign=open_catalog&userDocumentId=%7B27bf2834-9efe-385c-bad6-1015efe8b801%7D (accessed January 2021).

Ryzhenko, B.N., Kovalenko, N.I., and Prisyagina, N.I., 2006, Titanium complexation in hydrothermal systems: Geochemistry International, v. 44, p. 879–895, doi:10.1134/S0016702906090047.

Saha, A.K., 1994, Crustal Evolution of Singhbhum North Orissa Eastern India: Mem. Geolog. Soc. India, v. 27, p. 1–341.

Salazar, E., Barra, F., Reich, M., Simon, A., Leisen, M., Palma, G., Romero, R., and Rojo, M., 2020, Trace element geochemistry of magnetite from the Cerro Negro Norte iron oxide−apatite deposit, northern Chile: Mineralium Deposita, v. 55, p. 409–428, doi:10.1007/s00126-019-00879-3.

Sarkar, S.C., 1984, Geology and ore mineralization along the Singhbhum copper-uranium belt, eastern India: Jadavpur University Press, p. 263.

Sarkar, S.C., 1982, Uranium (-nickel-cobalt-molybdenum) mineralization along the Singhbhum copper belt, India, and the problem of ore genesis: Mineralium Deposita 1982 17:2, v. 17, p. 257–278, doi:10.1007/BF00206475.

Sarkar, S.C., and Gupta, A., 2012, Crustal evolution and metallogeny in India: 1–840 p., doi:10.1017/CBO9781139196123.

Sengupta, S., and Ghosh, S.K., 1997, The kinematic history of the singhbhum shear zone: Proceedings of the Indian Academy of Sciences, Earth and Planetary Sciences, v. 106, p. 185–196, doi:10.1007/bf02843446.

Sengupta, N., Mukhopadhyay, D., Sengupta, P., and Hoffbauer, R., 2005, Tourmaline-bearing rocks in the Singhbhum shear zone, eastern India: Evidence of boron infiltration during regional metamorphism: American Mineralogist, v. 90, p. 1241–1255, doi:10.2138/am.2005.1578.

Sengupta, N., Sengupta, P., and Sachan, H.K., 2011, Aluminous and alkali-deficient tourmaline from the Singhbhum Shear Zone, East Indian shield: Insight for polyphase boron infiltration during regional metamorphism: American Mineralogist, v. 96, p. 752–767, doi:10.2138/AM.2011.3560.

Sha, L.K., and Chappell, B.W., 1999, Apatite chemical composition, determined by electron microprobe and laser-ablation inductively coupled plasma mass spectrometry, as a probe into granite petrogenesis: Geochimica et Cosmochimica Acta, v. 63, p. 3861–3881, doi:10.1016/S0016-7037(99)00210-0.

She, H.-D., Fan, H.-R., Yang, K.-F., Li, X.-C., Wang, Q.-W., Zhang, L.-F., Liu, S., Li, X.-H., and Dai, Z.-H., 2021, In situ trace elements of magnetite in the Bayan Obo REE-Nb-Fe deposit: Implications for the genesis of mesoproterozoic iron mineralization: Ore Geology Reviews, v. 139, p. 104574, doi:10.1016/j.oregeorev.2021.104574.

Sievwright, R.H., Wilkinson, J.J., O'Neill, H.S.C., and Berry, A.J., 2017, Thermodynamic controls on element partitioning between titanomagnetite and andesitic–dacitic silicate melts: Contributions to Mineralogy and Petrology, v. 172, p. 62, doi:10.1007/s00410-017-1385-6.

Singh, Y., 2020a, Hydrothermal Veins, *in* Springer, Cham, p. 227–268, doi:10.1007/978-3-030-41353-8_6.

Singh, Y., 2020b, Rare Earth Element Resources: Indian Context:, doi:10.1007/978-3-030-41353-8.

Singoyi, B., Danyushevsky, L., Davidson, G.J., Large, R., and Zaw, K., 2006, Determination of trace elements in magnetites from hydrothermal deposits using the LA-ICP-MS technique. Abstracts of oral and poster presentations from the SEG 2006 conference., *in* Abstracts of Oral and Poster Presentations from the SEG 2006 ConferenceSociety of Economic Geologists, Keystone, USA, v. 95, p. 367–368, https://scholar.google.com/scholar?cluster=9997605946784494164&hl=en&as_sdt=2005&sciodt=0,5 (accessed May 2022).

Sinha, D.K., 2018, Uranium Potential of the Singhbhum Shear Zone, India: Future Prospects:, https://inis.iaea.org/search/search.aspx?orig_q=RN:49097488 (accessed May 2022).

Sinha, A.K., Hewitt, D.A., and Rimstidt, J.D., 1986, Fluid interaction and element mobility in the development of ultramylonites: Geology, v. 14, p. 883–886, doi:10.1130/0091-7613(1986)14<883:fiaemi>2.0.co;2.

Skublov, S., and Drugova, G., 2003, Patterns of trace-element distribution in calcic amphiboles as a function of metamorphic grade: Canadian Mineralogist, v. 41, p. 383–392, doi:10.2113/gscanmin.41.2.383.

Slack, J.F., 2006, High REE and Y concentrations in Co-Cu-Au ores of the Blackbird district, Idaho: Economic Geology, v. 101, p. 275–280, doi:10.2113/gsecongeo.101.2.275.

Sun, W., Yuan, F., Jowitt, S.M., Zhou, T., Liu, G., Li, X., Wang, F., and Troll, V.R., 2019, In

situ LA–ICP–MS trace element analyses of magnetite: genetic implications for the Zhonggu orefield, Ningwu volcanic basin, Anhui Province, China: Mineralium Deposita, v. 54, p. 1243–1264, doi:10.1007/s00126-019-00872-w.

Sverjensky, D.A., 1984, Europium redox equilibria in aqueous solution: Earth and Planetary Science Letters, v. 67, p. 70–78, doi:10.1016/0012-821X(84)90039-6.

Tait, J., Zimmermann, U.D.O., Miyazaki, T., Presnyakov, S., Chang, Q., Mukhopadhyay, J., and Sergeev, S., 2011, Possible juvenile Palaeoarchaean TTG magmatism in eastern India and its constraints for the evolution of the Singhbhum craton: Geological Magazine, v. 148, p. 340–347, doi:DOI: 10.1017/S0016756810000920.

Talapatra, A.K., 1968, Sulfide mineralization associated with migmatization in the southeastern part of the Singhbhum shear zone, Bihar, India: Economic Geology, v. 63, p. 156–165, doi:10.2113/gsecongeo.63.2.156.

Tan, W., Liu, P., He, H., Wang, C.Y., and Liang, X., 2016, Mineralogy and origin of exsolution in Ti-rich magnetite from different magmatic Fe-Ti oxide-bearing intrusions: Canadian Mineralogist, v. 54, p. 539–553, doi:10.3749/canmin.1400069.

Tanis, E.A., Simon, A., Tschauner, O., Chow, P., Xiao, Y., Shen, G., Hanchar, J.M., and Frank, M., 2012, Solubility of xenotime in a 2 M HCl aqueous fluid from 1.2 to 2.6 GPa and 300 to 500 °C: American Mineralogist, v. 97, p. 1708–1713, doi:10.2138/am.2012.4009.

Thurston, P.C., Kamber, B.S., and Whitehouse, M., 2012, Archean cherts in banded iron formation: Insight into Neoarchean ocean chemistry and depositional processes: Precambrian Research, v. 214–215, p. 227–257, doi:10.1016/j.precamres.2012.04.004.

Timofeev, A., Migdisov, A.A., Williams-Jones, A.E., Roback, R., Nelson, A.T., and Xu, H.,

2018, Uranium transport in acidic brines under reducing conditions: Nature Communications, v. 9, p. 1–7, doi:10.1038/s41467-018-03564-7.

Tobisch, O.T., Barton, M.D., Vernon, R.H., and Paterson, S.R., 1991, Fluid-enhanced deformation: transformation of granitoids to banded mylonites, western Sierra Nevada, California, and southeastern Australia:, https://www.sciencedirect.com/science/article/pii/019181419190074S (accessed April 2020).

Tollari, N., Barnes, S.J., Cox, R.A., and Nabil, H., 2008, Trace element concentrations in apatites from the Sept-Îles Intrusive Suite, Canada - Implications for the genesis of nelsonites: Chemical Geology, v. 252, p. 180–190, doi:10.1016/j.chemgeo.2008.02.016.

Toplis, M.J., and Carroll, M.R., 1995, An Experimental Study of the Influence of Oxygen Fugacity on Fe-Ti Oxide Stability, Phase Relations, and Mineral—Melt Equilibria in Ferro-Basaltic Systems: Journal of Petrology, v. 36, p. 1137–1170, doi:10.1093/PETROLOGY/36.5.1137.

Toplis, M.J., and Corgne, A., 2002, An experimental study of element partitioning between magnetite, clinopyroxene and iron-bearing silicate liquids with particular emphasis on vanadium: Contributions to Mineralogy and Petrology, v. 144, p. 22–37, doi:10.1007/s00410-002-0382-5.

Tornos, F., Velasco, F., and Hanchar, J.M., 2016, Iron-rich melts, magmatic magnetite, and superheated hydrothermal systems: The El Laco deposit, Chile: Geology, v. 44, p. 427–430, doi:10.1130/G37705.1.

Turner, M.B., Cronin, S.J., Stewart, R.B., Bebbington, M., and Smith, I.E.M., 2008, Using titanomagnetite textures to elucidate volcanic eruption histories: Geology, v. 36, p. 31–

34, doi:10.1130/G24186A.1.

Turnock, A.C., and Eugster, H.P., 1962, Fe—Al Oxides: Phase Relationships below 1,000°C: Journal of Petrology, v. 3, p. 533–565, doi:10.1093/petrology/3.3.533.

Upadhyay, D., Chattopadhyay, S., Kooijman, E., Mezger, K., and Berndt, J., 2014, Magmatic and metamorphic history of Paleoarchean tonalite–trondhjemite–granodiorite (TTG) suite from the Singhbhum craton, eastern India: Precambrian Research, v. 252, p. 180–190, doi:https://doi.org/10.1016/j.precamres.2014.07.011.

Valcke, S.L.A., De Bresser, J.H.P., Pennock, G.M., and Drury, M.R., 2015, Influence of deformation conditions on the development of heterogeneous recrystallization microstructures in experimentally deformed Carrara marble: Geological Society Special Publication, v. 409, p. 175–200, doi:10.1144/SP409.4.

Vidal, O., Parra, T., and Trotet, F., 2001, A Thermodynamic Model for Fe-Mg Aluminous Chlorite Using Data from Phase Equilibrium Experiments and Natural Pelitic Assemblages in the 100° to 600°c, 1 to 25 kb Range: American Journal of Science, v. 301, p. 557–592, doi:10.2475/AJS.301.6.557.

Vidal, O., Parra, T., and Vieillard, P., 2005, Thermodynamic properties of the Tschermak solid solution in Fe-chlorite: Application to natural examples and possible role of oxidation: American Mineralogist, v. 90, p. 347–358, doi:10.2138/AM.2005.1554.

Vinogradov, A., Tugarinov, A., Zhykov, C., Sapnikova, N., Bibikova, E., and Khorre, K., 1964, Geochronology of Indian Precambrians, *in* Proc. 22nd Int. Geol. Cong Section, 10, p. 553–567.

Waychunas, G.A., and Ribbe, P.H., 1991, Crystal chemistry of oxides and oxyhydroxides, *in* Oxide Minerals: petrologic and magnetic significance, De Gruyter, v. 25, p. 11–68,

doi:10.1515/9781501508684-005.

Webster, J.D., and Piccoli, P.M., 2015, Magmatic apatite: A powerful, yet deceptive, mineral: Elements, v. 11, p. 177–182, doi:10.2113/gselements.11.3.177.

Wechsler, B.A., Lindsley, D.H., and Prewitt, C.T., 1984, Crystal structure and cation distribution in titanomagnetites (Fe3-xTixO4).: American Mineralogist, v. 69, p. 754–770, https://pubs.geoscienceworld.org/msa/ammin/article/69/7-8/754/104867/Crystal-structure-and-cation-distribution-in?casa_token=6M87bJd3meAAAAAA:muSWAvd90dWoacJkOwyeHQghk0VZL4JZ5Kj4kUa-B4qKS73PheUf_G60_u2vsxQ6_-xCkYMk (accessed May 2022).

van der Weijden, C.H., and van der Weijden, R.D., 1995, Mobility of major, minor and some redox-sensitive trace elements and rare-earth elements during weathering of four granitoids in central Portugal: Chemical Geology, v. 125, p. 149–167, doi:10.1016/0009-2541(95)00071-S.

Wen, G., Li, J.W., Hofstra, A.H., Koenig, A.E., Lowers, H.A., and Adams, D., 2017, Hydrothermal reequilibration of igneous magnetite in altered granitic plutons and its implications for magnetite classification schemes: Insights from the Handan-Xingtai iron district, North China Craton: Geochimica et Cosmochimica Acta, v. 213, p. 255–270, doi:10.1016/j.gca.2017.06.043.

Whitney, D.L., and Evans, B.W., 2010, Abbreviations for names of rock-forming minerals: American Mineralogist, v. 95, p. 185–187, doi:10.2138/am.2010.3371.

Wright, T.L., and Weiblen, P.W., 1968, Mineral composition and paragenesis in tholeiitic basalt from Makaopuhi lava lake, Hawaii: GSA special paper, v. 115, p. 242–243.

Wu, C.-M., and Chen, H.-X., 2014, Revised Ti-in-biotite geothermometer for ilmenite- or

rutile-bearing crustal metapelites: Science Bulletin 2014 60:1, v. 60, p. 116–121, doi:10.1007/S11434-014-0674-Y.

Wu, C., Chen, H., Hong, W., Li, D., Liang, P., Fang, J., Zhang, L., and Lai, C., 2019, Magnetite chemistry and implications for the magmatic-hydrothermal ore-forming process: An example from the Devonian Yuleken porphyry Cu system, NW China: Chemical Geology, v. 522, p. 1–15, doi:10.1016/j.chemgeo.2019.04.022.

Xing, Y., Etschmann, B., Liu, W., Mei, Y., Shvarov, Y., Testemale, D., Tomkins, A., and Brugger, J., 2019, The role of fluorine in hydrothermal mobilization and transportation of Fe, U and REE and the formation of IOCG deposits: Chemical Geology, v. 504, p. 158–176, doi:10.1016/j.chemgeo.2018.11.008.

Zang, W., and Fyfe, W.S., 1995, Chloritization of the hydrothermally altered bedrock Igarap6 Bahia gold deposit, Carajas, Brazil at the: Mineral. Deposita, v. 30, p. 30–38.

Zeng, L.-P., Zhao, X.-F., Spandler, C., Hu, H., Hu, B., Li, J.-W., and Hu, Y., 2022, Origin of high Ti-magnetite in magmatic-hydrothermal systems: evidence from iron oxide apatite (IOA) deposits of eastern China: Economic Geology, v. 117, p. 923–942, doi:10.5382/ECONGEO.4901.

Zhao, J., Brugger, J., and Pring, A., 2019, Mechanism and kinetics of hydrothermal replacement of magnetite by hematite: Geoscience Frontiers, v. 10, p. 29–41, doi:10.1016/j.gsf.2018.05.015.

List of Publications

Published

Adak, S., Pal, D.C., Upadhyay, D., Mondal, R., 2021. Textural re-equilibration, hydrothermal alteration and element redistribution in Fe-Ti oxide pods, Singhbhum Shear Zone, eastern India. Geochemistry 81, 125679. https://doi.org/10.1016/j.chemer.2020.125679

Under review

Adak, S., Pal, D.C., Mandal, S., Geochemistry of magnetite and hydrothermal minerals from the Bagjata uranium deposit, Singhbhum shear Zone, India: implications for mineralization and use of trace elements as discriminators.

In preparation

Adak, S., Pal, D.C.: Magnetite from Fe-Ti oxide Pods and magnetite-apatite veins from Pathargora: impact of post-depositional processes and applicability of discriminator diagrams.

Adak, S., Pal, D.C., Das, A., Magenetite from banded magnetite quartzite in Turamdih and Mohuldih: constrains on anomalous chemistry and implications

Tables

Tables

Table 1 Major element composition of Magnetite from Bagjata U deposit

Sample Details	Na2O	F	MgO	Al2O3	Cl	P2O5	Cr2O3	MnO	FeO	ZnO	BaO	SiO2	K2O	CaO	TiO2	V2O3	Total
Association I	n.d.	n.d.	n.d.	n.d.	n.d.	n.d.	n.d.	n.d.	92.313	n.d.	n.d.	n.d.	n.d.	0.063	n.d.	0.823	93.311
Association I	n.d.	n.d.	n.d.	0.085	n.d.	n.d.	0.082	n.d.	92.248	n.d.	n.d.	n.d.	n.d.	n.d.	n.d.	1.295	93.924
Association I	n.d.	n.d.	n.d.	n.d.	n.d.	n.d.	0.051	n.d.	91.771	n.d.	n.d.	n.d.	n.d.	n.d.	n.d.	1.415	93.539
Association I	n.d.	n.d.	n.d.	0.071	n.d.	n.d.	0.049	n.d.	91.148	n.d.	n.d.	n.d.	n.d.	n.d.	n.d.	1.404	92.746
Association I	n.d.	n.d.	n.d.	0.168	n.d.	n.d.	0.097	n.d.	90.662	n.d.	n.d.	0.354	n.d.	n.d.	n.d.	1.649	93.097
Association I	n.d.	n.d.	n.d.	0.386	n.d.	n.d.	n.d.	n.d.	90.73	n.d.	n.d.	0.42	n.d.	0.073	n.d.	1.594	93.432
Association I	n.d.	n.d.	n.d.	0.048	n.d.	n.d.	n.d.	n.d.	86.563	n.d.	n.d.	0.083	n.d.	n.d.	n.d.	1.561	88.333
Association I	n.d.	n.d.	n.d.	0.064	n.d.	n.d.	n.d.	n.d.	87.18	n.d.	n.d.	n.d.	n.d.	n.d.	n.d.	1.556	88.866
Association I	n.d.	n.d.	n.d.	0.046	n.d.	n.d.	0.057	n.d.	87.761	n.d.	n.d.	0.303	n.d.	n.d.	n.d.	1.602	89.909
Association I	n.d.	n.d.	n.d.	0.047	n.d.	n.d.	0.053	n.d.	86.826	n.d.	n.d.	n.d.	n.d.	n.d.	n.d.	1.708	88.654
Association I	n.d.	n.d.	n.d.	0.089	n.d.	n.d.	n.d.	n.d.	88.025	n.d.	n.d.	0.448	n.d.	n.d.	n.d.	1.432	90.012
Association II	n.d.	n.d.	n.d.	0.088	n.d.	n.d.	n.d.	n.d.	92.64	n.d.	n.d.	n.d.	n.d.	n.d.	n.d.	0.51	93.401
Association II	n.d.	n.d	n.d.	0.063	n.d	n.d.	n.d.	n.d.	93.01	n.d.	n.d.	n.d.	n.d.	n.d.	n.d.	0.537	93.91

		.			.				1								1
Association II	n.d.	n.d.	n.d.	0.084	n.d.	n.d.	n.d.	n.d.	92.087	n.d.	n.d.	n.d.	n.d.	n.d.	n.d.	0.532	92.808
Association II	n.d.	n.d.	n.d.	0.093	n.d.	n.d.	0.16	n.d.	92.65	n.d.	n.d.	0.216	n.d.	n.d.	n.d.	0.496	93.755
Association II	n.d.	n.d.	n.d.	n.d.	n.d.	n.d.	0.062	n.d.	92.415	n.d.	n.d.	n.d.	n.d.	n.d.	n.d.	0.411	93.097
Association II	n.d.	n.d.	n.d.	0.057	n.d.	n.d.	n.d.	0.125	92.88	n.d.	n.d.	n.d.	n.d.	n.d.	n.d.	0.448	93.606
Association II	n.d.	n.d.	n.d.	n.d.	n.d.	n.d.	n.d.	n.d.	93.923	n.d.	n.d.	n.d.	n.d.	n.d.	n.d.	0.462	94.46
Association II	n.d.	n.d.	n.d.	n.d.	n.d.	n.d.	n.d.	n.d.	92.937	n.d.	n.d.	n.d.	n.d.	n.d.	n.d.	0.556	93.902
Association II	n.d.	n.d.	n.d.	0.091	n.d.	n.d.	n.d.	n.d.	92.68	n.d.	n.d.	n.d.	n.d.	n.d.	n.d.	0.518	93.502
Association II	n.d.	n.d.	n.d.	0.094	n.d.	n.d.	n.d.	n.d.	92.736	n.d.	n.d.	0.342	n.d.	n.d.	n.d.	0.518	93.795
Association II	n.d.	n.d.	n.d.	0.083	n.d.	n.d.	n.d.	n.d.	93.172	n.d.	n.d.	n.d.	n.d.	n.d.	n.d.	0.515	93.892
Association II	n.d.	n.d.	n.d.	0.132	n.d.	n.d.	0.185	n.d.	92.11	n.d.	n.d.	n.d.	n.d.	n.d.	n.d.	1.133	93.718
Association II	n.d.	n.d.	n.d.	0.127	n.d.	n.d.	n.d.	n.d.	91.767	n.d.	n.d.	n.d.	n.d.	n.d.	n.d.	1.261	93.341
Association II	n.d.	n.d.	0.145	0.712	n.d.	0.052	n.d.	n.d.	89.166	n.d.	n.d.	1.462	0.078	0.223	0.083	1.211	93.231
Association II	n.d.	n.d.	n.d.	0.119	n.d.	n.d.	n.d.	n.d.	92.075	n.d.	n.d.	n.d.	n.d.	n.d.	n.d.	1.053	93.493
Association II	n.d.	n.d.	n.d.	n.d.	n.d.	n.d.	0.257	n.d.	91.191	n.d.	n.d.	0.051	n.d.	n.d.	n.d.	1.036	92.801
Association II	n.d.	n.d.	n.d.	0.078	n.d.	n.d.	n.d.	0.108	91.221	n.d.	n.d.	n.d.	n.d.	n.d.	n.d.	1.249	92.798
Association II	n.d.	n.d	n.d.	0.062	n.d	n.d.	n.d.	n.d.	92.57	n.d.	n.d.	n.d.	n.d.	n.d.	n.d.	1.21	93.97

		.			.				6								7
Association II	n.d.	n.d.	n.d.	0.055	n.d.	n.d.	0.113	n.d.	90.638	n.d.	n.d.	n.d.	n.d.	n.d.	n.d.	1.152	92.068
Association II	n.d.	n.d.	n.d.	0.084	n.d.	n.d.	0.069	n.d.	92.201	n.d.	n.d.	n.d.	n.d.	n.d.	n.d.	1.138	93.718
Association II	n.d.	n.d.	n.d.	0.099	n.d.	n.d.	0.085	n.d.	91.288	n.d.	n.d.	n.d.	n.d.	n.d.	n.d.	1.075	92.895
Sample details	Na2O	F	MgO	Al2O3	Cl	P2O5	Cr2O3	MnO	FeO	ZnO	BaO	SiO2	K2O	CaO	TiO2	V2O3	Total
Association II	n.d.	n.d.	n.d.	0.126	n.d.	n.d.	0.061	n.d.	91.967	n.d.	n.d.	n.d.	n.d.	n.d.	n.d.	1.131	93.327
Association II	n.d.	n.d.	n.d.	0.063	n.d.	n.d.	n.d.	n.d.	91.976	n.d.	n.d.	n.d.	n.d.	n.d.	0.496	0.69	93.451
Association II	n.d.	n.d.	0.186	0.658	n.d.	n.d.	n.d.	n.d.	90.576	n.d.	n.d.	1.126	0.219	0.052	n.d.	0.69	93.681
Association II	n.d.	n.d.	n.d.	n.d.	n.d.	n.d.	n.d.	n.d.	91.799	n.d.	n.d.	1.118	n.d.	n.d.	n.d.	0.679	94.06
Association II	n.d.	n.d.	n.d.	0.141	n.d.	n.d.	n.d.	n.d.	93.696	n.d.	n.d.	0.203	n.d.	n.d.	n.d.	0.715	95.139
Association II	n.d.	n.d.	n.d.	n.d.	n.d.	n.d.	0.117	n.d.	92.796	n.d.	n.d.	n.d.	n.d.	n.d.	n.d.	0.609	93.756
Association II	n.d.	n.d.	n.d.	0.133	n.d.	n.d.	n.d.	n.d.	91.588	n.d.	n.d.	n.d.	n.d.	n.d.	n.d.	0.583	92.455
Association II	n.d.	n.d.	n.d.	n.d.	n.d.	n.d.	n.d.	n.d.	93.17	n.d.	n.d.	n.d.	n.d.	n.d.	n.d.	0.551	93.795
Association II	0.081	n.d.	0.616	1.077	n.d.	n.d.	n.d.	n.d.	89.162	n.d.	n.d.	1.91	0.395	n.d.	0.104	0.566	94.064
Association II	n.d.	n.d.	n.d.	0.059	n.d.	n.d.	0.087	n.d.	92.218	n.d.	n.d.	n.d.	n.d.	n.d.	n.d.	0.586	93.02
Association II	n.d.	n.d.	0.121	0.221	n.d.	n.d.	n.d.	n.d.	91.757	n.d.	n.d.	0.516	0.155	n.d.	n.d.	0.554	93.385
Association II	n.d.	n.d	n.d.	n.d.	n.d	n.d.	n.d.	n.d.	93.04	n.d.	n.d.	n.d.	n.d.	n.d.	n.d.	0.57	93.84

		.			.				1								5
Association II	0.072	n.d.	n.d.	n.d.	n.d.	n.d.	n.d.	n.d.	92.837	n.d.	n.d.	n.d.	n.d.	n.d.	n.d.	0.589	93.777
Association III	n.d.	n.d.	n.d.	0.076	n.d.	n.d.	0.115	n.d.	91.686	n.d.	n.d.	n.d.	n.d.	n.d.	n.d.	0.186	92.157
Association III	n.d.	n.d.	n.d.	0.065	n.d.	n.d.	0.091	n.d.	91.862	n.d.	n.d.	n.d.	n.d.	n.d.	n.d.	0.178	92.279
Association III	n.d.	n.d.	n.d.	0.037	n.d.	n.d.	0.303	n.d.	91.937	n.d.	n.d.	n.d.	n.d.	n.d.	n.d.	0.219	92.794
Association III	n.d.	n.d.	n.d.	0.055	n.d.	n.d.	0.148	n.d.	92.284	n.d.	n.d.	n.d.	n.d.	n.d.	n.d.	0.186	92.788
Association III	n.d.	n.d.	n.d.	0.049	n.d.	n.d.	0.055	n.d.	92.417	n.d.	n.d.	n.d.	n.d.	n.d.	n.d.	0.216	92.9
Association III	n.d.	n.d.	n.d.	0.015	n.d.	n.d.	0.105	n.d.	92.422	n.d.	n.d.	n.d.	n.d.	n.d.	n.d.	0.27	92.998
Association III	n.d.	n.d.	n.d.	0.051	n.d.	n.d.	n.d.	n.d.	92.958	n.d.	n.d.	n.d.	n.d.	n.d.	n.d.	0.207	93.372
Association III	n.d.	n.d.	n.d.	0.044	n.d.	n.d.	0.205	n.d.	92.892	n.d.	n.d.	0.056	n.d.	n.d.	n.d.	0.178	93.613
Association III	n.d.	n.d.	n.d.	0.058	n.d.	n.d.	0.133	n.d.	92.591	n.d.	n.d.	n.d.	n.d.	n.d.	n.d.	0.202	93.093
Association IV	n.d.	n.d.	0.371	0.096	n.d.	n.d.	n.d.	0.1	89.546	n.d.	n.d.	1.294	n.d.	n.d.	n.d.	0.094	91.655
Association IV	0.168	n.d.	0.328	0.696	n.d.	n.d.	n.d.	n.d.	88.177	n.d.	n.d.	2.325	0.107	0.299	n.d.	0.101	92.377
Association IV	n.d.	n.d.	0.357	0.327	n.d.	n.d.	0.062	n.d.	89.209	n.d.	n.d.	1.965	0.083	0.142	n.d.	0.078	92.359
Association IV	n.d.	n.d.	n.d.	0.089	n.d.	n.d.	n.d.	n.d.	91.954	n.d.	n.d.	n.d.	n.d.	n.d.	n.d.	0.059	92.21
Association IV	n.d.	n.d.	n.d.	0.051	n.d.	n.d.	n.d.	n.d.	90.834	n.d.	n.d.	n.d.	n.d.	n.d.	n.d.	0.077	91.135
Association	n.d.	n.d	n.d.	n.d.	n.d	0.04	n.d.	n.d.	91.58	n.d.	n.d.	0.17	n.d.	n.d.	n.d.	0.106	92.16

IV		.			.	4			5			8					7
Association IV	0.105	n.d.	0.536	0.699	n.d.	n.d.	n.d.	n.d.	84.838	n.d.	n.d.	2.577	0.159	0.29	0.104	0.104	89.862

Table 2 Trace element composition of magnetite from Bagjata U deposit and results of magnetite thermometry

Association No.	I	I	I	I	I	I	I	I	I
Temperature (TMg) in °C	418.14	332.76	680.32	627.22	417.91	341.84	445.56	327.81	576.38
Li7	0.52	0.20	13.88	8.06	0.56	0.25	0.93	0.07	4.15
Be9	4.42	0.00	3.37	7.14	7.37	0.00	7.84	0.00	8.46
Na23	633.57	17.93	344.01	755.29	134.17	6.02	181.69	10.20	527.04
Mg24	89.67	15.31	2,793.67	1,627.07	89.29	18.90	142.21	13.62	912.44
Al27	1,417.94	794.52	10,297.19	8,651.16	2,398.91	1,091.20	3,187.18	1,071.45	9,389.77
Si29	3,565.02	967.07	18,204.66	19,304.07	12,713.35	445.98	7,056.11	0.00	13,420.62
Ca44	182.44	225.22	294.25	775.29	0.00	35.66	189.93	0.00	583.04
Sc45	1.54	1.36	4.90	6.63	6.80	0.86	3.61	0.89	10.61
Ti49	575.93	235.19	955.32	1,818.97	422.85	346.25	319.72	270.02	464.74
V51	10,693.19	17,252.75	22,165.56	22,670.33	23,050.61	23,056.91	23,769.05	23,161.27	24,386.50
Cr52	39.62	202.60	157.55	176.48	39.83	96.17	200.27	213.03	188.89
Mn55	209.30	153.62	239.59	416.43	214.04	213.05	213.94	204.89	252.46
Co59	81.12	72.42	103.41	97.55	88.94	90.05	102.44	90.84	102.73
Ni60	754.60	571.47	742.42	707.62	705.72	729.71	685.73	663.95	743.67
Cu63	7.04	0.31	2.50	15.60	0.22	0.21	2.69	0.00	7.90
Zn66	8.17	5.95	14.42	19.70	7.78	7.66	6.98	5.66	11.68
Ga71	167.13	151.06	240.23	247.35	203.89	205.01	236.72	208.09	229.54
Ge73	6.08	6.57	8.27	7.92	7.05	5.76	9.64	11.00	6.16
As75	0.31	0.00	0.00	1.01	0.47	0.00	0.09	0.94	0.00
Rb85	0.71	0.01	64.05	39.76	0.34	0.00	3.49	0.00	28.37
Sr88	1.96	0.16	2.32	6.99	4.21	0.00	5.11	0.00	5.04
Y89	1.23	0.02	1.46	25.01	4.10	0.01	4.05	0.04	6.33
Zr90	0.00	0.03	0.10	0.20	0.10	0.00	0.00	0.03	0.17
Nb93	0.53	0.04	1.91	3.39	1.47	0.11	1.63	0.00	1.91

Mo95	0.00	0.00	0.00	1,056.32	0.00	0.00	0.96	0.06	1,080.45
Ag107	0.00	0.00	0.18	0.00	0.00	0.00	0.00	0.00	0.20

Continued Association I									
Cd111	0.00	0.26	0.00	0.52	0.06	0.04	0.25	0.00	0.00
In115	0.00	0.00	0.03	0.02	0.00	0.04	0.01	0.00	0.00
Sn118	1.69	0.86	1.10	3.69	2.57	1.34	2.43	0.24	2.85
Sb121	0.28	0.03	0.94	1.30	0.55	0.00	0.32	0.00	0.54
Cs133	0.15	0.00	2.10	1.80	0.01	0.00	0.15	0.00	0.81
Ba137	5.32	0.21	56.27	47.77	8.46	0.04	16.46	0.00	36.52
La139	0.02	0.01	0.16	52.97	0.17	0.00	0.29	0.00	0.32
Ce140	0.20	0.02	0.17	134.28	0.99	0.01	0.72	0.00	1.05
Pr141	0.06	0.01	0.04	15.40	0.27	0.00	0.10	0.00	0.14
Nd146	0.11	0.00	0.00	56.17	1.26	0.00	0.48	0.00	0.96
Sm147	0.00	0.04	0.00	13.86	0.82	0.03	0.03	0.00	0.28
Eu153	0.00	0.02	0.00	0.88	0.06	0.00	0.05	0.00	0.06
Gd157	0.07	0.04	0.00	13.51	1.20	0.00	0.39	0.00	0.42
Tb159	0.00	0.00	0.02	2.05	0.12	0.00	0.14	0.00	0.17
Dy163	0.25	0.00	0.33	11.73	0.65	0.00	0.96	0.00	1.60
Ho165	0.03	0.00	0.04	1.83	0.17	0.00	0.15	0.00	0.37
Er166	0.23	0.00	0.41	2.79	0.70	0.00	0.65	0.00	1.48
Tm169	0.07	0.00	0.04	0.37	0.11	0.00	0.08	0.01	0.17
Yb172	0.33	0.02	0.42	2.19	1.18	0.00	0.87	0.00	1.47
Lu175	0.04	0.00	0.00	0.30	0.21	0.00	0.19	0.00	0.22
Hf178	0.00	0.00	0.00	0.00	0.00	0.00	0.00	0.00	0.00
Ta181	0.04	0.01	0.18	0.28	0.21	0.00	0.12	0.01	0.13
W182	0.19	0.00	0.58	16.72	0.52	0.02	1.91	0.00	0.68
Au197	0.00	0.05	0.00	0.37	0.00	0.01	0.00	0.05	0.04
Pb208	1.46	1.21	6.46	6.76	0.09	0.03	0.47	0.02	1.84
Bi209	0.05	0.00	0.31	5.32	0.03	0.01	0.18	0.00	0.65

Th232	0.02	0.00	0.02	2.00	0.02	0.00	0.03	0.00	0.07
U238	0.69	1.11	4.40	7.78	0.55	0.16	5.14	0.00	2.30

Association No.	II	II	II	II	II	II	II	II	II	II	II
Temperature (TMg) in °C	390.71	426.53	490.46	409.87	360.25	363.04	468.12	359.16	486.65	585.80	346.36
Li7	0.12	0.31	0.19	1.85	0.04	0.06	0.53	0.03	0.19	2.09	0.25
Be9	0.08	0.27	0.21	0.29	0.00	0.03	0.68	0.00	0.00	0.22	0.06
Na23	31.62	23.12	118.30	41.34	6.41	21.38	112.50	10.78	253.37	74.45	11.66
Mg24	52.81	104.09	293.07	76.83	28.15	29.90	207.67	27.78	268.41	1,042.37	20.59
Al27	933.27	620.21	1,823.84	934.87	2,316.03	671.51	987.58	410.05	894.75	1,643.59	114.11
Si29	994.48	928.39	3,411.60	4,393.59	202.86	664.42	1,727.91	451.23	4,459.61	3,349.10	316.87
Ca44	409.76	74.40	119.25	73.30	55.68	0.00	195.22	0.00	304.19	0.00	2.57
Sc45	1.27	1.21	2.92	7.79	0.71	0.25	2.13	0.87	1.58	1.17	0.52
Ti49	100.76	108.18	108.02	119.40	96.09	83.71	365.71	176.92	151.82	290.81	28.00
V51	6,493.08	7,208.90	6,343.15	6,215.89	6,468.57	6,728.82	7,920.48	7,039.04	7,436.56	7,728.22	1,719.04
Cr52	226.61	611.36	274.63	319.37	835.45	909.85	173.78	787.12	441.69	123.35	92.90
Mn55	62.09	63.21	73.53	61.63	63.06	60.24	98.07	72.09	71.52	79.14	15.02
Co59	32.51	31.28	250.66	35.04	34.70	33.82	35.27	31.62	32.64	36.56	6.54
Ni60	243.84	269.90	729.01	293.88	256.73	254.78	285.97	257.11	256.32	299.28	61.13
Cu63	0.05	1.11	2,912.94	1.40	0.25	0.43	0.17	0.10	4.34	0.08	0.04
Zn66	1.92	2.77	36.90	7.02	4.67	3.91	5.19	3.01	23.12	5.02	1.79
Ga71	45.31	50.65	47.35	44.64	48.47	49.08	56.64	47.99	48.93	59.34	13.41

Ge73	6.45	4.84	4.92	6.19	4.91	6.36	4.49	4.97	4.54	5.74	0.86
As75	0.00	0.00	0.71	0.20	1.14	0.06	0.84	0.41	1.21	0.00	0.00
Rb85	0.03	0.35	0.31	0.32	0.01	0.03	0.76	0.01	1.22	9.98	0.17
Sr88	0.95	0.03	0.78	0.73	0.05	0.09	1.03	0.06	1.63	0.23	0.02
Y89	11.55	3.67	10.95	55.67	0.12	0.03	1.74	0.05	3.00	0.04	2.96
Zr90	0.91	480.44	0.17	8,605.70	0.05	0.01	0.06	0.01	0.25	0.00	537.16
Nb93	0.13	0.08	0.10	0.34	0.00	0.05	0.10	0.02	0.17	0.32	0.05
Mo95	0.00	0.06	0.15	0.10	0.05	0.00	0.08	0.02	0.03	0.01	0.00
Ag107	0.01	0.21	3.12	3.83	0.49	0.13	0.00	0.00	0.16	0.06	0.17
Cd111	0.08	0.56	0.23	1.11	0.13	0.98	0.00	0.02	0.37	0.01	0.08
In115	0.00	0.00	0.19	0.02	0.00	0.01	0.00	0.01	0.00	0.01	0.00
Sn118	1.19	0.26	1.08	0.63	0.49	0.52	0.82	0.30	0.65	0.66	0.06

Continued Association II											
Sb121	0.11	0.20	0.17	0.20	0.14	0.00	0.16	0.08	0.26	0.06	0.02
Cs133	0.01	0.04	0.01	0.03	0.00	0.00	0.12	0.00	0.05	0.27	0.01
Ba137	0.12	0.00	1.42	2.32	0.33	0.21	5.31	0.05	1.52	10.57	0.12
La139	112.82	0.00	11.83	3.49	0.14	0.05	0.20	0.09	1.17	0.02	0.00
Ce140	148.24	0.00	17.88	8.62	0.30	0.07	0.35	0.07	34.29	0.04	0.00
Pr141	9.68	0.00	1.62	0.88	0.03	0.00	0.05	0.01	0.19	0.00	0.00
Nd146	29.86	0.00	7.26	3.99	0.11	0.01	0.17	0.05	0.80	0.06	0.00
Sm147	3.97	0.00	2.03	1.52	0.04	0.00	0.04	0.00	0.32	0.00	0.01
Eu153	1.58	0.01	0.18	0.10	0.00	0.00	0.01	0.00	0.02	0.00	0.00
Gd157	4.00	0.05	2.60	1.54	0.04	0.02	0.14	0.02	0.19	0.01	0.04
Tb159	0.37	0.01	0.41	0.43	0.01	0.00	0.03	0.00	0.04	0.00	0.02
Dy163	2.41	0.31	2.63	5.53	0.00	0.01	0.24	0.01	0.37	0.00	0.12
Ho165	0.40	0.11	0.43	1.71	0.01	0.00	0.07	0.00	0.08	0.00	0.06
Er166	1.11	0.57	1.10	10.42	0.06	0.00	0.28	0.01	0.20	0.00	0.48
Tm169	0.11	0.24	0.15	3.25	0.00	0.00	0.06	0.00	0.06	0.00	0.20

Yb172	0.95	3.27	0.74	43.88	0.03	0.01	0.31	0.01	0.31	0.00	3.14
Lu175	0.08	0.99	0.10	9.80	0.01	0.00	0.04	0.00	0.08	0.01	0.84
Hf178	0.02	15.66	0.02	208.06	0.00	0.00	0.02	0.01	0.00	0.00	14.51
Ta181	0.00	0.01	0.01	0.42	0.00	0.00	0.01	0.00	0.00	0.01	0.03
W182	0.03	0.03	0.06	0.11	0.00	0.00	0.38	0.01	0.14	0.04	0.00
Au197	0.01	0.12	0.74	0.26	0.00	0.00	0.01	0.00	0.03	0.00	0.00
Pb208	0.21	0.23	8.25	2.87	0.32	0.72	0.44	0.57	9.02	0.46	0.05
Bi209	0.00	0.00	8.50	0.01	0.01	0.00	0.06	0.00	0.03	0.01	0.00
Th232	0.11	0.46	0.05	7.39	0.02	0.02	0.03	0.01	0.09	0.00	0.08
U238	0.76	2.74	2.16	49.51	0.17	0.11	0.04	0.01	0.43	0.01	5.12

Association No.	II	II	II	II	II	II	II	II	II	II	II
Temperature (TMg) in °C	363.15	565.26	431.41	419.69	399.75	542.40	412.96	719.10	510.98	857.38	354.09
Li7	0.09	0.19	0.50	<0.149	<0.33	0.55	0.18	5.52	0.53	16.95	2.78
Be9	0.00	<0.33	<0.00	1.19	<0.00	0.17	0.07	2.85	1.46	0.83	2.28
Na23	7.65	52.35	<8.02	28.24	<4.52	8.13	9.29	414.34	151.04	784.37	91.54
Continued Association II											
Mg24	29.98	776.52	110.75	89.82	63.09	596.06	80.70	3,969.76	390.70	11,915.81	812.14
Al27	534.21	794.95	736.55	805.34	637.99	1,290.33	725.10	7,692.96	1,522.58	20,083.12	2,896.04
Si29	494.80	6,179.72	<2674.65	4,597.01	<1459.63	2,639.75	4,109.09	16,482.49	3,477.60	35,246.87	8,253.05
Ca44	32.35	<166.14	<632.57	<166.05	<347.27	<395.84	<167.37	1,055.61	198.34	<248.40	29.53
Sc45	0.76	1.79	<3.91	1.39	<2.04	<2.38	1.41	7.97	3.14	7.93	2.01
Ti49	256.97	309.85	310.59	294.06	302.43	373.30	503.85	779.44	460.77	2,318.90	324.20
V51	8,280.24	5,107.08	4,753.01	4,216.58	4,048.33	4,176.68	5,334.50	4,641.66	4,198.98	3,988.12	3,824.83
Cr52	49.09	37.91	575.29	24.21	587.26	948.60	32.76	445.43	<7.10	332.24	83.46

Mn55	85.42	135.86	96.61	88.03	84.14	88.56	120.54	136.30	114.89	217.14	80.48
Co59	35.67	47.55	48.79	41.62	43.35	46.91	48.37	53.95	44.51	64.82	37.87
Ni60	314.90	322.30	325.10	271.65	298.65	315.49	322.00	357.37	293.93	453.00	300.10
Cu63	0.17	0.21	<1.09	1.53	<0.45	<0.51	<0.25	<0.49	113.10	<0.34	0.00
Zn66	7.23	6.52	<4.94	5.16	6.07	3.85	4.66	10.48	10.87	18.37	4.58
Ga71	68.14	69.63	70.69	62.85	63.91	72.19	68.32	74.78	63.11	80.17	58.10
Ge73	5.63	6.08	9.31	5.95	6.57	5.83	4.93	6.97	4.18	6.44	1.70
As75	0.00	<4.70	<16.37	<4.24	<9.02	<10.23	<4.19	<7.87	<3.92	<6.32	0.00
Rb85	0.02	<0.042	0.52	0.08	0.09	5.72	0.07	54.80	0.69	192.19	17.72
Sr88	0.08	0.11	<0.101	1.43	0.05	0.05	0.06	1.68	1.54	0.71	1.13
Y89	0.01	0.42	1.34	0.54	0.05	0.25	0.06	3.19	1.98	1.74	3.16
Zr90	0.00	0.05	448.29	<0.00	18.19	70.90	<0.00	11.84	0.01	175.88	0.00
Nb93	0.03	0.58	0.08	0.52	0.06	0.42	0.24	1.63	0.44	5.58	1.13
Mo95	0.03	<0.274	<0.51	<0.137	<0.29	<0.65	<0.34	<0.23	<0.23	<0.28	0.00
Ag107	0.04	<0.141	<0.58	<0.142	<0.31	<0.34	<0.131	<0.28	<0.125	<0.21	0.00
Cd111	0.01	<0.31	0.54	0.09	<0.64	<0.73	0.05	<0.00	0.52	<0.44	0.00
In115	0.01	n.a.	n.a.	n.a.	n.a.	n.a.	n.a.	n.a.	n.a.	n.a.	0.00
Sn118	0.68	1.60	<2.85	1.08	<1.55	1.85	0.83	2.10	2.13	4.92	0.90
Sb121	0.09	0.23	0.71	0.20	<0.31	<0.43	<0.159	0.45	0.45	0.48	0.02
Cs133	0.01	0.00	0.02	<0.0144	<0.042	0.16	0.01	1.96	0.14	6.16	0.54
Ba137	0.67	0.54	0.51	1.77	0.22	5.26	0.28	37.78	3.93	132.66	18.78
La139	0.02	0.00	<0.00	0.01	0.01	0.29	0.01	2.31	0.06	0.24	14.07
Ce140	0.01	0.02	0.01	<0.00	<0.032	0.51	0.00	4.82	0.15	0.64	20.77
Pr141	0.00	<0.00	<0.00	<0.0126	0.02	0.05	<0.00	0.60	0.03	0.07	2.37
Continued Association II											
Nd146	0.02	0.02	<0.00	<0.00	<0.226	0.16	<0.072	2.24	0.12	0.36	7.60
Sm147	0.00	0.02	<0.00	<0.00	<0.00	0.10	<0.122	0.39	0.02	0.14	2.60
Eu153	0.00	<0.00	0.02	<0.00	0.01	0.01	<0.00	0.07	0.01	0.02	0.38
Gd157	0.00	0.02	<0.00	0.04	<0.254	<0.00	<0.00	0.61	0.12	0.17	1.91
Tb159	0.00	<0.0136	<0.00	0.00	<0.00	<0.00	0.01	0.09	0.03	0.05	0.20
Dy163	0.00	0.09	0.09	0.05	0.02	<0.125	0.01	0.73	0.38	0.23	1.03

Ho165	0.00	0.02	0.07	0.02	<0.00	0.05	0.00	0.15	0.07	0.05	0.18
Er166	0.00	0.07	0.35	0.06	0.02	0.04	<0.00	0.37	0.19	0.36	0.25
Tm169	0.00	<0.00	0.14	0.01	0.02	<0.029	<0.00	0.10	0.04	0.09	0.02
Yb172	0.01	0.12	2.92	0.09	0.08	0.53	0.03	0.66	0.20	1.10	0.26
Lu175	0.00	0.02	0.49	0.02	0.02	0.14	<0.00	0.08	0.05	0.31	0.05
Hf178	0.00	<0.00	11.82	<0.00	0.47	1.70	<0.00	0.28	<0.037	4.79	0.00
Ta181	0.00	0.05	<0.044	0.03	0.01	0.04	0.01	0.15	0.03	0.32	0.08
W182	0.00	0.14	<0.176	0.05	0.02	<0.00	0.11	0.20	0.36	0.66	0.14
Au197	0.01	<0.57	<2.35	<0.57	<1.18	<1.33	<0.60	<1.08	<0.54	<0.87	0.01
Pb208	0.72	<0.080	<0.252	<0.067	<0.127	<0.152	<0.088	<0.147	1.03	1.51	0.24
Bi209	0.01	0.02	<0.082	<0.035	<0.060	<0.068	0.01	<0.045	0.12	0.08	0.01
Th232	0.00	<0.00	<0.00	<0.00	<0.00	0.01	<0.00	<0.00	0.02	0.20	0.03
U238	0.01	0.00	3.86	0.01	0.10	0.39	0.01	0.25	0.03	1.45	1.42

Association No.	II	II	II	II	II	II	II	II	II	II
Temperature (TMg) in °C	319.45	564.99	323.62	434.89	315.75	513.35	540.64	360.37	327.05	328.74
Li7	0.10	0.44	0.00	1.79	2.32	0.20	0.00	0.04	0.04	0.22
Be9	0.00	2.89	0.07	1.85	6.16	0.09	0.22	0.10	0.00	0.00
Na23	2.42	67.54	0.47	131.10	305.77	29.55	41.84	2.02	0.26	13.40
Mg24	12.42	120.34	10.17	412.58	595.09	29.07	13.45	13.94	11.15	25.08
Al27	585.51	1,069.15	497.62	3,760.30	3,888.09	757.90	593.29	396.15	669.80	667.17
Si29	1,127.36	2,869.56	293.24	4,000.85	6,560.98	1,396.53	446.94	1,555.45	51.95	497.51
Ca44	0.00	118.73	0.00	462.34	1,055.98	128.04	59.88	0.00	0.00	90.14
Sc45	0.38	0.75	0.26	2.05	1.95	0.00	0.00	0.12	0.00	0.86

Continued Association II										
Ti49	145.24	277.87	263.73	402.44	501.52	170.96	158.97	171.46	152.76	103.47
V51	3,771.82	3,691.19	3,621.31	4,141.29	4,032.06	3,541.47	3,490.55	3,617.08	3,622.20	3,231.92
Cr52	164.84	49.81	84.15	75.76	103.17	57.03	76.30	37.69	144.48	97.99
Mn55	54.55	70.88	67.81	104.08	77.79	78.50	65.77	63.64	61.67	62.25
Co59	39.47	38.86	36.72	41.45	44.85	39.11	22.12	39.70	39.74	42.79
Ni60	306.08	334.06	315.03	362.34	355.60	352.90	395.17	336.13	292.36	264.54
Cu63	0.00	0.21	0.00	0.41	0.02	0.00	0.62	23.93	0.04	0.00
Zn66	3.36	4.97	3.72	12.71	6.52	6.67	3.38	4.24	3.16	3.99
Ga71	56.27	56.04	51.63	67.61	72.00	38.88	43.14	43.85	57.70	52.99
Ge73	5.87	6.33	4.60	11.11	7.92	5.58	5.55	5.89	4.88	2.44
As75	0.00	0.00	0.00	0.00	4.36	0.00	0.00	0.21	0.00	0.00
Rb85	0.00	0.22	0.00	6.49	1.65	0.34	0.07	0.07	0.02	0.21
Sr88	0.01	1.18	0.01	2.02	3.41	1.09	0.10	0.01	0.04	0.31
Y89	0.00	0.76	0.30	17.84	6.87	1.11	0.18	0.02	0.01	0.84
Zr90	0.00	0.00	0.02	0.00	0.03	0.00	0.00	0.01	0.00	0.00
Nb93	0.07	0.63	0.17	0.50	0.96	0.27	0.17	0.05	0.08	0.09
Mo95	0.22	0.07	0.00	0.21	0.00	0.01	0.00	0.06	0.00	0.00
Ag107	0.09	0.00	0.04	0.00	0.15	0.00	0.00	0.00	0.06	0.00
Cd111	0.00	0.00	0.00	0.05	0.00	0.00	0.07	0.00	0.06	0.06
In115	0.02	0.00	0.00	0.00	0.02	0.01	0.01	0.00	0.00	0.02
Sn118	0.62	0.75	0.10	0.28	2.13	0.58	0.38	0.42	0.31	0.42
Sb121	0.15	0.26	0.00	0.34	0.53	0.09	0.03	0.00	0.04	0.10
Cs133	0.01	0.03	0.01	0.16	0.16	0.05	0.00	0.00	0.00	0.00
Ba137	0.12	2.38	0.00	8.26	11.35	3.53	0.48	0.22	0.00	0.24
La139	0.01	1.04	1.04	78.32	10.88	2.12	0.58	0.09	0.04	0.31
Ce140	0.02	1.96	2.38	142.25	20.74	3.89	0.74	0.30	0.05	1.02
Pr141	0.00	0.20	0.21	14.06	2.04	0.30	0.07	0.02	0.00	0.16
Nd146	0.02	0.97	0.83	53.83	7.44	1.58	0.26	0.10	0.02	0.52
Sm147	0.00	0.28	0.16	9.73	1.42	0.24	0.05	0.00	0.00	0.04
Eu153	0.00	0.03	0.01	1.02	0.15	0.04	0.04	0.00	0.00	0.03

Gd157	0.00	0.16	0.14	10.91	1.66	0.30	0.03	0.00	0.00	0.20
Tb159	0.00	0.04	0.01	1.24	0.26	0.07	0.00	0.00	0.00	0.03
Dy163	0.00	0.10	0.08	5.50	1.25	0.16	0.03	0.01	0.00	0.21
Ho165	0.00	0.04	0.01	0.94	0.22	0.06	0.01	0.00	0.00	0.04

Continued Association II										
Er166	0.00	0.09	0.04	2.00	0.77	0.04	0.02	0.01	0.00	0.10
Tm169	0.00	0.01	0.00	0.15	0.14	0.03	0.01	0.00	0.00	0.04
Yb172	0.00	0.11	0.01	1.06	1.15	0.22	0.08	0.00	0.02	0.10
Lu175	0.00	0.03	0.01	0.09	0.22	0.02	0.00	0.01	0.00	0.03
Hf178	0.00	0.00	0.00	0.00	0.00	0.00	0.00	0.00	0.00	0.00
Ta181	0.01	0.05	0.00	0.03	0.05	0.00	0.00	0.00	0.00	0.01
W182	0.00	38.37	0.00	15.18	0.99	0.03	0.00	0.00	0.00	0.00
Au197	0.06	0.00	0.05	0.10	0.00	0.00	0.05	0.05	0.00	0.01
Pb208	0.17	0.44	1.38	0.93	1.11	1.85	0.43	0.03	0.00	0.04
Bi209	0.00	3.36	0.01	0.10	0.29	0.01	0.01	0.01	0.00	0.00
Th232	0.00	0.01	0.00	0.15	0.01	0.00	0.00	0.00	0.00	0.00
U238	0.01	0.32	0.21	5.18	1.71	1.57	0.22	0.03	0.02	1.12

Association No.	III	III	III	III	III	III	III	III	III	III	III	III
Temperature (TMg) in °C	310.54	292.67	335.01	377.51	445.80	495.85	343.54	316.15	316.38	317.28	305.00	316.50
Li7	0.05	0.00	0.06	0.10	0.50	1.31	0.06	0.07	0.01	0.00	0.00	0.06
Be9	0.00	0.00	0.00	0.00	0.00	0.00	0.00	0.07	0.32	0.08	0.00	0.00
Na23	1.92	1.44	62.56	49.62	268.60	629.02	230.19	4.04	0.00	0.68	13.83	19.10
Mg24	8.84	5.54	16.15	40.69	145.44	318.91	19.69	10.25	10.30	10.54	7.72	10.34
Al27	520.14	404.27	755.21	810.03	1,560.8	4,943.36	535.09	496.79	796.83	583.88	549.51	617.15

					3							
Si29	474.16	1,264.41	1,719.29	1,650.21	117.12	6,124.45	1,024.31	1,069.09	1,423.77	804.83	1,163.45	1,895.10
Ca44	108.35	0.00	203.79	0.00	105.75	865.76	293.92	83.23	0.00	106.62	0.00	0.00
Sc45	0.00	0.27	0.00	0.90	0.00	0.76	0.49	0.39	0.15	0.24	0.00	1.05
Ti49	404.86	239.50	393.83	460.70	304.57	22,164.73	199.63	198.81	332.60	422.54	335.44	298.28
V51	1,610.25	1,427.92	1,861.36	1,648.18	2,258.58	1,992.45	2,068.65	1,674.93	1,767.37	1,858.36	1,803.19	1,786.52
Cr52	1,122.47	505.97	1,784.06	862.90	717.32	641.99	703.18	1,565.24	1,188.66	293.61	1,041.21	443.01
Mn55	66.59	48.80	62.69	90.39	72.38	873.75	59.79	69.15	87.62	98.84	88.22	76.18
Co59	46.31	43.85	47.87	48.64	48.88	54.19	48.03	54.95	56.14	59.88	59.70	58.56
Ni60	660.27	640.82	629.75	619.93	609.75	660.63	591.01	662.79	762.50	704.31	712.10	718.27
Cu63	0.15	0.00	0.22	0.13	0.22	3.03	3.99	0.00	0.39	0.15	0.17	0.00

Continued Association III												
Zn66	3.09	2.81	6.64	1.96	4.40	16.52	0.00	3.25	1.61	4.38	3.71	5.73
Ga71	40.79	42.84	41.05	37.93	34.77	30.94	31.81	43.33	51.17	52.63	51.54	50.97
Ge73	6.52	6.80	6.88	7.06	6.29	6.43	5.33	6.86	0.57	7.29	7.06	7.45
As75	0.08	0.10	1.06	0.00	0.80	0.45	0.00	0.00	0.00	0.00	0.25	1.26
Rb85	0.00	0.01	0.41	0.16	1.59	10.14	0.00	0.05	0.00	0.00	0.02	0.09
Sr88	0.03	0.01	0.17	0.32	0.21	1.35	0.28	0.00	0.03	0.00	0.02	0.02
Y89	0.00	0.01	0.03	0.43	0.15	1.44	0.05	0.02	1.98	0.02	0.01	0.11
Zr90	0.00	0.00	0.00	11.56	0.00	0.09	0.00	0.00	231.78	5.95	0.70	22.39
Nb93	0.81	0.43	0.93	0.73	0.84	73.27	0.00	0.05	0.32	0.06	0.53	2.40
Mo95	0.00	0.10	0.00	0.00	0.00	0.00	0.39	0.04	0.00	0.05	0.07	0.00
Ag107	0.03	0.10	0.00	0.00	0.29	0.00	0.20	0.00	0.00	0.00	0.05	0.00
Cd111	0.15	0.04	0.00	0.09	0.00	0.00	0.00	0.00	0.00	0.00	0.23	0.00
In115	0.00	0.00	0.02	0.01	0.03	0.05	0.00	0.00	0.00	0.01	0.01	0.03
Sn118	0.82	0.21	0.23	0.38	0.29	0.61	0.30	0.30	0.76	0.74	0.43	0.34
Sb121	0.00	0.00	0.22	0.12	9.11	0.00	0.13	0.05	0.14	0.00	0.06	0.37
Cs133	0.00	0.00	0.04	0.00	0.04	0.28	0.00	0.01	0.00	0.00	0.01	0.02
Ba137	0.14	0.24	0.92	1.44	3.30	16.05	1.95	0.41	0.15	0.00	0.00	0.40
La139	0.00	0.00	0.00	0.49	0.12	1.27	0.12	0.00	0.00	0.00	0.00	0.00
Ce140	0.01	0.00	0.00	1.16	0.39	2.39	0.26	0.00	0.00	0.01	0.00	0.03
Pr141	0.01	0.00	0.00	0.07	0.07	0.31	0.02	0.00	0.00	0.00	0.00	0.00
Nd146	0.00	0.00	0.00	0.45	0.32	1.21	0.16	0.00	0.00	0.00	0.00	0.00
Sm147	0.00	0.00	0.00	0.24	0.09	0.00	0.06	0.00	0.10	0.03	0.00	0.00
Eu153	0.01	0.00	0.00	0.00	0.00	0.10	0.00	0.00	0.00	0.00	0.00	0.00
Gd157	0.00	0.00	0.00	0.20	0.05	0.20	0.12	0.00	0.10	0.00	0.00	0.00
Tb159	0.00	0.00	0.00	0.02	0.01	0.09	0.01	0.00	0.00	0.00	0.00	0.00
Dy163	0.00	0.00	0.00	0.12	0.11	0.36	0.08	0.00	0.19	0.00	0.00	0.00
Ho165	0.00	0.00	0.00	0.02	0.01	0.06	0.02	0.00	0.08	0.00	0.00	0.00
Er166	0.00	0.01	0.00	0.09	0.00	0.35	0.00	0.00	0.31	0.01	0.00	0.00
Tm169	0.00	0.00	0.00	0.01	0.01	0.03	0.01	0.00	0.21	0.00	0.00	0.02
Yb172	0.02	0.00	0.00	0.08	0.00	0.50	0.00	0.00	1.66	0.03	0.00	0.15

Lu175	0.00	0.00	0.00	0.01	0.01	0.03	0.00	0.00	0.38	0.02	0.00	0.01
Hf178	0.00	0.00	0.00	0.44	0.00	0.00	0.00	0.00	6.07	0.30	0.13	0.27
Ta181	0.01	0.01	0.00	0.02	0.02	9.09	0.00	0.00	0.02	0.00	0.00	0.07
Continued Association III												
W182	0.00	0.00	0.00	0.02	0.03	1.25	0.00	0.01	0.00	0.00	0.00	0.03
Au197	0.00	0.03	0.09	0.00	0.00	0.00	0.21	0.02	0.02	0.02	0.00	0.00
Pb208	0.08	0.08	0.02	0.33	0.22	2.55	0.80	0.01	0.00	0.03	0.08	0.26
Bi209	0.01	0.00	0.00	0.00	0.04	0.03	0.00	0.00	0.04	0.01	0.00	0.01
Th232	0.00	0.00	0.00	0.25	0.01	0.00	0.01	0.00	0.06	0.00	0.00	0.01
U238	0.18	0.01	0.32	0.94	0.23	8.47	0.56	0.00	3.52	0.22	0.01	0.95

Association No.	IV	IV	IV	IV	IV	IV	IV	IV	IV	IV
Temperature (TMg) in °C	315.36	324.34	312.45	355.63	617.27	649.60	633.48	326.02	323.41	347.70
Li7	0.05	0.11	0.03	0.15	0.84	2.76	1.60	0.02	0.04	0.00
Be9	0.04	0.00	0.04	0.00	3.47	13.18	14.90	0.00	0.08	0.00
Na23	0.00	12.17	6.36	2.84	98.88	331.68	294.82	0.00	0.62	2.82
Mg24	9.99	12.32	8.91	25.36	1,442.35	2,001.24	1,718.08	12.65	11.69	20.97
Al27	331.08	391.91	230.74	220.71	1,062.93	2,521.44	1,900.48	326.54	393.23	413.38
Si29	169.89	1,039.12	590.73	808.82	7,184.22	7,760.02	7,150.64	884.97	455.33	2,173.86
Ca44	10.23	0.00	0.00	0.00	135.45	794.44	1,185.17	47.39	0.00	180.19
Sc45	0.90	0.31	0.09	0.00	2.79	14.15	13.77	0.16	1.04	0.00
Ti49	235.82	278.90	181.82	171.36	313.66	401.72	388.88	170.16	208.26	201.39
V51	351.35	473.68	696.11	776.26	666.05	634.22	623.51	647.17	667.67	677.21
Cr52	0.00	3.77	0.00	6.05	45.89	23.72	7.35	15.33	14.38	47.87
Mn55	42.60	46.60	34.95	33.83	117.71	100.62	96.49	41.50	43.00	35.57
Co59	31.05	29.64	29.45	30.57	33.74	32.38	32.30	31.10	29.03	32.24
Ni60	422.36	442.90	380.82	398.77	433.91	403.50	429.08	381.25	398.46	386.80
Cu63	0.02	0.37	0.00	0.00	0.25	0.34	0.28	0.07	0.27	0.15
Zn66	1.42	1.92	1.42	1.54	6.03	5.06	6.37	4.51	0.00	2.33
Ga71	35.32	34.15	34.76	31.93	40.25	39.44	39.81	33.12	34.68	32.61

Ge73	7.52	7.64	5.91	7.95	9.23	7.80	10.40	7.13	8.30	6.79
As75	0.34	0.00	0.57	0.46	1.38	2.19	1.66	0.00	0.18	0.00
Rb85	0.00	0.00	0.02	0.02	0.45	7.07	1.13	0.00	0.00	0.03
Sr88	0.00	0.05	0.08	0.00	0.68	5.98	5.97	0.00	0.00	0.02
Continued Association IV										
Y89	0.01	0.18	0.03	0.03	38.74	39.81	24.73	0.00	0.01	0.03
Zr90	0.00	0.00	0.00	0.00	4.89	0.04	0.08	0.00	0.02	0.00
Nb93	0.00	0.01	0.03	0.01	42.31	37.32	17.40	0.00	0.01	0.14
Mo95	0.03	0.05	0.00	0.04	0.17	0.04	0.00	0.00	0.12	0.04
Ag107	0.00	0.01	0.00	0.01	0.00	0.01	0.07	0.11	0.11	0.00
Cd111	0.15	0.00	0.12	0.06	0.04	0.00	0.00	0.00	0.12	0.06
In115	0.01	0.01	0.01	0.01	0.05	0.05	0.07	0.01	0.03	0.00
Sn118	2.05	2.78	1.35	1.25	7.97	9.04	10.40	1.39	1.89	1.55
Sb121	0.00	0.00	0.00	0.00	0.62	0.74	0.66	0.03	0.00	0.16
Cs133	0.00	0.00	0.00	0.00	0.04	0.27	0.04	0.00	0.00	0.00
Ba137	0.00	0.04	0.26	0.00	3.42	14.61	12.06	0.00	0.04	0.05
La139	0.00	0.03	0.00	0.01	1.69	0.43	0.67	0.00	0.01	0.00
Ce140	0.03	0.07	0.01	0.02	5.86	1.36	2.62	0.04	0.01	0.01
Pr141	0.00	0.00	0.00	0.00	0.85	0.23	0.40	0.00	0.01	0.00
Nd146	0.00	0.01	0.00	0.01	5.55	1.97	2.44	0.00	0.00	0.00
Sm147	0.00	0.01	0.00	0.02	2.23	0.91	1.26	0.00	0.00	0.00
Eu153	0.00	0.01	0.00	0.00	0.04	0.16	0.17	0.00	0.00	0.01
Gd157	0.00	0.00	0.00	0.00	3.20	2.24	2.76	0.00	0.00	0.00
Tb159	0.00	0.00	0.00	0.00	0.78	0.73	0.64	0.00	0.00	0.00
Dy163	0.00	0.02	0.01	0.00	6.43	6.98	5.64	0.00	0.02	0.00
Ho165	0.00	0.01	0.00	0.00	1.51	1.91	1.36	0.00	0.00	0.00
Er166	0.00	0.00	0.00	0.01	5.80	7.50	4.96	0.00	0.00	0.00
Tm169	0.00	0.00	0.00	0.00	1.00	1.34	0.86	0.00	0.01	0.01
Yb172	0.00	0.03	0.02	0.00	8.05	8.83	6.75	0.00	0.03	0.00
Lu175	0.00	0.00	0.00	0.00	1.40	1.16	1.11	0.00	0.00	0.00
Hf178	0.01	0.00	0.00	0.00	0.07	0.02	0.00	0.00	0.00	0.00

Ta181	0.00	0.00	0.00	0.01	1.02	0.37	0.28	0.00	0.00	0.01
W182	0.01	0.02	0.01	0.09	7.23	5.15	2.67	0.01	0.00	0.01
Au197	0.00	0.00	0.00	0.00	0.00	0.00	0.00	0.02	0.01	0.00
Pb208	0.03	0.57	0.05	0.10	0.32	0.62	0.88	0.05	0.11	0.09
Bi209	0.01	0.01	0.01	0.00	0.00	0.03	0.04	0.00	0.03	0.04
Th232	0.00	0.00	0.00	0.00	0.16	0.01	0.01	0.00	0.00	0.00
U238	0.00	0.07	0.01	0.01	3.18	3.18	1.79	0.00	0.01	0.02

Table 3 Major element Geochemistry of Biotite from Bagjata U deposit and results from biotite thermometry

Association no.	SiO2	TiO2	Al2O3	Cr2O3	FeO	MnO	MgO	NiO	Na2O	K2O	F	Cl	Total	Temp. at 0.3 Gpa/10 km depth (in °C)	Temp. at 0.06 Gpa/2 km depth (in °C)
I	37.29	0.87	15.29	0.02	18.81	0.05	11.45	0	0.19	9.56	<	0.28	94.098	446.90	431.10
I	36.66	0.91	15.98	0.00	19.95	0.17	11.21	0.138	0.24	9.73	<	0.20	95.547	446.71	430.91
I	37.33	0.97	15.28	0.04	18.34	0.14	11.88	0.122	0.10	9.71	<	0.20	94.369	451.80	435.82
I	37.25	1.02	15.55	0.00	19.18	0.15	11.90	0.158	0.15	9.68	<	0.16	95.397	451.84	435.86
I	36.55	0.95	16.48	0.00	19.35	0.00	10.84	0.16	0.22	9.58	<	0.22	94.539	459.71	443.45
I	36.87	0.95	15.77	0.00	19.42	0.01	11.26	0.091	0.16	9.67	<	0.19	94.605	454.56	438.49
I	36.95	0.97	15.69	0.01	19.56	0.00	11.14	0.236	0.17	9.44	<	0.30	94.652	458.49	442.28
I	36.85	1.13	15.53	0.00	19.70	0.09	11.44	0	0.27	9.66	<	0.21	95.326	466.11	449.63
I	36.88	1.13	15.56	0.04	20.02	0.00	11.53	0.116	0.16	9.73	<	0.33	95.785	464.61	448.18
I	36.59	1.10	15.40	0.00	20.18	0.07	11.43	0	0.16	9.75	<	0.32	95.466	461.66	445.34
I	37.37	1.04	15.85	0.02	18.15	0.07	12.62	n. a.	0.16	9.59	<	0.23	95.48	450.10	434.18
I	36.60	0.97	16.70	0.03	18.84	0.01	11.58	n. a.	0.19	9.90	<	0.17	95.352	452.80	436.79
I	36.92	0.94	15.42	0.00	18.51	0.00	11.89	n. a.	0.16	9.83	<	0.26	94.552	448.30	432.44
I	36.71	1.07	15.76	0.00	18.66	0.08	11.75	n. a.	0.19	9.95	<	0.24	94.757	459.97	443.70
I	36.26	0.89	15.87	0.06	19.64	0.04	12.01	n. a.	0.35	9.79	<	0.21	95.483	435.45	420.05
I	36.26	0.95	15.85	0.10	19.61	0.00	11.89	n. a.	0.36	9.84	<	0.26	95.458	443.58	427.89
I	36.31	1.11	15.62	0.03	19.62	0.03	11.96	n. a	0.17	10.07	<	0.29	95.559	456.30	440.16
II	37.52	0.92	15.45	0.00	18.37	0.00	12.72	0.026	0.19	9.75	<	0.33	95.487	436.99	421.54
II	37.33	0.92	15.30	0.08	18.72	0.08	12.69	0	0.18	9.58	<	0.35	95.409	435.90	420.49

II	37.85	0.94	15.27	0.01	17.85	0.05	12.65	0	0.18	9.61	<	0.33	94.882	442.51	426.87
II	37.29	0.95	15.21	0.02	17.42	0.10	12.95	0.101	0.20	9.66	<	0.34	94.431	440.23	424.67
II	37.30	0.86	15.12	0.01	18.15	0.00	12.59	0.078	0.13	9.69	<	0.35	94.502	433.26	417.94
II	37.40	1.01	15.37	0.00	17.98	0.14	13.04	0.148	0.12	9.81	<	0.21	95.439	441.53	425.92
II	37.82	0.89	15.56	0.13	18.34	0.02	13.02	0.091	0.24	9.62	<	0.26	96.119	430.00	414.80
II	37.50	0.89	15.21	0.00	18.27	0.00	12.59	0	0.17	9.71	<	0.32	94.838	435.66	420.26
II	36.60	0.98	15.49	0.00	19.89	0.06	11.78	0.147	0.20	9.31	<	0.32	94.898	448.46	432.60
II	37.10	0.90	15.29	0.00	18.13	0.00	12.92	0.152	0.17	9.56	<	0.34	94.824	433.27	417.95
II	37.20	0.86	15.35	0.00	18.39	0.00	12.38	0	0.23	9.54	<	0.24	94.422	434.90	419.52

Continued Association II															
II	37.01	0.87	15.74	0.06	18.31	0.11	13.22	n.a.	0.35	9.75	<	0.29	96.094	423.92	408.93
II	36.66	0.84	15.76	0.00	18.71	0.04	12.84	n.a.	0.30	9.81	<	0.26	95.514	423.95	408.96
II	36.40	0.84	15.54	0.00	18.46	0.00	13.24	n.a.	0.23	10.00	<	0.31	95.312	420.66	405.78
II	36.76	0.87	15.64	0.00	18.37	0.00	13.16	n.a.	0.24	9.76	<	0.32	95.557	425.49	410.44
II	36.58	0.90	15.70	0.03	18.05	0.00	13.38	n.a.	0.22	10.09	<	0.32	95.759	426.17	411.10
II	36.57	0.89	15.94	0.00	18.61	0.10	12.89	n.a.	0.21	9.83	<	0.29	95.679	427.85	412.72
II	36.60	0.95	15.91	0.07	18.13	0.07	12.97	n.a.	0.23	10.07	<	0.29	95.694	434.82	419.44
II	36.80	1.00	16.04	0.00	18.70	0.00	12.66	n.a.	0.25	9.81	<	0.31	95.913	442.09	426.46
II	36.66	0.87	15.59	0.03	19.65	0.09	12.97	n.a.	0.22	9.84	<	0.34	96.647	421.18	406.29
II	35.43	0.75	16.03	0.00	22.71	0.04	9.55	0.186	0.10	9.62	<	0.39	94.851	447.91	432.07
II	36.49	0.69	16.15	0.00	21.35	0.00	9.89	0	0.07	9.51	<	0.38	94.66	441.69	426.07
II	36.17	0.82	16.38	0.00	22.94	0.03	9.71	0	0.18	9.55	<	0.45	96.308	452.94	436.92
II	36.43	0.91	16.58	0.07	22.27	0.09	10.06	0.097	0.06	9.61	<	0.45	96.644	458.46	442.25
II	36.35	1.06	16.36	0.00	21.25	0.01	9.86	0	0.09	9.76	<	0.46	95.264	479.77	462.81
II	36.84	0.85	16.59	0.00	21.39	0.06	10.08	0.325	0.25	9.68	<	0.44	96.648	454.20	438.14
II	35.98	0.69	16.50	0.00	22.40	0.05	10.30	n.a.	0.21	9.64	<	0.41	96.385	429.84	414.64
II	35.50	0.83	16.27	0.02	22.41	0.11	10.05	n.a.	0.16	9.56	<	0.47	95.686	448.64	432.77
II	35.84	0.71	16.74	0.01	21.75	0.01	10.41	n.a.	0.10	9.77	<	0.37	95.849	432.51	417.22
II	35.79	0.81	16.57	0.06	21.41	0.00	10.11	n.a.	0.14	9.86	<	0.44	95.459	448.94	433.07

II	35.75	0.80	16.50	0.01	21.37	0.03	10.26	n.a.	0.09	9.89	<	0.43	95.286	445.56	429.81
II	36.16	1.01	16.56	0.00	21.42	0.04	10.46	n.a.	0.11	9.69	<	0.38	96.07	464.06	447.65
III	37.29	1.37	14.93	0.00	21.03	0.07	10.09	0.01	0.15	9.77	<	0.36	95.081	502.47	484.70
III	37.39	1.31	14.93	0.00	21.71	0.00	10.11	0.14	0.11	9.74	<	0.39	95.884	496.66	479.09
III	37.89	1.31	15.34	0.00	21.86	0.06	10.28	0.123	0.15	9.57	<	0.27	96.867	495.39	477.87
III	36.84	1.43	14.88	0.08	22.47	0.08	9.42	0.214	0.17	9.71	<	0.34	95.687	513.72	495.55
III	37.29	1.41	14.78	0.00	21.78	0.10	10.00	0.185	0.13	9.71	<	0.21	95.619	505.46	487.59
III	37.49	1.41	15.02	0.04	22.30	0.08	9.98	0.11	0.13	9.73	<	0.28	96.623	505.07	487.21
III	37.11	1.28	15.09	0.00	22.27	0.11	9.84	0.207	0.18	9.40	<	0.21	95.72	496.67	479.11
III	38.14	1.34	15.43	0.01	21.85	0.02	10.15	0.287	0.15	9.65	<	0.18	97.196	500.88	483.17
III	37.19	1.39	14.99	0.05	21.70	0.17	10.23	0.243	0.15	9.77	<	0.32	96.237	499.32	481.67
III	36.12	1.32	15.05	0.00	21.45	0.14	10.23	n.a.	0.12	10.07	<	0.20	94.979	491.50	474.13
III	36.89	1.15	15.59	0.02	21.77	0.01	10.27	n.a.	0.15	9.99	<	0.27	96.472	479.54	462.58
III	35.62	1.32	14.93	0.00	21.78	0.00	9.79	n.a.	0.12	9.95	<	0.34	94.086	496.67	479.11
III	36.47	1.29	15.55	0.00	21.58	0.16	10.30	n.a.	0.15	10.10	<	0.26	96.059	488.39	471.12

Table 4 Trace element composition of biotite of selected trace elements from Bagjata U deposit

Association No.	Ti49	V51	Mn55	Co59	Ni60	Ga71
I	6,518.37	1,384.52	380.10	88.16	769.55	81.39
I	7909	2013.73	561.07	132.14	1180.38	119.83
I	7810.97	2036.91	546.03	132.72	1228.02	122.72
I	8001.27	2144.35	558.62	135.11	1192.14	135.38
I	7991.88	2030.16	570.97	129.15	1136.22	130.51
I	8536.28	2234.5	564.94	136.61	1206.45	132.57
I	9170.03	2338.58	608.55	137.88	1251.13	138.38
II	4,923.40	1,091.65	294.35	75.34	643.21	44.21
II	6,039.25	1,195.36	304.18	76.86	685.06	48.75
II	5,790.94	1,235.46	307.48	79.65	648.43	50.02
II	5,725.50	1,226.66	312.71	79.75	663.45	51.27
II	5,388.94	1,261.19	302.01	80.17	603.24	52.79
II	5,691.91	1,276.20	294.00	78.14	607.22	46.62

II	5,505.13	1,212.75	290.30	76.52	628.88	50.52
III	8,660.13	198.08	533.20	99.11	1,248.55	39.34
III	8,430.51	205.89	458.88	101.96	1,203.16	33.25
III	8,690.96	299.28	512.64	102.41	1,105.30	32.30

Table 5 Major element geochemistry chlorite and results of chlorite thermometry

Association no.	SiO2	TiO2	Al2O3	FeO	MnO	MgO	Total	T1 (in °C)	T2 (in °C)	T3 (in °C)	T4 (in °C)
Association IV	24.60	0.04	19.97	28.31	0.00	13.36	86.32	338.00	363.00	369.00	319.34
Association IV	25.16	0.06	19.87	28.17	0.13	13.19	86.67	327.00	347.00	353.00	313.88
Association IV	24.31	0.05	20.10	29.15	0.07	13.36	87.22	349.00	379.00	385.00	299.19
Association IV	24.52	0.06	20.65	27.61	0.10	13.43	86.37	341.00	369.00	375.00	315.47
Association IV	24.95	0.06	20.53	27.86	0.15	13.66	87.22	337.00	362.00	368.00	299.33
Association IV	24.42	0.07	20.60	27.74	0.09	13.35	86.29	343.00	371.00	377.00	328.63
Association IV	25.78	0.10	20.27	29.27	0.14	13.36	89.42	329.00	348.00	355.00	293.097

Table 6 Major element geochemistry of apatite from Bagjata U deposit

Assoc. no.	Na2O	F	MgO	Al2O3	Cl	P2O5	Cr2O3	MnO	FeO	SiO2	K2O	CaO	TiO2	V2O3	NiO	Total
I	0.01	3.658	0	0.031	0.034	42.505	0.095	0	0.168	0	0.004	56.201	0	0	0	102.704
I	0.038	3.732	0	0	0.055	42.006	0.066	0.011	0.05	0	0	56.612	0	0.009	0	102.581
I	0.038	3.732	0	0	0.055	42.006	0.066	0.011	0.05	0	0	56.612	0	0.009	0	102.581
I	0.01	3.658	0	0.031	0.034	42.505	0.095	0	0.168	0	0.004	56.201	0	0	0	102.704
I	0.043	3.84	0	0.013	0.028	41.594	0	0	0.067	0.055	0	56.851	0	0	0	102.492
I	0.043	3.84	0	0.013	0.028	41.594	0	0	0.067	0.055	0	56.851	0	0	0	102.492
I	0.022	3.958	0	0	0.009	41.9	0	0.108	0	0.044	0	56.462	0	0	0	102.505
I	0.022	3.958	0	0	0.009	41.9	0	0.108	0	0.044	0	56.462	0	0	0	102.505
I	0.006	3.938	0	0	0.026	41.28	0.026	0.027	0.069	0	0	56.259	0.017	0	0	101.648
I	0.012	3.462	0.006	0	0.011	41.522	0	0	0	0	0	57.065	0	0.004		102.082
I	0.067	3.615	0.014	0.008	0	41.388	0	0	0.012	0.046	0.007	56.928	0.001	0.003		102.09
I	0.06	3.508	0.003	0	0.013	42.173	0.07	0.086	0	0	0	57.045	0	0.003		102.96
II	0.003	3.814	0	0.019	0.026	40.896	0.046	0.113	0	0.032	0.009	56.512	0	0.02	0	101.491
II	0.015	3.639	0	0	0.017	40.553	0	0	0	0.046	0	56.445	0	0.041	0	100.756
II	0.03	3.894	0	0.02	0.041	41.035	0	0.026	0	0.039	0.003	57.027	0	0.006	0.029	102.15
II	0.03	3.894	0	0.02	0.041	41.035	0	0.026	0	0.039	0.003	57.027	0	0.006	0.029	102.15
II	0.01	3.826	0	0	0.022	40.056	0.064	0	0.198	0	0.004	57.164	0.005	0	0	101.348

Table 7 Concentration of Vanadium and REEs in apatite from Bagjata U deposit

Assoc. no.	V51	La139	Ce140	Pr141	Nd146	Sm147	Eu153	Gd157	Tb159	Dy163	Ho165	Er166	Tm169	Yb172	Lu175
I	6.73	60.12	270.54	44.38	249.54	121.45	6.82	194.89	41.72	308.36	65.99	175.95	23.66	137.81	16.53
I	1.79	20.89	99.92	18.33	109.77	54.38	3.75	83.07	18.55	127.83	27.48	73.4	10.01	62.95	7.44
I	1.02	26.92	123.1	19.09	108.67	53.99	3.96	90.76	18.33	125.28	27.23	69.3	9.56	56.53	6.6

I	1.09	19.18	80.69	13.49	80.19	45.12	4.41	79.64	19.2	130.31	27.03	67.27	8.57	49.62	6.24
I	2.49	8.33	36.52	6.68	46.11	29.95	2.62	69.07	16.59	119.94	26.97	71.98	10.43	62.79	7.44
I	15.62	19.34	81.6	13.96	83.36	44.36	4.68	81.88	17.67	137.96	26.57	70.45	8.73	57.91	6.23
I	13.16	51.28	298.37	47.87	278.42	142.26	6.39	226.53	43.25	358.88	53.02	125.08	16.69	112.59	14.4
I	15.46	60.97	250.63	42.04	243.35	114.76	7.44	157	33.41	221.15	43.78	110.38	15.2	98.61	10.2
I	2.86	22.31	108.26	18.66	114.6	65.44	5.35	123.02	25.32	188.85	39.77	103.05	14.49	86.04	9.55
Continued															
Association no.	V51	La139	Ce140	Pr141	Nd146	Sm147	Eu153	Gd157	Tb159	Dy163	Ho165	Er166	Tm169	Yb172	Lu175
I	0.8	12.83	64.04	12.62	85.44	44.46	3.81	85.3	17.93	138.5	28.51	81	10.26	62.21	7.81
I	1.66	5.77	26.53	5.41	37.47	27.37	2.07	70.4	16.45	138.04	30.13	81.72	11.87	71.23	8.78
I	1.02	16.23	77.42	13.81	85.17	45.61	4.04	86.31	18.21	132.53	27.78	76.59	9.56	58.57	7.02
II	225.6	590.52	776.67	85.18	269.06	87.24	3.25	152.92	17.63	47.41	47.61	34.69	22.65	206.54	13.04
II	331.11	136.43	499.15	246.07	456.52	78	22.21	146.54	27.02	243.52	43.73	101.51	19.87	135.21	8.97
II	48.72	1160.54	2402.37	319.83	1226.31	141.78	19.61	137.69	27.28	181.29	40.93	140.91	19.71	150.11	21.1
II	399.91	1987.92	2044.12	350.75	788.6	117.59	8.16	79.88	11.68	75.27	18.53	66.97	11.16	77.3	10.67
II	173.15	680.29	8367.88	2694.82	6271.63	211.34	88.17	272.82	480.95	231.93	49.66	224.51	20.14	124.65	16.05

Table 8 Major element and REE composition of the host rocks of magnetite in Bagjata U deposit

Rock type	Apatite-magnetite rock	Biotite Schist	Biotite Schist	Biotite Schist	Chlorite schist	Chlorite schist	Chlorite schist	Chlorite schist	Chlorite schist
AIOCG1	0.16	0.81	0.57	0.83	0.38	0.35	0.31	0.41	0.41
AIOCG2	0.86	0.57	0.61	0.53	0.30	0.36	0.40	0.45	0.55
SiO2	25.96	47.31	47.62	49.59	72.92	60.94	59.87	62.34	47.10
TiO2	0.43	0.55	1.78	0.55	0.43	0.63	0.70	0.44	0.57
Al2O3	5.16	11.30	14.17	11.69	11.39	17.33	15.69	13.97	15.83
Fe2O3(T)	46.55	20.28	21.90	17.51	8.00	8.79	10.99	13.24	16.63
MnO	0.03	0.03	0.08	0.04	0.04	0.10	0.03	0.02	0.03
MgO	2.55	7.56	4.71	8.12	1.41	1.55	3.17	1.37	5.38
CaO	7.14	1.11	1.30	1.30	0.64	1.28	1.15	0.94	1.99
Na2O	0.39	0.51	2.21	0.34	1.53	2.84	1.90	2.42	3.46
K2O	0.70	5.38	5.17	5.37	1.61	2.60	1.50	2.88	4.21
P2O5	4.59	0.53	0.19	0.74	0.36	0.50	0.11	0.05	0.90
LOI	2.81	3.00	0.84	3.12	1.65	2.03	2.98	1.30	2.12
Total	96.30	97.56	99.96	98.37	99.97	98.59	98.09	98.97	98.21

Composition of REEs in host rock									
La	1,160.00	195.00	63.80	274.00	163.00	193.00	34.70	63.90	574.00
Ce	2,200.00	388.00	127.00	562.00	319.00	385.00	61.10	108.00	1,140.00
Pr	255.00	43.00	14.30	65.20	34.40	42.60	6.77	11.60	132.00
Nd	967.00	149.00	52.20	242.00	115.00	148.00	24.60	42.20	495.00
Sm	205.00	35.50	10.40	47.80	19.90	26.60	4.80	9.65	94.10
Eu	20.60	4.33	1.10	4.65	1.33	1.86	0.99	1.78	7.98
Gd	155.00	30.00	8.48	36.70	12.50	17.10	3.60	7.80	73.30
Tb	23.40	5.63	1.51	5.86	1.86	2.91	0.54	1.12	11.40

Dy	120.00	33.50	9.79	32.10	10.40	17.80	3.16	5.31	65.90
Ho	20.30	6.31	2.08	5.57	2.07	3.64	0.69	0.79	12.70
Er	50.90	16.50	6.37	14.60	5.95	10.40	2.06	1.98	36.10
Tm	6.97	2.33	0.91	2.13	0.89	1.46	0.34	0.31	5.48
Yb	40.70	14.30	5.72	12.90	5.65	8.99	2.36	2.09	33.80
Lu	6.07	2.14	0.86	1.69	0.87	1.34	0.40	0.34	4.41

Table 9 Major element geochemistry of magnetite and hematite from Pathargora

AREA	Association No.	Mineral	Na2O	F	MgO	Al2O3	Cl	P2O5	Cr2O3	MnO
Pathargora	Association I	Magnetite	n.d.	n.d.	n.d.	0.158	n.d.	n.d.	0.216	n.d.
Pathargora		Magnetite	n.d.	n.d.	n.d.	0.164	n.d.	n.d.	0.664	0.071
Pathargora		Magnetite	0.074	n.d.	0.071	0.123	0.067	n.d.	0.283	n.d.
Pathargora		Magnetite	n.d.	n.d.	n.d.	0.114	n.d.	n.d.	0.258	n.d.
Pathargora		Magnetite	n.d.	n.d.	0.071	0.123	n.d.	n.d.	0.254	n.d.
Pathargora		Magnetite	n.d.	n.d.	n.d.	0.084	n.d.	n.d.	0.452	n.d.
Pathargora		Magnetite	n.d.	n.d.	0.078	0.13	n.d.	n.d.	0.096	n.d.
Pathargora	Association IA	Hematite	n.d.	n.d.	n.d.	0.178	n.d.	n.d.	0.247	n.d.
Pathargora		Hematite	n.d.	n.d.	0.083	0.174	n.d.	n.d.	0.381	n.d.
Pathargora		Hematite	n.d.	n.d.	0.081	0.338	n.d.	n.d.	0.302	n.d.

Pathargora		Hematite	0.074	n.d.	n.d.	0.291	n.d.	0.109	0.444	n.d.
Pathargora		Hematite	0.08	n.d.	n.d.	0.223	n.d.	0.12	0.484	n.d.
Pathargora		Hematite	0.074	n.d.	n.d.	0.223	n.d.	0.14	0.454	n.d.
Pathargora	Association II	Magnetite	0.026	0.014	0.017	0.08	0	0	0.038	0
Pathargora		Magnetite	0	0	0.065	0.032	0	0.009	0.047	0
Pathargora		Magnetite	0	0	0.406	0.074	0.002	0	0.034	0
Pathargora		Magnetite	0.003	0.002	0.104	0.066	0.028	0	0.107	0.049
Pathargora		Magnetite	0	0	0.024	0.113	0	0.001	0.184	0
Pathargora		Magnetite	0.004	0	0.111	0.077	0.009	0	0.012	0
Pathargora		Magnetite	0.032	0.004	0.045	0.086	0	0.049	0.111	0.002
Pathargora		Magnetite	0.036	0	0.028	0.075	0.036	0.068	0.044	0.044
Pathargora		Magnetite	0	0.007	0.044	0.058	0.002	0	0	0
Pathargora		Magnetite	0.006	0.008	0.037	0.02	0.007	0.013	0	0
Pathargora		Magnetite	0.042	0	0.047	0.071	0.019	0	0.132	0.054
Pathargora		Magnetite	0	0	0.027	0.044	0	0	0	0.047
Pathargora		Magnetite	0.012	0.02	0.055	0.238	0.028	0.194	0.005	0
Pathargora		Magnetite	0	0	0.032	0.044	0.045	0.078	0	0
Pathargora		Magnetite	0	0	0.01	0.021	0	0	0.094	0
Pathargora		Magnetite	0.065	0	0.177	0.003	0.016	0	0.065	0.097
Pathargora		Magnetite	0	0.001	0.032	0.072	0.028	0	0	0.072
Pathargora		Magnetite	0	0.004	0.061	0.003	0.016	0	0	0.075

Continued

AREA	Association No.	Mineral	FeO	SiO2	K2O	CaO	TiO2	V2O3	NiO	Total
Pathargora	Association I	Magnetite	91.678	n.d.	n.d.	n.d.	0.11	0.924	n.a.	93.159
Pathargora		Magnetite	92.214	n.d.	n.d.	n.d.	n.d.	0.912	n.a.	94.067
Pathargora		Magnetite	91.949	n.d.	n.d.	n.d.	0.13	0.893	n.a.	93.612
Pathargora		Magnetite	90.874	n.d.	n.d.	n.d.	0.188	0.955	n.a.	92.5
Pathargora		Magnetite	93.302	n.d.	n.d.	n.d.	0.192	0.879	n.a.	94.875
Pathargora		Magnetite	92.213	n.d.	n.d.	n.d.	0.215	0.923	n.a.	93.976
Pathargora		Magnetite	91.915	n.d.	n.d.	n.d.	n.d.	0.804	n.a.	93.091
Pathargora	Association IA	Hematite	87.939	0.002	n.d.	n.d.	n.d.	0.706	n.a.	89.163

Pathargora		Hematite	87.651	0.216	n.d.	n.d.	0.114	0.943	n.a.	89.637
Pathargora		Hematite	86.852	0.257	n.d.	n.d.	n.d.	0.947	n.a.	88.882
Pathargora		Hematite	87.727	0.22	n.d.	n.d.	0.411	0.894	n.a.	90.255
Pathargora		Hematite	86.391	0.262	n.d.	n.d.	0.055	0.975	n.a.	88.682
Pathargora		Hematite	87.041	0.262	n.d.	n.d.	0.075	0.975	n.a.	88.682
Pathargora	Association II	Magnetite	92.266	0.036	0	0	0.016	0.348	0.063	92.903
Pathargora		Magnetite	92.53	0	0	0	0	0.313	0.266	93.262
Pathargora		Magnetite	88.901	0.998	0.008	0.06	0.106	0.452	0.262	91.302
Pathargora		Magnetite	91.74	0.009	0	0	0	0.379	0.051	92.539
Pathargora		Magnetite	91.693	0.048	0	0.009	0.03	0.357	0.263	92.722
Pathargora		Magnetite	92.845	0.119	0	0.011	0.014	0.306	0.155	93.664
Pathargora		Magnetite	89.214	0.113	0.01	0.018	0	0.24	0.15	90.074
Pathargora		Magnetite	89.443	0.097	0	0.032	0.011	0.215	0.186	90.316
Pathargora		Magnetite	91.754	0	0	0	0	0.218	0	92.084
Pathargora		Magnetite	91.862	0.018	0	0	0	0.228	0.039	92.239
Pathargora		Magnetite	95.46	0	0	0	0.003	0.346	n.a.	96.175
Pathargora		Magnetite	94.357	0	0	0.004	0.012	0.397	n.a.	94.888
Pathargora		Magnetite	88.576	0.153	0	0.074	0	0.338	n.a.	89.693
Pathargora		Magnetite	95.176	0.008	0	0	0.001	0.385	n.a.	95.767
Pathargora		Magnetite	92.585	0.019	0	0	0	0.331	n.a.	93.061
Pathargora		Magnetite	90.261	0.323	0	0	0.025	0.448	n.a.	91.48
Pathargora		Magnetite	86.349	4.951	0.003	0.04	0.05	0.374	n.a.	91.972
Pathargora		Magnetite	91.878	0.059	0	0	0.004	0.361	n.a.	92.461

Table 10 Trace element geochemistry of magnetite and hematite from Pathargora and results of magnetite thermometry

MINERAL	Magnetite	Hematite
Association no.	Association I	Association IA

TMg (in °C)	412.5568	405.3447	457.8048	444.7474	386.9456	458.6337	399.1137						
Li7	0.2	0.5	0.9	0.5	<0.28	0.5	0.3	<0.38	0.5	<0.58	<0.98	<0.27	<0.25
Be9	<0.55	<0.00	0.1	<0.47	<0.52	<1.00	0.2	<0.81	0.5	0.4	0.9	0.8	0.2
B11	<2.83	<3.00	3.60	<2.82	<2.81	<6.25	<3.26	<3.71	5.70	<6.43	<6.09	5.90	9.40
Na23	34.63	28.46	72.27	96.07	61.05	46.10	42.17	88.40	116.13	236.99	<20.00	212.21	160.75
Mg24	80.4	70.7	176.4	140.5	50.1	179.3	62.6	92.9	301.9	124.8	152.5	86.3	74.5
Al27	1046.92	1193.55	957.63	827.75	917.06	1127.41	907.81	786.36	1077.63	1066.92	2566.27	1174.57	2531.59
P31	<38.90	<48.22	<36.44	<42.74	<45.93	110.5	50.7	126	201.2	146.7	132.3	194.4	121.4
K39	57.5	46	120.5	70.9	115.4	64.1	69.1	136	385.1	163.2	<38.50	183.6	104.1
Ca44	<203.82	<244.55	<191.14	274.62	<245.78	<504.77	<264.07	<318.02	<191.29	<522.70	<556.85	<311.91	<228.87
Sc45	6.6	9.6	5.5	5.2	6.8	4.2	3.7	10.2	10.2	7.8	11.4	9.9	8.6
Ti49	97.8	1854.4	57.5	47.5	80.3	80.5	77.5	3426.1	683.9	77.8	508.5	101.2	89.3
V51	6944.9	7339.4	7619.9	6876.1	7455.2	8484.7	5769.8	5954.7	7095.1	8068.8	8430.8	7208.4	7908.3
Cr52	2609.3	4226.5	2094.4	2072.8	2445.1	3280.6	707.4	2632.9	3959.5	2218.8	3291.9	3038.5	3486.3
Mn55	47.2	81.9	86.6	97.4	53.2	47.9	37.5	78.3	40.6	38.3	39.3	31.7	29.1
Fe57	712623.2	716789.6	714729.7	706373.6	725246.8	716781.9	714465.4	683559.4	681320.9	675110.1	681911.6	671526.7	671526.8
Co59	58.3	60.9	58.9	53.4	57	60.3	54	86.6	95.3	93	42.4	96.7	77.1
Ni60	599.8	668.1	615.5	640.8	623.4	680.3	534.5	686.7	668.3	719.3	758.2	670.2	688.7
Cu63	<0.38	<0.53	2.2	5.1	1.2	1.6	0.7	16.6	27.9	18.7	9.7	14.5	12.2
Zn66	9.8	11.5	34	54.9	24.5	24.7	11.5	11.9	24.5	24.8	15.1	5.4	13.9
Ga71	145	159	161.2	153.4	160.9	183.4	125.2	161.3	168.7	178.1	177.5	175.6	169.7
Ge73	5	8	6.9	6.7	7.2	4	6.3	6.2	7.9	9.7	13.3	5.2	7.4
As75	<6.15	<6.73	<5.38	<6.49	<6.63	<14.61	<7.39	<6.98	<4.73	<13.08	<13.32	<8.45	<6.06
Rb85	0.3	0.3	2	2.3	1	0.5	0.4	0.2	3.7	0.5	0.5	0.2	0.2
Sr88	0.1	0.1	3.1	1.8	0.5	1	0.1	0.4	0.6	2.1	1	1.1	0.4

Y89	0	0	<0.031	0.1	0.1	0.3	0.1	2.1	2.7	2.6	1.8	2.6	1.7
Zr90	0	0.1	<0.00	0	<0.00	1.5	<0.096	5.5	17.4	3.8	10	13	9.8
Nb93	0.1	1.6	0.5	0.6	0.4	1.5	0.1	3.9	2.3	0.9	1.1	0.9	0.9
Mo95	0.1	<0.33	<0.159	<0.28	0.2	<0.59	<0.224	5.7	10.5	9.8	5.8	8.8	7.7

Continued

Mineral	Magnetite							Hematite					
Association no.	Association I							Association IA					
Cd111	<0.39	<0.28	0.2	0.2	0.2	0.5	0.2	<0.42	<0.22	<0.76	<0.68	0.2	0.3
In115	n.a.	n.a.	n.a.	n.a.	n.a.	n.a.	n.a.	n.a.	n.a.	n.a.	n.a.	n.a.	n.a.
Sn118	1.6	1.6	2.9	2.6	2.9	<2.95	2.4	1.9	3.5	3	3.3	<1.51	2.6
Sb121	<0.244	<0.32	0.5	0.5	<0.29	<0.59	0.3	1.3	0.8	1	<0.69	<0.31	<0.26
Cs133	0.1	0.1	0.3	0.3	0.1	0.1	0	<0.027	0.1	<0.070	<0.063	<0.029	<0.022
Ba137	0.6	0.3	10.2	8	2.8	5.4	0.4	2	6.1	7.8	3.9	3.3	3.3
La139	<0.0236	0	0	0	0	0.1	0	0.1	0.1	0.1	0.1	0.1	0.1
Ce140	0	<0.028	0	0	<0.025	0.1	0	0.2	0.3	0.3	<0.43	0.4	0.3
Pr141	0	0	0	<0.0186	<0.0204	0	<0.0211	0.1	0.1	0.1	0.1	0.1	0.1
Nd146	<0.00	<0.096	<0.00	<0.00	0	0.2	<0.00	0.4	0.4	0.7	0.4	0.4	0.2
Sm147	<0.112	<0.00	<0.00	0	0	<0.00	<0.154	0.4	0.3	0.7	0.4	0.2	0.5
Eu153	<0.00	<0.041	<0.0278	<0.035	<0.00	0.1	<0.00	0	0	0	0	0	<0.035
Gd157	0	<0.107	<0.00	<0.00	<0.00	<0.00	<0.00	0.5	0.5	0.5	0.5	0.3	0.3
Tb159	<0.00	<0.00	<0.00	<0.00	<0.00	<0.042	<0.00	0.1	0.1	0.1	0.1	0.1	0
Dy163	<0.00	0.1	<0.00	0	0	<0.164	0.1	0.5	0.5	0.6	0.5	1	0.4
Ho165	0	<0.00	0	<0.00	<0.00	0	0	0.1	0.2	0.1	0.1	0.2	0.1
Er166	0	0	0	0	<0.00	0.1	<0.064	0.2	0.2	0.4	0.5	0.4	0.2
Tm169	<0.0149	0	<0.00	0	0	<0.00	<0.00	0	0.1	0	0	0	0
Yb172	<0.070	<0.071	0	0	<0.00	0.1	0	0.2	0.4	0.2	0.2	0.3	0.2

Lu175	<0.00	<0.00	<0.00	<0.00	0	<0.00	<0.0217	0	0	0	0	<0.025	0
Hf178	<0.00	<0.00	<0.00	<0.00	<0.00	0.1	<0.00	0.2	0.8	0.2	0.4	0.5	0.4
Ta181	0	0.2	0.1	0.1	0.1	0.3	0	0.8	0.4	0.1	0.1	0.1	0.1
W182	0.1	0.3	1	1.9	0.3	0.5	0.1	1.9	6.7	4.6	2.7	3.7	2.8
Au197	<0.58	<0.78	<0.61	<0.70	<0.68	<1.54	<0.75	<0.92	<0.49	<1.75	<1.58	<1.05	<0.74
Pb208	0.3	0.4	3	4.5	2.3	6.8	0.4	25.6	28.4	18.6	9.7	14.2	9.8
Bi209	0	<0.051	0.2	0.3	0.1	0.2	0.1	0.1	0.2	0.3	0.1	<0.057	0.1
Th232	<0.00	0.1	0	0	<0.00	0.2	0	19.3	32.8	22.3	38.6	45.6	37.3
U238	0	0.3	0.1	0	0	0.8	0	11.9	15.7	17.6	14.1	17.8	10.4

MINERAL	Magnetite of Association II								
Association no.	Association II								
TMg (in °C)	371.85874	598.11202	653.62607	397.93377	583.05682	377.5467	437.9441	431.59574	410.18382
Li7	<0.34	<0.51	0.39	<0.34	0.82	<0.29	<0.34	0.33	<0.46
Be9	0.18	0.21	2.24	<0.00	4.78	<0.00	2.21	0.61	<1.46
B11	<6.85	<6.83	<5.75	<7.53	<5.73	<6.16	<8.86	7.76	<9.08
Na23	<4.23	13.28	42.97	7.24	45.2	32.09	204.8	180.57	51.68
Mg24	36.44	1202.11	2102.36	61.08	999.46	41.24	122.88	110.38	77.01
Al27	317.49	797.55	811.57	594.48	801.76	679.05	1380.79	826.93	650.08
P31	<60.96	<65.41	186.1	<64.14	<47.89	<52.26	918.26	814.89	146.32
K39	72.02	<41.03	44.28	<41.14	51.48	<35.32	126.25	101.04	<43.52
Ca44	<592.33	<632.36	<511.70	<646.53	<503.72	<550.05	475.6	523.24	<581.06
Sc45	<4.89	<5.05	<4.20	<5.03	4.43	<4.58	6.9	<3.93	<4.69
Ti49	132.97	190.64	405.1	267.32	264.73	183.54	32.63	68.53	94.7
V51	2874.98	2851.2	3604.69	3297.27	2879.42	2742.6	2114.47	2188.04	1968.85
Cr52	49.95	<15.42	<12.36	32.76	383.32	78.02	753.2	15.77	27

Mn55	117.02	118.6	136.75	121.18	113.82	111.65	107.53	128.66	140.17
Co59	41.33	39.73	40.29	41.56	40.62	39.56	69.47	56.9	55.82
Ni60	775.79	815.91	1064.59	982.07	585.79	678.49	595.34	603.12	599.32
Cu63	<0.57	2.42	176.87	8	<0.61	<0.72	377.94	314.4	101.3
Zn66	12.18	<6.79	11.2	12.6	5.88	9.17	37.78	15.71	<7.81
Ga71	89.6	85.54	91.63	89.02	77.34	80.4	46.9	48.5	50.22
Ge73	9.95	10.54	9.37	17.8	<4.82	<6.03	8.56	6.47	<7.58
As75	n.a.	n.a.	n.a.	n.a.	n.a.	n.a.	n.a.	n.a.	n.a.
Rb85	<0.49	<0.54	<0.38	<0.36	<0.27	<0.32	<0.39	<0.35	<0.33
Sr88	0.06	<0.179	0.39	0.217	0.118	0.018	4.95	3.88	0.141
Y89	<0.228	<0.37	1.93	<0.216	0.77	<0.33	5.99	5.32	0.8
Zr90	<0.280	<0.30	0.138	<0.00	0.04	<0.00	32.76	14.67	2.94
Nb93	<0.14	0.194	1.01	<0.162	<0.30	<0.203	2.88	2.55	0.42
Mo95	<1.23	<1.61	19.44	<1.74	<0.76	0.71	193.39	161.54	22.3
Ag107	n.a.	n.a.	n.a.	n.a.	n.a.	n.a.	n.a.	n.a.	n.a.
Cd111	n.a.	n.a.	n.a.	n.a.	n.a.	n.a.	n.a.	n.a.	n.a.
In115	n.a.	n.a.	n.a.	n.a.	n.a.	n.a.	n.a.	n.a.	n.a.
Continued									
Sn118	<2.28	<2.55	<2.09	<2.51	<1.98	<2.07	3.52	<2.27	<2.56
Sb121	<0.54	<0.70	<0.60	<0.47	<0.57	<0.59	<0.89	<0.85	<0.97
Cs133	0.041	<0.065	<0.050	0.022	0.017	0.0091	<0.00	0.0098	<0.00
Ba137	0.18	0.106	0.97	0.59	0.54	<0.55	16.29	14.07	1.13
La139	<0.00	<0.125	0.353	0.061	0.13	0.012	3.05	2.65	0.298
Ce140	0.011	0.13	2.92	0.68	0.49	<0.00	3.89	5.74	6.74
Pr141	<0.00	0.022	0.119	0.06	0.085	<0.00	0.51	0.54	0.085
Nd146	<0.00	0.134	0.91	0.25	0.63	<0.00	2.04	2.56	0.115
Sm147	0.136	<0.00	0.4	<0.47	0.35	<0.59	0.46	0.48	0.2
Eu153	<0.00	0.02	0.033	0.019	0.058	<0.00	0.15	0.016	0.018
Gd157	<0.00	0.145	1.02	0.067	0.47	<0.00	0.99	0.86	0.19
Tb159	<0.057	<0.00	0.131	<0.00	0.09	<0.00	0.255	0.204	0.019
Dy163	<0.00	0.089	0.2	0.041	0.064	<0.00	1.46	1.07	<0.23

Ho165	<0.00	0.011	0.075	<0.00	0.033	<0.00	0.364	0.248	0.069
Er166	<0.00	<0.00	0.24	0.03	0.07	<0.00	0.94	0.58	0.139
Tm169	0.0087	<0.055	0.059	<0.060	<0.045	<0.00	0.053	0.124	<0.053
Yb172	0.041	0.24	0.48	0.089	0.208	<0.00	0.52	0.68	<0.00
Lu175	<0.00	0.011	0.027	<0.00	0.016	0.0083	0.169	0.067	0.029
Hf178	<0.00	<0.00	<0.00	<0.00	<0.00	<0.00	0.56	0.144	<0.00
Ta181	<0.00	0.0101	0.067	<0.00	0.044	0.0077	<0.00	<0.00	0.0088
W182	<0.00	0.42	3.4	0.71	0.53	<0.00	1.61	2.62	0.219
Au197	<0.149	<0.111	<0.148	0.038	<0.090	<0.149	<0.162	0.017	<0.166
Pb208	0.123	0.131	1.42	3.12	<0.122	<0.116	14.38	8.38	0.71
Bi209	<0.132	<0.172	<0.114	<0.142	<0.121	<0.094	0.28	<0.145	<0.185
Th232	<0.00	0.0103	<0.00	<0.00	0.0074	<0.00	0.366	0.008	<0.00
U238	0.0061	0.106	21.57	0.66	0.025	0.0054	38.89	30.18	7.14

MINERAL	Magnetite								
Association no.	Association II								
TMg (in °C)	419.68879		656.41481	467.33044			657.14614	564.65158	588.04766
Li7	<0.52	17.65	1.78	<0.33	-155.63	184.31	2.25	0.71	0.35
Be9	1.07	<-0.00	6.27	<0.64	<-0.00	<-0.00	5.88	4.02	0.32
B11	<8.76	954.15	3.9	15.28	-2544.23	1993.12	5.14	3.4	<2.56
Na23	101.35	n.a	n.a	n.a	n.a	n.a	n.a	n.a	n.a
Mg24	91.76	<-100.56	2295.33	197.95	<-368.70	<-920.45	2211.96	753.06	1062.19
Al27	2141.66	<-771.65	1685.91	1514.3	<-2767.28	<-12229.32	2223.66	1360.57	418.04
P31	415.5	-762.14	<37.48	944.44	8161.53	<-185956.55	295.39	112.43	62.89
K39	<47.54	-1994.01	431.16	74.7	-15226.74	<-74563.00	1035.2	337.04	41.3
Ca44	<659.18	n.a	n.a	n.a	n.a	n.a	n.a	n.a	n.a.

Sc45	7.37	-138.32	25.12	9.96	-1236.01	<-6744.53	14.33	20.87	1.46
Ti49	84.16	<-1348.23	236.49	166.72	<-2972.46	<-17969.90	395.2	341.96	224.07
V51	1966.55	<-147.87	3022.27	3341.36	<-569.56	<-2013.16	3046.57	2765.28	2797.04
Cr52	<17.43	<-3420.92	134.93	204.32	<-13039.51	<-57281.47	<11.96	<8.71	<8.65
Mn55	162.92	<-456.06	114.14	95.31	<-1514.27	<-6824.38	107.26	80.87	81.2
Co59	63.14	<-28.45	83.32	88.03	<-77.47	<-0.00	147.75	90.93	82.02
Ni60	595.05	<-166.06	719.26	738.14	<-521.59	<-3054.84	759.93	640.02	733.55
Cu63	238.43	-4.86	0.54	1516.89	<-332.46	<-1742.27	664.93	171.17	58.1
Zn66	<9.31	<-438.02	5.57	7.85	<-1754.79	<-8590.74	7.32	9.7	6.31
Ga71	44.87	<-0.00	50.48	52.15	<-128.88	<-0.00	72.04	64.13	57.62
Ge73	<8.91	<-857.86	4.74	8.64	<-2150.70	<-4846.60	7.01	5.33	5.48
As75	n.a.	-180.28	<6.07	<8.92	-209.6	-11015.34	<7.60	<5.50	<5.68
Rb85	<0.54	-15.55	1.09	<0.151	29.17	452.39	7.24	0.82	0.299
Sr88	0.42	<-0.00	1.33	0.86	<-0.00	<-236.60	1.82	0.9	0.25
Y89	5.59	<-0.00	5.53	8.78	<-0.00	<-0.00	5.18	5.66	0.345
Zr90	17.79	<-0.00	<0.084	1.38	<-0.00	<-0.00	<0.099	0.031	<0.00
Nb93	7.15	8.33	0.8	0.438	15.84	<-0.00	0.62	0.85	0.1
Mo95	39.09	-4.51	<0.268	36.22	-19.07	<-980.35	14.47	3.07	1.46
Ag107	n.a.	77	<0.197	<0.34	-14.14	-409.47	<0.193	<0.149	<0.165
Cd111	n.a.	53.25	<0.30	<0.42	108.37	1035.8	0.077	0.162	0.053
Continued									
Sn118	<2.75	<-352.60	3.52	<1.52	<-1140.29	<-5015.51	1.33	2.61	<0.89
Sb121	<1.37	32.85	0.47	<0.33	-88.94	-334.96	0.5	0.262	0.21
Cs133	<0.099	<-0.00	0.1	<0.0276	<-0.00	68.61	0.097	0.024	0.039
Ba137	2.09	<-0.00	4.83	4.66	60.38	<-0.00	5.12	2.97	0.75
La139	0.75	2.57	0.143	1.55	<-0.00	<-0.00	0.575	0.748	0.077
Ce140	10.58	<-0.00	0.82	6.71	<-0.00	<-0.00	16.92	6.07	1.49
Pr141	0.21	<-0.00	0.117	0.656	<-0.00	<-0.00	0.236	0.57	0.0154
Nd146	0.71	<-0.00	0.85	3.73	<-0.00	<-0.00	1.65	2.95	0.187
Sm147	<0.43	<-0.00	0.306	1.54	<-0.00	<-0.00	0.66	1.88	<0.00
Eu153	0.044	3.02	0.07	0.129	<-0.00	<-0.00	0.049	0.052	<0.027

Gd157	0.55	<-0.00	0.86	1.73	<-0.00	<-0.00	0.95	2.45	0.042
Tb159	0.096	1.74	0.245	0.423	<-0.00	<-93.34	0.199	0.401	0.0065
Dy163	1.23	<-0.00	1.81	3.04	<-0.00	<-0.00	1.27	1.89	<0.061
Ho165	0.121	<-0.00	0.234	0.432	<-0.00	<-0.00	0.339	0.25	0.031
Er166	1.4	<-0.00	0.74	0.97	<-0.00	<-0.00	0.61	0.79	0.066
Tm169	0.066	<-0.00	0.121	0.078	<-0.00	<-0.00	0.139	0.124	0.006
Yb172	0.66	<-0.00	0.99	1.19	<-0.00	<-0.00	0.8	0.57	0.042
Lu175	0.097	-0.21	0.144	0.16	<-0.00	<-0.00	0.091	0.086	0.0063
Hf178	0.45	5.63	0.013	0.018	<-0.00	<-0.00	0.015	<0.050	<0.00
Ta181	0.022	<-0.00	0.098	<0.022	<-0.00	<-0.00	0.095	0.164	0.043
W182	1.57	<-0.00	1.25	1.41	<-0.00	<-0.00	0.83	2.04	0.242
Au197	<0.215	21.9	<0.77	<1.18	2.29	-2249.55	<1.01	<0.75	<0.74
Pb208	2.64	5.37	0.388	4.2	-38.25	<-410.31	1.18	0.363	0.378
Bi209	<0.236	3.74	0.113	0.12	9.19	<-188.85	0.126	0.08	0.046
Th232	<0.00	<-0.00	0.063	<0.00	<-0.00	<-0.00	0.03	<0.00	0.003
U238	25.9	<-0.00	0.127	39.43	<-0.00	<-0.00	14.34	3.68	1.16

Table 11 Result of mass-balance calculation between magnetite and hematitized magnetite/hematite

Concentration	Mineral	TiO2	Cr2O3	FeO	Al2O3	V2O3	Na23	B11	Mg24	Al27	Si29
	Magnetite	0.17	0.32	92.02	0.13	0.9	54.39	3.6	108.57	996.88	2315.95
	Hematite	0.16	0.39	87.27	0.24	0.91	162.9	7	138.82	1533.89	2673.7
Loss/Gain		-0.26	-0.08	-0.28	0.41	-0.23	1.27	0.48	-0.03	0.17	-0.12
Concentration	Mineral	P31	K39	Sc45	Ti49	V51	Cr52	Mn55	Fe57	Co59	Ni60
	Magnetite	80.6	77.64	5.94	327.93	7212.86	2490.87	64.53	715287	57.54	623.2

	Hematite	153.67	194.4	9.68	814.47	7444.35	3104.65	42.88	677493	81.85	698.57
Loss/Gain		0.45	0.9	0.24	0.88	-0.22	-0.05	-0.5	-0.28	0.08	-0.15
Concentration	Mineral	Cu63	Zn66	Ga71	Ge73	Rb85	Sr88	Y89	Zr90	Nb93	Mo95
	Magnetite	2.16	24.41	155.44	6.3	0.97	0.96	0.1	0.4	0.69	0.15
	Hematite	16.6	15.93	171.82	8.28	0.88	0.93	2.25	9.92	1.67	8.05
Loss/Gain		4.83	-0.5	-0.16	0	-0.31	-0.26	16.07	17.81	0.84	39.71
Concentration	Mineral	Cd111	Sn118	Sb121	Ba137	La139	Ce140	Nd146	Eu153	Dy163	Er166
	Magnetite	0.26	2.33	0.43	3.96	0.02	0.02	0.1	0.1	0.05	0.02
	Hematite	0.25	2.86	1.03	4.4	0.1	0.3	0.42	0	0.58	0.32
Loss/Gain		-0.27	-0.07	0.81	-0.16	3.55	10.38	2.16	-1	7.85	11.01
Concentration	Mineral	Yb172	Hf178	Ta181	W182	Pb208	Bi209	Th232	U238	∑LREE	∑HREE
	Magnetite	0.03	0.1	0.11	0.6	2.53	0.15	0.06	0.17	0.06	0.06
	Hematite	0.25	0.42	0.27	3.73	17.72	0.16	32.65	14.58	1.28	1.82
Loss/Gain		6.59	2.16	0.77	3.72	4.32	-0.19	411.81	63.53	15.18	22.01

Table 12 Major and trace element composition of Sandwich type and composite Type I ilmenite lamella

Lamella	Sandwich ilmenite				Composite Type I ilmenite								
Assoc. No.	Association I		Association IA		Association I				Association IA				
Na2O	n.d.	0.06	n.d.	n.d.	n.d.	0.05	n.d.	n.d.	n.d.	n.d.	n.d.	n.d.	n.d.
F	n.d.	n.d.	n.d.	n.d.	n.d.	n.d.	n.d.	n.d.	n.d.	n.d.	n.d.	n.d.	n.d.
MgO	0.18	0.14	0.27	0.27	0.15	0.11	0.14	0.13	0.25	0.23	0.17	0.17	0.25
Cl	n.d.	n.d.	n.d.	n.d.	n.d.	n.d.	n.d.	n.d.	n.d.	n.d.	n.d.	n.d.	n.d.
P2O5	n.d.	0.05	0.06	0.06	n.d.	n.d.	n.d.	n.d.	n.d.	n.d.	n.d.	n.d.	n.d.
K2O	n.d.	n.d.	n.d.	n.d.	n.d.	n.d.	n.d.	n.d.	n.d.	n.d.	n.d.	n.d.	n.d.
CaO	n.d.	n.d.	n.d.	n.d.	n.d.	n.d.	n.d.	n.d.	n.d.	n.d.	n.d.	n.d.	n.d.
TiO2	50.51	49.30	50.21	50.14	46.94	43.86	47.68	48.90	50.96	49.50	49.77	49.77	50.96
Cr2O3	0.12	n.d.	n.d.	n.d.	n.d.	n.d.	n.d.	0.10	0.10	n.d.	n.d.	n.d.	0.10
FeO	46.30	47.72	46.92	47.02	49.67	53.95	48.78	47.74	47.98	47.58	47.67	47.67	47.98
MnO	0.87	0.70	0.62	0.62	0.42	0.48	0.69	0.54	0.60	0.70	0.60	0.60	0.60
Al2O3	0.14	0.13	0.13	0.13	0.13	0.15	0.17	0.15	0.19	0.12	0.14	0.14	0.19
SiO2	n.d.	n.d.	n.d.	n.d.	n.d.	n.d.	n.d.	n.d.	n.d.	n.d.	n.d.	n.d.	n.d.
V2O3	0.13	0.19	0.18	0.20	0.15	0.38	0.29	0.18	0.08	0.14	0.16	0.16	0.08
Total	98.31	98.33	98.44	98.44	97.52	99.04	97.79	97.80	100.18	98.33	98.58	98.58	100.18

Lamellae Type	Association no.	Li7	Be9	B11	Na23	Mg24	Al27	Si29	P31	K39
Sandwich ilmenite	Association I	3	1	<5.71	143.64	1273.8	85.21	<1831.53	<77.29	345.9
		3.3	<0.00	<14.27	43.48	1449	89.04	<5045.01	<204.28	<79.44
		3.15	1	n.c.	93.56	1361.4	87.125		n.c.	345.9
	Association IA	2.9	<0.00	8.2	61.3	2127	756.6	<2533.05	138.3	87
		3.1	<0.63	<3.30	9.88	1952.9	170.52	<1298.19	<55.11	<20.95
		3	n.c.	8.2	35.59	2039.95	463.56	n.c.	138.3	87
Composite Type I ilmenite	Association I	4.2	0.4	<3.73	40.25	1253.8	302.79	<1359.12	<55.56	45.1
		3.3	<0.00	<5.19	99.12	1298.2	1464.3	2400.34	102	100.1
		3.5	<0.73	<4.36	12.41	1305.9	62.57	<1544.82	<62.96	47.1
		1.8	0.7	<3.95	63.95	1093.3	1054.11	1682.87	64	40.4
		3.2	0.55	n.c.	53.9325	1237.8	720.9425		83	58.175

	Association IA	<0.46	0.3	<5.12	48.04	1073.9	629.63	2015.43	147.1	64.9
		2.4	<0.00	<2.47	4.81	1659.1	86.41	<925.03	<40.77	17
		1.3	0.3	3.5	34.79	1150.2	423.5	1662.18	<41.20	77
		2.3	<0.00	<5.69	82.37	1691	148.37	<1938.97	<82.71	125.2
		2.5	<1.01	<7.09	35.85	1509.3	312.75	<2425.38	<102.69	48
		2.125	0.3	3.5	41.172	1416.7	320.132	n.c.	147.1	66.42
Lamellae Type	Association no.	Ca44	Sc45	Ti49	V51	Cr52	Mn55	Fe57	Co59	Ni60
Sandwich ilmenite	Association I	<413.98	852.4	392181.3	2243	130.3	7061.4	359879.5	81.6	66.3
		<1120.6	1067.9	461151	3009.1	203.9	7990	370948.4	73.8	48.8
			960.15	426666.15	2626.05	167.1	7525.7	365413.95	77.7	57.55
	Association IA	<610.51	864	424866.8	3028.5	615.7	6437.4	364737.6	88	126.4
		<304.34	701.7	393877.1	2829.8	472.3	5963	364737.6	92.4	105.3
		n.c.	782.85	409371.9	2929.15	544	6200.2	364737.6	90.2	115.85
Composite Type I ilmenite	Association I	<309.88	934.30	404266.90	2781.70	155.60	6877.60	386113.70	75.40	65.50
		<416.64	1005.80	432950.70	3580.00	225.40	7080.30	419374.90	76.50	73.40
		<343.49	953.10	426958.50	3208.30	176.00	6934.40	379164.60	78.20	68.60
		<327.41	669.40	385201.40	2514.30	88.00	6290.80	371065.00	67.20	60.90
		n.c.	890.65	412344.38	3021.08	161.25	6795.78	388929.55	74.33	67.10
	Association IA	<442.94	314.80	241304.10	3271.70	634.80	3849.50	372984.90	77.60	199.60
		<225.11	385.90	342469.50	2444.10	129.20	6870.80	369805.70	91.70	66.10

Lamellae Type	Association no.	Ca44	Sc45	Ti49	V51	Cr52	Mn55	Fe57	Co59	Ni60
Composite Type I ilmenite	Association IA	<222.90	348.20	290060.90	3175.10	426.60	5251.50	370544.10	91.20	152.50
		<445.64	498.70	390724.20	4133.70	225.60	5864.10	370544.10	83.30	70.70
		<558.88	682.00	342293.20	3692.90	640.50	5172.60	372984.90	92.00	220.30
		n.c.	445.92	321370.38	3343.50	411.34	5401.70	371372.74	87.16	141.84
Lamellae Type	Association no.	Cu63	Zn66	Ga71	Ge73	As75	Rb85	Sr88	Y89	Zr90
Sandwich ilmenite	Association I	16.9	145.7	1.6	3.7	<11.28	3.8	2.9	3.3	0.2
		25.6	116.3	2.5	<9.19	<30.78	<0.37	<0.17	0.6	0.7
		21.25	131	2.05	3.7	n.c.	3.8	2.9	1.95	0.45
	Association	83.4	97.8	19.5	<7.10	<15.12	0.3	0.5	2.9	8.8

	IA	40.8	96.4	11.3	3.9	<8.47	0.1	0.3	0.6	0.7
		62.1	97.1	15.4	3.9	n.c.	0.2	0.4	1.75	4.75
Composite Type I ilmenite	Association I	16.8	92.2	7.2	<2.54	<8.15	0.5	0.7	0.5	1.1
		18.9	123.2	52.1	3.1	<11.44	0.9	1.4	0.7	0.6
		16.5	90.6	4.2	2.4	<9.23	0.3	0.4	1.5	0.7
		14.8	94.6	4.6	2.7	<9.25	0.3	1	1.6	1
		16.75	100.15	17.025	2.733333	n.c.	0.5	0.875	1.075	0.85
	Association IA	90.7	76.1	42	2.3	<10.25	0.3	0.6	4.2	20.7
		85.1	104.4	2.3	<2.25	<5.57	0.1	0.2	0.6	1.9
		101.8	86.5	28.3	2.6	<5.67	0.5	0.4	1.8	5.6
		114.3	139	5.7	<3.49	<11.79	0.2	0.9	6.2	3.2
		65.5	95.7	36.8	<4.08	<14.69	<0.24	0.6	2.9	5.7
		91.48	100.34	23.02	2.45	n.c.	0.275	0.54	3.14	7.42
Lamellae Type	Association no.	Nb93	Mo95	Ag107	Cd111	Sn118	Sb121	Cs133	Ba137	La139
Sandwich ilmenite	Association I	361.6	0.6	<0.25	<0.63	35.9	0.6	0.7	15.9	<0.076
		454	<1.37	<1.00	<1.62	118.7	<1.16	<0.108	1.6	<0.00
		407.8	0.6	n.c.	n.c.	77.3	0.6	0.7	8.75	n.c.
	Association IA	592.4	2.7	<0.54	<0.71	23.9	0.8	0	3.2	<0.085
		463.2	0.6	<0.30	0.1	35.5	0.7	0	0.3	7.32
		527.8	1.65	n.c.	0.1	29.7	0.75	0	1.75	7.32
Composite Type I ilmenite	Association I	384.7	<0.46	<0.27	<0.45	79.3	<0.42	0.1	2.3	0
		421.4	0.6	0.5	0.7	85.5	0.7	0.2	6.1	0
		394.9	0.4	<0.31	<0.51	83.4	<0.35	0.1	0.8	<0.044
		441.5	0.3	<0.220	0.3	37.1	0.4	0.2	3.1	0.1
		410.625	0.4333333	0.5	0.5	71.325	0.55	0.15	3.075	0.0333333
	Association IA	225.7	4.3	<0.42	<1.04	23.6	<0.41	0	2.4	0.1
		308.9	0.4	<0.225	<0.30	41.9	0.3	<0.020	0.7	0
		252.7	2.2	<0.181	0.1	29.4	0.6	0	2.1	0.1
		449.1	1.7	<0.41	<0.89	61.9	0.6	<0.041	4.5	0.1
		354.2	2.5	<0.52	<1.28	32.6	<0.64	0	1.9	0.2

		318.12	2.22	n.c.	0.1	37.88	0.5	0	2.32	0.1
Lamellae Type	Association no.	Pr141	Nd146	Sm147	Eu153	Gd157	Tb159	Dy163	Ho165	Er166
Sandwich ilmenite	Association I	<0.035	0	<0.00	0	0.2	0	0.3	0.1	0.6
		0	<0.00	<0.00	<0.00	0.3	0	0.1	<0.098	0.3
		0	0	n.c.	0	0.25	0	0.2	0.1	0.45
	Association IA	<0.039	0.2	<0.28	<0.00	0.6	0	0.7	0.1	0.2
		0	0.1	0.1	<0.00	0.1	0	0.2	0	0.1
		0	0.15	0.1	n.c.	0.35	0	0.45	0.05	0.15
Composite Type I ilmenite	Association I	0	0	0.1	<0.00	<0.171	<0.027	0.1	0	0.1
		0	0	0.1	<0.065	0.1	0	0.2	<0.00	0.1
		0	0.1	0.2	0	0.3	0	0.3	0.1	0.3
		<0.027	0.1	0.2	<0.050	0.1	0.1	0.3	0.2	0.3
		0	0.05	0.15	0	0.1666667	0.0333333	0.225	0.1	0.2
	Association IA	0.1	0.5	0.4	<0.00	0.6	0.1	0.6	0.2	0.6
		<0.0164	<0.101	0.1	<0.00	<0.112	<0.0174	0.1	0	0.1
		0	0.4	<0.125	<0.032	0.3	0	0.3	0.1	0.2
		0.1	0.7	0.5	0.1	0.4	0.1	0.9	0.2	1
		0.1	0.2	0.2	0.1	0.3	0.1	0.7	0.1	0.4
		0.075	0.45	0.3	0.1	0.4	0.075	0.52	0.12	0.46

Lamellae Type	Association no.	Yb172	Lu175	Hf178	Ta181	W182	Au197	Pb208	Bi209	Th232
Sandwich ilmenite	Association I	1.1	0.1	0.1	70.6	12	<1.33	67.7	0.2	0.7
		<0.41	0.1	0.1	81.1	5.2	<3.47	1.1	<0.120	0
		1.1	0.1	0.1	75.85	8.6	n.c.	34.4	0.2	0.35
	Association IA	0.3	0.1	0.4	75.1	6.2	<1.69	13.8	<0.137	21.7
		0.1	0	0.1	56.4	11.5	<0.98	1.8	0.1	4.1
		0.2	0.05	0.25	65.75	8.85	n.c.	7.8	0.1	12.9
Composite Type I ilmenite	Association I	0.2	<0.026	<0.087	61.3	10.4	1.3	4.5	0.1	0.1
		0.2	0	<0.120	69.9	14.4	<1.16	2.7	0.1	0.1
		1.3	0.2	0	61.8	8	1.2	0.2	<0.046	0.1
		0.5	0	0.1	69.8	28.6	<0.96	23.8	<0.079	0.6
		0.55	0.0666667	0.05	65.7	15.35	1.25	7.8	0.1	0.225
	Association IA	0.5	0.1	0.9	40.7	10	<1.34	40.8	0.2	55.5
		0.1	0	0.1	53.2	9.4	<0.57	9.5	0	4.2
		0.2	0	0.3	45.6	10	<0.65	34.6	0.2	13.9
		2.9	0.5	0.4	74.2	78.2	<1.31	19.8	<0.080	13.6
		0.5	0.1	0.3	65.9	6.4	<1.54	15.8	0.2	8.1
		0.84	0.14	0.4	55.92	22.8	n.c.	24.1	0.15	19.06

Table 13 Major element geochemistry of apatite from Pathargora

Mineral	Apatite	Apatite	Apatite	Apatite	Apatite	Apatite	Apatite	Apatite
Assoc. No.	II	II	II	II	II	II	II	II
Na2O	0.016	0.013	0.052	0.01	0.081	0.036	0.032	0.043
F	3.823	3.836	3.91	3.823	3.914	3.913	4.03	3.986
MgO	0	0	0	0	0	0	0	0
Al2O3	0	0.005	0.027	0.033	0.027	0.008	0	0.001
Cl	0.006	0.019	0.076	0.045	0.049	0.026	0.035	0.034

P2O5	41.009	40.859	40.189	40.725	40.811	40.733	40.844	41.17
Cr2O3	0.038	0.048	0	0	0	0	0	0.046
MnO	0	0	0.094	0.018	0.026	0.024	0.017	0
FeO	0	0	0	0.077	0.05	0.075	0	0
Continued								
SiO2	0.017	0	0	0	0.028	0.025	0.029	0.005
K2O	0.015	0	0.003	0.007	0	0	0	0
CaO	56.568	56.191	56.292	56.295	56.349	56.696	56.833	56.297
TiO2	0	0	0	0	0	0	0	0
V2O3	0.032	0	0	0.017	0	0.023	0	0
NiO	0.155	0	0	0	0	0.033	0	0.02
Total	101.678	100.971	100.643	101.05	101.334	101.591	101.82	101.6

Mineral	Apatite	Apatite	Apatite	Apatite	Apatite	Apatite	Apatite	Apatite
Assoc. No.	II	II	II	II	II	II	II	II
Na2O	0.018	0.022	0.04	0.018	0.025	0.018	0.005	0.045
F	4.044	3.947	3.808	3.98	3.86	4.044	4.064	3.983
MgO	0	0	0	0	0	0	0	0
Al2O3	0	0.003	0.001	0	0	0	0	0.025
Cl	0.045	0.022	0.015	0.019	0.037	0.045	0.054	0.036
P2O5	41.265	42.216	40.701	41.217	40.488	41.265	44.018	43.516
Cr2O3	0.038	0.013	0.066	0	0.049	0.038	0	0
MnO	0	0.052	0.066	0.108	0	0	0.06	0.011
FeO	0.047	0.146	0	0.047	0	0.047	0	0

SiO2	0	0	0	0.054	0	0	0.014	0.053
K2O	0.001	0	0	0	0	0.001	0	0.007
CaO	56.568	56.974	56.786	56.574	56.45	56.568	56.472	56.599
TiO2	0.005	0	0	0	0	0.005	0	0
V2O3	0	0.023	0.038	0	0	0	0	0.012
NiO	0.007	0	0.095	0.002	0	0.007		
Total	102.036	103.419	101.616	102.018	100.91	102.036	104.688	104.286

Mineral	Apatite	Apatite	Apatite	Apatite	Apatite	Apatite	Apatite	Apatite
Assoc. No.	II	II	II	II	II	II	II	II
Na2O	0.051	0.103	0.03	0.023	0.067	0.012	0.07	0.028
F	4.261	3.963	4.085	4.295	4	3.946	3.43	3.778
MgO	0	0	0	0	0	0	0	0
Al2O3	0	0	0.017	0.004	0.002	0	0	0
Cl	0.03	0.047	0.029	0.035	0.049	0.007	0.009	0.035
P2O5	44.462	44.178	45.324	43.879	44.023	44.524	40.166	39.814
Cr2O3	0.062	0.022	0	0	0	0	0.024	0
MnO	0.043	0	0	0.013	0.093	0.016	0.142	0.081
FeO	0.088	0.111	0.025	0	0	0.051	0.06	0.032
SiO2	0	0.02	0.025	0.009	0	0.036	0	0
K2O	0.01	0	0.004	0	0.001	0	0	0
CaO	57.393	57.406	57.629	57.384	57.333	57.781	55.504	54.77
TiO2	0.01	0	0	0	0	0	0	0
Continued								
V2O3	0.036	0	0	0.049	0.004	0	0	0
NiO	n.a.	n.a.	n.a.	n.a.	n.a.	n.a.	n.a.	n.a.
Total	106.446	105.849	107.167	105.691	105.572	106.373	99.406	98.538

Mineral	Apatite	Apatite	Apatite	Apatite	Apatite	Apatite
Assoc. No.	II	II	II	II	II	II
Na2O	0.013	0.021	0.039	0.016	0.028	0.06
F	3.732	3.495	3.787	3.853	3.712	3.502
MgO	0	0	0	0	0	0
Al2O3	0	0.008	0.015	0.004	0	0
Cl	0.061	0.029	0	0.011	0.033	0.031
P2O5	40.676	39.913	41.259	40.511	40.826	40.349
Cr2O3	0.11	0	0.097	0.004	0.053	0
MnO	0.067	0	0	0.055	0.059	0
FeO	0	0	0.072	0.137	0	0
SiO2	0	0.019	0.022	0	0.005	0
K2O	0	0.009	0	0	0	0
Continued						
CaO	55.241	55.033	55.493	55.531	55.897	54.91
TiO2	0	0.017	0	0.025	0	0
V2O3	0	0.008	0.026	0	0	0.018
NiO	n.a.	n.a.	n.a.	n.a.	n.a.	n.a.
Total	99.9	98.554	100.809	100.147	100.612	98.869

Table 14 Composition of selected trace element and REEs in Apatite from Pathargora

Association No.	Mg24	V51	Mn55	Sr88	Y89	Pb208	Th232	U238
II	49.94	bdl	190.06	104.07	710.42	0.457	0.506	0.911
II	197.69	3.59	162.41	120.93	930.97	0.74	0.97	1.18
II	57.92	bdl	152.2	81.74	425.89	0.689	0.23	0.745
II	235.4	7.96	130.23	133.05	763.91	4.47	310.01	4.14
Association No.	Mg24	V51	Mn55	Sr88	Y89	Pb208	Th232	U238
II	2529.08	bdl	3595.73	2355.1	3339.22	33.51	3.72	16.76
II	36.84	1.13	110.75	74.27	428.88	0.783	0.17	0.438

II	29.29	bdl	118.77	159.54	635.12	0.571	0.197	0.306
II	27.27	0.78	136.34	127.63	857.42	0.519	0.672	0.69
II	563.53	bdl	232.87	86.43	313.63	8.63	1.8	9.48
II	2096.9	53.5	828.44	342.37	564.77	19.95	0.75	4.5
II	28.53	0.56	124.58	140.79	519.23	0.338	0.284	0.652
II	35.54	bdl	142.6	135.63	624.57	0.433	0.424	0.743
II	267.51	14.55	384.8	529.48	5137.47	75.81	1.25	560.46
II	38.33	bdl	148.6	151.56	492.18	1.14	0.29	0.761
II	35.57	1.28	137.4	116.29	657.97	0.291	0.227	0.689
II	43.93	0.92	131.14	113.04	918.45	1.57	2.81	1.28
II	34.08	1.6	123.31	112.49	603.82	0.323	0.311	0.94
II	47.57	0.81	98.75	94.76	1523.51	1.07	2.99	1.53
Continued								
II	40.97	0.53	125.76	117.65	715.76	0.281	0.32	0.519
II	30.25	0.47	112.85	112.5	627.28	0.278	0.194	0.681
II	29.94	1.61	105.37	109.18	647.64	0.229	0.24	0.564
II	34.7	1.41	117.08	104.52	682.49	0.352	0.352	0.552
II	40.54	bdl	141.92	130.65	662.51	0.278	0.379	0.711
II	48	0.76	138.93	95.09	967.39	0.388	0.62	0.751
II	37.88	0.269	118.72	109.73	511.94	0.242	0.306	0.657
II	44.92	0.6	133.5	128.13	695.03	0.239	0.336	0.615
II	38.6	0.257	123.02	111.03	557.42	0.274	0.305	0.64
II	36.37	bdl	109.85	117.99	580.15	0.322	0.126	3.19
II	21.45	0.48	88.2	116.91	582.39	0.262	0.146	0.614
II	7850.54	bdl	bdl	38.56	46.48	bdl	20	123.04

Assoc. No.	La139	Ce140	Pr141	Nd146	Sm147	Eu153	Gd157	Tb159	Dy163	Ho165	Er166	Tm169	Yb172	Lu175

II	54.71	210.4	34.54	200.18	91.68	6.71	160.86	29.23	170.76	30.24	70.45	8.25	46.01	5.32
II	27.32	80.92	17.26	128.36	81.84	2.99	128.53	22.94	269.8	24.27	78.05	7.82	47.67	5.47
II	22.1	98.57	17.35	103.47	49.14	3.27	85.4	15.36	83.25	16.54	37.82	3.8	22.86	3.07
II	60.85	186.44	35.59	269.42	147.72	5.92	240.59	42.42	208.42	34.81	72.61	8.38	53.58	6.13
II	729.72	3311.81	416.5	641.94	1057.7	29.3	786.95	124.65	498.03	41.06	156.91	7.42	17.37	11.8
II	25.28	116.59	23.41	159.3	76.07	3.97	104.05	17.76	98.73	16.27	35.65	4.11	24.01	3.24
II	3.67	21.37	5.1	39.7	34.48	2.25	93.39	19.49	138.21	25.93	62.13	7.53	42.84	5.15
II	28.21	146.42	30.16	189.89	99.28	4.88	154.96	29.94	181.25	34.39	80.17	9.63	53.05	6.64
II	19.63	170.27	23.51	111.27	38.14	6.99	151.39	21.33	161.43	22	72.22	8.39	59.02	7.12
II	140.13	292.29	70.47	1553.16	145.93	12.43	197.04	33.47	106.5	18.78	13.55	12.31	26.88	2.33
II	16.94	88.68	17.13	102.14	57.31	6.23	94.88	19.21	115.56	22.11	51.22	6.69	41.83	5.06
II	18.75	80.47	16.27	103.88	60.45	6.24	112.84	22.66	138.18	26.85	64.24	8.16	47.2	5.86
II	13647.99	19895.29	1798.24	8546.3	1772.14	116.88	1752.11	214.9	1514.58	175.18	278.35	40.64	332.69	21.76
Continued														
Assoc. No.	La139	Ce140	Pr141	Nd146	Sm147	Eu153	Gd157	Tb159	Dy163	Ho165	Er166	Tm169	Yb172	Lu175
II	29.5	102.02	18.45	120.06	61.52	8.7	101.27	17.79	111.69	21.08	51.51	7.13	44.18	5.17
II	52.08	222.45	36.49	201.78	83.83	5.24	123.14	23.57	145.89	26.75	61.15	7.58	41.88	5.01
II	426.22	1278.54	167.46	850.41	289.35	13.46	289	49.28	259.72	42.15	87.76	9.45	51.75	5.92
II	38.72	189.7	31.15	181.39	91.09	5.86	130.42	23.19	144.94	26.27	61.71	7.32	39.24	4.81
II	383.33	1337.35	189.59	893.53	321.09	15.53	352.23	60.04	314.75	59.87	125.78	13.85	74.49	8.51
II	58.47	221.14	38.67	218.76	96.03	6.18	138.46	26.6	158.43	30.53	69.77	8.23	45.94	5.38
II	26.56	125.29	23.11	143.24	77.27	5.52	119.63	22.71	137.15	25.83	57.92	7.45	37.77	4.92
II	24.5	109.46	21.42	142.9	76.3	5.43	124.22	23.56	147.56	27.16	65.01	7.79	43.7	5.49
II	47.03	212.07	38.45	222.04	105.33	5.81	142.84	25.96	153.21	28.17	66.15	7.58	41.17	5.15
II	33.02	146.08	26.83	150.44	78.69	6.65	126	24.55	149.54	28.3	65.2	7.72	45.08	5.05

II	51.49	230.1	38.84	241.08	128.49	5.76	204.98	39.42	221.38	41.67	88.38	9.78	56.61	6.77
II	26.76	124.66	21.99	123.44	64.16	5.39	92.16	17.93	108.23	21.4	50.73	6.1	34.07	4.33
II	35.44	127.11	21.49	126.33	65.62	4.46	116.96	22.43	147.49	29.95	69.99	8.26	45.89	5.39
II	33.99	136.18	26.29	148.07	71.41	6.13	108.65	19.65	120.52	22.8	55.57	6.56	36.44	4.47
II	14.27	77.89	15.02	103.8	60.29	5.59	107.29	20.55	126.91	24.61	56.41	7.26	37.73	4.7
II	10.66	50.9	11.78	84	53.28	4.94	98.39	19.13	121.91	23.41	56.3	6.92	37.93	4.73
II	bdl	51.27	bdl0.00	125.55	bdl	bdl	141.35	21.87	bdl	bdl	63.2	20.03	93.04	21.09

Table 15 Biotite composition from Pathargora and results from thermometry

Association no.	II	II	II	II	II	II	II	II	II	II
SiO2	38.512	39.427	38.63	39.443	38.749	38.552	39.322	38.822	38.892	38.563
TiO2	1.07	0.719	0.833	0.868	0.891	0.694	0.625	0.808	0.801	0.888
Al2O3	14.75	14.609	14.514	14.556	14.471	14.928	14.654	14.795	14.641	13.711
Cr2O3	0	0	0	0.07	0	0	0.095	0.071	0.231	0.015
FeOtotal	14.464	15.313	15.528	15.773	15.435	16.658	15.851	15.728	15.473	14.726
MnO	0	0	0.08	0	0.149	0.063	0.063	0.071	0.084	0
Continued										
MgO	14.161	15.351	14.771	15.332	14.803	14.871	14.892	14.574	14.823	15.36
NiO	0.093	0	0.039	0.195	0.056	0.098	0.092	0.117	0	
CaO	0.07	0.006	0.008	0	0	0	0.063	0.053	0.061	0.013
Na2O	0.09	0.151	0.091	0.12	0.065	0.121	0.072	0.156	0.135	0.105
K2O	8.786	9.628	10.032	9.768	9.683	9.746	9.552	9.199	9.134	9.467
F	0	0	0	0	0	0	0	0	0	0
Cl	0.197	0.169	0.307	0.213	0.215	0.161	0.254	0.174	0.16	0.196
Temperature at 0.3 Gpa/10 km depth (in °C)	458.17151	401.22348	418.29304	416.13232	425.00087	394.68421	390.95704	418.49379	417.23935	425.82048

Table 16 Major element geochemistry of magnetite from Mohuldih and Turamdih

Association No.	Association T							
Na2O	0.006	0.053	0.056	0.038	0.035	0	0.035	0
F	0.008	0.002	0.003	0.007	0.006	0.004	0.006	0.006
MgO	0.089	0.036	0.047	0.026	0.053	0.048	0.053	0.034
Al2O3	0.027	0.088	0.049	0.09	0.017	0.038	0.017	0
Cl	0	0.004	0.004	0	0	0	0	0
P2O5	0	0	0.003	0.009	0.009	0.032	0.009	0
Cr2O3	0	0	0	0	0.029	0.025	0.029	0.053
MnO	0.006	0.014	0.015	0.077	0.03	0	0.03	0.081
FeO	92.279	91.714	93.433	92.023	91.314	92.288	91.314	91.406
SiO2	0.014	0.016	0.017	0	0.015	0.013	0.015	0.001
K2O	0	0	0	0	0	0	0	0
CaO	0	0.013	0	0.002	0.028	0	0.028	0
TiO2	0.01	0	0.03	0	0.003	0	0.003	0.013
V2O3	0.402	0.407	0.407	0.415	0.429	0.438	0.429	0.463
NiO	n.a.	n.a.	n.a.	n.a.	n.a.	n.a.	n.a.	n.a.
Total	92.841	92.347	94.065	92.686	91.969	92.885	91.969	92.058

Association No.	Association T							
Na2O	0	0	0	0	0	0	0	0
F	0.006	0.002	0.006	0.006	0	0	0	0
MgO	0.034	0.028	0.033	0.033	0.053	0.053	0.043	0.043
Al2O3	0	0.003	0.002	0.002	0.008	0.008	0.04	0.04
Cl	0	0.007	0.015	0.015	0.003	0.003	0.011	0.011
P2O5	0	0.008	0.041	0.041	0	0	0	0
Cr2O3	0.053	0	0	0	0.013	0.013	0	0
MnO	0.081	0	0.004	0.004	0	0	0.062	0.062
FeO	91.406	91.967	91.416	91.416	92.24	92.24	91.713	91.713
SiO2	0.001	0.021	0.032	0.032	0	0	0	0

K2O	0	0	0.02	0.02	0	0	0.003	0.003
CaO	0	0.034	0.001	0.001	0.002	0.002	0.001	0.001
TiO2	0.013	0	0.019	0.019	0	0	0.071	0.071

Continued

Association No.	Association T							
V2O3	0.463	0.533	0.55	0.55	0.551	0.551	0.563	0.563
NiO	n.a.	n.a.	n.a.	n.a.	n.a.	n.a.	n.a.	n.a.
Total	92.058	92.603	92.14	92.14	92.871	92.871	92.506	92.506

Association No.	Association M						
Na2O	0	0	0	0	0	0	0
F	0.001	0.017	0.001	0.001	0.001	0.017	0.001
MgO	0.043	0.058	0.043	0.043	0.043	0.058	0.043
Al2O3	0.035	0	0.035	0.035	0.035	0	0.035
Cl	0.034	0.016	0.034	0.034	0.034	0.016	0.034
P2O5	0.01	0.002	0.01	0.01	0.01	0.002	0.01
Cr2O3	0.014	0	0.014	0.014	0.014	0	0.014
MnO	0	0.071	0	0	0	0.071	0
FeO	91.088	91.987	91.088	91.088	91.088	91.987	91.088
SiO2	0.173	0.029	0.173	0.173	0.173	0.029	0.173
K2O	0.026	0.001	0.026	0.026	0.026	0.001	0.026
CaO	0	0.017	0	0	0	0.017	0
TiO2	0.012	0	0.012	0.012	0.012	0	0.012
V2O3	0.175	0.248	0.175	0.175	0.175	0.248	0.175
NiO	0.017	0.064	0.017	0.017	0.017	0.064	0.017
Total	91.628	92.509	91.628	91.628	91.628	92.509	91.628

Association No.	Association M						
Na2O	0	0	0	0	0.056	0	0.006

F	0.017	0.001	0	0.002	0	0.002	0
MgO	0.058	0.043	0.111	0.047	0.053	0.047	0.015
Al2O3	0	0.035	0	0.021	0.009	0.021	0.003
Cl	0.016	0.034	0	0.023	0	0.023	0
P2O5	0.002	0.01	0.03	0	0	0	0
Continued							
Association No.	Association M						
Cr2O3	0	0.014	0.114	0	0.067	0	0
MnO	0.071	0	0	0	0	0	0.046
FeO	91.987	91.088	91.258	91.759	90.313	91.759	92.66
SiO2	0.029	0.173	0.013	0.006	0.013	0.006	0.01
K2O	0.001	0.026	0.001	0	0	0	0.021
CaO	0.017	0	0.004	0	0.006	0	0
TiO2	0	0.012	0	0	0	0	0
V2O3	0.248	0.175	0.311	0.215	0.296	0.215	0.322
NiO	0.064	0.017	0.15	0	0	0	0
Total	92.509	91.628	91.992	92.074	90.813	92.074	93.084

Table 17 Trace element geochemistry of magnetite samples from Turamdih and Mohuldih and results of magnetite thermometry

Association no.	Association T							
TMg (in °C)	469.9828891	387.1012526	414.0684181	448.3691416	347.6230256	335.23561	359.7550884	402.2219387
Li7	0.38	<0.30	<0.41	<0.36	<0.39	<0.231	0.23	0.79
Be9	1.22	0.17	0.16	0.32	<0.00	0.14	0.15	0.47
B11	<7.97	<5.22	<5.49	<5.80	<6.12	<4.92	<5.77	<4.93
Na23	4.48	<3.45	4.36	20.24	4.08	10.41	<3.57	19.1
Mg24	215.03	49.4	84.25	151.17	21.34	16.23	27.89	66.06
Al27	537.32	222.37	425.74	349.97	160.49	237.53	222.91	477.41
P31	<60.45	<50.62	<50.38	<54.41	<52.12	49.99	53.26	<43.97
K39	<37.01	<30.33	<30.69	<32.76	46.78	57.69	<29.58	31.05
Ca44	<547.23	<454.81	<464.98	<486.68	<494.17	<441.97	<454.67	<445.14

Sc45	<4.15	3.96	4.51	6.24	<3.81	<3.20	<3.60	<3.50
Ti49	197.52	153.67	226.59	224.7	174.47	126.63	209.96	140.1
V51	3782.04	4273.32	3920.83	3772.43	5505.87	3780.8	4754.75	4274.35
Cr52	<13.69	<11.23	23.89	98.34	<11.59	<10.36	11.83	106.73
Mn55	111.06	98.88	106.24	95.82	100.65	74.75	106.1	85.23
Co59	42.08	41.89	42.94	33.53	39.74	33.85	34.02	34.2
Ni60	415.55	433.31	416.11	435.72	562.5	378.64	425.75	403.98
Continued								
Association no.	Association T							
Cu63	1.07	<0.31	<0.48	<0.66	3.76	48.76	0.36	<0.45
Zn66	39.46	28.83	24.85	23.49	15.85	17.36	28.94	32.84
Ga71	51.24	43.71	47.66	44.85	45.91	43.04	48.13	45.52
Ge73	8.12	6.76	11.55	10.23	<6.10	5.03	6.26	7.77
Rb85	<0.42	<0.27	<0.29	<0.38	<0.42	0.32	<0.35	<0.32
Sr88	0.132	0.039	0.037	0.35	0.074	0.016	<0.130	0.21
Y89	0.21	<0.22	0.142	0.29	0.99	0.123	<0.173	2.52
Zr90	0.102	0.045	<0.00	0.63	77.9	0.151	0.24	111.52
Nb93	<0.18	<0.150	<0.163	<0.184	0.144	<0.154	0.079	<0.109
Mo95	<1.30	<0.68	0.58	<1.02	<1.28	<0.98	<0.97	<0.97
Sn118	2.26	1.75	<1.65	<1.73	<1.84	<1.53	<1.53	2.22
Sb121	<0.47	0.49	<0.66	<0.42	<0.38	<0.41	<0.41	<0.54
Cs133	0.024	<0.00	0.02	0.0098	0.013	<0.00	<0.050	<0.050
Ba137	0.62	<0.60	1.19	<0.52	0.8	0.37	0.24	0.98
La139	<0.00	<0.064	<0.099	0.013	0.017	<0.00	<0.065	<0.00
Ce140	<0.110	0.011	0.021	0.021	<0.00	0.019	<0.00	0.061
Pr141	<0.052	<0.061	0.017	<0.00	0.012	0.145	0.016	<0.00
Nd146	<0.00	<0.264	<0.00	<0.00	0.072	0.094	<0.00	0.16
Sm147	<0.00	0.134	0.126	<0.00	0.085	0.22	<0.00	<0.32
Eu153	<0.00	<0.00	0.016	<0.00	<0.00	0.014	<0.00	<0.00
Gd157	<0.00	0.061	0.057	<0.35	<0.00	0.102	<0.00	<0.00
Tb159	<0.00	0.0096	<0.00	<0.055	0.012	0.008	<0.00	<0.00

Dy163	0.085	<0.00	0.036	0.106	0.096	<0.00	0.033	0.25
Ho165	0.022	<0.00	0.018	<0.00	0.012	0.0081	<0.00	0.08
Er166	<0.00	<0.00	<0.00	0.026	0.24	<0.00	<0.00	0.53
Tm169	<0.00	<0.041	<0.089	<0.071	0.022	<0.073	0.023	0.048
Yb172	<0.00	<0.00	<0.00	0.077	0.47	<0.00	<0.00	1.02
Lu175	<0.053	0.019	0.0088	0.0088	0.06	<0.00	<0.00	0.26
Hf178	<0.00	<0.00	<0.164	<0.00	2.41	<0.00	<0.00	1.15
Ta181	0.02	0.0086	0.024	<0.00	<0.00	<0.00	<0.00	<0.042
W182	<0.00	<0.00	<0.00	0.229	<0.00	0.174	<0.00	<0.17
Au197	<0.108	<0.089	0.018	<0.109	<0.00	0.016	<0.090	<0.128
Continued								
Association no.	Association T							
Pb208	1.21	<0.119	1.46	0.313	1.22	0.52	0.284	1.48
Bi209	<0.114	<0.094	<0.151	<0.124	0.093	<0.110	<0.116	0.113
Th232	<0.00	0.018	<0.00	0.2	0.124	0.23	<0.00	0.76
U238	0.015	<0.00	<0.00	0.048	0.66	0.287	<0.00	3.25

Association no.	Association T							
TMg (in °C)	331.3556601	396.4993996	459.0389692	434.1497873	349.1743288	347.4859033	636.8491009	495.0761193
Li7	<0.206	<0.33	<0.30	<0.25	<0.240	<0.41	0.92	0.21
Be9	0.49	1.91	2.4	0.13	<0.90	<0.00	17.13	4.67
B11	<5.68	<6.55	<5.09	<4.84	<6.41	<5.71	<4.76	<3.87
Na23	<3.64	335.27	55.3	4.11	16.45	<3.52	141.44	106.39
Mg24	14.67	59.56	178.92	117.94	22.32	21.49	1823.37	312.91
Al27	115.08	463.25	377.83	290.23	192.31	197.85	1962.25	760.95
P31	<45.94	913.5	<42.82	<41.17	<44.20	<43.03	40.71	37.16
K39	<29.41	184.41	97.02	<28.03	<30.69	<30.93	305.47	133
Ca44	<476.38	<550.92	<444.03	<454.84	<490.48	<504.63	<462.51	<351.37
Sc45	<3.64	10.79	4.96	<3.77	<3.94	<4.11	35.89	6.45
Ti49	97.66	154.38	291.12	166.17	161.39	171.56	238.75	164.74

V51	4409.83	5541.53	4004.29	4221.64	4206.5	4505.29	4168.86	4359.94
Cr52	<11.07	<13.04	88.56	51.97	<11.89	<11.96	41.22	16.45
Mn55	83.43	93.84	104.42	82.45	89.23	97.76	92.03	83.62
Co59	30.68	38.96	32.96	30.08	37.29	39.01	39.48	34
Ni60	391.49	436.48	410.28	853.38	450.04	434.91	388.21	361.14
Cu63	16.14	1667.94	0.39	3.41	67.34	<0.49	82.73	0.83
Zn66	11.91	25.44	29.35	17.68	22.4	31.03	26.58	22.81
Ga71	43.36	45.5	40.14	36.14	37.54	41.28	40.04	35.08
Ge73	7.1	12.02	<5.30	8.12	<6.44	10.5	8.76	<3.27
Rb85	<0.33	<0.42	<0.37	<0.27	<0.36	<0.39	1.07	<0.26
Sr88	0.11	2.22	0.87	0.134	0.054	<0.144	4.09	3.24
Y89	0.24	7.82	2.1	<0.105	<0.31	0.13	5.31	2.98
Zr90	<0.24	54.62	3.11	0.035	0.59	<0.24	13.48	90.63
Continued								
Association No.	Association T							
Nb93	0.193	<0.179	0.32	0.123	0.042	0.11	1.68	0.43
Mo95	<1.07	9.54	<0.94	<0.83	1.02	<0.90	<0.88	<0.36
Sn118	<1.64	<2.28	<1.79	<1.96	<2.07	2.82	<1.98	<1.46
Sb121	<0.45	<0.74	0.72	<0.41	<0.52	<0.48	0.6	0.41
Cs133	0.0099	0.01	<0.066	<0.067	<0.00	0.038	0.114	0.063
Ba137	<0.47	16.88	1.01	<0.00	0.081	<0.00	4.81	3.37
La139	<0.00	0.43	0.056	<0.00	0.025	1.12	0.271	0.174
Ce140	<0.059	1.17	0.15	0.0082	0.079	<0.00	0.382	0.303
Pr141	0.017	0.166	0.022	<0.00	<0.00	0.026	0.089	0.095
Nd146	<0.00	1.13	0.091	<0.00	<0.00	<0.29	0.55	0.51
Sm147	<0.00	<0.64	<0.45	<0.00	0.18	0.064	0.39	0.37
Eu153	<0.00	<0.160	0.027	<0.00	0.015	<0.087	0.167	0.031
Gd157	0.058	1.42	0.1	<0.00	0.056	<0.00	1.16	0.61
Tb159	0.0091	0.258	0.031	<0.00	0.0087	<0.00	0.274	0.077
Dy163	0.18	1.89	0.43	<0.00	0.068	0.036	0.8	0.34
Ho165	0.037	0.297	0.14	<0.046	<0.00	<0.00	0.22	0.035

Er166	0.053	1.12	0.51	<0.00	<0.142	<0.00	0.53	0.196
Tm169	0.0084	0.131	0.063	0.0065	0.0079	<0.063	0.071	0.023
Yb172	0.039	1.62	0.43	0.031	<0.00	<0.208	0.86	0.33
Lu175	0.018	0.146	0.111	<0.00	0.0083	<0.00	0.112	0.058
Hf178	<0.00	1.41	0.076	<0.148	0.028	<0.00	0.46	0.79
Ta181	<0.046	<0.00	0.083	<0.00	0.016	<0.00	0.196	0.038
W182	0.198	0.257	0.156	<0.00	0.175	<0.00	1.42	0.231
Au197	<0.100	<0.091	0.014	<0.113	<0.087	0.016	<0.083	<0.085
Pb208	0.49	2.11	1.15	<0.089	0.227	<0.095	1.02	0.44
Bi209	<0.113	<0.159	0.284	<0.113	<0.088	0.083	0.193	<0.077
Th232	0.042	0.43	0.173	0.0064	0.023	0.0081	3.4	0.061
U238	0.271	6.22	0.62	0.096	0.131	0.011	0.75	0.281

Assoc. no.	Association M						
TMg (in °C)	298.254408	308.6690707	329.6868575	368.413812	304.7789298	355.1643858	441.4163303
Li7	<0.36	<0.39	0.33	<0.47	<0.44	0.38	0.53
Be9	0.22	0.4	2.13	0.85	<1.49	1.55	104.14
B11	<5.45	<6.33	<6.76	<6.74	<7.11	<5.53	<7.57
Continued							
Association no.	Association M						
Na23	4.91	7.36	47.37	88.33	43.82	95.27	211
Mg24	6.37	8.44	14.05	33.47	7.56	25.42	133.12
Al27	101.74	122.58	211.31	204.92	156.09	196.42	1395.95
P31	<61.73	<59.64	<56.93	<69.97	<61.92	57.6	<63.51
K39	<36.32	<36.10	86.75	109.23	56.36	64.14	551.77
Ca44	<596.06	<596.95	1518.06	<668.09	<580.55	<513.15	1368.41
Sc45	<4.49	<4.34	7.5	5.66	<4.64	<4.02	30.78
Ti49	451.74	80.29	191.69	119.93	78.23	85.92	342

V51	1891.99	1902.22	1995.66	1964.33	2097.87	1991.69	2119.86
Cr52	149.75	57.74	1936.95	946.82	199.17	486.48	442.26
Mn55	50.94	53.58	43.63	52.56	52.65	61.94	53.55
Co59	42.53	39.74	38.84	38.98	37.44	36.56	37.2
Ni60	390.84	410.8	352.86	400.88	400.57	358.75	384.51
Cu63	0.84	<0.42	4.67	1.07	5.66	5.37	0.98
Zn66	12.88	<6.56	26.49	22.52	<7.52	11.57	9.38
Ga71	20.09	22.62	14.67	16.91	23.24	25.02	34.33
Ge73	9.44	8.26	5.44	10.33	16.03	6.4	6.7
Rb85	<0.48	<0.49	1.36	<0.54	<0.45	<0.46	<0.53
Sr88	0.073	0.114	1.16	1.2	0.256	1.84	12.82
Y89	0.7	<0.23	4.73	<0.44	1.53	1.57	16.57
Zr90	28.64	0.21	5.66	<0.50	61.35	65.88	4.84
Nb93	3.56	<0.144	0.36	0.73	<0.31	0.27	0.85
Mo95	<0.66	<0.91	<0.59	<0.79	<0.62	<1.42	<1.26
Sn118	<2.09	<1.96	<1.94	<2.22	<2.19	<1.88	3.3
Sb121	<0.75	<0.77	<0.70	0.97	<0.77	<0.63	<0.75
Cs133	0.065	<0.066	<0.085	<0.114	<0.063	<0.084	0.022
Ba137	<0.00	0.53	1.28	1.98	<0.55	1.34	13.76
Continued							
Association no.	Association M						
La139	<0.00	0.016	0.279	0.254	0.35	0.124	0.5
Ce140	0.056	0.039	0.91	0.48	0.48	0.34	1.49
Pr141	0.011	<0.28	0.131	0.045	0.065	0.064	0.252
Nd146	0.072	<0.00	0.75	0.28	0.137	0.29	2.06
Sm147	<0.44	0.16	0.89	<0.53	0.24	<0.39	1.42
Eu153	<0.00	<0.110	<0.100	<0.00	0.042	0.035	0.44
Gd157	<0.40	0.14	0.29	0.076	0.22	0.123	4.14
Tb159	<0.00	<0.00	0.046	0.012	<0.059	0.019	0.72
Dy163	0.048	<0.00	0.78	0.094	0.138	0.23	4.41
Ho165	0.061	<0.00	0.187	0.024	0.047	0.049	0.8

Er166	0.14	<0.00	0.53	<0.217	0.167	0.14	1.61
Tm169	0.033	<0.00	0.17	0.011	0.064	0.036	0.208
Yb172	0.58	<0.00	0.4	<0.00	0.95	0.59	1.2
Lu175	0.06	<0.00	0.079	<0.00	0.08	0.133	0.172
Hf178	0.41	0.038	0.116	<0.00	1.91	2.46	0.034
Ta181	0.187	<0.00	0.031	0.021	<0.00	<0.00	0.13
W182	1.22	<0.00	0.84	3.08	0.54	1.35	6.52
Au197	0.024	0.022	0.023	0.023	<0.163	<0.153	<0.136
Pb208	0.3	<0.091	2.13	2.17	0.87	2.18	0.29
Bi209	0.184	<0.154	<0.132	<0.141	<0.130	<0.131	<0.142
Th232	0.09	<0.00	0.117	0.022	0.257	0.143	0.095
U238	0.67	0.03	0.279	0.062	1.43	1.16	0.087

Assoc. no.	Association M						
TMg (in °C)	411.9074847	439.3378943	434.264284	506.4938878	405.9988147	343.6067345	361.0599394
Li7	<0.25	0.48	<0.25	0.71	<0.34	<0.31	0.31
Be9	47.31	38.61	0.88	0.18	0.4	<0.00	1.16
B11	<6.16	7.7	<5.52	<6.22	5.32	<7.32	<4.53
Na23	98.64	126.48	207.08	33.24	26.21	<4.59	16.26
Mg24	79.71	128.49	117.97	369.38	70.1	19.58	29.11
Al27	736.97	668.52	6306.2	483.47	163.56	47.48	433.91
Continued							
Association no.	Association M						
P31	53.77	<57.07	424.07	96.01	53.84	<61.05	103.77
K39	136.65	192.89	89.94	<40.29	65.75	<41.97	58.46
Ca44	613.82	662.73	<521.25	<625.94	<459.23	<656.04	<441.45
Sc45	22.28	19.29	10.9	<4.95	<3.79	<5.32	<3.70
Ti49	208.04	184	45.28	431.42	100.01	34.09	71.93
V51	2065.56	1981.22	2262.47	2336.79	2403.35	2427.36	2318.56
Cr52	376.7	990.7	201.84	255.31	21.89	16.87	23.9

Mn55	52.36	51.98	149.02	162.03	142.13	137.52	152.87
Co59	37.96	38.75	27.6	23.25	24.28	23.98	24.99
Ni60	365.6	384.55	465.05	475.9	571.61	495.27	521.17
Cu63	8.58	2.88	32.02	5.37	6.09	<0.77	1.93
Zn66	26.98	49.98	22.45	25.91	37.82	31.69	22.91
Ga71	27.05	27.07	55.54	53.41	47.44	50.56	40.37
Ge73	7.77	5.76	12.11	11.69	15.25	6.98	5.34
Rb85	<0.42	0.75	<0.39	<0.49	0.71	<0.46	<0.189
Sr88	5.5	5.56	2.1	0.87	0.28	<0.130	0.132
Y89	14.26	12.5	5.67	1.23	3.77	<0.36	10.12
Zr90	31.13	0.137	159.5	4.65	58.92	0.33	128.65
Nb93	0.53	0.46	<0.213	1.41	0.98	<0.154	<0.110
Mo95	<1.31	<0.88	<1.07	<2.00	1.85	<1.64	<1.17
Sn118	<1.84	2.33	<2.03	<2.42	<1.74	<2.87	<1.74
Sb121	<0.62	0.79	0.44	0.91	<0.41	<0.69	0.52
Cs133	<0.067	0.072	<0.00	0.031	<0.00	<0.00	<0.00
Ba137	4.67	5.28	3.6	2.84	2.28	<0.59	0.59
La139	0.32	0.166	0.243	0.51	0.29	<0.00	0.122
Ce140	0.69	0.54	0.88	0.89	0.87	0.026	0.41
Pr141	0.109	0.064	0.069	0.14	<0.056	<0.085	0.046
Nd146	0.91	0.57	0.71	0.29	0.26	0.067	0.62
Sm147	1.14	1.29	0.17	<0.47	<0.29	0.16	<0.55
Eu153	0.108	0.07	0.043	0.035	<0.00	<0.00	0.038
Gd157	1.43	0.62	1.08	0.25	0.14	<0.40	0.55
Tb159	0.34	0.166	0.191	0.068	0.133	0.011	0.154
Continued							
Assoc. no.	Association M						
Dy163	1.98	1.19	1.51	0.62	0.78	<0.00	1
Ho165	0.6	0.46	0.192	0.039	0.222	<0.00	0.42
Er166	1.64	0.93	0.61	0.028	0.82	<0.00	1.69
Tm169	0.221	0.116	0.174	0.027	0.088	<0.00	0.222

Yb172	1.26	0.54	1.22	0.166	0.19	<0.00	2.33
Lu175	0.135	0.143	0.44	0.047	0.114	<0.060	0.223
Hf178	0.6	<0.00	3.61	0.128	0.87	0.037	3.53
Ta181	0.031	0.018	<0.00	0.088	0.099	<0.00	0.076
W182	4.21	0.38	0.73	0.56	0.38	0.038	0.071
Au197	<0.122	<0.116	<0.090	<0.119	<0.074	<0.159	0.037
Pb208	0.56	0.9	10.61	0.84	0.43	<0.152	0.94
Bi209	<0.128	<0.070	<0.121	<0.130	<0.074	<0.159	0.086
Th232	0.048	0.045	9.56	0.115	0.52	<0.00	14.3
U238	0.234	0.088	29.22	8.97	16.68	<0.00	11.14

Table 18 Major element composition and concentration of V in Apatite from Turamdih and Mohuldih

Association No.	Na2O	F	MgO	Al2O3	Cl	P2O5	Cr2O3	MnO
T	0.02	3.711	0	0.012	0.008	42.381	0	0
	0.003	3.787	0	0.023	0.016	43.064	0	0.021
	0.02	3.711	0	0.012	0.008	42.381	0	0
	0.02	3.711	0	0.012	0.008	42.381	0	0
	0.02	3.711	0	0.012	0.008	42.381	0	0
M	0.004	3.718	0	0.015	0.037	41.959	0	0.036
	0.002	3.906	0	0.015	0	42.995	0	0
	0.023	3.788	0	0	0.011	42.373	0.02	0
	0.011	3.582	0	0	0.013	43.368	0.01	0
	0.009	3.732	0	0.023	0.017	42.864	0	0
	0.043	3.807	0	0	0	41.209	0.034	0
	0.061	3.881	0	0	0.011	42.087	0	0.066
	0.039	3.899	0	0	0.021	41.032	0	0
	0.049	4.035	0	0	0.009	40.849	0.142	0.032
	0.043	3.807	0	0	0	41.209	0.034	0
	0.061	3.881	0	0	0.011	42.087	0	0.066

Continued								
Association No.	FeO	SiO2	K2O	CaO	TiO2	V2O3	NiO	Total
T	0	0	0	56.111	0	0.004		102.248
	0.054	0	0	56.238	0.013	0.01		103.229
	0	0	0	56.111	0	0.004		102.248
	0	0	0	56.111	0	0.004		102.248
	0	0	0	56.111	0	0.004		102.248
M	0	0.001	0.009	55.695	0.011	0	0	101.486
	0.085	0.035	0	55.985	0	0.024	0	103.048
	0	0	0	55.447	0	0	0.09	101.752
	0	0	0	56.334	0.01	0.012	0	103.34
	0.022	0	0	56.731	0	0	0.011	103.41
	0	0.094	0	56.403	0.017	0.015	0.07	101.692
	0	0.022	0	56.456	0	0.035	0.068	102.688
	0.037	0	0	56.707	0	0.066	0	101.8
	0.034	0	0	56.721	0	0.014	0	101.886
	0	0.094	0	56.403	0.017	0.015	0.07	101.692
	0	0.022	0	56.456	0	0.035	0.068	102.688

V in Association T apatite					V in Association M apatite									
1.42	1.02	2.13	2.09	<0.69	1.29	18.9	64.3	2.63	<12.88	0.87	2.86	1.29	24.8	<0.77	<0.72

Abbreviations used in the tables	n.a.	n.d.	b.d.l.	assoc.
	not analyzed	not detected	below detection limit	association